

DTIC FILE COPY

(2)

AD-A219 840

AFOSR TR-90-0355

AFOSR FINAL TECHNICAL REPORT

REPORTING PERIOD: 1 NOVEMBER 1986 - 31 OCTOBER 1989

FUNDAMENTAL STUDIES ON SPRAY COMBUSTION
AND TURBULENT COMBUSTION

DTIC
EXE
MAR 29 1990
S D

AFOSR GRANT 860016D

PREPARED BY:

W.A. SIRIGNANO, CO-PRINCIPAL INVESTIGATOR
G.S. SAMUELSEN, CO-PRINCIPAL INVESTIGATOR
R.H. RANGEL, ASSOCIATE INVESTIGATOR
C.-H. CHIANG, RESEARCH ASSISTANT
B.E. STAPPER, RESEARCH ASSISTANT

Approved for publication and
distribution unlimited.

DEPARTMENT OF MECHANICAL ENGINEERING
UNIVERSITY OF CALIFORNIA, IRVINE

SUBMITTED TO: J.M. TISHKOFF

1 JANUARY 1990

90 03 28 167

Contents

I SUMMARY	1
II INTRODUCTION	2
A Atomization Experiment	3
B Atomization Theory	4
C Turbulent Reactive Flows	4
D Vaporizing Droplet Calculations	5
III RESEARCH DISCUSSION	7
A Atomization Experiment	7
B Atomization Theory	15
C Turbulent Reactive Flow	24
D Vaporizing Droplet Calculations	35
IV REFERENCES	53
A Publications Resulting from AFOSR Grant	57
B Participating Professionals	59
C Degrees Awarded	59
D Interactions	60

Accession For	
NTIS CRA&I	✓ □ □
DTIC TAB	
Unannounced	
Justification	
By	
Distribution /	
Availability Codes	
Dist	Availability or Special
A-1	



I SUMMARY

A three-year program under AFOSR sponsorship has concluded. Four major tasks are described: An atomization experiment, an atomization analysis, a turbulent reactive flow analysis, and a vaporizing droplet analysis. The atomization theoretical and experimental studies consider the nonlinear distortion of a planar liquid fuel stream. Various modes of surface instabilities are identified and analyzed in detail. Critical values of parameters related to surface tension, stream velocities, disturbance wavelength, stream densities, and liquid stream thickness are identified as the separation between stable and unstable interfaces. Measurements of the resulting spray characteristics are also presented.

The analysis for turbulent reactive flows emphasizes molecular mixing and chemical reaction within a vortical structure. Isolated vortices are examined. The vortices are at the interface between two flows of different composition. Probability density functions (pdf) and concentration and velocity profiles are determined and compared to existing experimental data. Temporally-developing and spatially-developing mixing layers are simulated. Merging and pairing of vortices is shown to be the major entrainment mechanism. The larger values of the pdf on the high-speed-stream side of the simulated mixing layer agree with experiment but are shown to be caused by a velocity bias rather than by larger mixing rates.

The study of vaporizing droplets involves Navier-Stokes solution for the axisymmetric flow around and within fuel droplets. Extensions to the existing theory have been made in two major areas: (1) variable transport and thermophysical properties are considered and (2) interactions between neighboring droplets moving in tandem are analyzed. The dependencies of drag coefficients, Nusselt numbers and Sherwood numbers upon Reynolds number and transfer numbers are determined. The vaporization rates, droplet velocities, and spacing between droplets are determined as functions of time. Critical parameters dividing regions where droplets collide from regions where they separate are identified.

II INTRODUCTION

This final report details the work performed on each of four major tasks in the AFOSR-sponsored study. A brief description of each study is given in this section with a more detailed presentation given in the next section. A reader seriously interested in any of the tasks is strongly encouraged to read the publications that have resulted from this research. They are listed in Appendix A of this report.

While the funding has ceased and several publications have resulted on each of the four tasks, the work is by no means completed. Needs for continued study exist, and the investigators are committed to pursuing further research in each of the major areas.

The AFOSR and, in particular, Dr. Julian M. Tishkoff are acknowledged for their support of these efforts. Their understanding of the importance of these problem areas in aerospace science is deeply appreciated. The research effort has been reinforced in that it relates nicely to other ongoing research at UCI sponsored by other federal agencies (including another office in the Air Force) and industry.

The fundamental study has been productive in terms of research results leading to a high number of publications and presentations, including several invited talks and papers as indicated in the appendices. The investigators were very active in spray combustion and in turbulent flows before the three-year study began; the position of UCI in these fields has, however, been strengthened as a result of this study, and we believe it is leading nicely to further studies on these problems.

Some major indications of practical impacts are already evident. Several industrial organizations have sought recently to align themselves with UCI in the areas of spray combustion and atomization related to gas turbine combustors and liquid propellant rocket combustion. These organizations include: Allison Gas Turbine Division of General Motors, Pratt and Whitney (West Palm Beach), United Technologies Research Center (UTRC), Metrolaser, Societe Europeenne Propulsion (Vernon, France), and Mitsubishi Heavy Industries (Tokyo). Discussions about a related spray experiment have been conducted with Dr. T. Jackson of AFWRDC; an experiment to be performed by Dr. Jackson could be guided by theoretical efforts here. Similarly, an experiment being conducted by Professor L. Melton of the University of Texas and Dr. M. Winters of UTRC is being guided by our theories.

A Atomization Experiment

It is well known that the efficiency and stability of many liquid-fueled combustors can depend critically upon the initial sizes and velocities of the droplets formed upon atomization of liquid injected into the combustor. In this program, we have both an experimental approach and a theoretical/computational approach to address important questions about basic mechanisms for distortion of the injected stream and formation of ligaments and droplets. Relatively little understanding of these vital processes has existed.

The present study explores the basic mechanisms of breakup and addresses, in particular, the extent to which properties of the liquid affect breakup. Three liquids, selected with varying values of viscosity and surface tension, are introduced through a twin-fluid, two-dimensional nozzle. A pulsed laser imaging system is used to determine the sheet structure at breakup, the distance and time to breakup, and the character of the ligaments and droplets formed. Experiments are conducted at two liquid flow rates and five flow rates of co-flowing air. Two breakup mechanisms are identified. The first, termed "cellular breakup," exhibits waves of equal strength in the streamwise and spanwise directions, with membranes stretched between. In this case, the streamwise waves are broken off the sheet. The second, termed "streamwise ligament stretching breakup," occurs at low liquid and air flow conditions. It is dominated by streamwise ligaments with thin membranes of liquid stretched between them. The drop size distribution of the spray is characterized by the breakup mechanism. The cellular breakup, which is obtained by increasing the air and/or liquid velocity, results in larger drops at the centerline and slightly smaller drops near the edge of the spray. For the stretched streamwise ligament, the Sauter mean diameter (SMD) at the centerline remains constant, while the SMD increases significantly away from the centerline. Overall, SMD decreases with increasing air/liquid relative velocity. The liquid properties in the range evaluated do not change the breakup mechanisms but do contribute to an altered form of the breakup in terms of the time and length scales. The ethanol (lower surface tension compared to water and ethylene glycol) displays smaller scale structures on the sheet, and a greater tendency to breakup into droplets rather than form streamwise ligaments. The ethylene glycol (higher viscosity compared to water and ethanol) stretches further before breakup, which results in the streamwise ligaments

reaching smaller diameters before fragmenting into drops. The breakup time of the sheet is dependent on liquid properties and the relative velocity of the liquid and air. The ethanol (lower surface tension) demonstrates decreased breakup time, while the ethylene glycol (higher viscosity) exhibits increased breakup time relative to water.

B Atomization Theory

Linear and nonlinear analyses of planar liquid fuel injection have been conducted theoretically and computationally. The liquid-gas interfaces have been treated as vortex sheets that have density, as well as velocity, discontinuities across them. Surface tension is also taken into account. Two general cases have been considered: 1) surface disturbance wavelength is very short compared to liquid stream thickness and 2) surface disturbance wavelength is comparable or much greater than the liquid stream thickness.

The method of vortex dynamics is powerful in that full nonlinearities can be retained. The current method also allows for continual refinement in order to obtain the required resolution. The method does not resolve viscous layers, however. Since the calculations are two-dimensional, distortion of the stream but not break-up is predicted. Nevertheless, good estimates of major ligament dimensions can be obtained.

The results indicate that surface tension is a stabilizing factor in the roll-up of the vortical disturbances at the liquid-gas interfaces. The stability of various regions is identified in terms of a dimensionless wave number. For a liquid stream of finite thickness, two types of waves, shifted-symmetric and symmetric waves, were considered. The dependence of the critical dimensionless wavenumber (that divides stable from unstable domains) upon the ratio of stream thickness to wavelength was identified. For moderate or no surface tension, the vorticity tends to accumulate near one point in the wave, resulting in the tendency to roll-up the interface. Density ratio does affect the behavior.

C Turbulent Reactive Flows

The study addresses mixing and chemical reactions within vortical structures of the type found in turbulent mixing layers. A series of investigations has been performed in a sequence that adds more realism to the model. First,

an isolated vortical structure with molecular mixing and chemical reaction in the windings of the structure was analyzed. Then an infinite row of vortices simulating a temporally-developing mixing layer was studied. Next, the vortices in the infinite row were assigned different ages in order to simulate better a spatially-developing mixing layer. Finally, merging of the vortical structures was analyzed to allow for mixing layer growth.

The major results indicate a strong dependence of the mixing rate on the vortical strength as defined by the Reynolds number and a very weak dependence on Schmidt number. The probability density functions (pdf's) do show a peak on the high-speed-stream side of mixing layer as found in experiments. However, this is not indicative of a larger mixing rate on that side of the stream as interpreted by others; rather, it indicates that there is a velocity bias in measurement. The pairing and merging of vortices is found to be a major factor in the entrainment of fluid into the mixing layer.

D Vaporizing Droplet Calculations

The effects of variable properties and droplet spacing on droplet vaporization and drag are very important considerations for practical spray combustion. This computational study is aimed at improving our basic understanding and our computational data base in these areas. The theory has been extended to consider variable transport and thermophysical properties. Also, the behaviors of two droplets in a tandem trajectory are considered.

The extension to variable properties produces significant quantitative differences. Our study, which emphasizes higher ambient temperatures and oxidizing environments, has produced notably different results for drag coefficients, Nusselt numbers, and Sherwood numbers from the calculations of Renksizbulut and co-workers who emphasized moderate ambient temperatures and fuel vapor environments. In general, dependencies on initial droplet Reynolds numbers, ambient temperature, initial droplet temperature, and fuel characteristics were carefully studied. Correlations for drag coefficients, Nusselt numbers, and Sherwood numbers were found to depend primarily upon Reynolds number and transfer numbers.

Droplet trajectories were analyzed for two droplets interacting in tandem. Results indicated that droplet spacing could increase or decrease in time, depending upon various factors. The drag coefficient of the lead droplet tended to be similar to that of an isolated droplet until the droplets were separated by

only a very few diameters. Drag coefficients of the following or downstream droplet were lower than those of the lead droplet. Above some critical initial spacing, the droplet spacing would increase with time for droplets of the same initial size and velocity. The smaller the downstream droplet relative to the lead droplet, the more likely that separation of the droplets would occur. The nature of the heating of the surface of the downstream droplet changes as the two droplets become sufficiently close that the downstream droplet reaches the near wake of the lead droplet.

III RESEARCH DISCUSSION

A Atomization Experiment

Introduction

The atomization experiment is a study of the breakup of a two-dimensional liquid sheet in the presence of co-flow air shear. The objectives are to identify the mechanisms of sheet break-up and to relate these mechanisms to the fuel droplet distribution.

Related Research

Rizk and Lefebvre (1980) conducted some of the first research using a two-dimensional airblast atomizer. Their studies focused not on the breakup of the sheet, but on the resulting drop size distribution. They determined that SMD decreases with increasing air velocity, liquid flow rate, and air/liquid ratio, and that SMD decreases with decreasing initial sheet thickness. Beck, Lefebvre, and Koblish (1989) developed a two-dimensional airblast atomizer in which the shear air impinges at a 30° angle. They determined that SMD increases with increasing surface tension, and decreases with increasing air/liquid mass ratio. Increased viscosity was found to slightly increase drop size. Others have studied the break-up of the sheet. Sattelmayer and Wittig (1986), for example, studied sheet breakup in a prefilming two-dimensional airblast atomizer. They determined that the breakup process was periodic, and that the frequency of separation increased with increasing air velocity. They found that several liquid waves move to the edge of the sheet between each event in which the liquid is separated. Arai and Hashimoto (1985 and 1986) performed experiments using a two-dimensional nozzle placed inside a wind tunnel to provide a source for the coflowing shear air. They noted that the instability on the sheet consisted of two wave motions, a stationary wave in the streamwise direction, and a progressive wave in the spanwise direction. They showed that the sheet breakup length decreased with increasing relative velocity, and increased with increasing liquid velocity and viscosity. Using preliminary results with a two-dimensional airblast atomizer, Mansour and Chigier (1989) note a cellular structure which forms on the sheet as it disintegrates. The cellular structure appears as small membranes stretched between ligaments, and is attributed to the different length scales of turbulence in the shear air streams. Tokuoka, et al. (1985) experimented with the

effects of the angle of impingement of a shear air jet on a liquid sheet. They determined that at higher air velocities, the sheet breakup length decreased as the angle of impingement increased from 45° to 90° .

The present study addresses both the liquid sheet breakup, and the resultant droplet size distribution. In addition, the SMD distribution is resolved spatially. Parameters of interest include the liquid and co-flow air velocities and the physical properties of the liquid.

Experiment

The experimental apparatus consists of a test fixture and a supporting facility. By way of summary, the test fixture is a two-dimensional parallel flow plane sheet nozzle, a cross section of which is shown in Figure A-1. The nozzle consists of a pair of triangular wedges, which are separated by shims to achieve the desired thickness for the liquid sheet. The sheet that is produced is 4.7 cm wide and 508 cm thick. A Plexiglass plenum surrounds the wedges to contain the shear air as it passes on either side of the sheet. The air plenum converges slightly as it approaches the nozzle tip to maintain straight flow. A schematic of the shear flow facility is given in Figure A-2. The nozzle flow is directed downwards, and the liquid is driven through the system by a gear pump with a maximum capacity of 157 g/sec at 1.72 MPa. The two shear air lines can each deliver 0.126 kg/sec.

To properly image the atomization of the liquid sheet, a non-intrusive method for measuring the dimensions of the spray elements was created. A pulsed nitrogen laser (PRA Model LN1000) was used to back light the sheet. The short duration of the laser pulse (1 nsec) is an attractive feature for freezing the sheet dynamics. The UV laser pulse was expanded and directed to impinge on a sheet paper behind the liquid sheet. The fluorescence of the paper created a visible back light. The resultant image was photographed using a 35 mm camera (Pentax Superprogram) and Professional Ektachrome film (P800/1600). Developing was pushed two stops. An Aerometrics phase Doppler laser interferometer was used to obtain information on drop size distribution and on the axial velocity of the spray. The properties of the liquids used for are given in Table A-1. Three different liquids with widely varying physical properties (e.g., viscosity, density and surface tension) were chosen to examine the influence of liquid properties on sheet breakup.

Table A-1. LIQUID PROPERTIES

Liquid	Viscosity (Pa.sx10)	Surface Tension (mN/m)	Density (kg/m3)
Water, H ₂ O	0.89	72	998
Ethanol, C ₂ H ₆ O	1.39	22	789
Ethylene Glycol, C ₂ H ₆ O ₂	14.72	48	1114

The test matrix for the experiment is given in Table A-2. The shear air velocity of the sheet was varied from 0 to 60 m/sec, with the same velocity on both sides of the sheet. The liquid velocity was set at one of two values: 1 or 5 m/sec.

Table A-2. EXPERIMENTAL TEST MATRIX

Case	Velocity (m/sec)		
	Liquid	Air I	Air II
11	5	0	0
12	5	20	20
13	5	30	30
14	5	40	40
15	5	50	50
16	5	60	60
21	1	0	0
22	1	20	20
23	1	30	30
24	1	40	40
25	1	50	50
26	1	60	60

Results

Two mechanisms of sheet breakup have been identified in the experiments. The first of these, labelled in this study as "cellular breakup," occurs at higher relative air-to-liquid velocities, but where the breakup is well displaced from the nozzle tip. This breakup mechanism, illustrated in Figure A-3, is characterized by the presence of spanwise waves that are approximately equal in strength to the streamwise vortical waves. As the sheet is extruded by the shearing action of the air, the membranes stretch between the spanwise waves and the streamwise vortical waves, forming cell-like structures. Eventually, the streamwise vortices are stretched to the point where (1) the streamwise waves and connecting membranes burst, and (2) the spanwise waves separate into spanwise ligaments. The small droplets in the resultant spray distribution originate from the bursting membranes. Larger droplets are associated with the breakup of the streamwise waves. The largest droplets are associated with the fragmentation of the spanwise ligaments.

The second breakup mechanism, referred to as "stretched streamwise ligament breakup," occurs at low liquid velocities. As shown in Figure A-4 for Case 22, this mechanism is dominated by the streamwise vortical waves in the breakup process. As the sheet is stretched by the co-flowing air, the streamwise vortices amplify with thin liquid membranes stretched between. The sheet is a corrugated structure with the membranes stretched sinusoidally about the plane of the sheet. A side view of this process is presented in Figure A-4b. As a result, the membranes are stretched by the co- and counter-rotation of the bounding vortices. When the membranes burst, the liquid film forms small drops, while the vortical waves form streamwise ligaments. These ligaments are then stretched by the shearing action of the air, transit to higher rotating velocities, and finally fragment into relatively large drops when the surface tension forces can no longer keep the ligaments intact.

Measurements of drop size distribution were made at two liquid velocities and three air velocities. Figure A-5a shows the size distributions for a sheet with a liquid velocity of 5 m/sec and air velocities of 50 and 60 m/sec (a 40 m/sec case produced drop sizes that exceeded the capability of the instrument). These curves demonstrate the drop sizes produced as a result of the cellular breakup mechanism. In this case, the breakup is uniform, as the membranes, the streamwise ligaments, and the spanwise ligaments break

up along the centerline of the spray. The drop size decreases at the edges of the spray because the angular momentum generated by the cellular breakup mechanism is not sufficient to penetrate the shear air jets. Figure A-5b shows the size distribution for a liquid sheet with a velocity of 1 m/sec and air velocities of 40, 50, and 60 m/sec. The SMD is constant along the centerline of the spray. Farther from the centerline, the SMD decreases with increasing air velocity. The minimum that occurs at the centerline is more pronounced at the lower air velocity case. This is a result of the stretched streamwise ligament breakup mechanism, in which the streamwise ligaments form a corrugated structure, as described in Figure A-4b. The thin membranes burst and are carried downstream along the centerline of the spray, while the streamwise ligaments are literally flung from the sheet with sufficient angular momentum to penetrate the shear air jets before breakup. Their subsequent fragmentation results in the formation of the larger droplets away from the center of the spray.

The variation in the liquid properties considered did not alter the general character of the two breakup mechanisms. However, the change in liquid properties had a pronounced effect on the time and length scales. Results are presented first for the influence of liquid properties on sheet breakup length and sheet breakup time. This provides a global perspective. Secondly, an examination of the effect of liquid properties is presented for both the cellular breakup and for the stretched streamwise ligament breakup mechanisms. For the latter, select conditions are presented where the photographs are most illustrative of the effects.

Although the liquid properties of the three liquids vary, the liquids were selected for their substantial variation in viscosity and surface tension. Water has relatively high surface tension and relatively low viscosity, ethanol has a three-fold lower surface tension and a slightly higher viscosity (50%) than water, and ethylene glycol has a viscosity much greater than water while its surface tension is slightly lower (30%). While it is likely that the liquid property effects presented are dominated by the differences in surface tension and viscosity, the variation in other physical properties and the limited number of fluids considered preclude an unequivocal determination of the precise role of viscosity and surface tension. As a consequence, the results are presented in terms of the generic names of the liquids with a parenthetical note of the relative values of surface tension and viscosity. Measurements were made of the length from the nozzle tip to the point at which the thin film membranes

fragment.

The results, presented in Figure A-6a, reveal that the higher liquid velocity leads to longer sheet breakup lengths. The breakup lengths were strongly correlated with the liquid sheet- air residence time of interaction. In Figure A-6b, the data are replotted in terms of interaction time and air-to-liquid relative velocity, where interaction time is defined as the breakup length divided by the liquid velocity at the nozzle tip. Based on these data, it is apparent that the liquid properties have a notable effect on the required air-liquid interaction time to breakup. The required interaction time of the ethanol is the shortest, while the ethylene glycol generally has the longest required time. The former is the lowest in surface tension and density of the three liquids, while the latter is the highest in viscosity and density.

The effect of liquid properties on the cellular breakup mechanism is presented in Figure A-7a by comparing the face view of sheets of water and ethanol for Case 13. Spanwise waves are formed closer to the injector inlet for ethanol (the lower surface tension liquid), and the cellular structures that form are smaller than those of water. It is also noteworthy that the streamwise ligaments fragment into droplets at the point the spanwise ligament breaks off, while in the case of water, the streamwise ligaments persist well downstream of the sheet breakup. The rapid breakup of the ethanol is illustrated effectively by a side view of sheets of water and ethanol (Figure A-7b, Case 26). Figure A-7c demonstrates the characteristics of ethylene glycol relative to the cellular breakup mechanism (Case 14). The high viscosity of the ethylene glycol dampens out the small scale structures in the sheet as it exits the nozzle. The spanwise waves develop in a shorter time, and appear more dominant than the streamwise waves. The cellular structure in the ethylene glycol sheet is not as uniform as in the water sheet. After the spanwise ligaments break off the sheet, the streamwise ligaments formed by the ethylene glycol (higher viscosity fluid) remain intact for a longer time than those formed by the water.

The stretched streamwise ligament breakup mechanism is also affected by the liquid properties. Figure A-8 is a face view of the three liquids at a low liquid flow condition (Case 22). The membrane formed between the streamwise waves is broken up rapidly into small drops in the case of the lower surface tension liquid (ethanol). The streamwise ligaments of the water break off and form globules and then break up further downstream into drops. The ethylene glycol stretches further, and the streamwise ligaments persist longer

than those for either water or ethanol.

Conclusions

Over the range of conditions and liquid properties examined, the following conclusions can be made:

- The sheet breakup follows one of two basic breakup mechanisms: cellular breakup or stretched streamwise ligament breakup. Cellular breakup occurs at higher liquid and relative velocities. It is characterized by the presence of spanwise waves that are approximately equal in strength to the streamwise vortical waves, forming cell-like structures. Stretched streamwise ligament breakup occurs at low liquid velocities or where the breakup occurs relatively close to the nozzle at relatively high air velocities. It is characterized by the dominance of the streamwise vortical waves in the breakup process.
- Changes in air and liquid velocity alter the basic mechanisms of sheet breakup.
- Sheet breakup length and time decrease with increasing relative air/liquid velocity.
- SMD decreases with increasing air/liquid relative velocity. The cellular breakup mechanism produces a uniform breakup which results in a uniform drop size distribution. The stretched streamwise ligament breakup mechanism results in a minimum in the SMD along the centerline.
- Inherent liquid properties (e.g., surface tension, viscosity, and density) do not appreciably affect the basic mechanisms of sheet breakup.
- Inherent liquid properties do affect the time and length scales of the sheet.

Future Work

The two-dimensional airblast atomizer that was developed for this study will be utilized to conduct additional unsupported research. Higher liquid

flow rates will be studied to determine at what point pressure atomization becomes a factor in the breakup and to add to the data on liquid momentum and relative velocity effects. The effect of air/liquid momentum ratio and of the relative velocity of the two shear air streams will also be evaluated.

B Atomization Theory

The mechanism of flame propagation in a liquid-fuel combustor is directly related to the spatial spray distribution resulting from the atomization process. Therefore, an understanding of this highly nonlinear problem is a crucial step in the design of efficient spray-combustion systems. Atomization is typically characterized by the formation of droplets with an average diameter much smaller than the thickness/diameter of the liquid sheet/jet. Our approach to the study of this process is characterized by considering a thin but finite sheet of one fluid bounded on each side by a surface of discontinuity (vortex sheet) separating it from another fluid of different density and including the effect of surface tension. When an interface is subject to an initial disturbance of infinitesimal amplitude, well known results from linear theory can be used to predict a dimensionless cut-off wave number which divides the wave number spectrum into a region of stable travelling waves and a region of exponentially growing waves (Lamb, 1932). The dimensionless cut off wave number is given by:

$$W_c = \frac{K\sigma}{\Delta U^2} \left(\frac{1}{\rho_1} + \frac{1}{\rho_2} \right) = 1 \quad (1)$$

where K is the wave number, σ is the surface tension, ΔU is the velocity discontinuity across the interface, and ρ_1 and ρ_2 are the densities of the two fluids $\rho = \rho_1/\rho_2$ where ρ_1 is the gas-phase density. Exponential growth corresponds to $W < 1$ and the optimum gas-phase density. Exponential growth occurs for $W = 2/3$. The dimensionless disturbance evolution is given by $\eta \sim \exp(\omega t)$ where:

$$\omega = i\pi \frac{\rho_2 - \rho_1}{\rho_2 + \rho_1} + 2\pi \frac{[(1 - W)\rho_1\rho_2]^{0.5}}{\rho_2 + \rho_1} \quad (2)$$

Here i is the imaginary unit so that the first term on the right hand side gives a travelling wave and the second one gives the exponential growth. The linear

result ceases to be valid when the disturbance amplitude is no longer small and later-time evolution of such a disturbance cannot be predicted.

In the initial calculations reported, only one side of the liquid sheet was considered. This can be interpreted as the case in which the sheet thickness is much larger than the wavelength. The situation under study is depicted in Figure B.1. The frame of reference is moving with a velocity $U_{\text{ref}} = (U_1 + U_2)/2$ where U_1 and U_2 are the velocities of the upper and lower fluid, respectively. The velocity discontinuity is $\Delta U = U_1 - U_2$.

In the vortex-method approach employed here, the initially disturbed vortex sheet is discretized into point vortices which then proceed to move under the location of the interface at successive time steps. The location of the vortices at any time is found by solving the equation:

$$\frac{d\tilde{x}_i}{dt} = \sum_{j=1}^N \tilde{u}_{ij} \quad (3)$$

where \tilde{u}_{ij} is the velocity induced by vortex j on vortex i and the summation is taken over all vortices. The velocity \tilde{u}_{ij} will, in general, be a function of the distance between vortices i and j , and of the strength (circulation) of vortex j .

The development of the vortex discretization method and the difficulties associated with it may be found in Fink and Soh (1978) and Van de Vooren (1980) and in the references cited therein. As a result of the density discontinuity across the interface and the presence of the surface tension associated with it, the circulation of an individual vortex does not remain constant in time. An evolution equation for the circulation associated with each vortex may be derived. In dimensionless form:

$$\frac{d\gamma_i}{dt} = 2At \left(\frac{d\tilde{u}_i}{dt} \right) + \frac{1}{4}At \frac{\partial}{\partial s} \left(\frac{\gamma_i}{\Delta s_i} \right)^2 \Delta s_i - We^{-1} \frac{\partial \kappa_i}{\partial s} \Delta s_i \quad (4)$$

where γ_i is the circulation of vortex i , $At = (\rho_2 - \rho_1)/(\rho_2 + \rho_1)$ is the Atwood number, $We = (\rho_1 + \rho_2)\lambda(\Delta U)^2/\sigma$ is the Weber number, Δs_i is the segment of the interface associated with vortex i , κ_i is the curvature of the interface at the location of vortex i , and s is the coordinate along the interface. Here we note that the first two terms on the right hand side of (4) are due to the density jump across the interface, and the last term is due to the surface tension σ . Realize that we are concerned with large velocity discontinuities

and small wave lengths λ so that the Froude number $Fr = (\Delta U)^2/(\lambda g)$ is large compared to one, and gravity effects are therefore negligible.

The evolution of an initially sinusoidal disturbance is determined by tracking the motion of the discretized vortices. This is done by simultaneously integrating the equations for the vortex location and circulation (vorticity). At $t = 0$ the interface is discretized into N vortices equally spaced along the interface coordinate s . As time evolves, some portions of the interface become stretched while other portions become compressed. Consequently, vortices located in stretching parts of the interface are further separated while those located in compressing parts of the interface tend to agglomerate. In order to handle this behavior, the technique employed here consists in rediscrctizing the interface after each integration step by means of linear interpolation and introducing a new vortex whenever the vortex separation measured along s increases beyond an established percentage of the initial separation. Once the interface is rediscrctized by redistributing the vortices, the individual vortex strengths are recalculated by interpolation of the functional variation of the strength versus the interface coordinate.

The evolution of an initially small sinusoidal disturbance such as the one described above is controlled by three dimensionless parameters which are: the density ratio, ρ (or equivalently, the Atwood number $At = (1 - \rho)/(1 + \rho)$); the dimensionless wave number, W (or equivalently, the Weber number $We = 8\pi/(W(1 - A^2))$) and the dimensionless initial amplitude, ϵ . The effect of viscosity, which is an important dampening mechanism, is not considered in this calculation. In all the cases considered in the present investigation, the dimensionless initial amplitude is $\epsilon = 0.025$ which falls within the range of validity of the linear theory. In fact, linear theory is used to obtain the initial vorticity distribution. We do not consider cases in which the disturbance amplitude is initially large.

The effect of weak surface tension can be seen in Figure B.2 which shows the time evolution of the interface shape (column (a)) and the vorticity distribution (column (b)) for the case of $\rho = 1$ and $W = 0.1$. At a dimensionless wave number $W = 2/3$, which corresponds to the maximum growth rate predicted by the linear theory, the surface tension is strong enough to prevent roll-up. This occurs because the high curvature gradient existing at the center of each wave restricts the accumulation of vorticity and the formation of the singularity. In Figure B. 3 we show the time evolution of the interface (column (a)) and the vorticity distribution (column (b)) for the case of $\rho = 1$

and $W = 2/3$. As seen in this figure, the qualitative features of the evolution are entirely different from those corresponding to zero or weak surface tension. Initially and up to about $t = 0.4$, the interface evolves as predicted by the linear theory with vorticity being accumulated at the midpoint. Beyond this point, however, the increasing curvature gradient at the center, together with the high surface tension coefficient, results in a strong restoring force that prevents the vorticity from further accumulating at the midpoint. Instead, two relative vorticity maxima are formed on the sides of the center point where the curvature gradient is smaller. Under this condition, the interface cannot roll-up but instead stretches with increasing amplitude. (Note that the y-scale is different in the last frame of Figure B.3.a.) This situation is particularly important here because it implies that the fastest growing waves (those for which $W \simeq 2/3$) do not roll-up. The foregoing discussion indicates that the unstable portion of the spectrum ($0 < W < 1$) is divided into at least two distinct regions, one corresponding to weak surface tension (or longer waves) in which roll-up occurs and the other corresponding to strong surface tension (or shorter waves) in which roll-up does not occur. In addition, there is the stable region of the spectrum (very strong surface tension or very short waves) corresponding to $W > 1$, as predicted by the linear theory. In order to illustrate the transition from the roll-up region to the non-roll-up region in the spectrum, Figure B.4 shows the variation with time of the maximum vorticity for selected values of the dimensionless wave number W . For $W = 0$, vorticity accumulates at the center of the wave and grows without bounds for increasing time to develop a vorticity singularity. When a moderate surface tension coefficient exists (or for slightly shorter waves), vorticity still tends to accumulate and form a singularity at the center of the wave although it does so at a lower rate ($W = 0.1$). At a higher value of the dimensionless wave number ($W = 0.4$), a transition period is observed between $t = 0.5$ and $t = 1.0$ during which an inflection in the maximum vortex strength curve occurs. During this transition period, the surface tension force is able to temporarily slow down further accumulation of vorticity. Eventually, enough vorticity has been concentrated and the vorticity runaway occurs. At values of the dimensionless wave number above 0.155, the growth is dominated by the restoring action of the surface-tension force and, although some roll-up occurs, a vorticity singularity is not formed. At larger times ($t = 2$), the maximum vortex strength is higher for $W = 1/3$ than for $W = 2/3$ because the former case involves substantially

more stretching of the interface. The effect of different density ratios is also investigated for $W = 2/3$, since this corresponds to the optimum growth rate. Figure B.5 illustrates the effect of the density ratio on the maximum vortex strength for $W = 2/3$. There is an optimum density ratio that results in the fastest accumulation of vorticity. This may be explained by the fact that, at the optimum dimensionless wavelength number ($W = 2/3$), the Weber number increases with decreasing density ratio thus producing the strongest surface-tension force when $\rho_1 \simeq \rho_2$. These cases are surface tension stabilized (shorter waves). As $\rho \rightarrow 0$ the importance of the surface-tension force is diminished (longer) waves, but the gradual shift of the center of vorticity accumulation results in stable traveling waves. These cases are inertially stable.

The next effort was aimed at extending the mathematical and numerical model described above (see also Rangel and Sirignano, 1988) in order to simulate the behavior of a finite-thickness liquid sheet in contact with a stream of air on each side of it. In this context, we should note that our previous analysis of a single interface represents the limit of an infinitely thick sheet or, more realistically, a case in which the sheet thickness is much larger than the disturbance wavelength and the disturbance amplitude. Linear theory may be used also in the finite-sheet case to predict the initial growth of disturbances on the liquid sheet. Figure B.6 is a schematic of two limiting situations that can be investigated.

We consider the surface-tension-affected Kelvin-Helmholtz instability of a finite-thickness sheet of an inviscid fluid in contact with two semi-infinite streams of a different fluid. Figure B.6 illustrates the two configurations investigated. In both cases, the undisturbed thickness of the sheet is $2d$ and the velocity difference across each interface is ΔU . We considered temporal instabilities so that periodic boundary conditions are used at $x = 0$ and $x = \lambda$. In our frame of reference and in the absence of a disturbance, the sheet moves with velocity $-U$ while the semi-infinite streams move with velocity U . Two possible disturbance modes are considered and illustrated in Figure B.6: shifted symmetric waves (a) and symmetric waves (b). These are defined below.

The linearized equations for the inviscid shear flow of a fluid sheet are (Squire, 1953):

$$\nabla^2 \phi_1 = 0, \quad \nabla^2 \phi_2 = 0, \quad (5)$$

where subscript 1 refers to the fluid on one side of the sheet and subscript 2 refers to the fluid within the sheet. The fluid on the other side of the sheet need not be treated explicitly if symmetric or shifted-symmetric conditions are used. The kinematic and dynamic conditions at the interface are:

$$-\frac{\partial \phi_1}{\partial y} = \frac{\partial \eta}{\partial t} + \frac{1}{2} \frac{\partial \eta}{\partial x}, \quad (6)$$

$$-\frac{\partial \phi_2}{\partial y} = \frac{\partial \eta}{\partial t} - \frac{1}{2} \frac{\partial \eta}{\partial x}, \quad (7)$$

$$(1 + \rho) \left(\frac{\partial \phi_1}{\partial t} + \frac{1}{2} \frac{\partial \phi_1}{\partial x} \right) - (1 + \rho^{-1}) \left(\frac{\partial \phi_2}{\partial t} - \frac{1}{2} \frac{\partial \phi_2}{\partial x} \right) = \frac{W}{2\pi} \frac{\partial^2 \eta}{\partial x^2} \quad (8)$$

where

$$W = \frac{2\pi\sigma}{\lambda(\Delta U)^2} \left(\frac{1}{\rho_1} + \frac{1}{\rho_2} \right) \quad (9)$$

is the dimensionless wavenumber, σ is the surface-tension coefficient, λ is the disturbance wavelength, ΔU is the velocity difference across the interface, ρ_1 and ρ_2 are the densities of the fluids, and $\rho = \rho_1/\rho_2$ is the density ratio. The dimensionless variables are the time t , the parallel and normal coordinates x and y , the velocity potential ϕ , and the location of the interface η . The characteristic length and time used in the nondimensionalization are λ and $\lambda/\Delta U$, respectively. The previous equations are solved by means of modal analysis for the cases of shifted-symmetric and symmetric waves. In both cases the interface initially located at $y = d$ is perturbed according to the relation: $\eta_1 = \exp[i(\omega t + 2\pi x)]$, where ω is the dimensionless complex frequency. For the shifted-symmetric waves (also referred to as antisymmetric (Squire, 1953) or sinusoidal waves), the interface initially located at $y = -d$ behaves as $\eta_2(x, t) = -\eta_1(x + \frac{1}{2}, t)$, whereas for the symmetric or dilational (Hagerty and Shea, 1955) waves, the interface at $y = -d$ behaves as $\eta_2(x, t) = -\eta_1(x, t)$. In addition, the boundary conditions away from the interface require that the disturbance vanish as $y \rightarrow \infty$.

Shifted-symmetric (sinusoidal) waves:

In this case, the solution of Eqs. (5) that satisfies the kinematic boundary conditions and the conditions far from the sheet yields the velocity potentials

as:

$$\phi_1 = i(\omega + \pi) \exp[i(\omega t + 2\pi x)] \frac{\exp[-2\pi(y - h)]}{2\pi}, \quad (10)$$

$$\phi_2 = -i(\omega - \pi) \exp[i(\omega t + 2\pi x)] \frac{\sinh(2\pi y)}{2\pi \cosh(2\pi h)}, \quad (11)$$

where $h = d/\lambda$ is the ratio of the half thickness to the wavelength of the undisturbed sheet.

The dimensionless complex frequency ω is obtained from the dynamic condition, Eq. (8) as:

$$\omega = \frac{\tanh(2\pi h) - \rho}{\tanh(2\pi h) + \rho} \pi \pm 2\pi \left(\frac{\rho}{1 + \rho} \right)^{\frac{1}{2}} \frac{\{W[\tanh(2\pi h) + \rho] - (1 + \rho) \tanh(2\pi h)\}^{1/2}}{\tanh(2\pi h) + \rho}. \quad (12)$$

Exponentially growing waves occur when the second term of this equation becomes imaginary. Squire (1953) and Hagerty and Shea (1955) limited their analysis of Eq. (12) to the case of small density ratios ($\rho \ll 1$) as corresponds to a water sheet in air at normal conditions. Squire further limited his analysis to long waves so that the approximation $\tanh(2\pi h) = 2\pi h$ could be used.

The dimensionless thickness, $h = d/\lambda$, can be written as the product of H and W in order to unmask the presence of the wavenumber in h . The new dimensionless thickness H is given by:

$$H = \frac{d(\Delta U)^2}{2\pi\sigma} \frac{\rho_1\rho_2}{\rho_1 + \rho_2} \quad (13)$$

In the general case of arbitrary density ratio, the right-hand side of Eq. (12) becomes imaginary, implying the existence of unstable waves, when the dimensionless wavenumber is below a critical value ($W < W_c$). The critical dimensionless wavenumber is given by:

$$W_c = \frac{1 + \rho}{1 + \rho \coth(2\pi H W_c)}. \quad (14)$$

Equation (14) defines a critical dimensionless wavenumber below which unstable waves exist. In the limit of a very thick sheet ($h > 0.43$ for practical

purposes), unstable waves occur for $W < 1$. On the other hand, as the thickness decreases, the critical wavenumber decreases below 1. Eq. (14) also indicates that there is a finite thickness $H = H_c$ below which all shifted-symmetric waves are stable. This critical thickness corresponds to the value of H that makes $W_c = 0$ in Eq. (14). For $H < H_c$, the critical wavenumber W_c becomes negative. To determine H_c we note that, for H in the neighborhood of H_c , $H_c W \rightarrow 0$ and therefore $\coth(2\pi HW) \rightarrow 1/(2\pi HW)$ in Eq. (14). After simplifying one obtains:

$$H_c = \frac{1}{2\pi} \frac{\rho}{1 + \rho} \quad (15)$$

Symmetric (dilational) waves:

The solution of Eqs.(5) that satisfies the kinematic boundary conditions and the conditions away from the shift for the symmetric waves yields the same velocity potential (Eq. 10) for the fluid above the sheet, while the velocity potential for the fluid in the sheet becomes:

$$\phi_2 = -i(\omega - \pi) \exp[i(\omega t + 2\pi x)] \frac{\cosh(2\pi y)}{2\pi \sinh(2\pi h)}. \quad (16)$$

The expression for the dimensionless frequency is obtained again from the dynamic condition and is:

$$\omega = \frac{\coth(2\pi h) - \rho}{\coth(2\pi h) + \rho} \pi \pm 2\pi \left(\frac{\rho}{1 + \rho} \right)^{\frac{1}{2}} \frac{\{W[\coth(2\pi h) + \rho] - (1 + \rho) \coth(2\pi h)\}^{1/2}}{\coth(2\pi h) + \rho}. \quad (17)$$

Unstable waves occur for $W < W_c$ where:

$$W_c = \frac{1 + \rho}{1 + \rho \tanh(2\pi H W_c)} \quad (18)$$

Again, the critical dimensionless wavenumber approaches 1 as the half-thickness-to-wavelength ratio increases above 0.43 for practical purposes. In contrast with the shifted-symmetric waves, the critical wavenumber of the

symmetric waves is greater than zero for any finite H and remains greater than zero in the limit of an infinitely thin sheet, $W_c \rightarrow (1 + \rho)$ as $H \rightarrow 0$.

Our non-linear investigation is based, as it was in the single-interface case, on the vortex discretization method. It is described in detail by Rangel and Sirignano (1988). The existence of a second interface means that a second row of vortices, located a distance h below the first one, must be considered. This two-fold increase in the number of vortex elements translates into approximately a four-fold increase in computational time. Surface-tension and density ratio effects are included in the form of an evolution equation for the vortex strength of each interface. Other details of the procedure are basically the same ones described above and need not be repeated here.

Some results are shown in Figs. B.7. through B.11. These figures show the evolution of disturbances for different configurations of interest. Figure B.7 shows a situation that approaches the infinitely-thick-sheet behavior. Here the disturbance wavelength is one half of the liquid sheet thickness (note that the x and y scales are different) and each interface evolves almost independently of the other. Therefore, the roll-up proceeds as in that case. When the liquid sheet thickness is reduced so that the disturbance wavelength is twice the liquid thickness (Figure B.8), the effect of the other interface begins to become noticeable. In the limit of zero thickness the two air streams are stable because they have the same velocity. When surface tension is present, the roll-up features are gradually eliminated. At the most unstable case, the liquid sheet evolves as illustrated in Figure B.9, where it may be argued that two ligaments will be produced for each wavelength. The symmetric case is illustrated in Figs. B.10 and B.11 for two different sheet thicknesses. The roll-up features again disappear as the thickness is decreased, and only one ligament is formed for each wavelength of the disturbance. Thus, the symmetric mode appears to yield larger liquid ligaments and presumably larger droplets than the shifted-symmetric mode.

Further developments are expected to include a parametrization of the surface-tension and density-ratio effects for the finite-thickness liquid sheet perturbed in the symmetric and shifted-symmetric modes. Extension to the case of the two air streams moving with different velocities should follow. By studying the non-linear evolution of these disturbances, it is hoped that some inferences will be made about the size of the characteristic ligaments and effects of the various different parameters on this size.

C Turbulent Reactive Flow

This task comprises three parts. In the first part, molecular mixing and chemical reaction in an isolated vortex was investigated using the approach of Marble (1985). The second part considers a similar approach for the study of mixing within a vortex row (approximating a mixing layer), including the effect of the splitter plate in an approximate manner. In the third part, the fluid dynamics of vortex pairing and merging were added and their effect on molecular mixing was investigated.

Mixing and reaction in the field of a vortex were investigated in the first part of this task. The results are included in the work of Cetegen and Sirignano (1988) and summarized as follows.

The characteristics of the probability density functions (pdf's) for nonreacting and reacting scalars in the field of a viscous line vortex were explored in this study. The dependence of the pdfs on vortex strength and time at Schmidt numbers typical of gases and liquids were studied. The pdfs are characterized by two probability peaks at the unmixed concentrations far from the vortex center and a vortex core region where finite probabilities of intermediate concentrations exist. Other peaks of mixing are due to the molecular diffusion in the outer regions. As the vortex strength increases, the probabilities in the mixed core region become greater. The increasing vortex strength also steepens the local concentration gradients through stretching, although the probability of the high concentrations gradients decreases with higher vortex circulation since the interface layers within the vortical flow winding become thinner with increasing strain. The mixedness parameter (given by a second moment of the pdf) shows that molecular mixing is enhanced by increasing vortex strength. The mixedness appears to be proportional to $Re = \frac{\Gamma}{2\pi\nu}$ up to $Re = 500$. At large Schmidt numbers, the pdf exhibits two peaks at unmixed concentrations and a small peak in the core region.

Comparison of the nonreacting and finite rate chemically reacting scalar pdfs indicates the development of an additional probability peak at the depleted reactant concentration in the core region of the reacting vortex. However, the peaks at the mixed concentrations for the nonreacting vortex disappear for the reacting vortex.

The study of mixing of a passive scalar within a vortex row originating from a splitter plate has been described by Miralles-Wilhelm et al (1989). The major results are presented here.

Figure C.1 shows the distortion of the initially horizontal material line separating the two species at certain instants after the vortices are initiated ($Re = 50$). Note that each one of the viscous cores is activated periodically in time, so that the aging process of the vortical structures is considered here.

The instantaneous species concentration contours for a case where $Re = 50$ and $Sc = 1$ are presented in Figure C.2. As time increases and layers of both fluids roll-up into each other, diffusion takes place through the interface separating the species. The growth of the diffusion core in time is shown by the spread of intermediate concentrations into the free streams. The contours in both arms of each vortex far away from the center resemble those for the unperturbed flow, i.e. - a sudden change in the value of C . As one moves towards the vortical center, better mixing is caused by the intense interaction between the vorticity and the molecular diffusion. The concentration values in the central region are found to be close to the perfect-mixed value of $C = 0.5$, as shown by the irregularly shaped contours around the vortical centers. These characteristics were also verified for other Re and Sc cases.

In Figure C.3, the concentration profiles for the case $Re = 50, Sc = 1$ are shown, as measured by a probe located at different heights above the mixing plane originally dividing the two species. Notice that as the height y of the probe decreases approaching the mixing plane, a well mixed region is encountered (i.e. the vortex core). It is in this region where the process occurs more efficiently, as expected. On the other hand, when the height of the probe increases, an increasing tendency towards non-mixing can be observed, until no mixing at all is reached far away from the vortex center. In a frame of reference attached to the vortical center, it has been shown by Cetegen and Sirignano (1988) that the concentration profiles exhibit an antisymmetry so that $C(x, y, t) = 1 - C(-x, -y, t)$. That antisymmetry is not found here, for a frame of reference attached to a probe moving through the vortical structure. The oscillations in the concentration profiles are caused by the simultaneous rotation and translation of the vortical structures as they pass through the measuring probe. Each concentration jump represents the probe crossing the material interface across which diffusion is taking place, which is tightly wound at the time that the vortical center reaches the probe.

The probability density distribution constructed from these concentration profiles is shown in Figure C.4 for the case where $Re = 50, Sc = 1$. As noted before, the higher peaks correspond to the unmixed concentrations ($C = 0$ and $C = 1$) far away from the vortex center, i.e.-the unperturbed flow. Finite

probabilities of intermediate concentrations develop in the vortex core region as a result of mixing by molecular diffusion and vortex interaction. The probability of concentrations in the mid-range (0.4 - 0.6), therefore, increases in the core of the vortex, and the peaks at $y > 0$ for $C > 0.5$ and those at $y < 0$ for $C < 0.5$ are results of the vortex motion bringing the high concentrations from the lower plane to the upper plane and vice/versa.

The effects of the two important dimensionless parameters are shown in Figures C.5 through C.8. Both an increase in the Reynolds number and a decrease in the Schmidt number lead to a larger well-mixed region around the vortical center. In the first case, increasing the vortex strength enhances the mixing process, since the rolling-up of the fluid layers into each other is augmented. On the other hand, as Sc increases, the well mixed region is diminished because adjacent stratifications within the vortex have not diffused due to the low molecular diffusivity.

The numerical results for the pdf constructed with instantaneous data taken throughout the structure exhibit a characteristic antisymmetry whereby $pdf(y, C) = pdf(-y, 1 - C)$, while the experimental evidence (Dimotakis, 1986, 1989; Masutani and Bowman, 1986) (for pdf's constructed from time-varying data as the structure flows past a probe) shows that the peaks that occur on the high speed stream side of the flow are greater than those on the low speed stream side. For this reason, the relative difference between the pdf at a given (y, C) pair and its antisymmetrical counterpart $(-y, 1 - c)$ is plotted in Figure C.9. This plot shows a new variable:

$$R = \frac{(pdf)_{high-speed} - (pdf)_{low-speed}}{(pdf)_{low-speed}} \quad (1)$$

The numerical calculations and the shape of the graph reveal three important facts. First of all, R can be nonzero as shown at various y locations, and, therefore, antisymmetry is not found. Secondly, the pdf peaks for the high speed stream are not always greater than those for the low speed stream (R can be a negative quantity). The other important issue showed by this graph is that the absolute value of R is much greater when R is positive. This means that when the peaks in the high speed stream are greater than those in the low speed stream, the relative difference between them is much greater (of the order of 5 times) than that in the opposite case (when the low speed stream peaks are higher than the high speed stream ones). This last result tends to agree with the experimental results presented by Masutani

and Bowman (1986). The results also support the idea that these experimental results are a consequence of the measurement bias, rather than a result of a real difference in mixing rate. This idea is in disagreement with the conclusions reported by Dimotakis (1986, 1989), which are that a difference exists in mixing rate between the fluid streams.

The high speed side of the vortical structure moves faster on average towards the probe than the low speed side, so that the probe sees a different concentration profile and a different pdf from that seen in a frame of reference attached to the vortical structure. In the frame of reference moving with the structure, mixing rates are identical on the high speed and low speed sides, as shown in Figure C.10 for the time evolution of the pdf. These time-evolving pdf's are constructed using instantaneous data over the vortical structure.

Figure C.11 illustrates the characteristics of a spatially developing pdf. When the probe is located further downstream, the vortical structures reach it at later instants of time. Meanwhile, fluid is being mixed, developing the peaks at intermediate concentrations in time. In this way, as one moves downstream, the mixed cores are larger in size and the probabilities of finding concentrations in the mid-range are increased. The same characteristics regarding the difference between the high-speed and the low-speed streams are observed in these results. However, once the flow is developed, the pdf remains practically invariant as the probe is located further downstream. Insignificant numerical differences are found in the pdf computed when the probe is located at 6 or at 9 characteristic lengths downstream of the splitter plate. It is believed however that pairing and merging of the vortical structures would result in continued development of the pdf.

A theoretical explanation of the lack of antisymmetry of the concentration field can be obtained in terms of the conservation equation for the moment of the species concentration. This moment is an important characteristic of the pdf. Analysis of this equation yields:

$$\begin{aligned} \frac{1}{2}\bar{u}\frac{\partial\bar{C}^2}{\partial x} + \frac{1}{2}\bar{v}\frac{\partial\bar{C}^2}{\partial y} = \frac{1}{2}D\frac{\partial^2\bar{C}^2}{\partial x^2} + \frac{1}{2}D\frac{\partial^2\bar{C}^2}{\partial y^2} - \overline{u'C'}\frac{\partial\bar{C}'}{\partial x} \\ - \overline{v'C'}\frac{\partial\bar{C}'}{\partial y} - \overline{u'\bar{C}'}\frac{\partial\bar{C}}{\partial x} - \overline{v'\bar{C}'}\frac{\partial\bar{C}}{\partial y} - D\overline{\left(\frac{\partial\bar{C}'}{\partial x}\right)^2} - D\overline{\left(\frac{\partial\bar{C}'}{\partial y}\right)^2} \end{aligned} \quad (2)$$

In a frame of reference attached to the vortical structure, the first term on the left-hand side of this equation can be antisymmetric. In other frames of

reference after a Galilean transformation that term cannot be antisymmetric. Other terms are forced to be also non-antisymmetric in order to satisfy the conservation principle. From the calculations performed, the dominant terms are the third and fourth terms on the right-hand side, and the first two terms on the right-hand side of the equation, which are all non-antisymmetric. It is seen that the moment $C'C'$ and therefore the pdf will be modified by a Galilean transformation.

Figure C.12 shows the plot of the mixedness parameter as a function of the height above the mixing plane and the Reynolds number. Based on the analysis of these results, there seems to be a weak dependence on the molecular diffusion process, represented by the Schmidt number. This fact is in agreement with the results presented by Cetegen and Sirignano (1987). On the other hand, the effect of mixing enhancement by the vortical structures appears to be clear; an increase in the vortex strength (i.e. the Reynolds number) increases considerably the mixedness in the layer. The mixedness parameter presented here is based upon the pdf determined by the simulated experimental probe and therefore reflects the measurement bias. That bias causes a higher value of the mixedness parameter on the high-speed side. When the instantaneous data is used to construct the pdf, an antisymmetrical situation results, and the results for $+y$ and $-y$ collapse into one curve. Also, when an isolated vortex is considered, the local mixedness is higher away from the mixing plane, as compared to that for the infinite row of vortices. For a value of y near the mixing plane, the local mixedness is practically identical. For all the cases considered, a dependence on \sqrt{Re} is observed.

The mixedness parameter can be averaged over y , as in Cetegen and Sirignano (1987). Figure C.13 shows a comparison between the isolated vortex and the mixing layer approximation for this case. The calculations show a linear dependence on Re for the isolated vortex, and a dependence on $Re^{0.8}$ for the infinite row of vortices. The first of these results is in agreement with those reported by Cetegen and Sirignano. The non-linear behavior of the overall mixedness parameter f for the mixing layer could be explained by the presence of the surrounding vortices, which increase the shear as one moves away from $y = 0$, as compared to the case of an isolated vortex where there is pure rotation.

Figure C.14 shows the streamlines for the infinite row of vortices. Close to the vortical center the streamlines resemble those for an isolated vortex, but for increasing heights above the mixing plant the flow evolves to a parallel

flow. In this way, this increase in shear results in a decrease in the rolling up of fluid layers away from the mixing plane, and hence a decrease in the mixing process. This explains the difference in mixedness between the cases of the isolated vortex and the row of vortices for $y \neq 0$.

The analysis of vortex pairing and merging, which represents the third part of this subtask, has been investigated by means of vortex dynamics.

In the method used here, a continuous distribution of vorticity is discretized into vortex lines or vortex cylinders (sometimes named vortex points and blobs, respectively, because such is their appearance in the two-dimensional cross section). While a vortex line is singular and has zero cross-sectional area, a vortex cylinder has a finite core and produces a velocity field like that of a Rankine vortex. The vortex cylinder is thus sometimes viewed as an evolution from the vortex line if diffusion were allowed to act for some time. The use of finite-core vortex cylinders was introduced by Chorin and Bernard (1972) as a means of reducing the numerical instability inherent to this problem. For an arbitrary array of vortex lines, or for a representation of a vortex tube as a sum of a large number of vortex lines, the line vortex equations (Lamb, 1932) are employed to follow the evolution of the structure defined by the vortex array. When vortices with a finite cross section are used, these equations are corrected for vortices falling inside the core of another vortex. In radial coordinates, the velocity field produced by a finite-core vortex (Rankine vortex) is:

$$\begin{aligned} u_\theta &= \frac{\Gamma r}{2\pi r_c^2}; r < r_c \\ u_\theta &= \frac{\Gamma}{2\pi r}; r \geq r_c \end{aligned} \quad (3)$$

When the continuous and periodic distribution of vorticity represented by a vortex sheet of wavelength λ is approximated by a discrete distribution of vorticity with N line vortices per wavelength, these equations become:

$$\begin{aligned} u &= -\frac{1}{2\lambda} \sum_{j=1}^N \frac{\Delta\Gamma_j \sinh \kappa(y - y_j)}{\cosh \kappa(y - y_j) - \cosh \kappa(x - x_j)} \\ v &= -\frac{1}{2\lambda} \sum_{j=1}^N \frac{\Delta\Gamma_j \sin \kappa(x - x_j)}{\cosh \kappa(y - y_j) - \cosh \kappa(x - x_j)} \end{aligned} \quad (4)$$

where $\Delta\Gamma_j = \gamma_j\Delta s_j$ is the circulation associated with the segment of sheet Δs_j represented by vortex j .

Since the vorticity is simply convected by the flow field, the motion of the various vortex elements is obtained by integrating the equations

$$\frac{dx_i}{dt} = u_i, \quad \frac{dy_i}{dt} = v_i \quad (5)$$

An initial distribution of vorticity along any given line may become weakened or strengthened depending on whether the flow dynamics stretches or compresses the line. In order to retain the resolution implied by the initial discretization, two approaches have been adopted depending on whether vortex lines or vortex cylinders are employed. In the first approach, using vortex lines, numerical instability may occur because of the singular character of the velocity field in the vicinity of any of the vortices. To prevent the onset of this numerical instability, a rediscritization technique is used whereby the nonuniformly-distributed vortex elements are replaced by a new set of uniformly-distributed vortices after each integration step. This technique has been described in a study of interface instability using vortex dynamics (Rangel and Sirignano, 1988). Let (x_j, y_j) with $j = 1$ to N be the locations of N vortices defining a certain surface (a path in our two-dimensional view). Setting $s = s_1 = 0$ at the location of the first element (x_1, y_1) , the coordinate along the path is measured as:

$$s_j = s_{j-1} + \sqrt{(x_j - x_{j-1})^2 + (y_j - y_{j-1})^2} \quad (6)$$

At the beginning of the numerical calculation, the separation between any two consecutive vortices is the same for the whole array. After one time integration, the vortices move to new space locations (x_j, y_j) and, in general, the inter-vortex separations are no longer the same for all vortices. As demonstrated by Fink and Soh (1978), the approximation of a continuous distribution of vorticity by a discrete set of vortices deteriorates when the inter-vortex spacing does not remain the same for all vortices. In the rediscritization scheme employed here, the s coordinates are calculated with Eq. (6) and the total length, equal to s_{N+1} , is determined. For a closed array of vortices, there is no $N + 1$ vortex and, instead, the loop ends at the first vortex. The next step is to calculate a new and uniform inter-vortex distance given by s_{N+1}/N and determine the new s -coordinate of each vortex as:

$$s_i = s_{i-1} + \frac{s_{N+1}}{N} \quad (7)$$

with $s_1 = 0$. To complete the procedure, the new vortex locations (x_1, y_1) and strengths γ_i are determined by interpolation between the old locations and strengths, using s_j and s_i coordinates. In order to retain the initial resolution, a new vortex is introduced in the array whenever the vortex separation distance s_{N+1}/N exceeds the initial separation by a given factor (5 percent in our calculations). Since the overall circulation must be conserved according to Kelvin's theorem, $\Gamma = \sum \Delta\Gamma_j = \text{constant}$, this condition is used to monitor the accuracy of the calculations.

In the second approach, using vortex cylinders, no rediscritization is performed because the presence of a core prevents the growth of the smaller, numerically-related instabilities. Since the vortices are allowed to move closer to or farther away from each other, the initial resolution does not remain fixed in time. In order to prevent the resolution from deteriorating in regions where vorticity is being stretched and in order to eliminate unnecessary calculations in regions where the vorticity agglomerates, addition of new vortices and combination of vortices is performed. Whenever the separation between any two consecutive vortices decreases below a certain value (typically one half of the initial separation), these two vortices are combined and replaced by an equivalent single vortex. The location of the merged vortex is determined by a circulation-averaged mean:

$$x_m = \frac{\Delta\Gamma_i x_i + \Delta\Gamma_{i+1} x_{i+1}}{\Delta\Gamma_i + \Delta\Gamma_{i+1}} \quad (8)$$

and the circulation of the merged structure is the sum of the two contributing circulations:

$$\Delta\Gamma_m = \Delta\Gamma_i + \Delta\Gamma_{i+1} \quad (9)$$

On the other hand, when two consecutive vortices become too separated (by moving apart to twice their initial separation), a new vortex is introduced halfway between these two vortices:

$$x_n = \frac{x_i + x_{i+1}}{2} \quad (10)$$

The circulation per unit length of the new vortex is the average of the strengths of the two neighboring vortices:

$$\gamma_n = \frac{\gamma_i + \gamma_{i+1}}{2} \quad (11)$$

The circulation of the introduced vortex, $\Delta\Gamma_n$, as well as that of the neighboring vortices, $\Delta\Gamma_i$ and $\Delta\Gamma_{i+1}$, is calculated from their respective strengths, γ and the lengths Δs of the segments they represent.

We have investigated the rollup, pairing, and merging of vortical structures formed during the evolution of an inviscid vortex sheet subjected to a sinusoidal disturbance and one or more of its subharmonics. In this case, the surface of discontinuity is discretized into a large number of vortex lines or vortex cylinders, depending on the method of solution employed. A sinusoidal disturbance and any desired subharmonics are then applied to the interface. Corcos and Sherman (1984) investigated this problem including viscous effects using a finite-difference method. Acton (1976) studied the evolution of the inviscid vorticity field using vortex dynamics. Since no rediscrctization or insertion of the new vortices was performed, the structure of the eddy was lost once it was formed. With the method employed here, the initial resolution can be maintained to the extent of the calculation. In the following figures, lengths have been made dimensionless with the disturbance wavelength, λ , while time has been made dimensionless with a residence time defined as $\lambda/\Delta U$, where ΔU is the magnitude of the velocity discontinuity at the undisturbed interface. To illustrate the difference between the two numerical methods described above, Figure C.15 shows the rollup of a single disturbance at a dimensionless time of 2. In both cases the calculations are started with twenty vortical structures per wavelength. In Figure C15a, line vortices have been used with rediscrctization after each time step. This method retains the initial resolution at all times.

In Figure C.15b, vortices with a fixed core of radius equal to twice the spacing between vortices are used. This ratio follows the advice from Leonard (1980). In this case, merging and insertion of vortices is performed as explained above. Because the second method allows the vortices to get closer together, it results in a higher resolution of the rollup region. Note, however, that the first method does not require the use of a core to eliminate numerical instabilities. Note also that both methods predict essentially the same amplitude growth which further indicates that the main difference is in

the resolution of the core.

Figure C.16 illustrates a situation in which a sinusoidal disturbance and its first subharmonic, both of dimensionless amplitude 0.025, are simultaneously imposed on the interface at $t = 0$. These calculations correspond to the second method described above (using vortex cylinders and no rediscrctization), and the number of vortex elements n is indicated at each time frame. Figure C.16 shows how the presence of the first subharmonic forces the pairing of every two structures in the manner described in the experiments of Ho and Huang (1982). No complete merging occurs because there is no diffusion mechanism present to spread the vorticity away from the interface.

Figure C.17 shows the results for a case in which the second subharmonic is present in addition to the fundamental. In this case, grouping of every three structures occurs and, most importantly, the transverse thickening of the layer occurs more rapidly since there are now three structures rolling up together. (Note that the x and y scales in Figure C.17 are different from those of Figure C.16.)

Figure C.19 shows the amplitude of the disturbance as a function of time for the case of a single disturbance, a disturbance plus the first subharmonic (Figure C.16), and a disturbance plus the second subharmonic (Figure C.17). The exponential growth rate predicted by the linear theory is valid until a dimensionless time of 0.8, approximately. From then on, the single-disturbance grows slowly to a maximum and then actually decreases due to the strong shear generated by the resulting vortex row and the absence of viscous diffusion. The cases containing the first and second subharmonics continue to grow nearly linearly until a dimensionless time of 3. From this point on, the case containing the first subharmonic reaches a maximum amplitude and then decreases also due to the absence of merger in the presence of strong shear. The amplitude of the case containing the second subharmonic continues to grow linearly, although at a faster rate induced by the three structures that begin to roll up together. Eventually, as a result of shearing and the absence of viscosity, the amplitude of this case should also reach a maximum and start decreasing, although the calculations have not been extended beyond the stage shown.

The study of mixing during the pairing and merging of vortical structures has concentrated on the prediction of the diffusion of a passive scalar in the presence of one, two, three or more vortical structures. In addition to the study of the concentration or mass fraction field, there has also been a study

of the development of the probability density function during the pairing and merging. We have studied situations of temporal growth in which the instantaneous pdf indicates that mixing is antisymmetric. We have also studied cases in which the spatial development of the layer is approximated in the temporal growth studies by starting the calculations with a nonuniform distribution of vorticity. This nonuniform distribution of vorticity is such that the size of the vortices increases in the downstream direction, thus giving some sense of spatial development. Upstream and downstream of the calculation domain, periodic boundary conditions are still used and, therefore, the representation is only approximate.

Figure C.20 shows the evolution of the interface when four vortical structures are present. The two on the right are larger than the two on the left, thus the former are located downstream and pair first. In Figure C.21, the mass fraction contours of a passive scalar are shown. The initial distribution is a step function, with zero function, and one mass fraction below and above the interface, respectively. Figure C.22 shows the instantaneous pdf constructed at each time step corresponding to those of Figure C.21. As seen in this graph, the antisymmetry is lost, but there is no indication of preferred entrainment from either stream. This argument is further strengthened by examining the path lines of Figures C.23 and C.24. The path lines indicate where the fluid particles actually go and are different from the streamlines which merely indicate the direction of the velocity at each instant. The path-line plots of Figs. C.23 and C.24 indicate that, to this level of resolution, the same amount of fluid is entrained from above and below the interface and, thus, that no preferred mixing occurs.

D Vaporizing Droplet Calculations

There are two tasks in this study. The first task is the detailed analysis of a vaporizing droplet in a convective environment. The second task is the detailed examination of the interacting effects between two vaporizing droplets, which are moving in tandem with respect to the free stream, in an intermediate-Reynolds-number flow. This research has been focusing on the accurate investigation of the local transport processes as well as the overall parameters describing the system such as net drag force, heat and mass transfer around the droplets. The main objective is to obtain the relationship between the transfer coefficients and some important fluid parameters, such as heat and mass transfer numbers and Reynolds number, as well as geometric parameters, such as droplet spacing and size ratio.

We have considered internal circulation and transient heating of the liquid phase, the forced convection of gas phase, the transient deceleration of the flow and variable properties. It is then necessary to solve simultaneously the complete set of unsteady Navier-Stokes, energy and species equations, combined with appropriate boundary conditions. The nonlinear and highly coupled equations make the analytical solution almost impossible. We have to resort to an implicit finite-difference numerical algorithm.

The governing equations are represented in generalized coordinates which conform to changing boundaries due to decreasing droplet radii associated with liquid component evaporation. A pressure correction equation is employed to satisfy indirectly the continuity equation in the gas phase. The liquid stream function and gas pressure correction equations are solved by the successive over relaxation (SOR) method. The momentum, energy and species equations of the gas phase, as well as the vorticity and energy equations of the liquid phase, are solved by an alternating-direction-predictor-corrector (ADPC) method. The non-linear gas/liquid interface boundary equations are treated by a quasi-linearization technique and solved directly by the inversion of tridiagonal block matrices. The governing equations of motion, as well as the interface boundary conditions, are solved sequentially in an interactive sequence until convergence is achieved for each time-step of the calculation.

It is noted that the generation of the computational grid for the multiple-

droplet case requires more detailed considerations. The grid lines have to conform to the shapes of the droplet surfaces to avoid errors due to interpolation. In the present calculation, the TOMCAT code is employed to accommodate the changing boundary shapes due to droplet regression, as well as the changing droplet spacing due to drag differences. See Raju and Sirignano (1987) or Chiang and Sirignano (1990). The computational grid is generated from the solution of a system of two Poisson equations in which the source terms are used to control the attraction between grid lines. This quasi-linear elliptic system of equations is solved by finite difference discretization using the SOR technique.

Since the reference frame is fixed to the liquid droplet (the lead droplet, in the two-droplet arrangement), the evaluation of the drag force and its associated velocity correction for the gas phase are incorporated in the iterative process. In order to maintain a dense grid distribution at the droplet interface, the grid locations have to be adjusted at each time step to accommodate droplet surface regression. For the two-droplet case the adjustment of the inter-droplet spacing results in an update of grid coordinates as well. Obviously the metrics of the transformation have to be updated whenever the grid system is moved.

The overall procedure iterates the sequential solutions of the governing equations and boundary conditions with grid and relative velocity adjustment until convergence is achieved. The number of iterations required for convergence in the pressure-correction equation, as well as within the overall iteration loop, is dependent upon the physical parameters used in each case. For the cases of decreased vaporization rates or small relative velocity between two droplets, the requisite numbers are very much reduced. After convergence is reached, the drag coefficients and average Nusselt and Sherwood numbers are evaluated at prescribed time intervals.

Our production runs do provide some promising results toward a better understanding of the vaporizing droplets' behaviors. We expect these results to create an important benchmark for the evaluation of numerous other simplified models available today. These comparisons are essential since the results from the simplified models should be used extensively in practical applications.

The results are included in the works of Chiang, Raju and Sirignano [1989], Raju and Sirignano [1987, 1988], and Chiang and Sirignano [1990] and summarized as follows.

SINGLE DROPLET CALCULATIONS

The detailed analysis of a vaporizing droplet in a convective field with variable thermophysical properties has been examined in this study. A parameterization has also been conducted by changing the initial droplet temperature, ambient temperature, initial Reynolds number, fuel type, and droplet heating model.

The base case study is selected as a cold n-octane fuel droplet suddenly injected into the hot gas stream. The values of physical parameters in the base case are given in Table D-1. Table D-2 summarizes the main parameters used for different cases examined in this research.

The results are presented in the following five subsections. The first three subsections give a description of the local, as well as overall, behavior of the single droplet for the baseline case. The variation of drag coefficient due to different parameters is given in the fourth subsection. The subsequent subsection presents the possible correlations for the drag coefficient and Nusselt and Sherwood numbers. The time scale used for the following discussion is the gas-phase hydrodynamic diffusion time.

Results of the Global Flow Field

Typical contour plots of mass fraction, temperature, and vorticity, as well as liquid-phase streamlines and the gas-phase velocities, at time ≈ 25 are presented in Figure D- 1(a-e). The convective effect is apparent by the fore-aft asymmetry in each plot. The boundary layers surrounding the droplet can be easily observed from the gas-phase velocity distribution. At early times, there is no indication of flow separation because the separation is suppressed by the surface movement (which will be explained later). At later time the boundary layers only cover up to 138° in azimuthal position, and a near wake region appears behind the droplet. The magnitude of velocity has been reduced, owing to the retardation by the drag force. The temperature and mass fraction contours do show the presence of the boundary layer and wake. The diffusing fuel-vapor is convected downstream, forming a concentration wake at the rear.

The liquid-phase streamlines show a single large vortex, roughly resembling a Hill's spherical vortex, in the interior of droplet. The strength of cir-

ulation shows a decrease with time. The vorticity contours are concentrated at the front portion of the droplet and then are convected downstream. At later time the vorticity has been diffused outward and the intensity is weakened, mainly due to the reduction in Reynolds number. A small loop, which represents a recirculating eddy attached at the surface, is observed. When flow separation occurs, the distribution becomes highly asymmetric. The surface blowing inhibits the appearance of a small secondary internal vortex of opposite direction which might occur near the rear stagnation point.

The detailed droplet heating history may be seen from Figure D- 2(a-c). During the very early time (≤ 1) a large temperature gradient exists near the surface, and the motion of the liquid phase is negligible. The energy transfer mode within the droplet is dominated by the conduction. As the strength of internal circulation increases, the transport mechanism switches to convection gradually. The isotherms at time = 6 show the large temperature variation from the surface to the vortex center. The similarity between the isotherms and streamlines in the liquid phase shows the influence of internal circulation. The assumption of high Peclet number used in a vortex model (Prakash and Sirignano [1980], Lara-Urbaneja and Sirignano [1981], Tong and Sirignano [1982]) is reliable at this stage. When the gas phase shear stresses decrease, the circulation strength lessens gradually such that the convection region becomes smaller and the region for conduction grows again. This behavior is more evident for the lower transfer number case where the Peclet number is smaller.

Local Properties Along the Droplet Surface

Since the overall drag coefficient, Nusselt and Sherwood numbers of the droplet are very sensitive to the transporting processes occurring at the gas/liquid interface, it is necessary to have a detailed understanding of some important properties at droplet surface. The surface shear stress distribution at different times shown in Figure D- 3(a) indicates that the shear stress decreases with time. This can be realized by the following facts: (1) with the onset of surface motion, the velocity gradient at the droplet surface decreases; (2) the surface blowing effect, which increases the thickness of the boundary layer and reduces the velocity gradient, is growing as vaporization becomes stronger; and (3) as droplet heating continues, the mass fraction at

the surface also keeps increasing, thus yielding lower values of viscosity of the mixture.

The decrease of strength of the negative shear stress is due to the decrease of volume and strength of the wake recirculation which is mainly caused by the reduction of the Reynolds number.

The time variation of the surface tangential velocity distribution shown in Figure D- 3(b) seems to vary with $\sin\theta$ which is in qualitative agreement with the classical vortex solution. The surface tangential velocity, originally zero, is brought to a maximum by the shear stresses and then decreases as shear stresses diminish. It is also noted that the angular location of the maximum velocity remains unchanged except during the final period when the location of maximum shifts forward of the $\theta = 90^\circ$ plane.

The distribution of vorticity along the droplet surface during the transient development is very similar to that of the shear stress. The surface vorticity is obtained from

$$\omega_l = \frac{\mu'_g}{\mu'_l} \left[\frac{\partial V_{g,\theta}}{\partial n} - \frac{V_{g,\theta}}{a} + \frac{1}{a} \frac{\partial V_{g,n}}{\partial \theta} \right]_s - 2 \frac{\partial V_{l,\theta}}{\partial n} |_s \quad (1)$$

The dominating term is $\frac{\partial}{\partial n} V_{g,\theta}$ which is also the main term contributing to the shear stress. It is clear that $\omega \sim \frac{1}{\delta} \sim Re_g^{1/2}$. Hence it is expected that the effects of internal circulation, boundary layer blowing and reduction of gas-phase Reynolds number will cause the surface vorticity to diminish. If the flow separation point is determined by the point where vorticity changes sign, the results indicate that separation occurs at a very early time. When the surface starts moving, the separation is suppressed. At later time the strength of surface velocity is reduced, and the normal surface blowing velocity increases. As a result, the separation point moves in the upstream direction. This behavior is different from that of the low transfer number case where the surface velocity is usually small. The surface motion can only delay the onset of flow separation. The flow separation is observed throughout the droplet lifetime. The theoretical separation point for the liquid sphere (Clift, Grace, and Weber [1978]) moves rearward as the Reynolds number decreases with time. The prediction of the separation point for a vaporizing droplet is hence totally different from that for a nonvaporizing liquid sphere.

Figure D- 3(c) shows the pressure distribution on the droplet surface. The recirculation wake dissipates part of the kinetic energy. As a result,

the pressure cannot recover to the stagnation value. The pressure profile is essentially determined from the balance between the diffusive and convective transport of vorticity. Vaporization enhances the outward convection of vorticity and thus causes more pressure loss. However, the additional kinetic energy resulting from surface blowing is absorbed by the recirculation wake. This can result in some pressure recovery.

The angular variation of local Nusselt number at different times is shown in Figure D- 3(d). The Sherwood number behaves similarly. The temperature (or mass fraction) gradient at the surface, and thus Nu_{local} (or Sh_{local}), is greatest at the front stagnation point and decreases with polar angle; see also Figure D- 1(b) and D- 1(c). The minimum does not necessarily occur aft of the separation point, as for the case of low transfer number. The increase at the rear of the droplet is caused by the action of the recirculating wake. The reduction in the Nusselt and Sherwood numbers with time is mostly attributed to the decay in Reynolds number.

Figure D- 3(e) shows the time variation of the surface temperature distribution. The surface temperature is nonuniform during most of the droplet lifetime. The rise of temperature at the rear portion is predominantly caused by the hot far-stream fluid returned by the recirculating wake. After droplet heating begins to diminish, the surface temperature shows some degree of uniformity. However, the constant surface temperature assumption is improper when the droplet heating persists.

The transient development of surface normal velocity is shown in Figure D- 3(f). The gas surface normal velocity is primarily determined by the rate of evaporation. Hence, the normal velocity increases when the surface temperature increases with time. As the surface temperature approaches the wet-bulb temperature, the fuel-vapor mass-fraction at the surface remains constant and the boundary layer thickness keeps growing. As a result, the normal velocity decreases. The maximum normal surface velocity occurs at the front stagnation point, while the minimum is located near the separation point.

Obviously, droplet vaporization is an inherently transient process. A summary of transient droplet life history is presented in Figure D- 4. The results indicate that both transient droplet heating and reduction in Reynolds number persist during most of the droplet lifetime even though the droplet has reached practically wet-bulb temperature when only 20% of the mass is vaporized. These two transient effects constitute the major sources of the

unsteady behavior of this problem.

Overall Transfer Coefficients

We now switch our attention to the overall characteristics of momentum, heat and mass transfer to the droplet. Figure D- 5 shows the variation of drag coefficients of droplets initially at three different ambient temperatures (Cases 1, 2, and 3) as a function of hydrodynamic diffusion time. Also shown in this figure is the H-N-R (Haywood, Nafziger and Renksizbulut [1989]) drag correlation which is based on the numerical results of an isolated moving drop vaporizing in its own fuel vapor. The H-N-R correlation is given by,

$$C_D(1 + B_{H,film})^{0.2} = \frac{24}{Re_m}(1 + 0.2Re_m^{0.63}); \quad 10 \leq Re_m \leq 300 \quad (2)$$

where $B_{H,film}$ is defined to account for droplet heating. The gas film condition is the average of ambient and droplet surface conditions.

$$B_{H,film} = \frac{Cp'_{g,film}(T'_\infty - T'_s)}{L'_s} \left(1 - \frac{Q'_l}{Q'_g}\right)$$

Due to the sudden injection of the drop into a uniform flow-field, the time required for the flow-field to relax from the initially impulsive motion can be estimated as $\Delta t_{relax} \sim \frac{2R_\infty}{U_\infty} \sim 0.4$ diffusion times. During the initial relaxation period the drag coefficient falls rapidly. Subsequently C_d increases as a result of a reduction in the Reynolds number. However, for the higher ambient temperature case, where the large heat flux makes droplet vaporization grow fast during the early portion of its lifetime, the drag coefficient is therefore significantly decreased due to the boundary layer blowing. For all cases, C_d tends to increase with time during the final portion of the calculation, which implies that the reduction in Reynolds number takes control in determining drag coefficients. The H-N-R drag correlation does not seem applicable in our cases. The deviation can be as much as 20% of total drag.

Three components of drag coefficients are shown in Figure D- 6. It is clear that the major difference in total drag coefficients for the three different ambient temperature cases comes from the friction drag and also from the pressure drag coefficients. Higher surface blowing can reduce the friction drag by a large amount. The pressure drag coefficients increase steadily as

a result of the reductions in upstream velocity. It is noteworthy that the thrust drag is no longer negligible for the high transfer number case. The contribution from the $-V_{g,n}V_{g,\theta}\sin^2\theta$ term may account for more than a 10% in reduction of the total drag. This term physically represents the thrust force as the reaction of tangential momentum being convected radially outwards and serves to accelerate the droplet. The recoil force due to the impact of the outward flux, $V_{g,n}V_{g,n}\sin 2\theta$, is negligible.

Figure D- 7 shows the average Nusselt numbers of these three cases and their corresponding H-N-R Nusselt number correlations which can be expressed as

$$Nu_{film}(1 + B_{H,film})^{0.7} = 2 + 0.57Re_m^{1/2}Pr_{film}^{1/3} \quad (3)$$

The Nusselt number falls during the initial relaxation period. Further reduction in Nusselt number is attributed mainly to a Reynolds number reduction and an increase of boundary layer thickness due to surface blowing. Again our numerical results do not agree with the H-N-R correlation. However, the discrepancy becomes smaller during the final part of the calculation when the surface temperature approaches the wet-bulb temperature.

The Sherwood number, which represents the transient dynamics of the mass transfer, is shown in Figure D- 8. The general trend of variation is very similar to that of Nusselt number. The relaxation of large mass fraction gradient caused by the sudden injection of a droplet into the hot gas-stream contributes mainly to the early reduction of Sherwood number. A more general decrease of Sherwood number is then observed, which may be due to the decay of Reynolds number. Our numerical value is lower than the value predicted by the correlation of H-N-R which is given by

$$Sh_{film}(1 + B_{M,film})^{0.7} = 2 + 0.87Re_m^{1/2}Sc_{film}^{1/3} \quad (4)$$

where $B_{M,film} = \frac{Y_{f,s} - Y_{f,\infty}}{1 - Y_{f,s}}$

The Parameter Study

Results for different initial droplet temperatures (300K vs 400K as in Cases 1 and 8, respectively) are shown in Figure D- 9. It is very clear that for the higher initial droplet temperature case, the surface blowing effect is more significant than that of the lower droplet temperature case during a

large portion of the droplet lifetime. Hence, the former experiences lower drag than the latter. Figure D- 10 shows the portion of total heat flux that goes into heating of the drop interior. The droplet with higher initial temperature would spend most of the available heat energy for the evaporation process. On the contrary, the droplet with lower initial temperature has to spend most of the available energy to heat itself first, with the remaining energy for vaporization. The heating process for the low initial droplet temperature case is slower and will persist longer than for the high initial droplet temperature case. As the surface temperatures of both cases approach asymptotically the same wet-bulb temperature (i.e. same transfer number), the drag coefficient is essentially controlled by the Reynolds number. Also shown in Figure D- 9 is the solid sphere correlation (see Clift, Grace, and Weber (1978)) which can be grossly inaccurate due to the high mass transfer at the surface. Since the surface blowing effect is much stronger for the high initial droplet temperature case, the Nusselt and Sherwood numbers are smaller than those for the low droplet temperature case.

The effect of variable thermophysical properties is very important for the large range of temperatures considered in the present study. A calculation has been conducted by assuming constant properties (except for gas-phase density) that are based upon the values at the free stream (Cases 1 and 4). Since the global behavior is evaluated at the interface, where the mixture gas-phase composition is very different from the pure gas at the free stream, the constant property calculations are expected to predict totally different transfer coefficients. The results in Figure D- 9 show that the constant property case can overestimate the drag coefficient by 20% or more compared to the variable property case. The discrepancy is attributed to the change in thermo-physical properties at the interface and the change in the flow field caused by the property gradients.

Figure D- 9 shows a comparison of results from an infinite conductivity liquid-phase model, where the liquid-phase temperature is assumed to be uniform in space but varying with time (Cases 1 and 5). The no slip boundary condition is also applied at the droplet surface. The results indicate that the infinite conductivity case predicts higher drag during most of the droplet lifetime. For the infinite conductivity model, the liquid phase has to distribute all the available heat flux to the droplet interior. Thus, the surface temperature rises slowly resulting in a very weak vaporization rate, as well as in a high drag coefficient. The transient heating period is relatively short.

Because of the larger driving temperature potential, the droplet eventually receives more heat flux than that calculated from our model. As a result, the surface temperature does eventually increase very significantly, and the vaporization grows quickly while the drag coefficient is reduced significantly. The final portion of drag coefficient is primarily determined by the reduction of Reynolds number as already illustrated in previous cases.

Calculations for three different initial Reynolds numbers (Cases 1, 6, and 7) are presented in Figure D- 11. It is observed that a lower initial Reynolds number results in a higher drag coefficient at early times due to the smaller convective momentum transport which usually causes the lower pressure recovery at the rear of the droplet. It is also noteworthy that the three drag coefficients again asymptotically approach a certain form which is governed by the Reynolds number only. This is because the same effective transfer number has been reached for all three cases.

The final parameter study is concerned with the fuel volatility (Cases 1, 9 and 10). The more volatile fuel uses a large fraction of the energy flux to provide the latent heat for vaporization and vaporizes faster than the heavier fuels. The less volatile fuel spends most of the available energy to heat the droplet. As a result, the surface temperature rises very slowly and the effect of surface blowing is less noticeable. The reduction of drag due to surface blowing is more pronounced for volatile fuels as indicated in Figure 12.

Correlations for the Drag Coefficient, Nusselt and Sherwood Numbers

With the results of the above cases, which cover a wide range of transfer numbers, as well as Reynolds and liquid Peclet numbers, it is desirable to obtain the correlations of drag coefficient, Nusselt and Sherwood numbers as a function of some important parameters. Since these transport quantities are determined by the combined influence of surface blowing and vaporization, the internal circulation, and the unsteady effects related to the droplet deceleration, a complete correlation which covers a wide range of all parameters is not easy to achieve. The parameters and functional form selected in this work are the same as in the H-N-R's correlation. The following modified correlations for drag coefficient, Nusselt and Sherwood numbers, show a good agreement (within 4%, 2% and 6% discrepancy, respectively) with our numerical results as shown in Figure D- 5, D-7 and D-8.

$$C_D(1 + B_{H,film})^{0.32} = \frac{24}{Re_m}(1 + 0.41 Re_m^{0.405}) \quad (5)$$

$$Nu_{film}(1 + B_{H,film})^{0.7} = 2 + 0.46 Re_m^{0.6} Pr_{film}^{1/3} \quad (6)$$

for $.6 \leq B_{H,film} \leq 6$; $30 \leq Re_m \leq 250$

The correlation of Sherwood number is approximated by

$$Sh_{film}(1 + B_{M,film})^{0.7} = 2 + 0.46 Re_m^{0.6} Sc_{film}^{1/3} \quad (7)$$

for $.3 \leq B_{M,film} \leq 4.5$

The major difference between our modified drag coefficient correlation and the H-N-R correlation is the exponent of $(1 + B_{H,film})$. Our correlation has a higher exponent which emphasizes more reduction in drag coefficient by the effect of transfer number.

CALCULATION OF THE TWO DROPLETS MOVING IN TANDEM

In the present research, we extend the study of Raju and Sirignano [1988] to include the effect of variable properties. The single droplet code is modified with the addition of a grid generation routine and a treatment to the readjustment of the velocity of the downstream droplet, as well as the variation of spacing. This research obviously builds upon the single droplet results.

Table D-3 and Table D-4 summarize the values of physical parameters in the base case and the main parameters used for different cases examined in the present research, respectively. Since the problem involves a multidimensional variables, an exhaustive numerical study of all possible combinations of parameters would be extremely elaborate. Therefore, we have concentrated our attention on a detailed study of the interaction effects arising from the variation of Reynolds number, initial diameter ratio, and ratio of initial spacing to lead droplet diameter.

The results are presented in the following five subsections. The first three subsections give a description of the local, as well as overall, behaviors of the interacting droplets for the base case. Most of the results show that the behavior of the lead droplet is qualitatively in agreement with that of isolated droplet. Hence the discussion in these three subsections is primarily

concentrated on the behavior of the downstream droplet. The transient variation of the spacings for different initial spacing, initial size ratio, and initial Reynolds numbers is given in the fourth subsection. Subsection 5 presents a correlation for the drag coefficients of the lead droplet and the downstream droplet from the constant property calculation.

Results for the Global Flow Field

Figures D- 13(a-g) show the gas-phase velocities, as well as the contour plots of mass fraction, temperature, vorticity and liquid-phase streamlines, at time equals 2 when the spacing is reduced from 8 to 6. The spacings shown in the figures are nondimensionalized with respect to initial radius of the lead droplet. The gas-phase velocities plot clearly indicates the existence of recirculation zones behind the droplets. The wake length for the leading droplet is about one droplet diameter which is in close agreement with the single droplet analysis. There is only a small recirculation zone formed behind the second droplet. Due to the influence of the recirculation region of the first droplet, the velocities approaching the downstream droplet are less than the velocities upstream of the lead droplet. As a result, the relative velocity between the surrounding gas phase and the downstream droplet is considerably smaller than that of the lead droplet. It can be expected that the downstream droplet will receive less shear stress (less momentum transport from gas phase). This can also be illustrated from the diffusion and convection associated with the gas-phase vorticity at the gas/liquid interface. The magnitude of vorticity near the downstream droplet is remarkably smaller than that of vorticity at the region close to the lead droplet, as shown in the vorticity contours of Fig. D-13b. Also, the asymmetry of the vorticity distribution for the downstream droplet is not as apparent as that for the lead droplet. This means that the downstream droplet receives less convective effect from the gas phase.

In Fig. D-13c, the mass fraction contours show that a high concentration gradient occurs near the lead droplet while the concentration gradient is lower at the second droplet. The fuel vapor generated by the lead droplet is convected downstream and alters the mixture composition of the surrounding environment near the downstream droplet. The relatively rich fuel mixture is usually cold enough to change the surrounding thermal environment of

the downstream droplet significantly. The thermal boundary-layer thickness of the downstream droplet is larger than that of the lead droplet as shown in the isothermal contour plot in Fig. D-13d. Hence, the heat and mass transfer rates for the downstream droplet are much lower than those of the lead droplet due to the presence of fuel vapor.

The strength of the stream function in the liquid for downstream droplet is almost half of the strength for the lead droplet. This may be primarily attributed to the lower shear stress acting upon the downstream droplet. The liquid-phase isotherms of Fig. D-13g indicate that a thermal boundary layer exists at the interface for the lead droplet due to the convection effect. However, for the downstream droplet, it is not easy to identify the liquid thermal boundary layer. The heating mechanism for the downstream droplet is dominated by conduction. The smaller magnitude and more symmetric variation are two main characteristics for the liquid-phase vorticity of the downstream droplet. This also proves that the external flow can impose only little convective influence on the downstream droplet.

Local Properties Along the Droplet Surface

Figure D- 14(a) displays surface vorticity at different times as a function of angular position. As the downstream droplet approaches the near wake region of the lead droplet, it experiences less convection. As a result, the position for the maximum surface vorticity of the downstream droplet moves to the $\theta = 90^\circ$ plane. Interestingly, at time = 3, the surface vorticity at the rear portion is positive, and no flow separation may occur there. Since the downstream droplet is covered by the wake of the lead droplet at time = 3, the downstream droplet is in a very low Reynolds number flow field which makes separation impossible. The shear stress distribution is consistent with these conclusions as seen in Figure D- 14(b). The negative shear stress at the stagnation region of the downstream droplet is caused by the recirculating flow behind the lead droplet.

The tangential velocity, as seen in Figure D- 14(c), for the downstream droplet is much smaller than that of the lead droplet because of the lower shear stress acting on the surface.

Figure D- 14(d) demonstrates the pressure distribution. Due to the action of the recirculating wake, the pressure at the stagnation point of the

downstream droplet only slightly recovers from the pressure at the rear stagnation point of the lead droplet. As the spacing decreases, the recovery of the pressure at the stagnation point becomes less. It is expected that the pressure drag of the downstream droplet will become smaller when compared to that of the lead droplet as the droplets approach each other.

Figure D- 14(e) compares the local Nusselt number variation above the droplet surface for the two droplets. The decrease of the Nusselt number at the rear part of the lead droplet and at the stagnation region of the downstream droplet are caused by the approach of the downstream droplet. As the spacing is reduced, the increase of cold mixture density, combined with the decrease in velocities at the wake region, serve to retard the heat exchange. The increase of Nusselt number at the rear part of the downstream droplet is caused by the hot ambient stream entrained by the recirculating flow. A similar trend can be observed for the local Sherwood number as shown in Figure D- 14(f). Figure D- 14(g) gives the surface temperature distribution. The highly nonuniform distribution of the surface temperature for the downstream droplet is due to the slow circulation which cannot distribute energy efficiently in the streamwise direction. As a result, the distribution of surface temperature is similar to that of the local Nusselt number. The heat flux is diffused in the radial direction within the downstream droplet. It may cause a small cold region at the front and a large hot region at the rear of the droplet.

Overall Behaviors of the Two Droplets

In this subsection, the drag coefficient, Nusselt and Sherwood numbers, and average volumetric temperature for the lead droplet and the downstream droplet are presented. The results for an isolated droplet in the same convective flow field are also presented for comparison. Figure D- 15 shows that the drag coefficient of the lead droplet drops about 6 % from its isolated-droplet value due to the interaction with the downstream droplet. The discrepancy increases as the droplet spacing decreases. The downstream droplet experiences much lower drag because of the wake effect from the lead droplet. The three drag components are shown in Figure D- 16. The difference in friction drag seems to contribute most of the drag difference between the lead droplet and the isolated droplet. The sharp drop of the total drag at

the time when the two drops are about to collide is mainly attributed to the reduction in pressure drag. Figure D- 17 and Figure D- 18 present the overall Nusselt numbers, Nu , and average volumetric temperature, T_v , respectively. The difference in both Nu and T_v between two droplets indicate that wake effects tend to reduce significantly the heat transport to the downstream drop. For the lead droplet, the influence of the downstream droplet is not negligible even when the spacing is about four droplet diameters. Other results for the cases of separating drops show that the Nusselt numbers for the lead and downstream droplets behave as for the isolated droplet during the final period of calculation. The Sherwood number of the downstream droplet, shown in Figure D- 19, indicates a longer relaxation period for the mass exchange process, which is caused by the upstream droplet, throughout our calculation.

The Transient Variation of Spacing

The determination of whether two droplets are going to collide or separate after they are suddenly introduced into a combustor is of great interest. It can be easily shown that the droplet deceleration is proportional to its drag coefficient and inversely proportional to its radius. The change of spacing is proportional to the relative deceleration between two droplets. This can be expressed as follows:

$$\Delta S \text{ (differential change of spacing)} \propto (A_{d,2} - A_{d,1}) * (\Delta\tau_{Hg})^2 \\ \propto \left(\frac{C_{D,2}}{R_2} - \frac{C_{D,1}}{R_1} \right)$$

where A_d is the droplet deceleration and $\Delta\tau_{Hg}$ is a computational time step in gas phase hydrodynamic diffusion time scale. The subscripts 1,2 correspond to the lead and downstream droplet, respectively. Positive ΔS means that droplet separation occurs. Negative ΔS means that droplet coalescence prevails. In general, $C_{D,1}$ is larger than $C_{D,2}$. If R_2 is larger than or equal to R_1 , droplets will collide. On the contrary, if R_2 is much smaller than R_1 , droplet separation is most likely to occur.

The transient variation of center-to-center-spacings for the cases of different initial spacing is depicted in Figure D-"20. Droplet collision appears to be likely for initially equal-sized droplets, as long as the initial spacing is sufficiently small for the wake effects to be important. The drag coefficients of two droplets for initial spacing of 4, 8 and 16 are shown in Figure D- 21.

The smaller the initial spacing, the more the drag coefficient deviates from its isolated value for the lead droplet and the more the drag coefficient decreases for the downstream droplet. Figure D- 22 demonstrates how two droplets will separate or collide for the cases of different initial size ratio. The first observation is that the larger the difference in droplet size, the faster they approach each other (or separate). For the case of $R_2 = 0.75$, droplet separation occurs at a very early time, but eventually droplet coalescence prevails. The results of Raju and Sirignano [1988] indicate that there exists a bifurcation point depending upon the critical ratio of $R'_{2,0}/R'_{1,0}$ below which droplet coalescence becomes unlikely. They predict that $R_2 = 0.75$ is very close to the bifurcation point, so that the droplets spend more time under the influence of each other. Figure D- 23 displays the drag coefficients of two droplets for the cases of $R_2 \leq 1$. The drag coefficients of the lead droplets for the cases of smaller downstream droplet are all collapsed together. This means at this spacing the lead droplet receives little influence from the downstream droplet. The drag coefficients of the downstream droplets for the cases of droplet separation tend to increase with the reduction in Reynolds number. This is also the typical characteristic of an isolated droplet.

The influence of the initial Reynolds number for the case of droplet coalescence is shown in Figure D- 24. An increase in initial Reynolds number seems to increase the approach speed. Figure D- 25 indicates that by decreasing the initial Reynolds number for the case with droplet size ratio at the critical point, the droplet-motion pattern can be changed from coalescence to separation. However, for the case of small initial spacing, the initial Reynolds number does not play a role as shown by the results in Figure D- 26. From the results shown above, the initial spacing and initial Reynolds number are not as important as the droplet size ratio in the determination of droplet separation or coalescence.

Since the droplet interaction effects are determined by the combined influence of surface blowing and vaporization, the internal circulation, and the unsteady effects related to the droplet deceleration, a parameter study must cover a wide range of initial Reynolds number, size ratio, initial spacing, transfer number, etc., in order to obtain a meaningful set of correlations for the transfer coefficients. The correlations of the drag coefficient and Nusselt and Sherwood numbers for the lead and downstream droplet are still under investigation. Raju and Sirignano [1988] provided the following correlation for the drag coefficients of two droplets from the constant property

calculation.

$$C_{D,2} = \left(\frac{V_{\infty,1}^2}{V_{\infty,2}^2}\right)\left(\frac{R_2}{R_1}\right)C_{D,1} - 1.22\left(\frac{R_2}{V_{\infty,2}^2}\right)S_0^{-0.25}Re_{g,0}^{-0.18} \quad (8)$$

where $V_{\infty,i}$ is the relative velocity between far upstream gas phase and the i -th droplet.

The numerical results satisfy the above equation within 12 percent accuracy for the range of initial spacings between 4-30 and initial Reynolds numbers between 50-200.

Table D-1 VALUES OF PHYSICAL PARAMETERS USED IN THE ISOLATED DROPLET
BASE CASE COMPUTATION

Parameter	Value
Initial Reynolds number, gas phase $Re = 2a'_0 U'_{\infty,0} \rho'_{g,\infty} / \mu'_{\infty}$	100.0
Relative velocity of drop, m/s	25.0
Free stream temperature, [K]	1250.0
Combustor pressure, atm	10.0
Prandtl number, gas phase	0.74
Prandtl number, liquid phase	8.59
Schmidt number, gas phase	2.36
Molecular weight, oxidizer, Kg/Kmol	29.0
Molecular weight, fuel, n-octane, Kg/Kmol	114.2
Droplet initial temperature, [K]	300.0
Viscosity ratio, $\mu'_l / \mu'_{g,\infty}$	10.49
Density ratio, $\rho'_l / \rho'_{g,\infty}$	251.93
Specific heat at constant pressure ratio, $C'_{p,l,0} / C'_{p,g,\infty}$	1.87
Latent heat / Specific heat of liquid, [K]	135.95

Table D-2 MAIN PARAMETERS CONSIDERED IN EACH CASE OF THE ISOLATED
DROPLET STUDY

Case #	Ambient Temperature [K]	Initial Droplet Temperature [K]	Initial Reynolds #	Fuel Type	Droplet Heating Model	Physical Property
1.	1250	300	100	n-octane	two-dimensional	variable
2.	1000	300	100	n-octane	two-dimensional	variable
3.	800	300	100	n-octane	two-dimensional	variable
4.	1250	300	100	n-octane	two-dimensional	constant
5.	1250	300	100	n-octane	∞ conductivity	variable
6.	1250	300	150	n-octane	two-dimensional	variable
7.	1250	300	50	n-octane	two-dimensional	variable
8.	1250	400	100	n-octane	two-dimensional	variable
9.	1250	300	100	n-decane	two-dimensional	variable
10.	1250	300	100	n-hexane	two-dimensional	variable

Table D-3 VALUES OF PHYSICAL PARAMETERS USED IN THE TWO DROPLETS
BASELINE COMPUTATION

Parameter	Value
Initial Reynolds number, gas phase $Re = 2a'_0 U'_{\infty,0} \rho'_{g,\infty} / \mu'_{\infty}$	100.0
Relative velocity of drop, m/s	25.6
Free stream temperature, [K]	1000.0
Combustor pressure, atm	10.0
Prandtl number, gas phase	0.714
Prandtl number, liquid phase	14.92
Schmidt number, gas phase	3.26
Molecular weight, oxidizer, Kg/Kmol	29.0
Molecular weight, fuel, n-octane, Kg/Kmol	142.28
Droplet initial temperature, [K]	300.0
Viscosity ratio, $\mu'_l / \mu'_{g,\infty}$	21.44
Density ratio, $\rho'_l / \rho'_{g,\infty}$	209.19
Specific heat at constant pressure ratio, $C'_{p,l,0} / C'_{p,g,\infty}$	1.94
Latent heat / Specific heat of liquid, [K]	126.28

Table D-4 MAIN PARAMETERS CONSIDERED IN EACH CASE OF THE TWO DROPLETS
COMPUTATION

Case #	Ambient Temperature [K]	Initial Droplet Temperature [K]	Fuel Type	Initial Reynolds #	r'_2 / r'_1	$d' / (r'_0 \text{ spacing})$	Physical Property
1.	1000	300	n-decane	100	1	8	variable
2.	1000	300	n-decane	100	1	16	variable
3.	1000	300	n-decane	100	1	32	variable
4.	1000	300	n-decane	100	1	4	variable
5.	1000	300	n-decane	50	1	8	variable
6.	1000	300	n-decane	25	1	8	variable
7.	1000	300	n-decane	10	1	8	variable
8.	1000	300	n-decane	125	1	8	variable
9.	1000	300	n-decane	100	0.8	8	variable
10.	1000	300	n-decane	100	0.6	8	variable
11.	1000	300	n-decane	100	0.4	8	variable
12.	1000	300	n-decane	100	0.2	8	variable
13.	1000	300	n-decane	100	1.2	8	variable
14.	1000	300	n-decane	100	0.7	4	variable
15.	1000	300	n-decane	100	0.5	4	variable
16.	1000	300	n-decane	50	0.7	4	variable
17.	1000	300	n-decane	50	0.5	4	variable
18.	1000	300	n-decane	100	0.65	8	variable
19.	1000	300	n-decane	30	0.65	8	variable

IV REFERENCES

- Acton, E., *Journal of Fluid Mechanics*, **76**, 561-592, (1976)
- Arai, T., and Hashimoto, H., Behavior of Gas-Liquid Interface on a Liquid Film Jet, *Bulletin of JSME*, Vol. 28, No. 245 (1985)
- Arai, T., and Hashimoto, H., Disintegration of a Thin Liquid Sheet in a Cocurrent Gas Stream, *International Journal of Turbo and Jet Engines*, Vol. 3 (1986)
- Ashurst, W.T. and Meiburg, E., Three-dimensional Shear Layers via Vortex Dynamics, *Journal of Fluid Mechanics*, **189**, 87-116
- Batchelor, G.D., An Introduction to Fluid Dynamics, Cambridge University Press, (1970)
- Beck, J., Lefebvre, A., and Koblish, T., 1989, Airblast Atomization at Conditions of Low Air Velocity, AIAA 89-0217
- Browand, F.K. and Weidman, P.D., *Journal of Fluid Mechanics*, **76**, 127-144 (1976)
- Brown, G.L. and Roshko, A., *Journal of Fluid Mechanics*, **64**, 775-816 (1974)
- Cetegen, B.M. and Sirignano, W.A., Study of Mixing and Reaction in the Field of a Vortex, *Joint Meeting of the Combustion Institute Western States and Japanese Sections*, Paper no. 3B-44, Honolulu, Hawaii (1987). Also submitted to *Combustion Science and Technology*
- Cetegen, B.M. and Sirignano, W.A., Analysis of Molecular Mixing and Chemical Reaction in a Mixing Layer, *AIAA 26th Aerospace Sciences Meeting*, AIAA 88-0730, Reno, Nevada (1988)
- Chiang, C.H., Raju, M.S., and Sirignano, W.A., Numerical Analysis of Convecting, Vaporizing Fuel Droplet with Variable Properties, *AIAA Aerospace Sciences Meeting*, Paper 89-0834 (1989). Also to appear in *International Journal of Heat Transfer*

- Chiang, C.H. and Sirignano, W.A., Numerical Analysis of Interacting, Convecting, Vaporizing Fuel Droplet with Variable Properties, *AIAA Aerospace Sciences Meeting*, Paper 90-0357 (1990)
- Corcos, G.M. and Sherman, F.S., *Journal of Fluid Mechanics*, **139**, 29-65 (1984)
- Chorin, A.J. and Bernard, P.S., Univ. of California, Berkeley Engineering Rep. FM-72-5, (1972)
- Christiansen, J.P. and Zabusky, N.J., *Journal of Fluid Mechanics*, **61**, 219-243, (1973)
- Clift, R., Grace, J.R., and Weber, M.E., *Bubbles, Drops, and Particles*, Academic Press, New York, p. 43 (1978)
- Dimotakis, P. E., Turbulent Free Shear Layer Mixing, *AIAA Journal*, **24**, 1791-1796 (1986)
- Dimotakis, P.E., Turbulent Free Shear Layer Mixing, *AIAA 27th Aerospace Sciences Meeting*, AIAA 89-0262, Reno, Nevada (1989)
- Gerald, C.F. and Wheatley, P.O., *Applied Numerical Analysis*, Third Edition, Addison Wesley Publishing Company (1984)
- Ghoniem, A.F. and Givi, P., *25th AIAA Aerospace Sciences Meeting*, Paper 87-0225 (1987)
- Givi, P., Jou, W.H., and Metcalfe, R.W., *Twenty-First Symposium (International) on Combustion*, 1251-1261, 1251-1261, (1986)
- Hagerty, W.W. and Shea, J.F., *Journal of Applied Mechanics*, **22**, 509-514, (1955)
- Haywood, R.J., Nafziger, N., and Renksizbulut, M., A Detailed Examination of Gas and Liquid Phase Transient Processes in Convective Droplet Evaporation, *Journal of Heat Transfer*, **111**, 495-502, (1989)
- Karagozian, A.R., An Analytical Study of Diffusion Flames in Vortex Structures, Ph.D. Thesis, California Institute of Technology (1982)

Karagozian, A.R. and Marble, F.E., Study of a Diffusion Flame in a Stretched Vortex, *Combustion Science and Technology*, Vol. 45, 65-84 (1986)

Lamb, H., *Hydrodynamics*, 6th ed., Dover Publications, New York, (1932)

Lamb, H., *Hydrodynamics*, Chapter VII, Sixth Edition, Dover Publications, New York (1945)

Lara-Urbaneja, P. and Sirignano, W.A., Theory of Transient Multi-component Droplet Vaporization in a Convective Field, *Proceeding of Eighteenth Symposium (International) on Combustion*, Combustion Institute, *Proceeding of Eighteenth Symposium (International) on Combustion*, Combustion Institute, 1365-1374 (1981)

Leonard, A., Vortex Methods for Flow Simulation, *Journal of Computational Physics*, **37**, 289-335 (1980)

Mansour, A. and Chigier, N., Disintegration of Liquid Sheets, Poster Presentation at ILASS-Americas 3rd Annual Conference on Liquid Atomization and Spray Systems, (1989)

Matsutani, S.M. and Bowman, C.T., Structure of a Chemically Reacting Mixing Layer, *Journal of Fluid Mechanics*, **172**, 87-116 (1988)

Meiburg, E., Lasheras, J.C. and Ashurst, W.T., Topology of the Vorticity Field in Three-Dimensional Shear Layers and Wakes, *Fluid Dynamics Research*, **3**, 140-148, (1988)

Miralles-Wilhelm, F., An Analysis of Molecular Mixing in Vortical Structures within a Shear Layer, M.S. Thesis, University of California, Irvine, (1989)

Miralles-Wilhelm, F., Rangel, R.H. and Sirignano, W.A., An Analysis of Molecular Diffusion in A Mixing Layer, Bias in PDF Measurement, *AIAA 27th Aerospace Sciences Meeting*, AIAA 89-0482, Reno, Nevada, (1989)

Overman, E.A. and Zabusky, N.J., *Physics of Fluids*, **25**, 1297-1305, (1982)

Prakash, S. and Sirignano, W.A., Theory of Convective Droplet Vaporization with Unsteady Heat Transfer in the Circulating Liquid Phase, *International Journal of Heat and Mass Transfer*, **23**, 253-268, (1980)

Raju, M.S. and Sirignano, W.A., Unsteady Navier-Stokes Solution for Two Vaporizing Droplets, *AIAA Aerospace Sciences Meeting*, Paper 87-0300 (1987)

Raju, M.S. and Sirignano, W.A., Interaction Between Two Vaporizing Droplets in an Intermediate- Reynolds-Number Flow, submitted to *Physics of Fluids* (1988)

Rangel, R.H. and Sirignano, W.A., Nonlinear Growth of Kelvin-Helmholtz Instability: Effect of Surface Tension and Density Ratio, *The Physics of Fluids*, **31**, 1845-1855, (1988)

Rangel, R.H. and Sirignano, W.A., The Dynamics of Vortex Pairing and Merging, *AIAA 27th Aerospace Sciences Meeting*, AIAA 89-0128, Reno, Nevada (1989)

Rizk, N. and Lefebvre, A., The Influence of Liquid Film Thickness on Airblast Atomization, *ASME Journal of Engineering for Power*, Vol. 102 (1980)

Sattelmayer, T. and Wittig, S., Internal Flow Effects in Prefilming Airblast Atomizers: Mechanisms of Atomization and Droplet Spectra, *ASME Journal of Engineering for Gas Turbines and Power*, Vol. 108

Squire, H.B., *British Journal of Applied Physics*, **4**, 167-169 (1953)

Taylor, G.I., *Proceedings of the Royal Society of London A*, **253**, 296-312 (1959)

Tokuoka, N., Nagaosa, S., Hora, S., and Sato, G., Study on the Disintegration of a Liquid Film by Air Impingement, *Atomisation and Spray Technology*, Vol. 1 (1985)

APPENDICES

A Publications Resulting from AFOSR Grant

Raju, M.S. and Sirignano, W.A., Interaction Between Two Vaporizing Droplets in an Intermediate-Reynolds- Number-Flow, submitted to *Physics of Fluids*, 1987. Also see Unsteady Navier-Stokes Solution for Two Interacting Vaporizing Droplets, AIAA Preprint No. 87-0300, Reno, NV, January 1987.

Rangel, R.H. and Sirignano, W.A., Non-Linear Growth of Kelvin-Helmholtz Instability: Effect of Surface Tension and Density Ratio, *Physics of Fluids*, Vol. 31, 1845-1855, 1988. Also see Atomization of Liquid Fuels: Non-Linear Growth of Disturbances at an Interface, Spring 1987 Western States/Combustion Institute Meeting, Provo, UT, April 1987. Provo, UT, April 1987. Provo, UT, April 1987.

Cetegen, B.M. and Sirignano, W.A., Study of Mixing and Reaction in the Field of a Vortex, submitted for publication in *Combustion Science and Technology*. Also presented at the Joint Meeting of the Western States Section/Japanese Section of the Combustion Institute, Honolulu, HI, November 1987.

Cetegen, B.M. and Sirignano, W.A., Study of Molecular Mixing and a Finite Rate Chemical Reaction in A Mixing Layer, Twenty-Second Symposium (International) on Combustion, 489-494, 1988. Also see Analysis of Molecular Mixing and Chemical Reaction in a Mixing Layer, Preprint No. 88-0730, AIAA 26th Aerospace Sciences Meeting, Reno, NV, January 1988.

Sirignano, W.A., An Integrated Approach to Spray Combustion Model Development, *Combustion Science and Technology*, Vol. 58, 1-3, 231-251, 1988. Presented at the ASME 107th Winter Annual Meeting, Anaheim, CA 1986.

Chiang, C.H., Raju, M.S. and Sirignano, W.A., Numerical Analysis of Convecting, Vaporizing Fuel Droplet with Variable Properties, submitted to *International Journal of Heat and Mass Transfer*, 1989. Also

see Preprint No. 89-0834, AIAA Twenty-Seventh Aerospace Sciences Meeting, Reno, NV, January 1989.

Miralles-Wilhelm, F., Rangel, R.H. and Sirignano, W.A., An Analysis of Molecular Diffusion in a Vortical Structure: Bias in PDF Measurement, Preprint No. 89-0482, AIAA Twenty-Seventh Aerospace Sciences Meeting, Reno, NV, January 1989.

Rangel, R.H. and Sirignano, W.A., The Dynamics of Vortex Pairing and Merging, Preprint No. 89-0128, AIAA Twenty-Seventh Aerospace Sciences Meeting, Reno, NV, January 1989.

Sirignano, W.A., Review of Spray Combustion Theory, invited presentation for the Joint Meeting of the British and French Sections of the Combustion Institute, Rouen, France, April 1989.

Rangel, R.H. and Sirignano, W.A., PDF Analysis of Molecular Mixing in Turbulent Flows, (abstract only) presented at the SIAM 1989 Annual Meeting, San Diego, CA, July 1989.

Rangel, R.H. and Sirignano, W.A., A Computational Fluid Dynamics Approach to Jet-Blast Atomization Studies, invited presentation for Third Annual ILASS Conference on Liquid Atomization and Spray Systems, Irvine, CA, May 1989.

Chiang, C.H. and Sirignano, W.A., Numerical Analysis of Interacting, Convecting, Vaporizing Fuel Droplets with Variable Properties, submitted for presentation at the AIAA 28th Aerospace Sciences Meeting, Reno, NV, January 1990. Also to be submitted to *International Journal of Heat and Mass Transfer*.

Rangel, R.H. and Sirignano, W.A., The Linear and Nonlinear Shear Instability of a Fluid Sheet, to be submitted to *Physics of Fluids*.

Stapper, B.E. and Samuelson, G.S., An Experimental Study of the Breakup of a Two-Dimensional Liquid Sheet in the Presence of Co-Flow Air Shear, to be presented at the Twenty-Eighth Aerospace Sciences Meeting, Reno, NV, January 1990. Also to be submitted to AIAA Journal.

Stapper, B.E. Sowa, W.A. and Samuelsen, G.S., An Experimental Study of the Effects of Liquid Properties on the Breakup of a Two-Dimensional Liquid Sheet, to be presented at the Thirty-Fifth ASME International Gas Turbine and Aeroengine Congress and Exposition, Brussels, Belgium, June 1990. Accepted, ASME Journal of Engineering for Gas Turbines and Power.

B Participating Professionals

W.A. Sirignano, Professor, Principal Investigator

G.S. Samuelsen, Professor, Co-Principal Investigator

R.H. Rangel, Assistant Professor

M.S. Raju, Postdoctoral Research Associate

W.A. Sowa, Associate Director of UCI Combustion Laboratory

C.H. Chiang, Ph.D. candidate

F. Miralles-Wilhelm, M.S. candidate

B. Stapper, M.S. candidate

C Degrees Awarded

F. Miralles-Wilhelm

M.S. June 1989

B. Stapper

M.S. November 1989

C.H. Chiang

Ph.D. expected August 1990

D Interactions

W.A. Sirignano, Public Lecture, An Integrated Approach to Spray Combustion Model Development, 107th Winter Annual Meeting, Anaheim, CA, December 1986.

W.A. Sirignano, Public Lecture, "Theory of Combustion of Liquid Fuels," California State University, Fullerton, CA, February 1987.

W.A. Sirignano, Public Lecture, "Transient Spray Computations," AFOSR, Washington, D.C., February 1987.

W.A. Sirignano, Public Lecture, "Fundamental Studies on Turbulent Combustion and Spray Combustion," 1987 AFOSR/ONR Contractors Meeting on Combustion, University Park, PA, June 1987.

W.A. Sirignano, Public Lecture, "Two-Dimensional Modeling of Flame Propagation in Fuel Stream Arrangements," 11th International Colloquium on Dynamics of Explosions and Reactive Systems, Warsaw, Poland, August 1987.

W.A. Sirignano, Workshop on Experimental, Analytical and Computational Methods in Liquid Fuel Sprays, a series of three lectures at the Institute of Aeronautics and Astronautics, National Cheng Kung University, Tainan, Taiwan, November 1987.

W.A. Sirignano, Public Lecture, "Study of Mixing and Reaction in the Field of a Vortex," Western States Section of the Combustion Institute, Honolulu, HI, November 1987.

W.A. Sirignano, Public Lecture, "Droplet Vaporization Model for Spray Combustion Calculation," AIAA 26th Aerospace Sciences Meeting, Reno, NV, January 1988.

W.A. Sirignano, Public Lecture, "Analysis of Molecular Mixing and Chemical Reaction in a Mixing Layer," AIAA 26th Aerospace Sciences Meeting, Reno, NV, January 1988.

W.A. Sirignano, Public Lecture, "Mixing and Reaction in a Vortical Structure," UC San Diego, March 1988.

W.A. Sirignano, Public Lecture, "Review of Spray Combustion Theory: Remaining Challenges on the Workshop on Mass, Momentum, and Energy Exchange in Combusting Sprays: Droplet Studies, Sandia Droplet Scales," Workshop on Mass, Momentum, and Energy Exchange in Combusting Sprays: Droplet Studies, Sandia National Laboratories, Livermore, CA March 1988.

W.A. Sirignano, Public Lecture, "Fundamental Studies on Spray Combustion and Turbulent Combustion," 1988 AFOSR/ONR Contractors Meeting on Combustion, California Institute of Technology, Pasadena, CA, June 1988.

W.A. Sirignano, Public Lecture, "Molecular Mixing and Chemical Reaction in Vortical Structures," Sandia National Laboratory, December 1988.

W.A. Sirignano, Public Lecture, "Review of Spray Combustion Theory," plenary lecture for the Joint of the British and French Sections of the Combustion Institute, Rouen, France, April, 1989.

W.A. Sirignano, Public Lecture, "Review of Theory of Mixing and Reaction Within A Vortical Structure," presented at the Third International Conference on Numerical Combustion, Antibes, France, May 1989.

W.A. Sirignano, Public Lecture, "Mixing and Reaction Within a Vortical Structure," The University of Alabama at Huntsville, AL, May 1989.

W.A. Sirignano, Public Lecture, "Fundamental Studies on Spray Combustion and Turbulent Combustion," presented at the 1989 AFOSR/ONR Contractors Meeting on Combustion, Ann Arbor, MI, June 1989.

W.A. Sirignano, Public Lecture, "Potential Combustion Instability Mechanisms," keynote address presented at the JANNAF Workshop on Liquid Rocket Engine Combustion Driven Instability Mechanisms, Monterey, CA, July 1989.

W.A. Sirignano, Consultant, Sandia Laboratories, Livermore, CA, Dr. B. Sanders

W.A. Sirignano, Consultant, Allison Gas Turbines, Indianapolis, IN, Dr. H. Mongia

W.A. Sirignano, Consultant, United Technologies Research Center, East Hartford, Conn, Dr. A. Eckbreth

W.A. Sirignano, Consultant, Mitsubishi Heavy Industries, Tokyo, Mr. Ichinose

W.A. Sirignano, Consultant, Metrolaser, Tustin, CA, Dr. C. Hess

W.A. Sirignano, Informal Discussions for collaborations with Dr. T. Jackson, AFWAL

R.H. Rangel, "Vortex-Dynamics Modelling of Interface Instability," Harvard University, March 1988.

R.H. Rangel, "Analysis of Vortical Structures in Combustion Process," Princeton University, October 1988.

R.H. Rangel, "Analysis of Vortical Structures in Combustion Processes," Drexel University, December 1988.

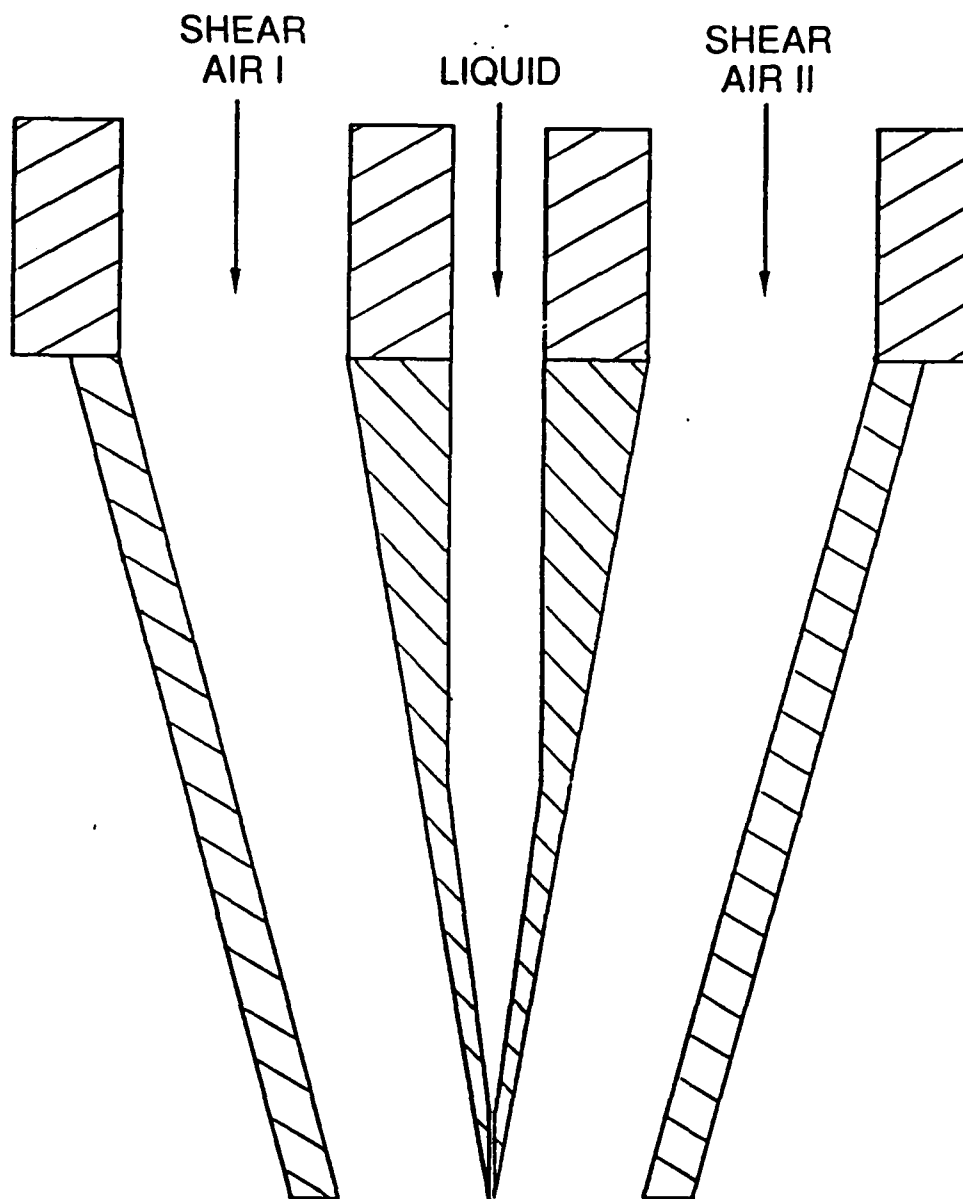


Figure A-1: Two-Dimensional Parallel Flow Plane Sheet Atomizer

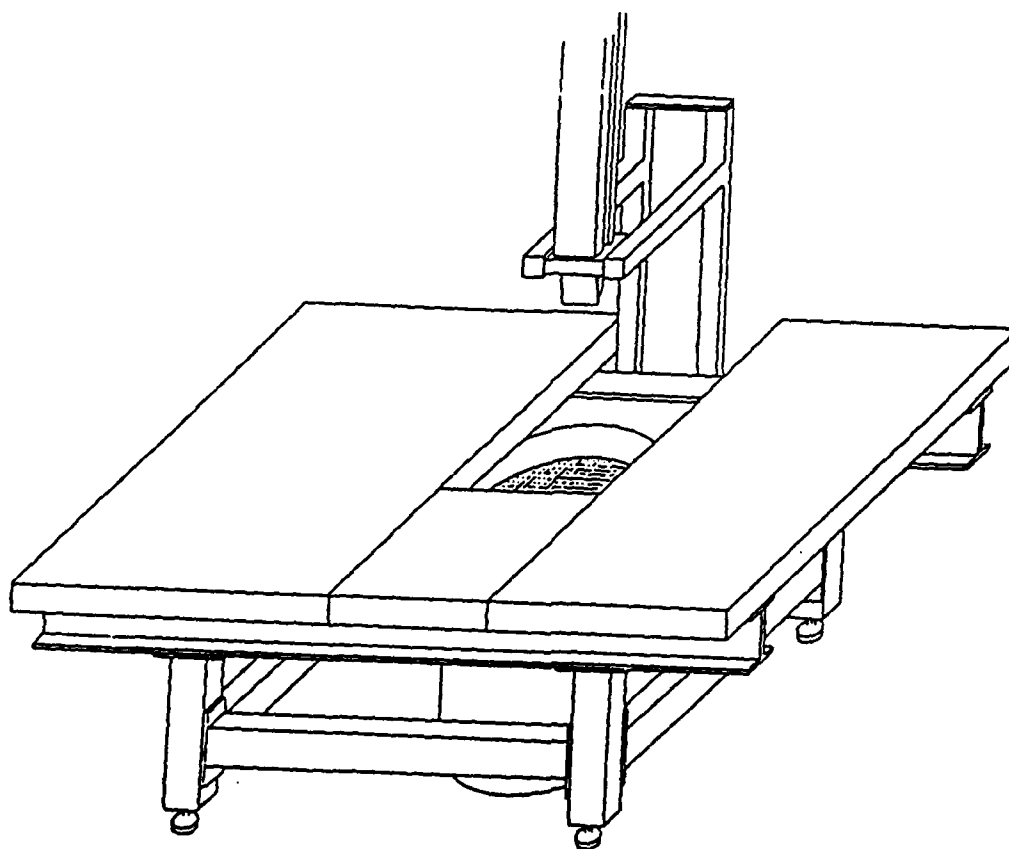
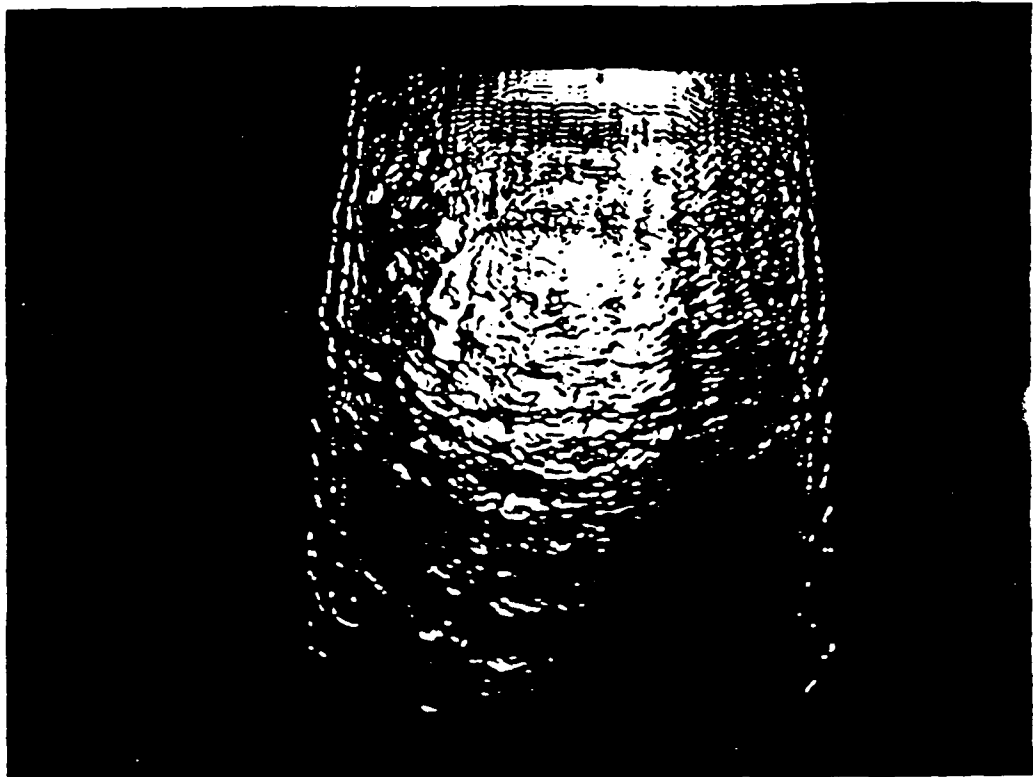


Figure A-2: Shear Flow Facility

(a)



(b)

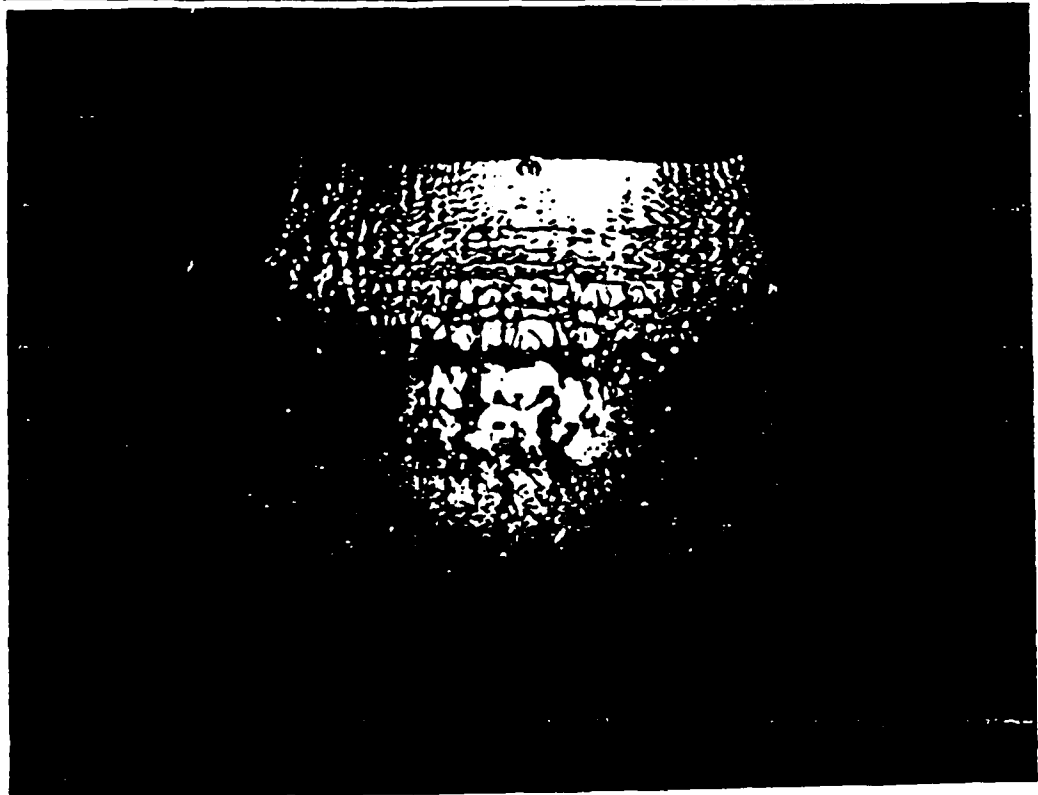
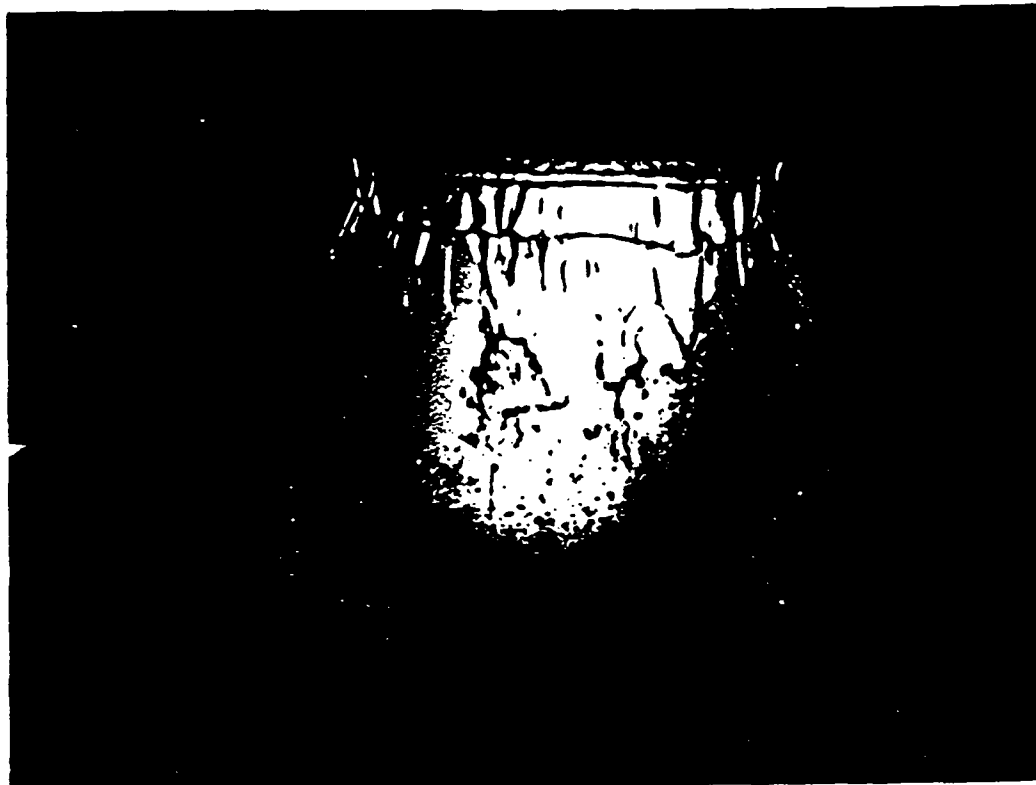


Figure A-3: "Cellular Breakup": Water Sheet at 5m/s with: (a) No Co-Flow Air, (b) 40m/s Co-Flow Air.

(a)



(b)

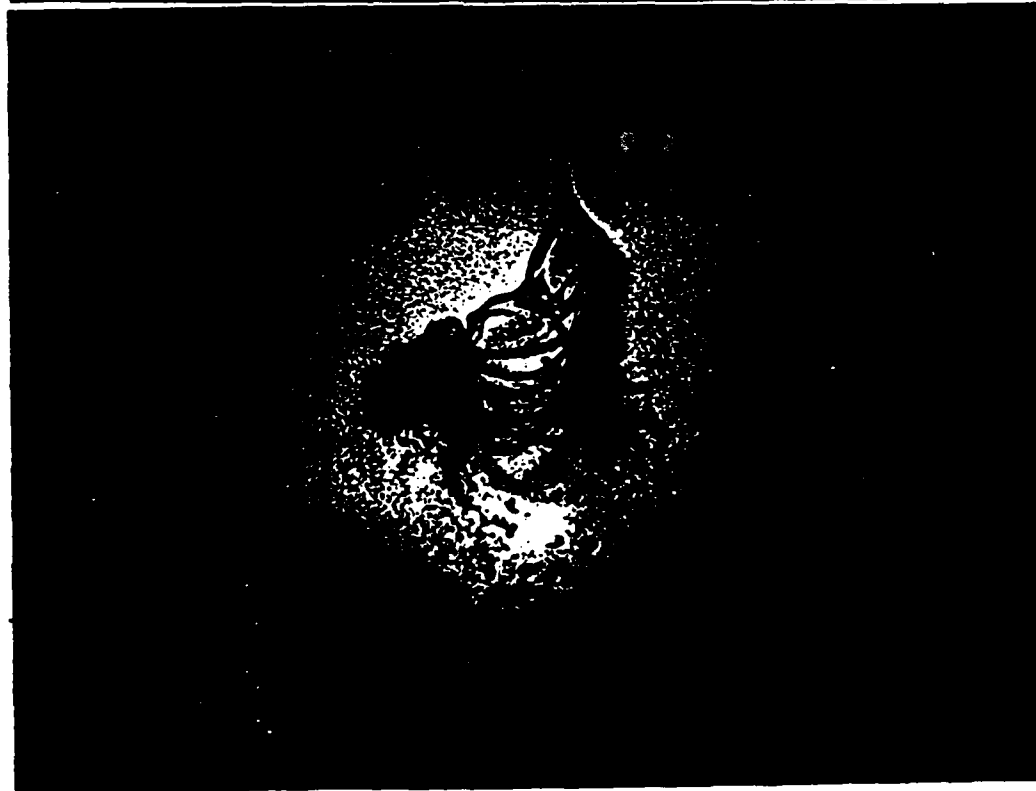
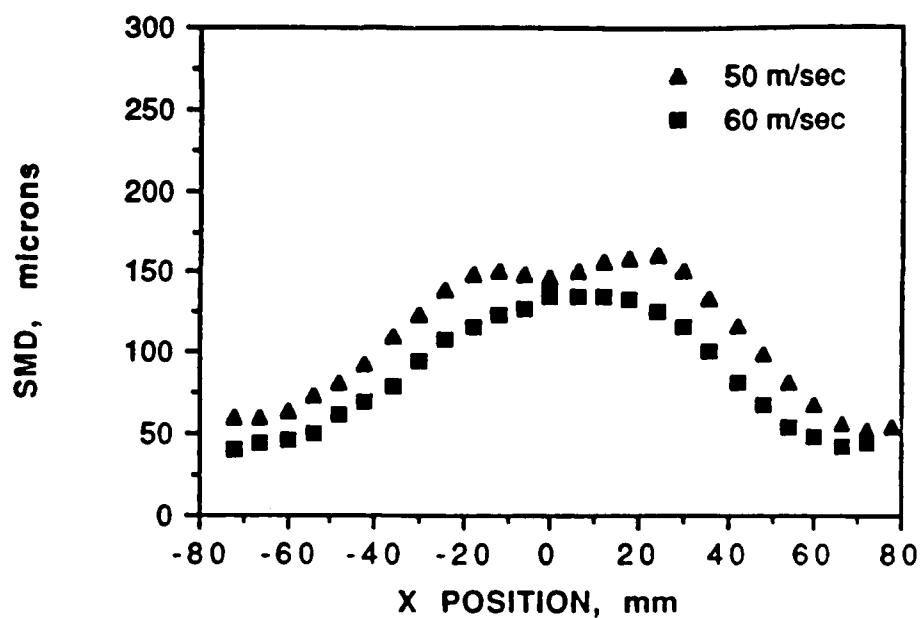


Figure A-4: "Stretched Streamwise Ligament Breakup": Water Sheet at 1m/s with 20m/s Co-Flow Air: (a) Face View, (b) Side View.

(a)



(b)

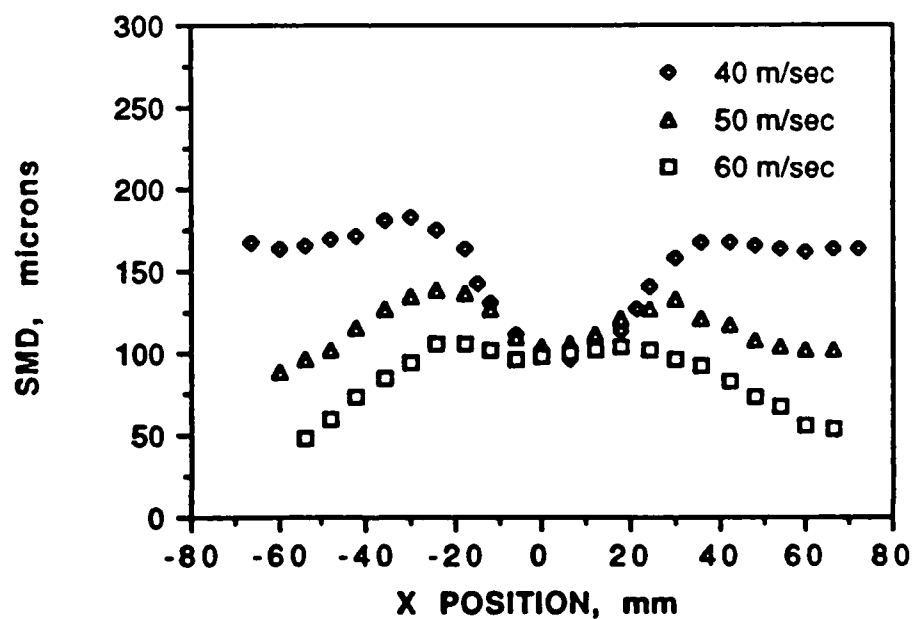
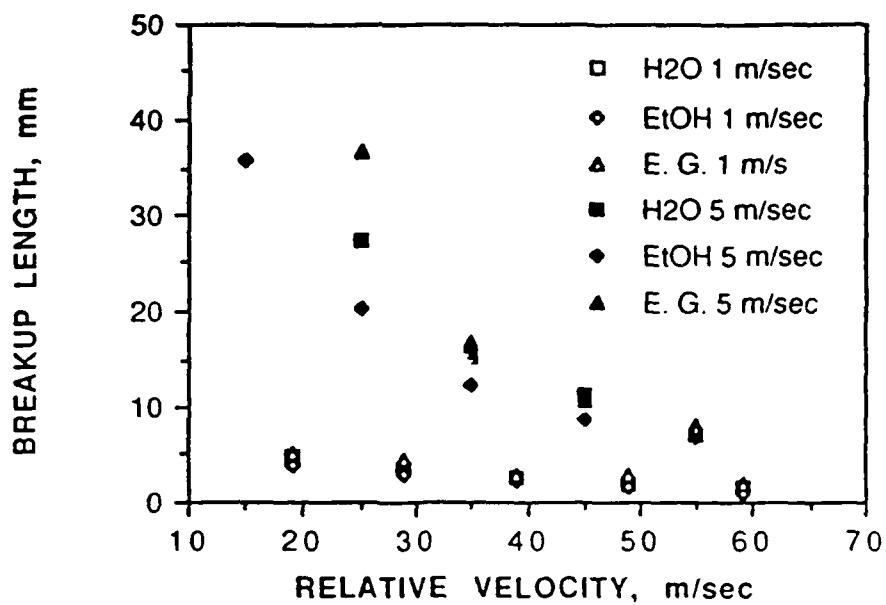


Figure A-5: Drop Size Distribution: (a) Cellular Breakup, (b) Stretched Streamwise Ligament Breakup

(a)



(b)

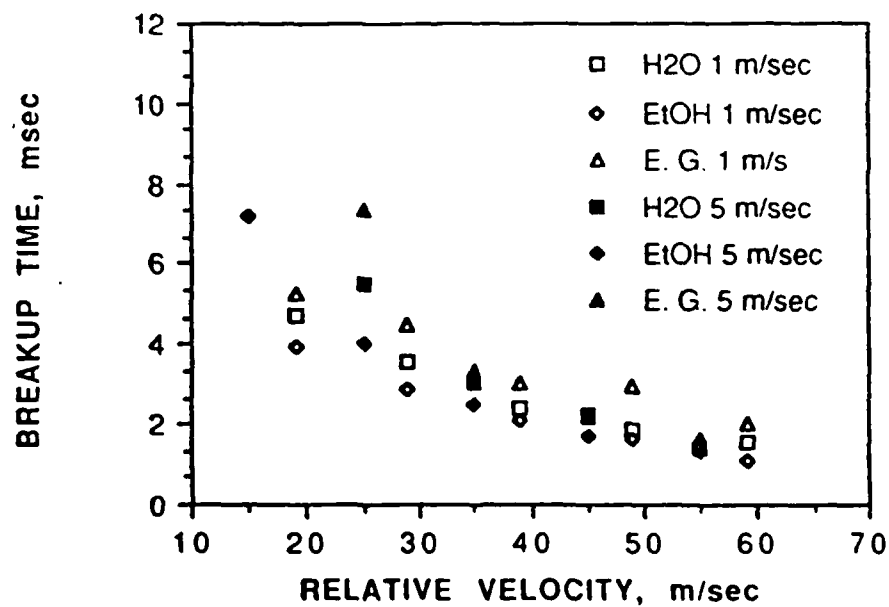
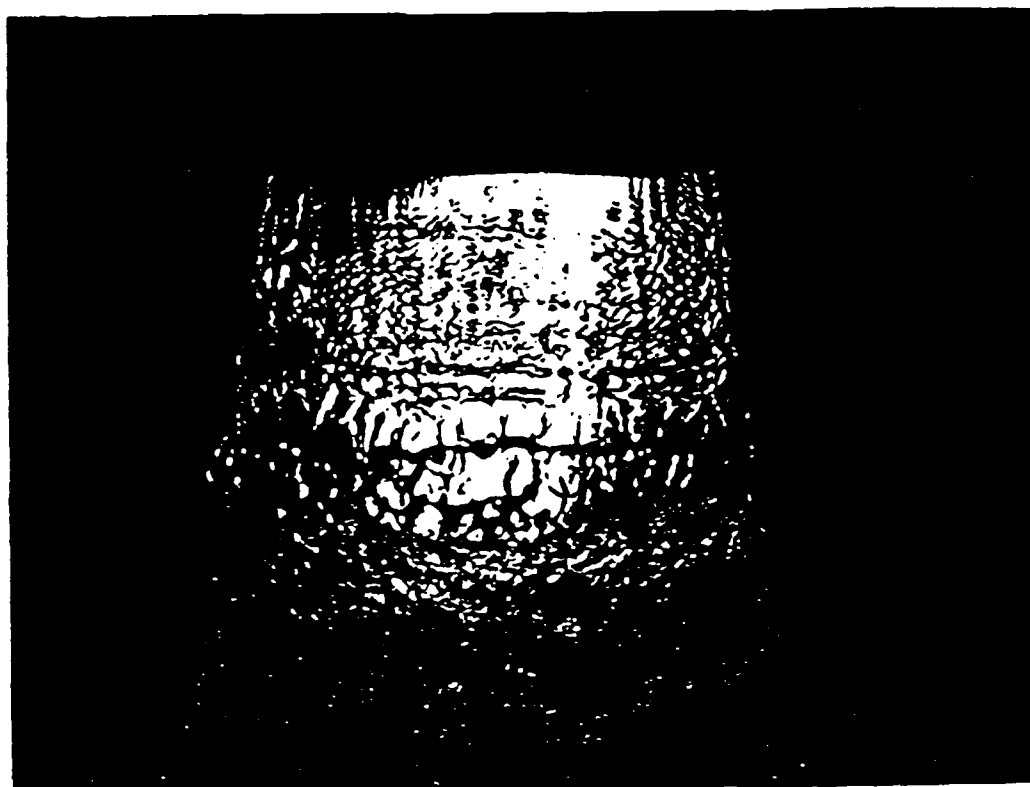
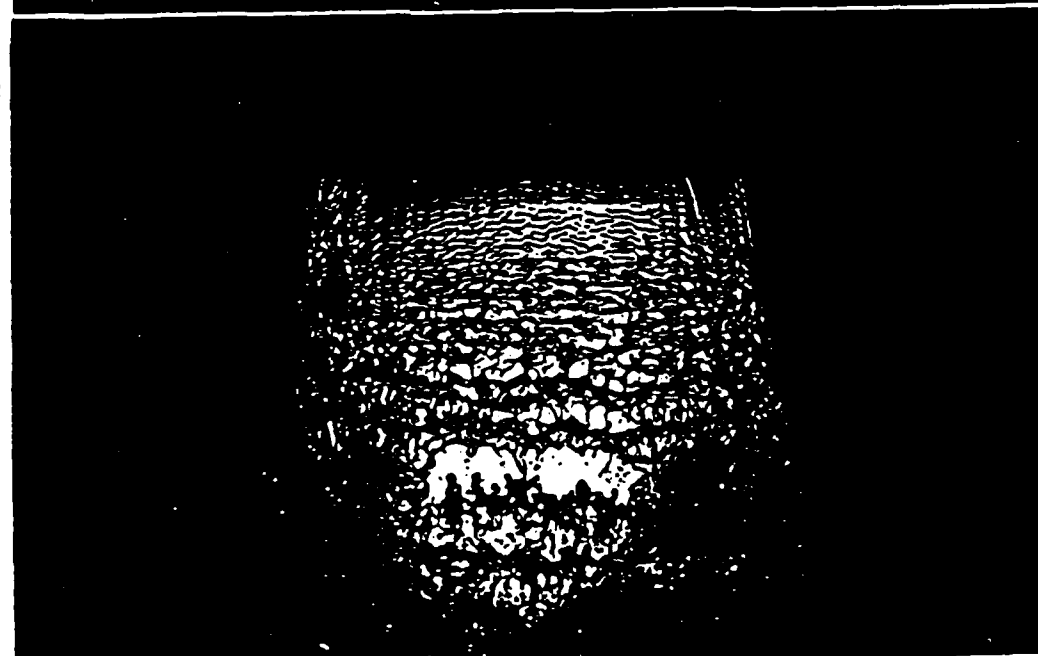


Figure A-6: Effect of Relative Velocity on: (a) Sheet Breakup Length, (b) Sheet Breakup Time.

Water:



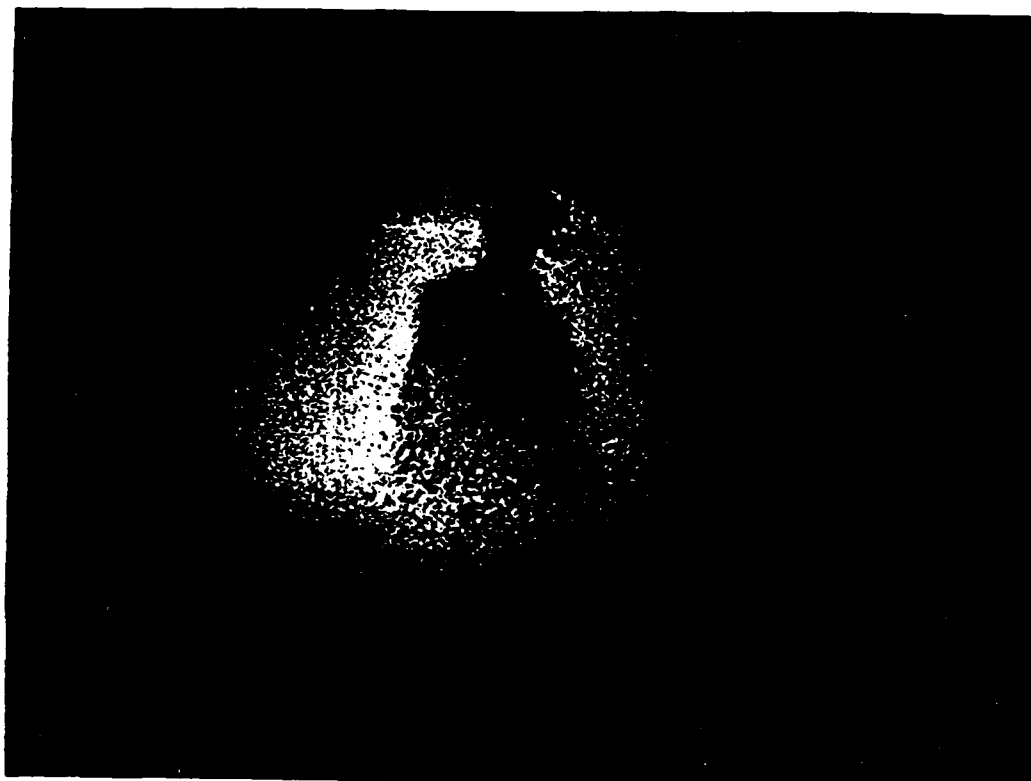
Ethanol:



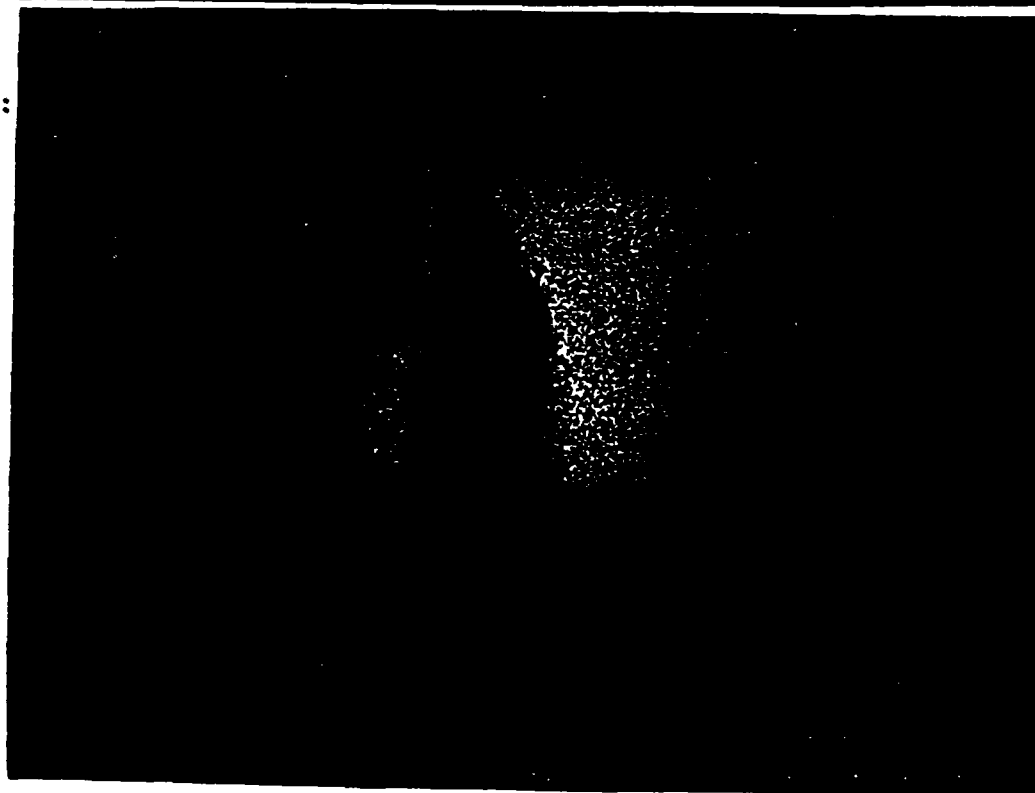
(a)

Figure A-7: Effect of Liquid Properties on "Cellular Breakup": (a) Face View, Water and Ethanol (Case 13) (b) Face View, Water and Ethanol (Case 26), (c) Face View, Water and Ethylene Glycol (Case 14).

Water.

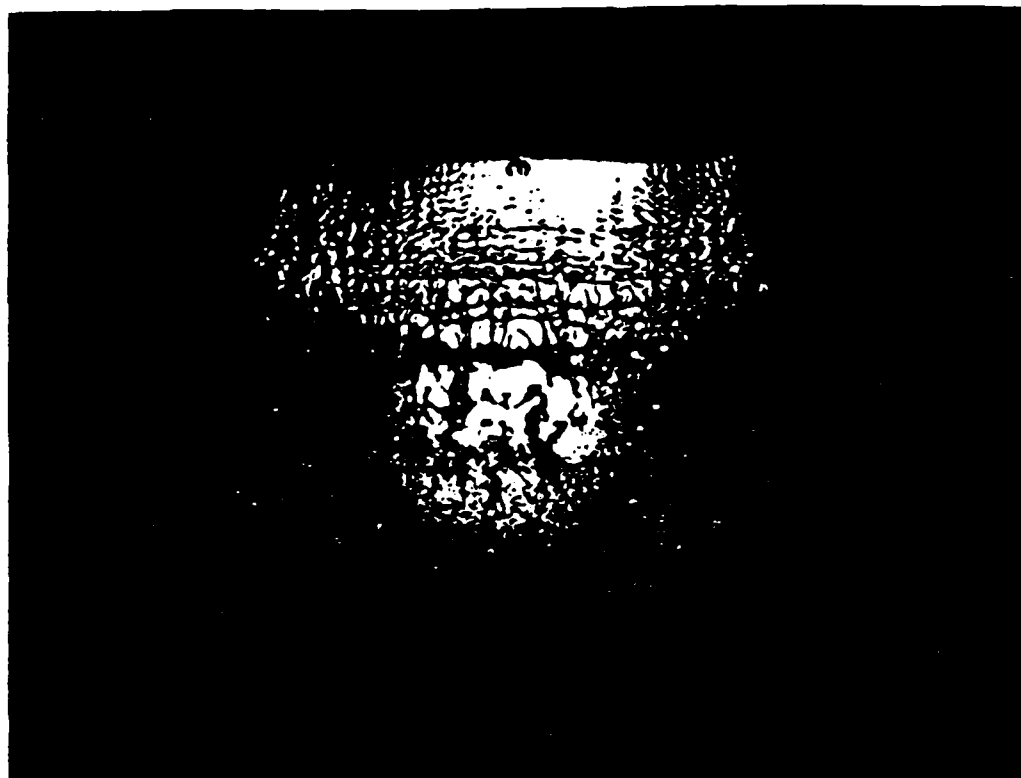


Ethanol:

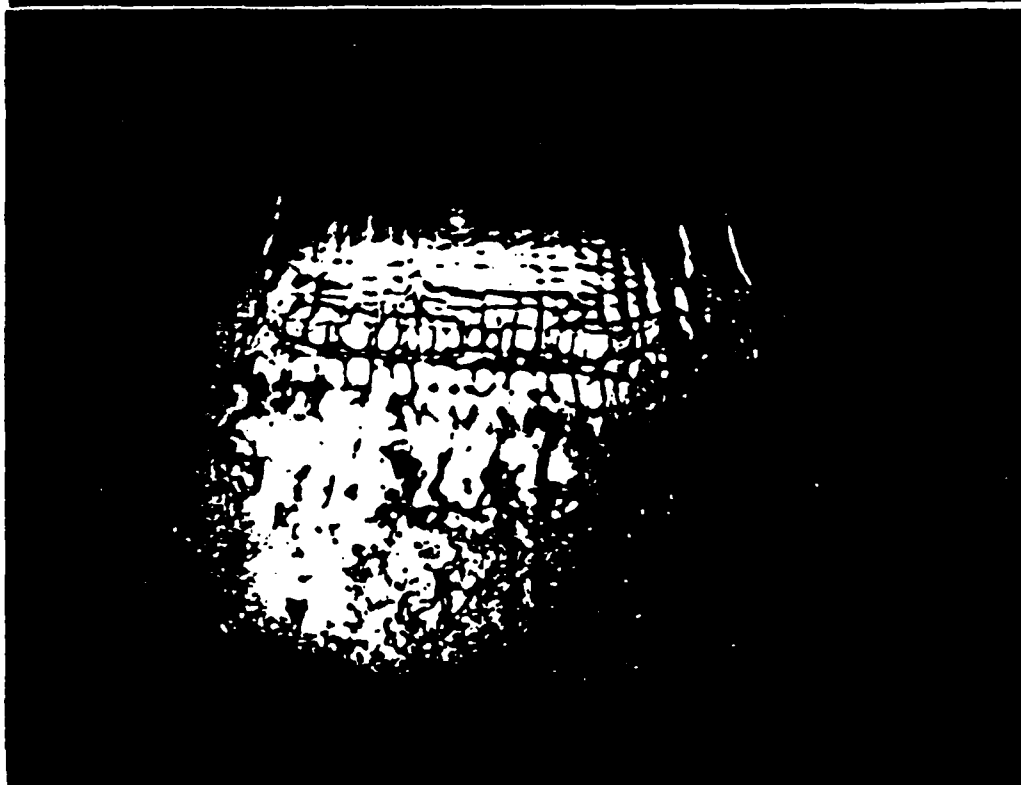


(b)

Water:

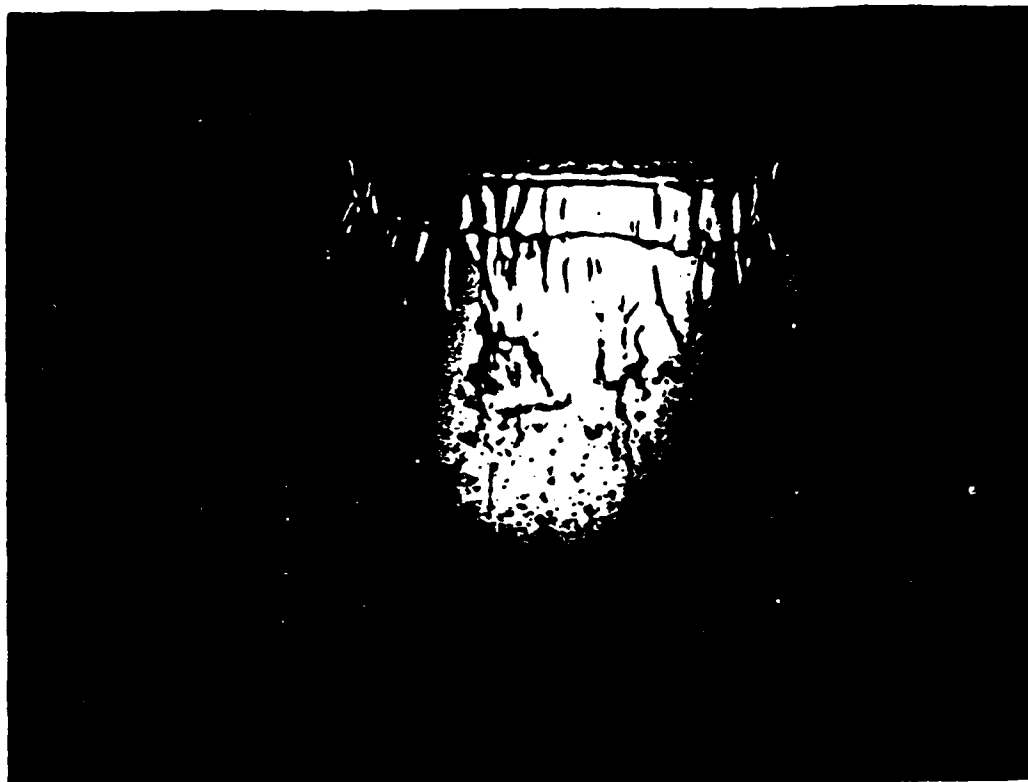


Ethylene
Glycol:



(c)

(a)



(b)

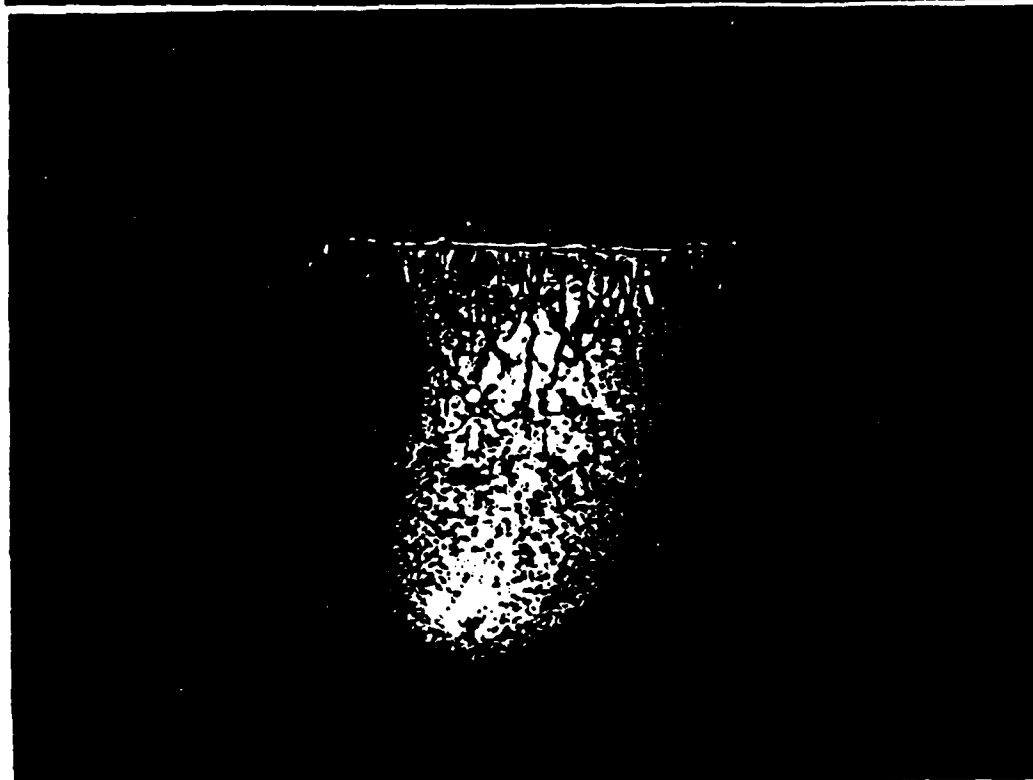


Figure A-8: Effect of Liquid Properties on "Stretched Streamwise Ligament Breakup" (Case 22): (a) Water, (b) Ethanol, (c) Ethylene Glycol.

(c)



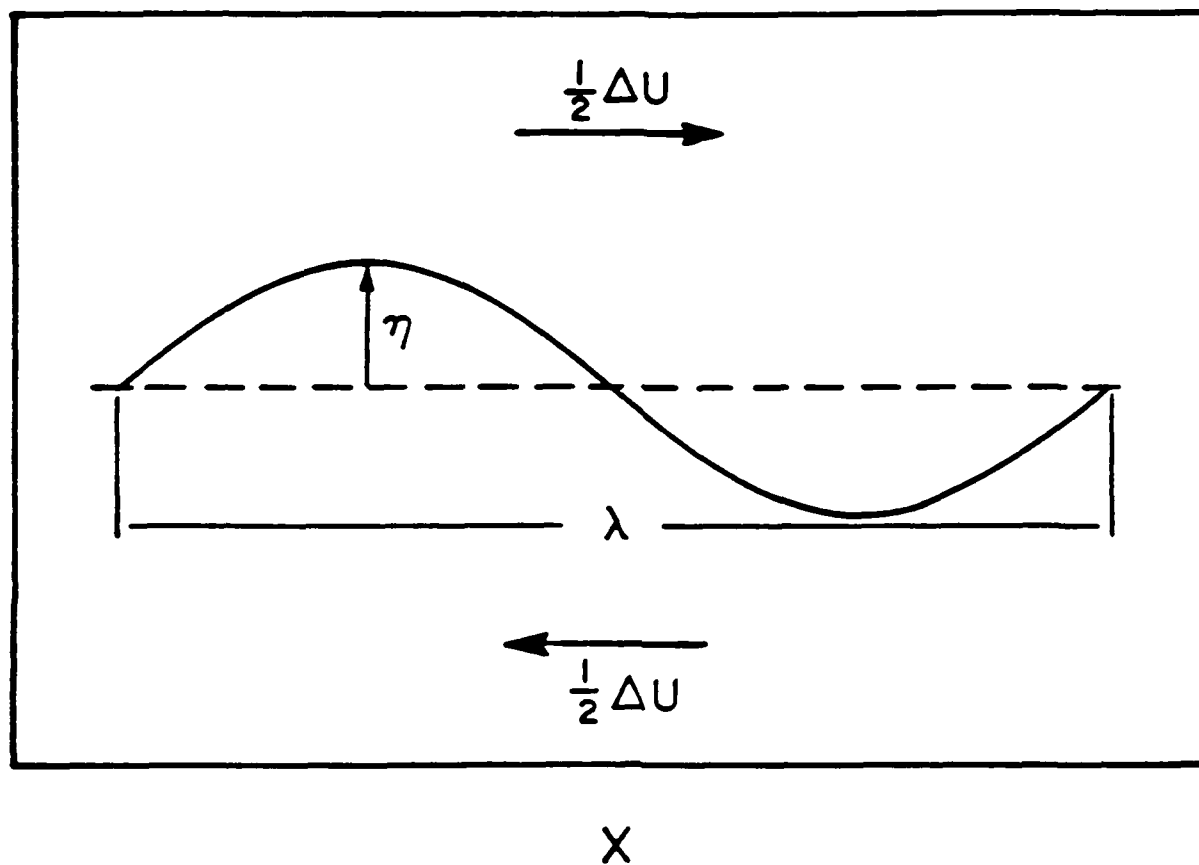


Figure B-1: Schematic of the problem of interface instability.

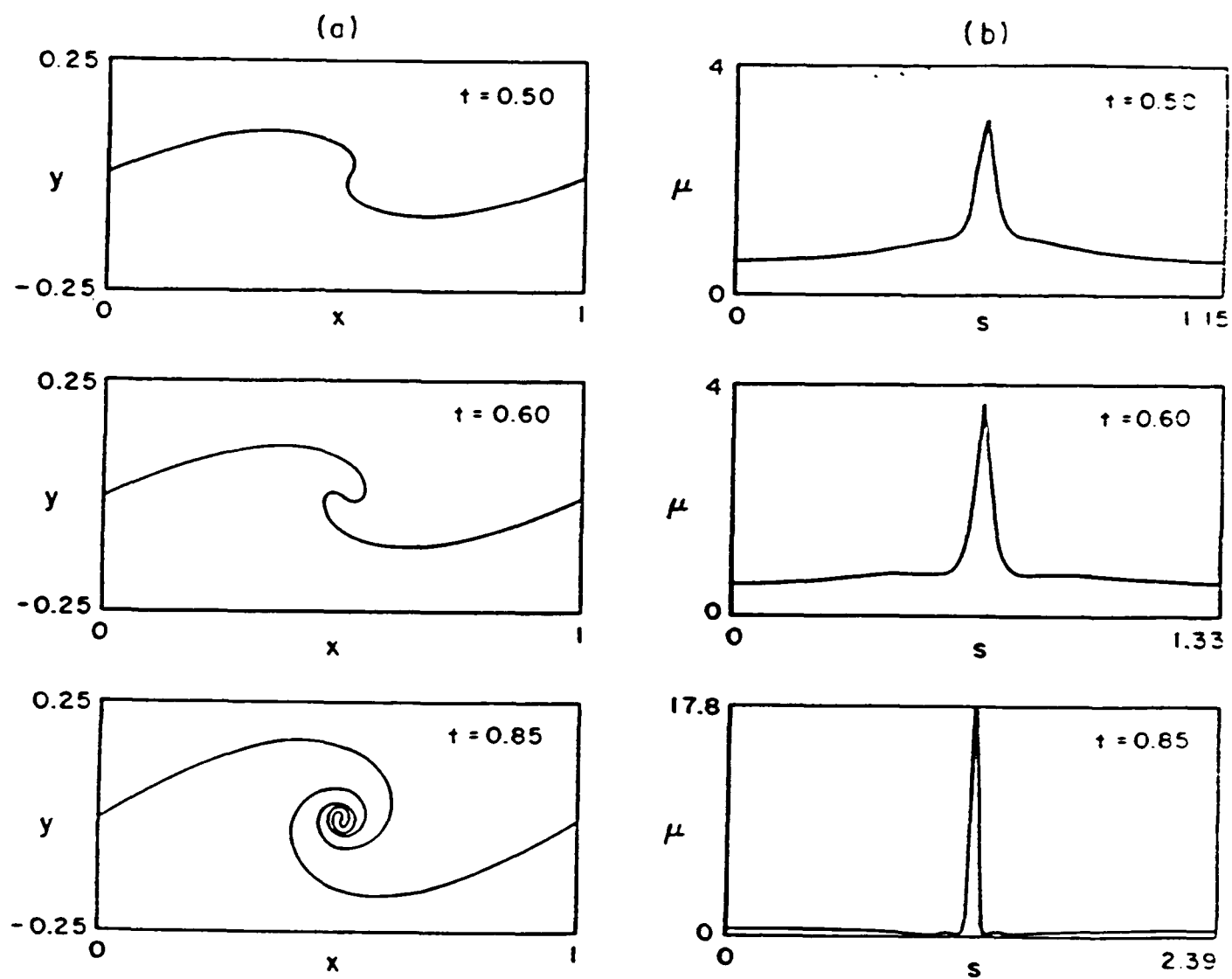


Figure B-2: Evolution of the interface shape (a) and the interface vorticity (b) for $\rho = 1$, $W = 0.1$

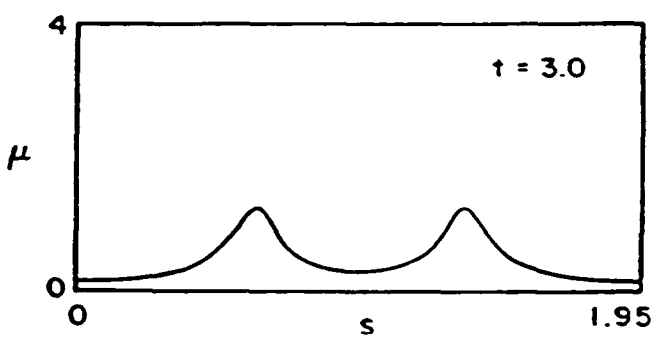
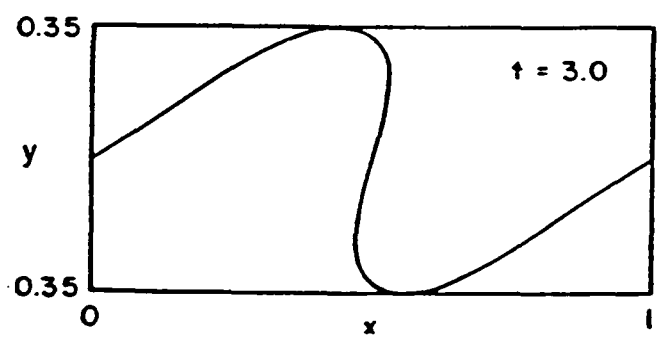
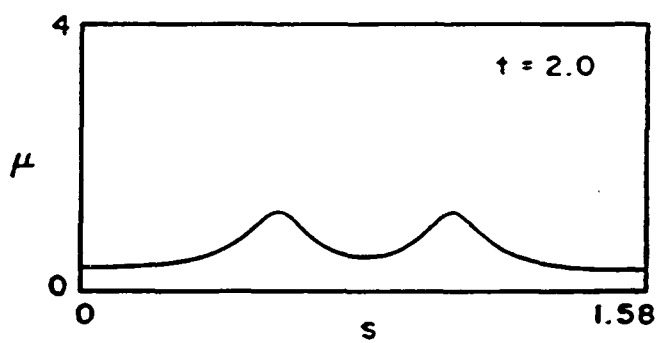
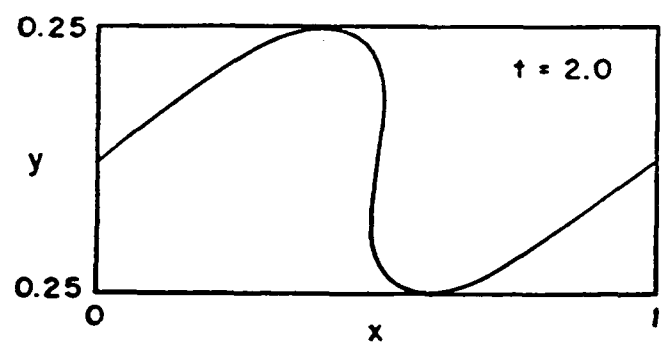
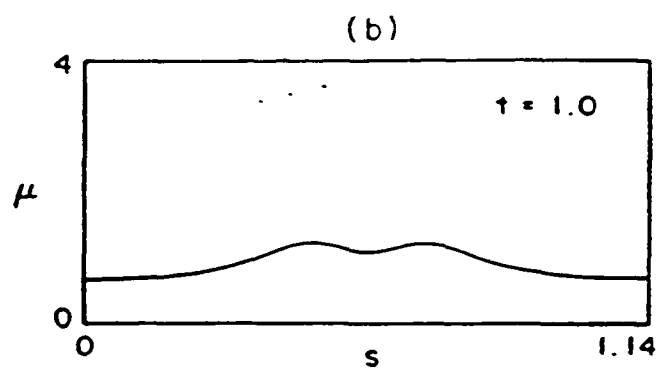
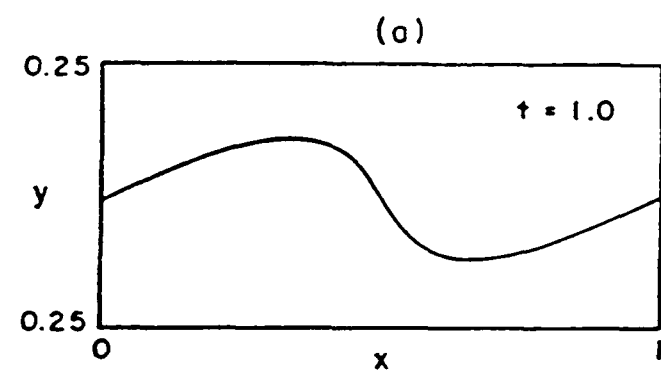


Figure B-3: Evolution of the interface shape (a) and the interface vorticity (b) for $\rho = 1, W = 2/3$

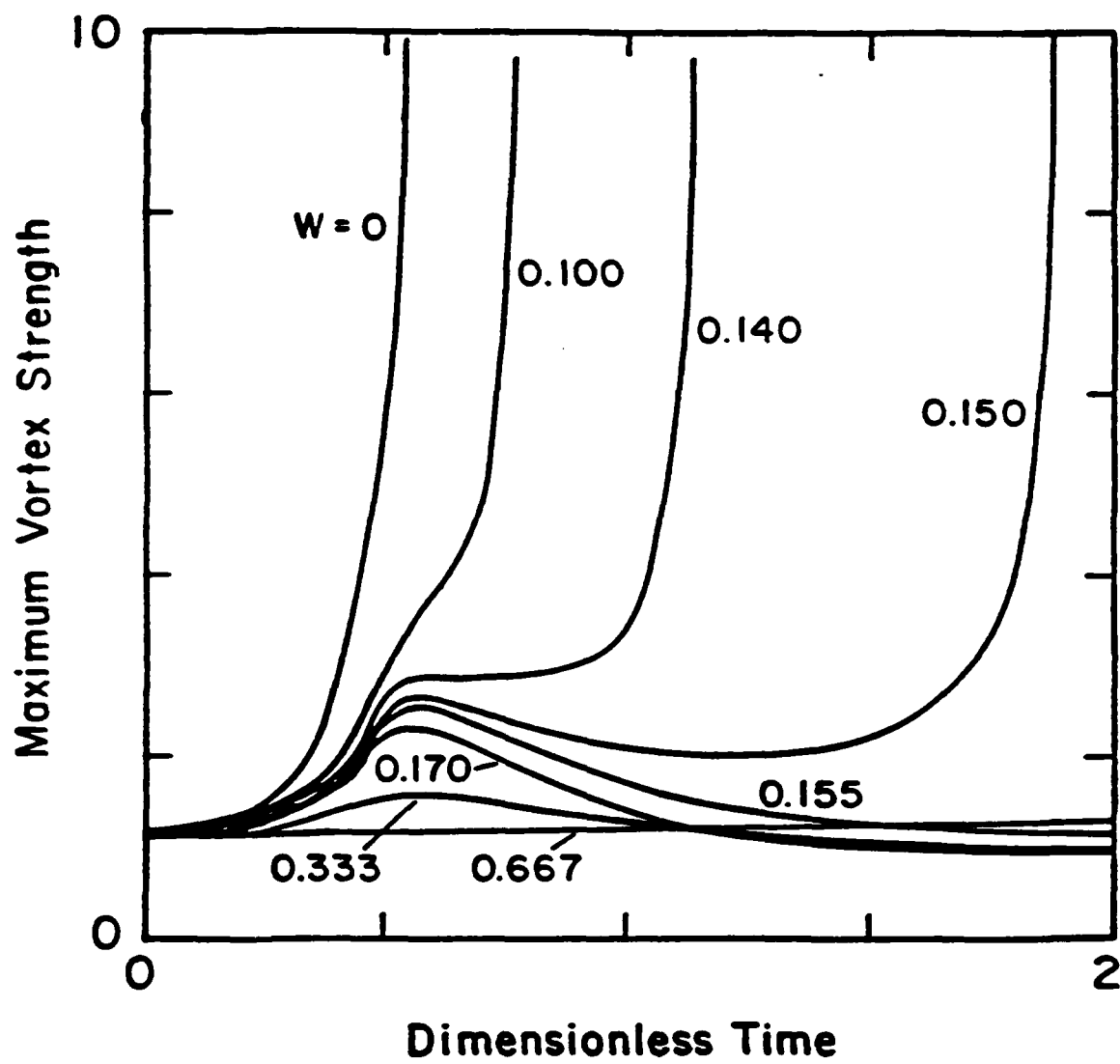


Figure B-4: Maximum vortex strength vs. time for $\rho = 1$ and selected values of W .

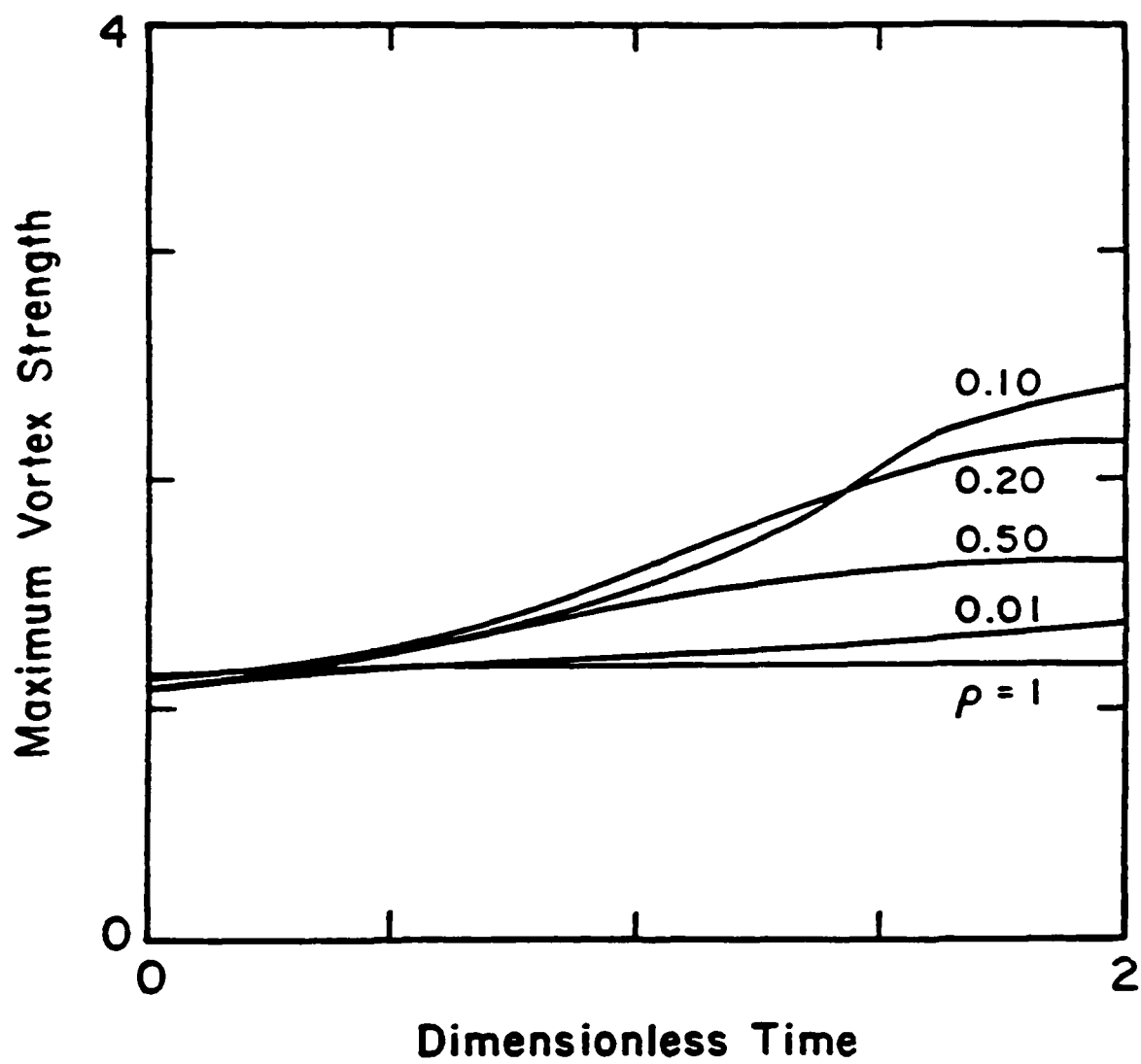


Figure B-5: Maximum vortex strength vs. time for $W = 2/3$ and selected values of ρ .

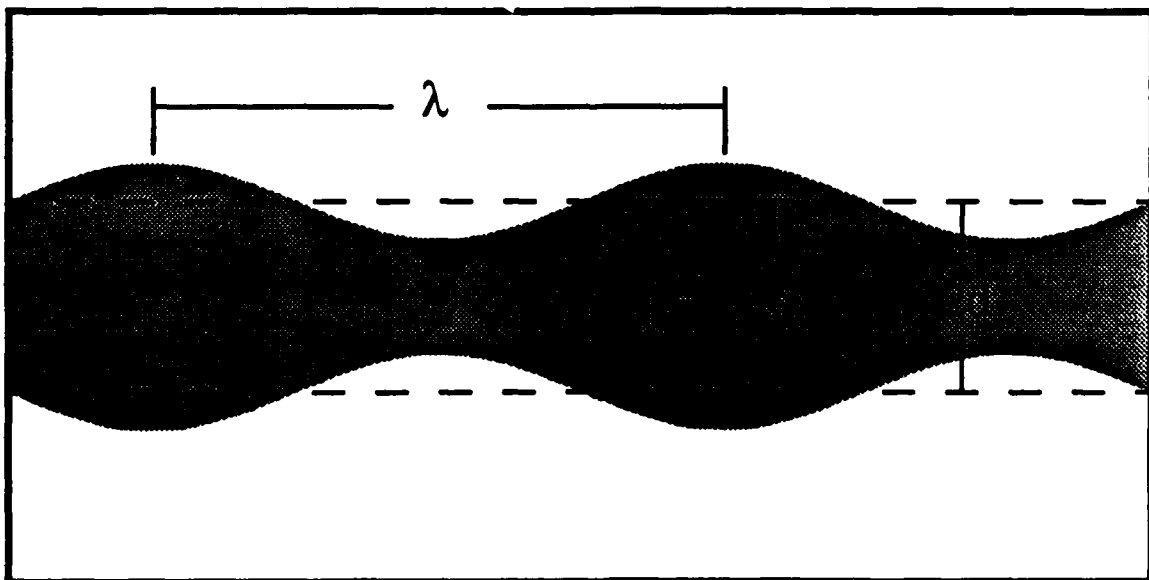
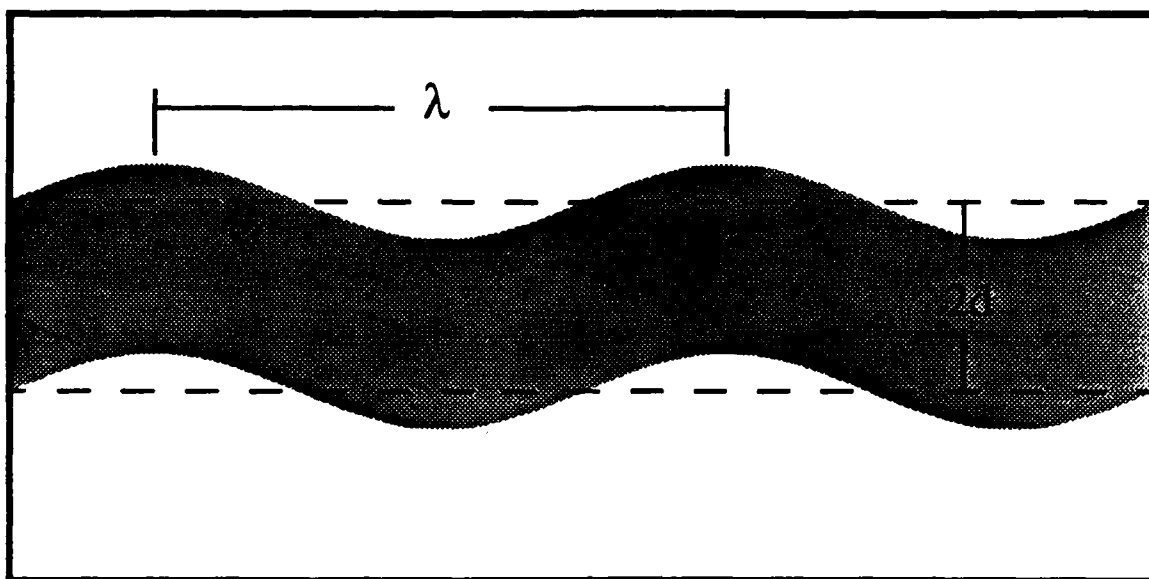


Figure B-6: Shear instability of a planar fluid sheet.

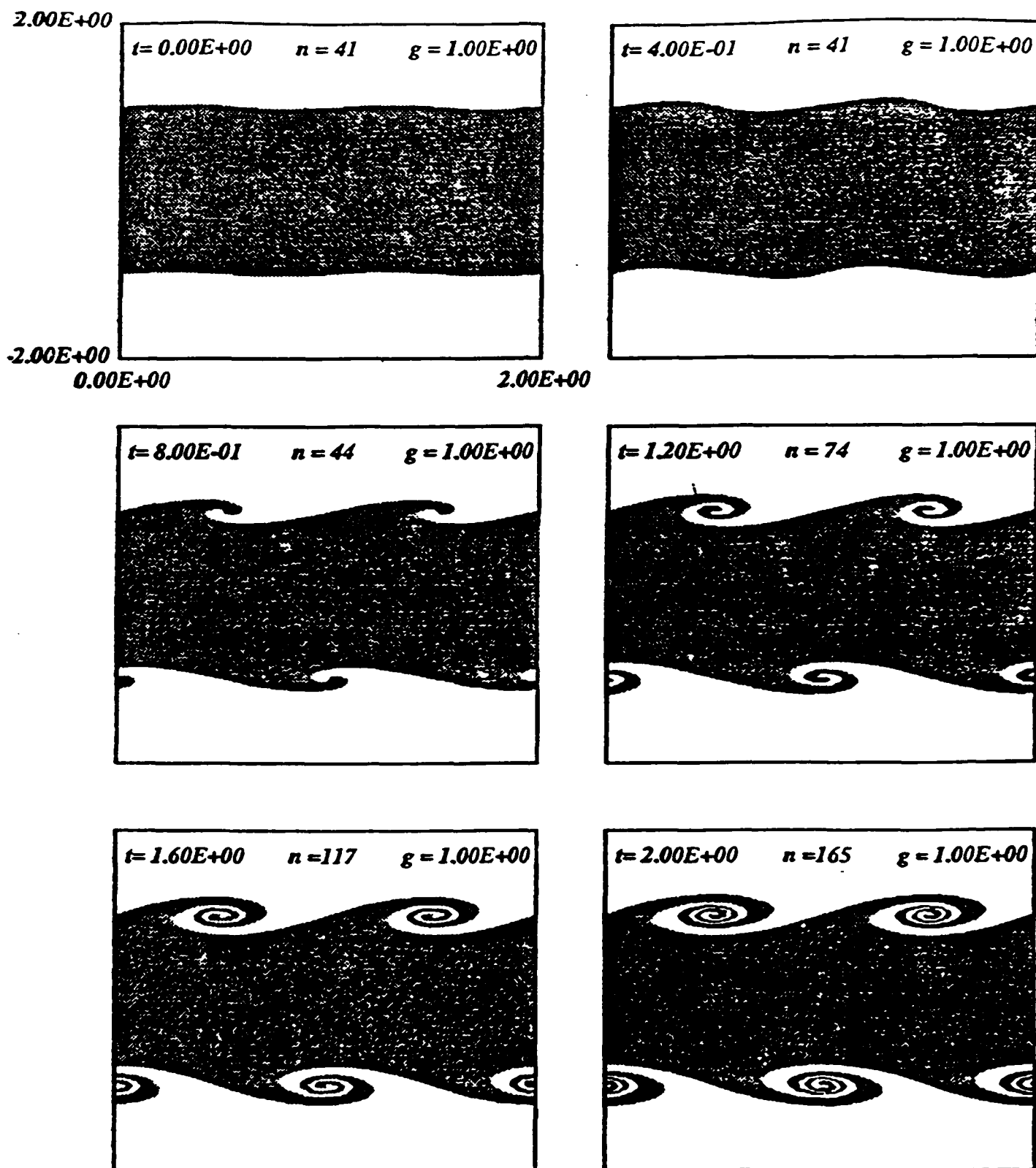


Figure B-7: Sheet evolution for a thickness-to-wavelength ratio of 2. Density ratio = 1. Surface tension = 0. (shifted-symmetric mode).

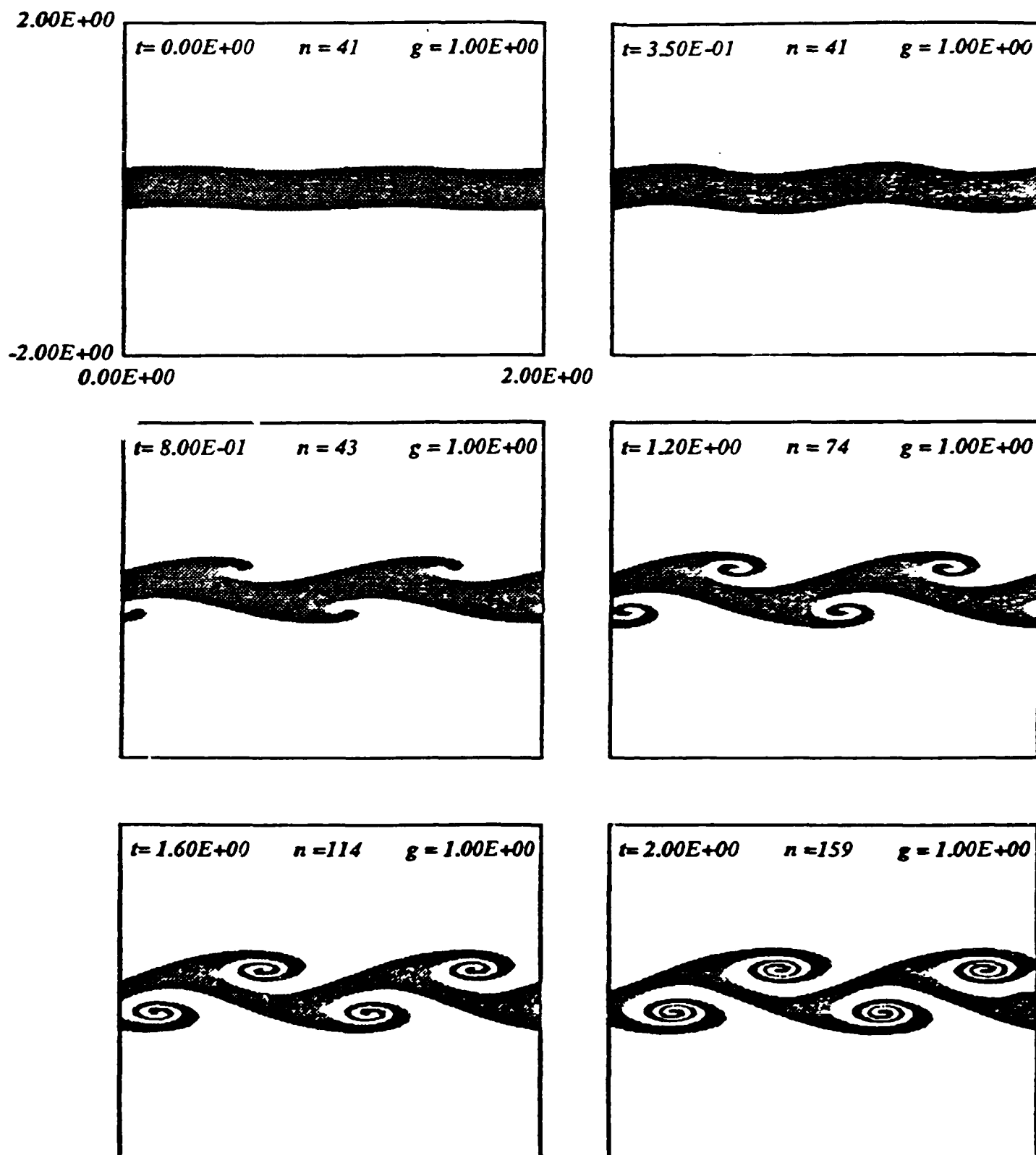


Figure B 8: Sheet evolution for a thickness to wavelength ratio of $1/2$. Density ratio = 1. Surface Tension = 0. (shifted symmetric mode)

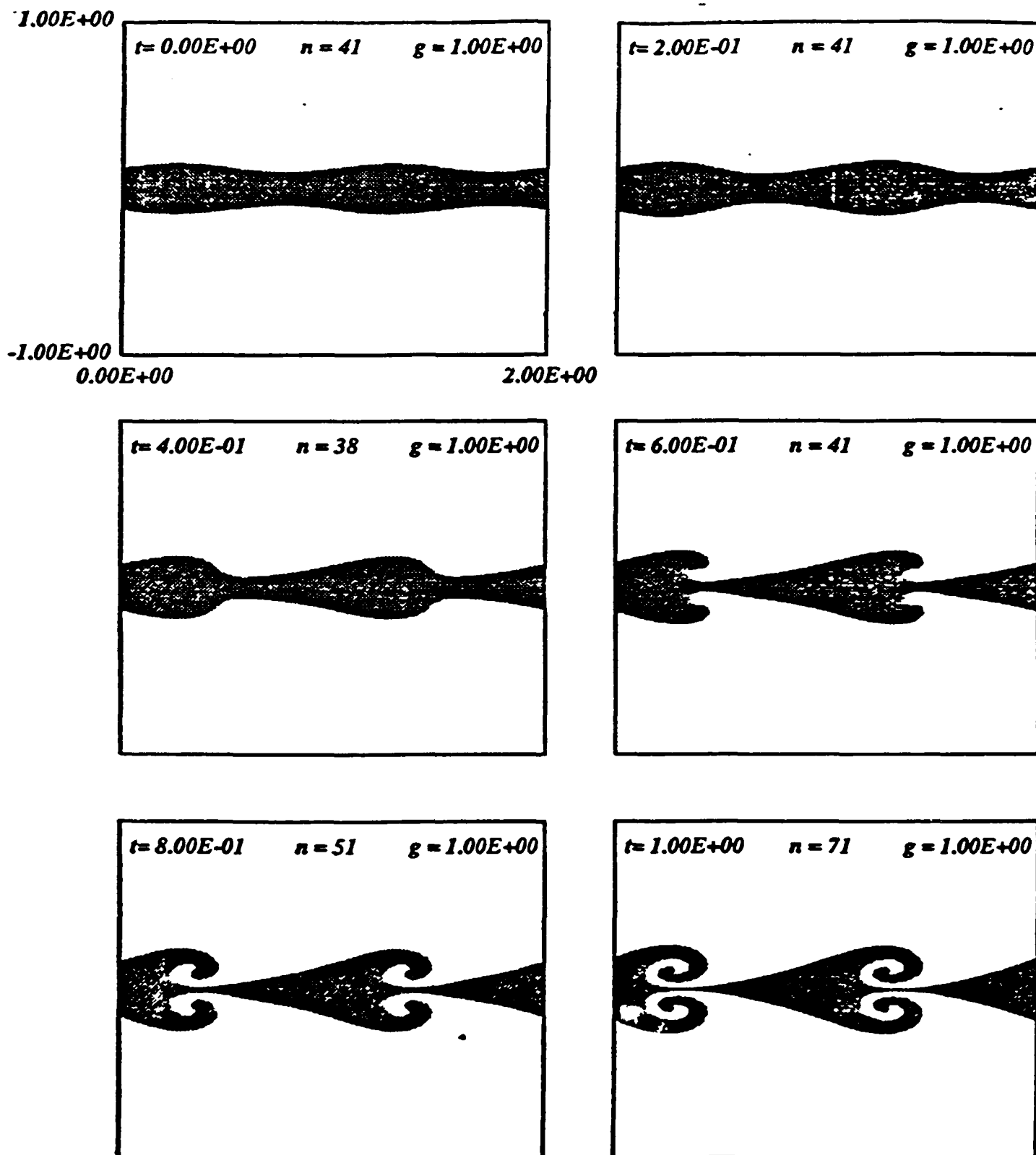
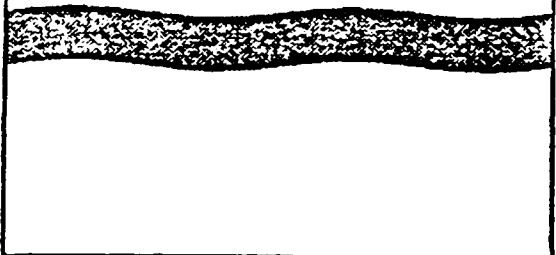


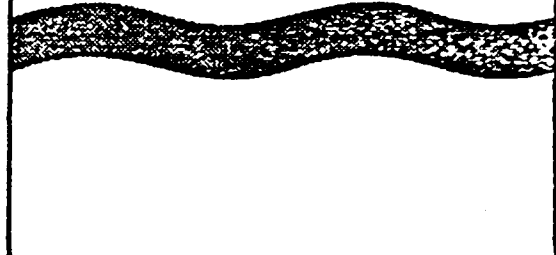
Figure B-9: Sheet evolution for a thickness-to-wavelength ratio of 1/4. Density ratio = 1. No surface tension. (symmetric mode)

1.00E+00

$t = 0.00E+00$ $n = 41$ $g = 1.00E+00$



$t = 5.00E-01$ $n = 41$ $g = 1.00E+00$

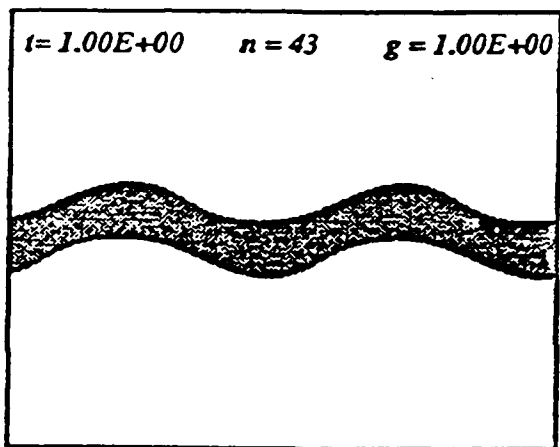


1.00E+00

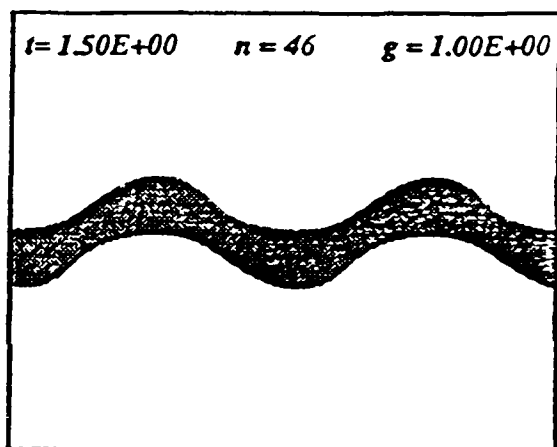
0.00E+00

2.00E+00

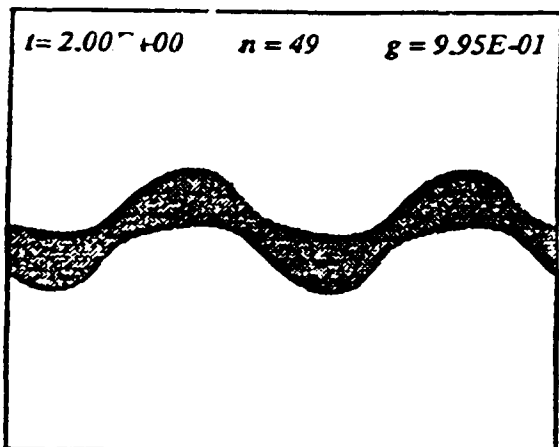
$t = 1.00E+00$ $n = 43$ $g = 1.00E+00$



$t = 1.50E+00$ $n = 46$ $g = 1.00E+00$



$t = 2.00E+00$ $n = 49$ $g = 9.95E-01$



$t = 2.50E+00$ $n = 51$ $g = 9.99E-01$

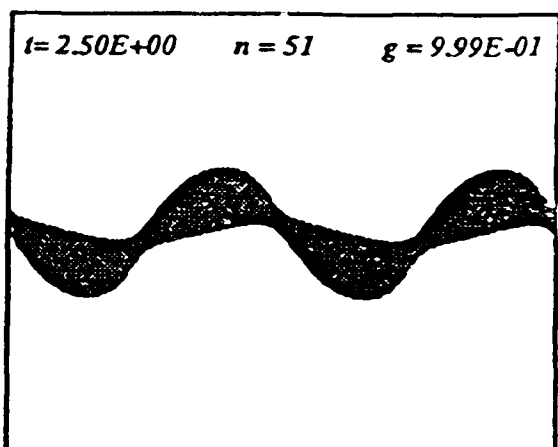


Figure B-10: Sheet evolution for a thickness-to wavelength ratio of $1/4$. Density ratio = 1. Optimum dimensionless wavenumber. (shifted symmetric mode)

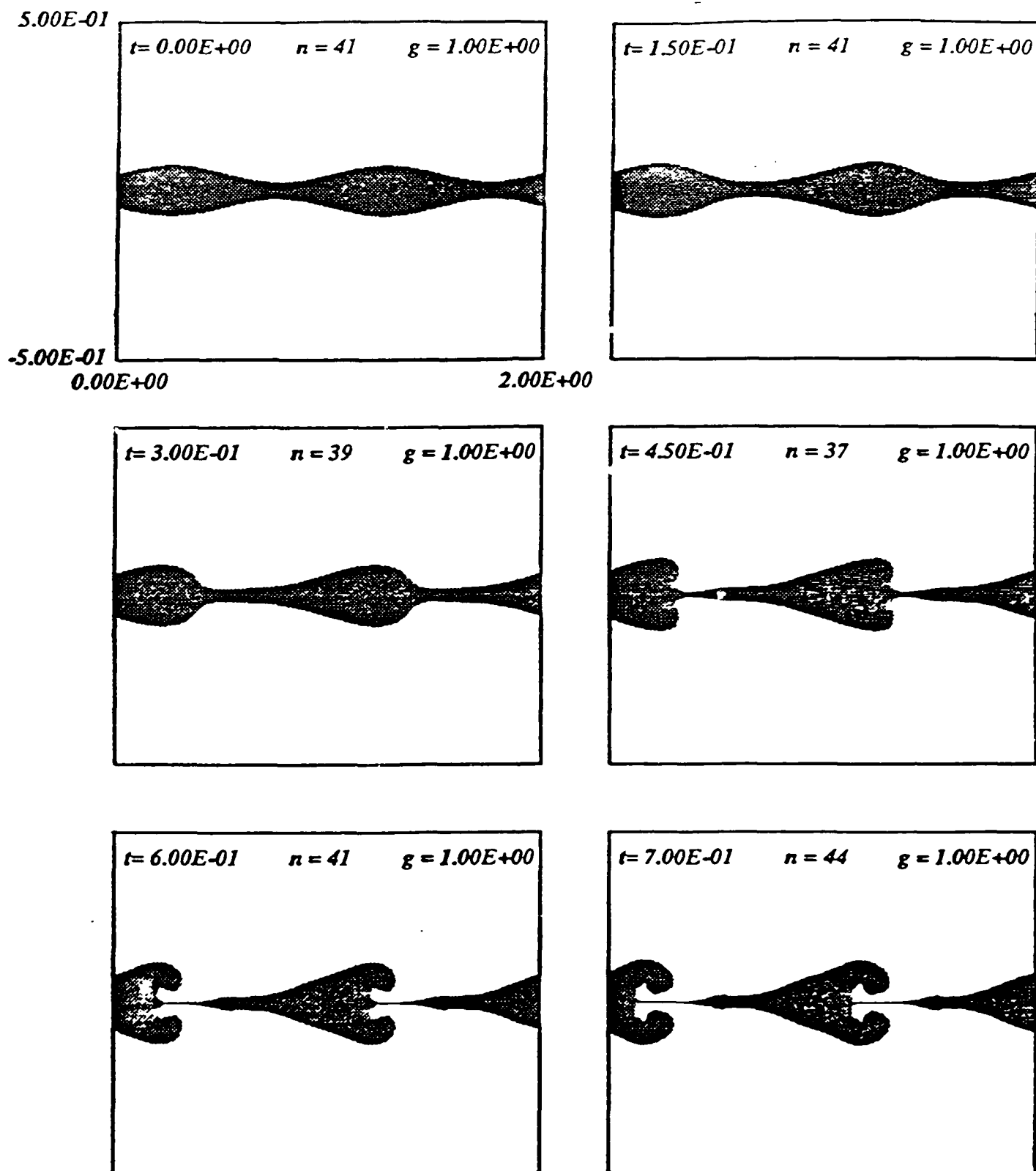


Figure B 11: Sheet evolution for a thickness- to wavelength ratio of $1/8$. Density ratio = 1. No surface tension (symmetric mode)

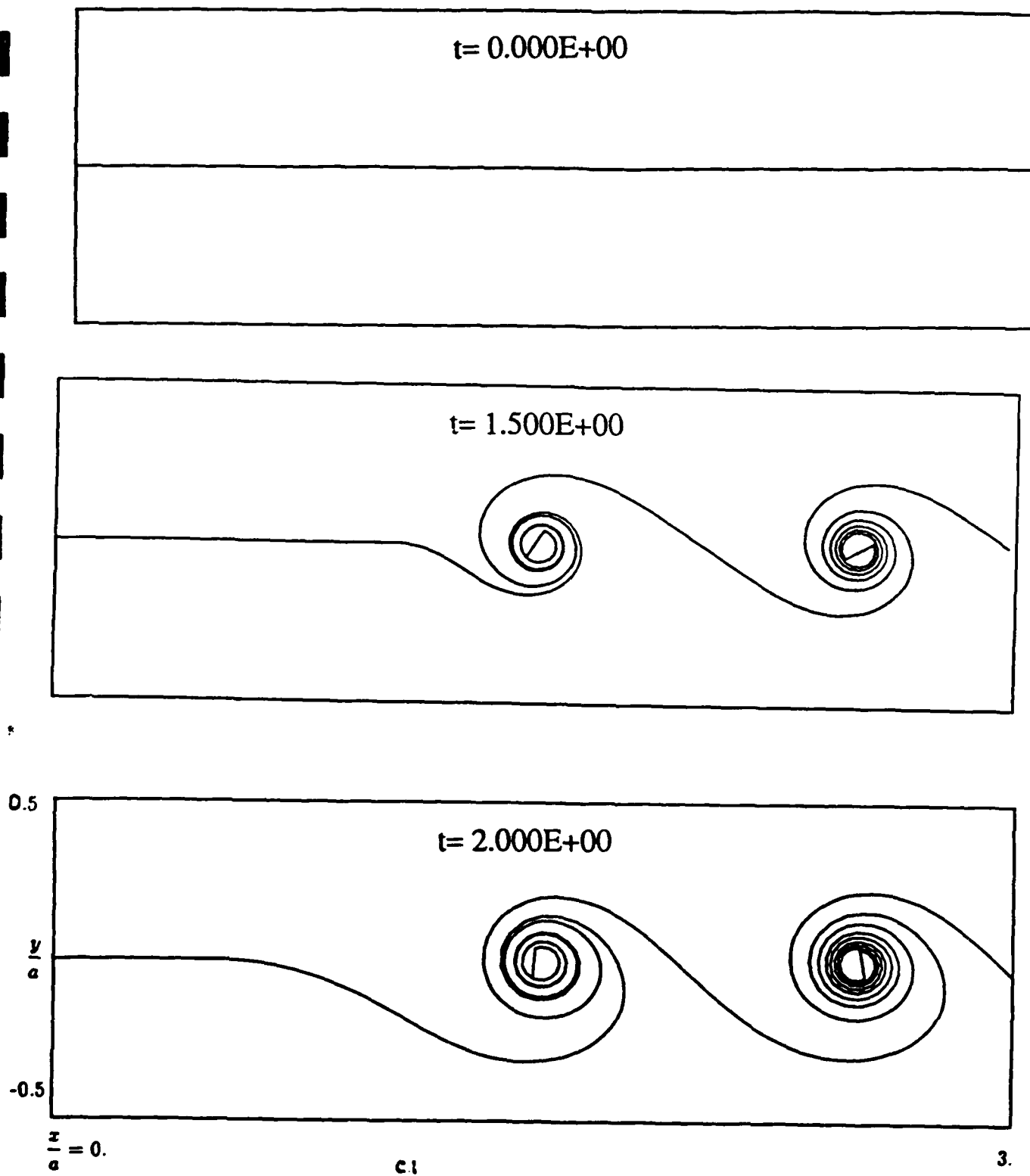


Figure C-1: Evolution of the interface for $Re = 50$

contour interval: 1.00E-01 from: 0.00E+00 to: 1.00E+00

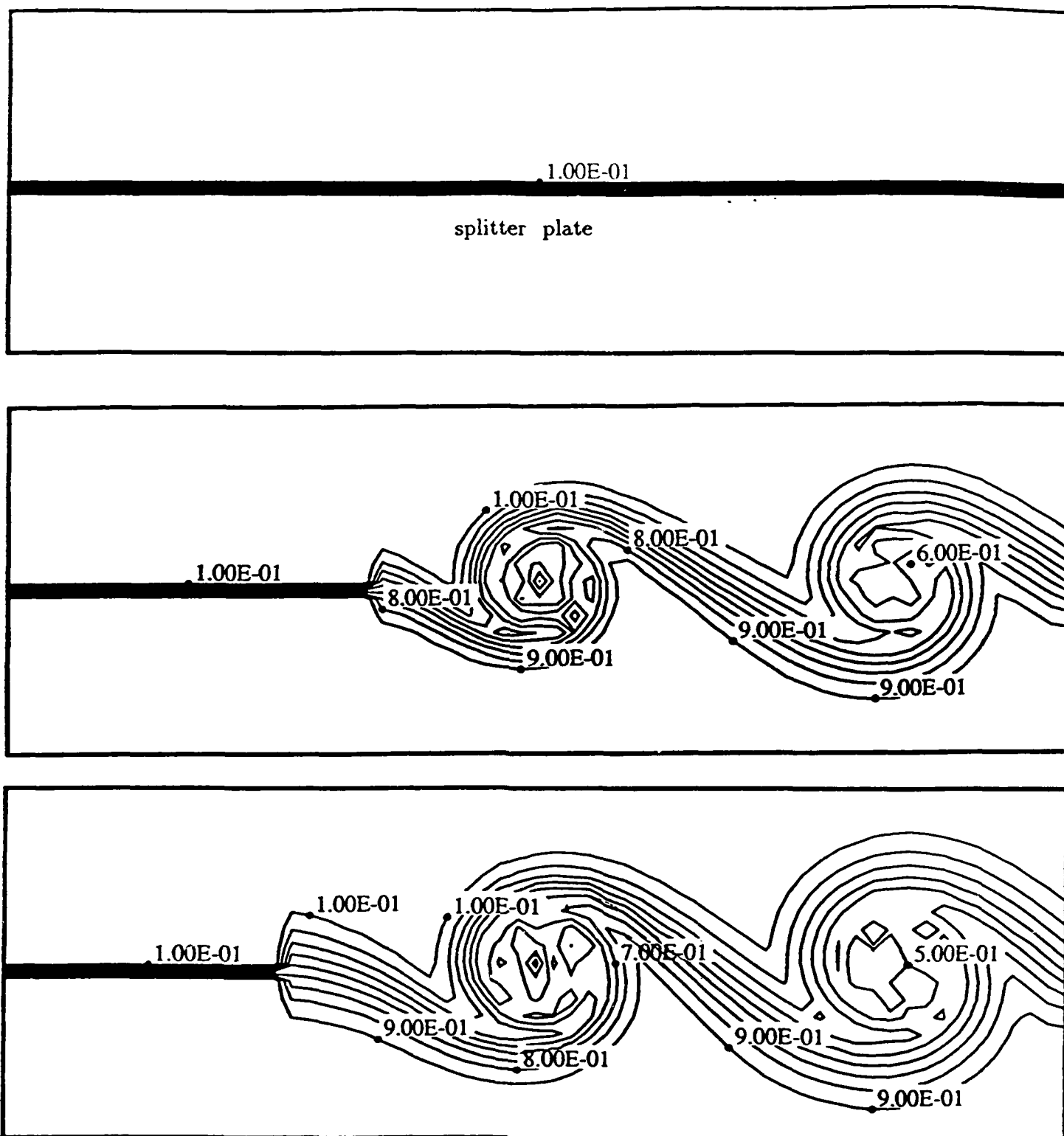


Figure C-2: Species Concentration contour plots for $Re = 50$ and $Sc = 1$.

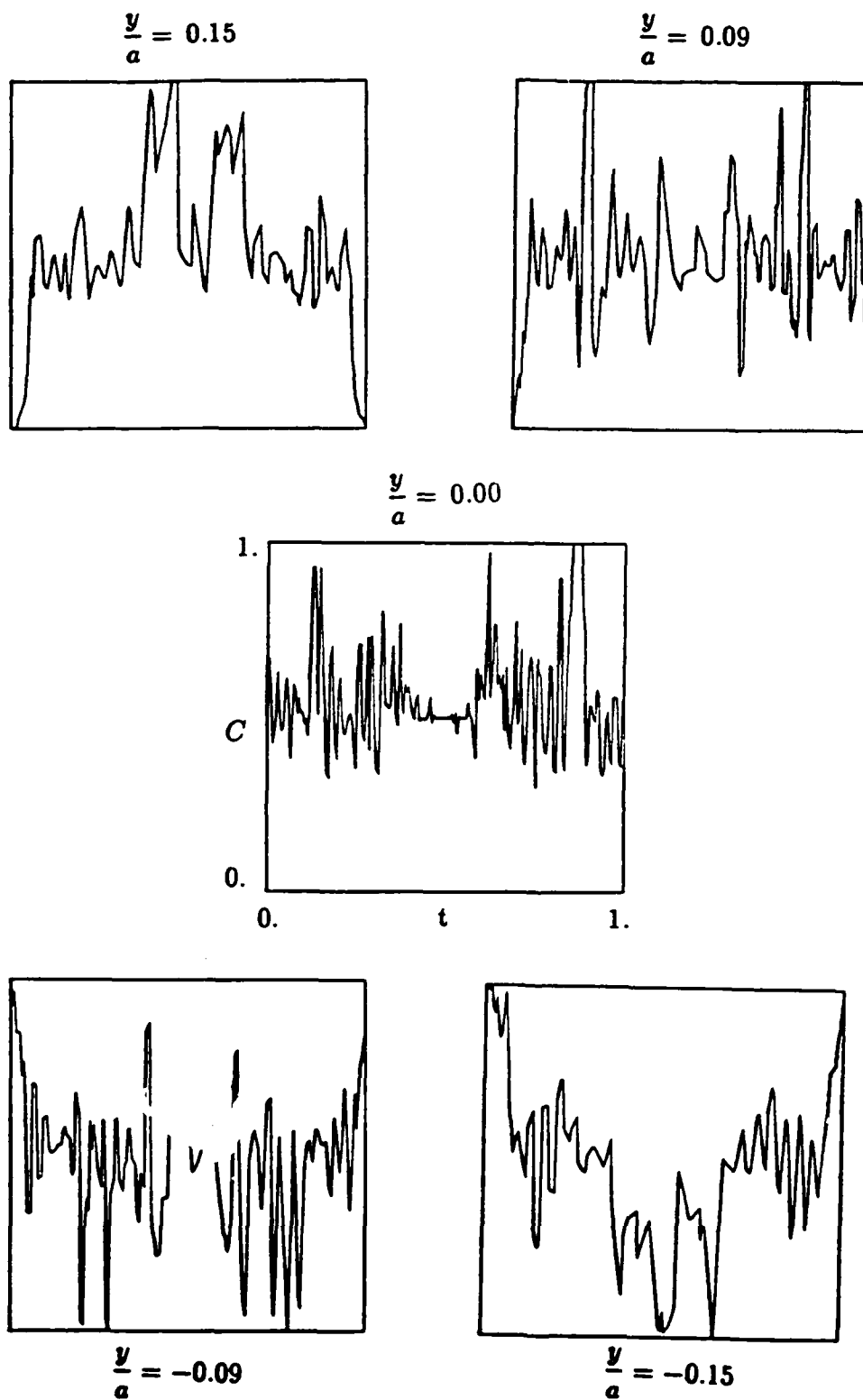


Figure C-3: Concentration profiles at different heights above the mixing plane.

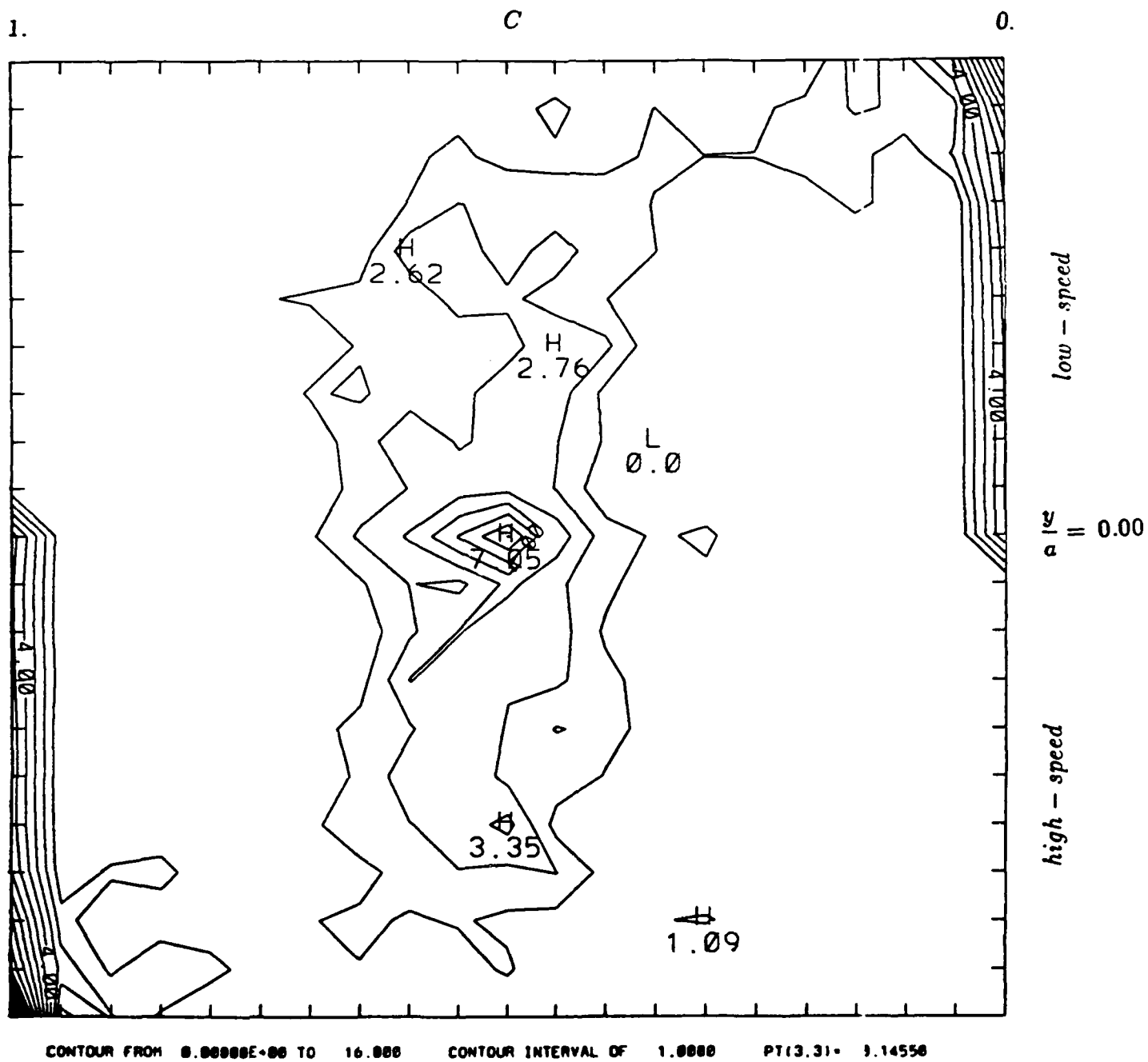
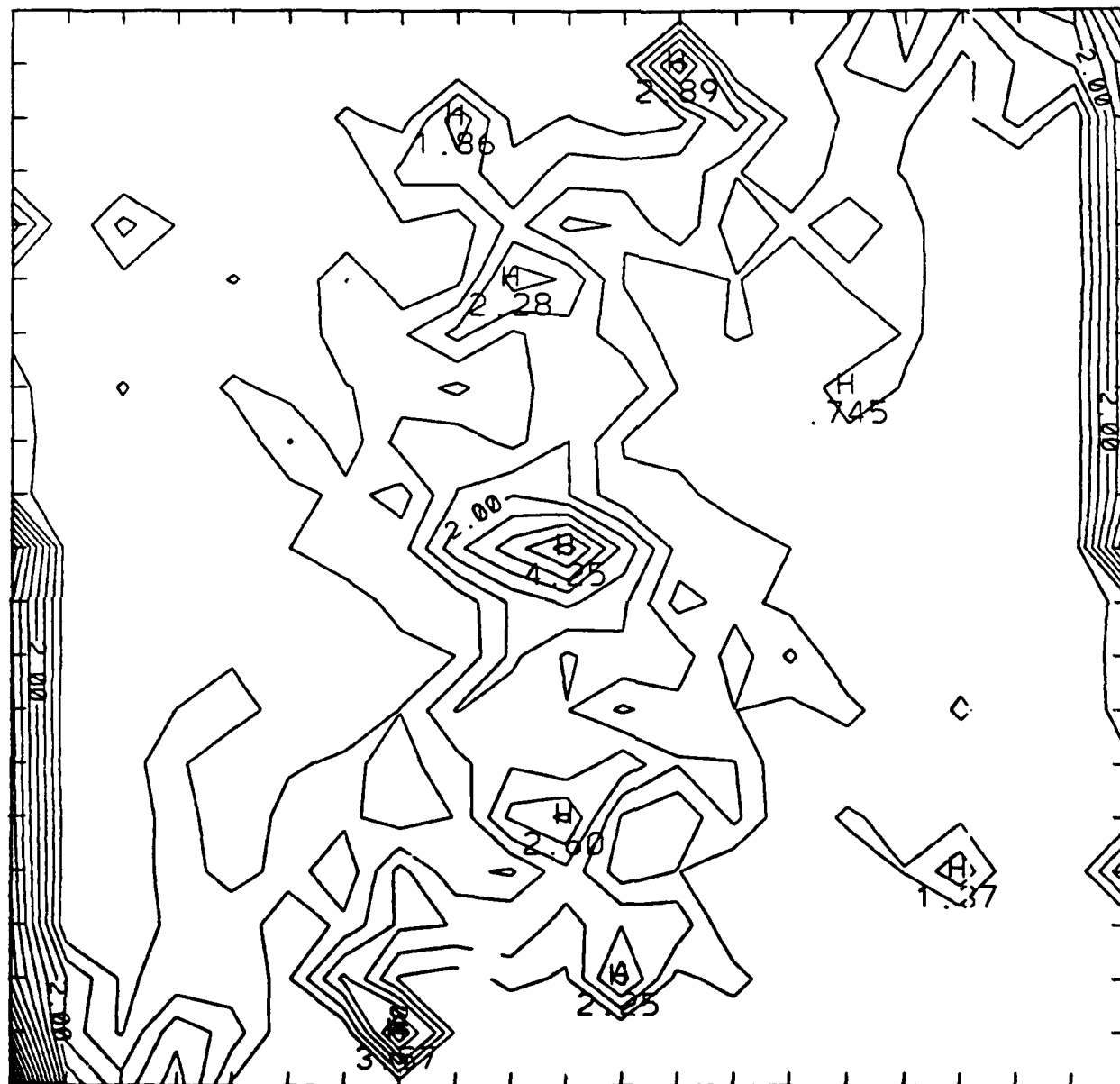
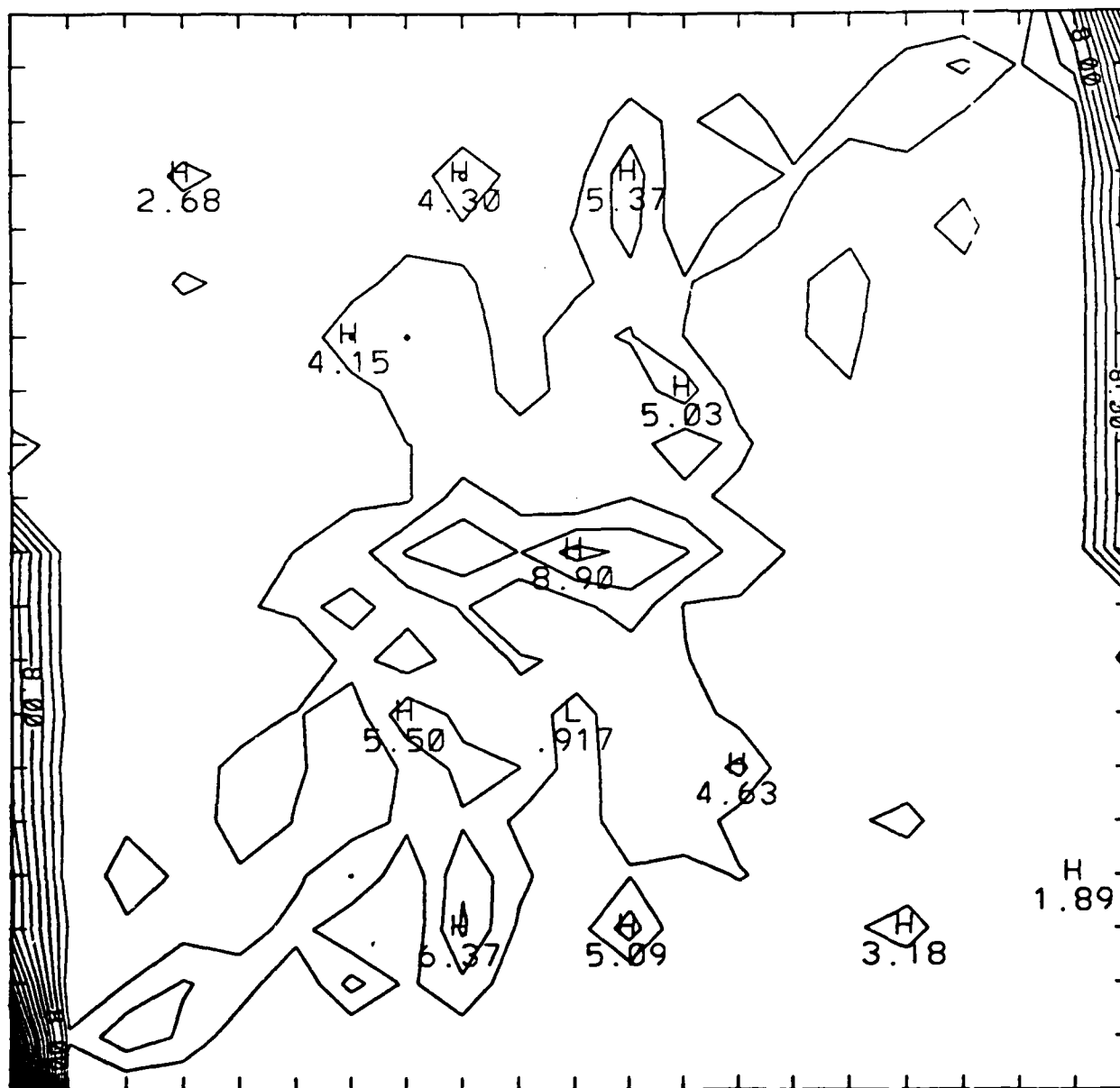


Figure C-4: Species Concentration PDF constructed from the profiles in Figure C-2.



CONTOUR FROM 0.00000E+00 TO 9.0000 CONTOUR INTERVAL OF 0.50000 PT(3,31)= 9.42070

Figure C-5: PDF for $Re = 10$ and $Sc = 1$.



CONTOUR FROM 0.00000E+00 TO 46.000 CONTOUR INTERVAL OF 2.0000 PT(3.31)= 1.9290

Figure C-6: PDF for $Re = 100$ and $Sc = 1$.

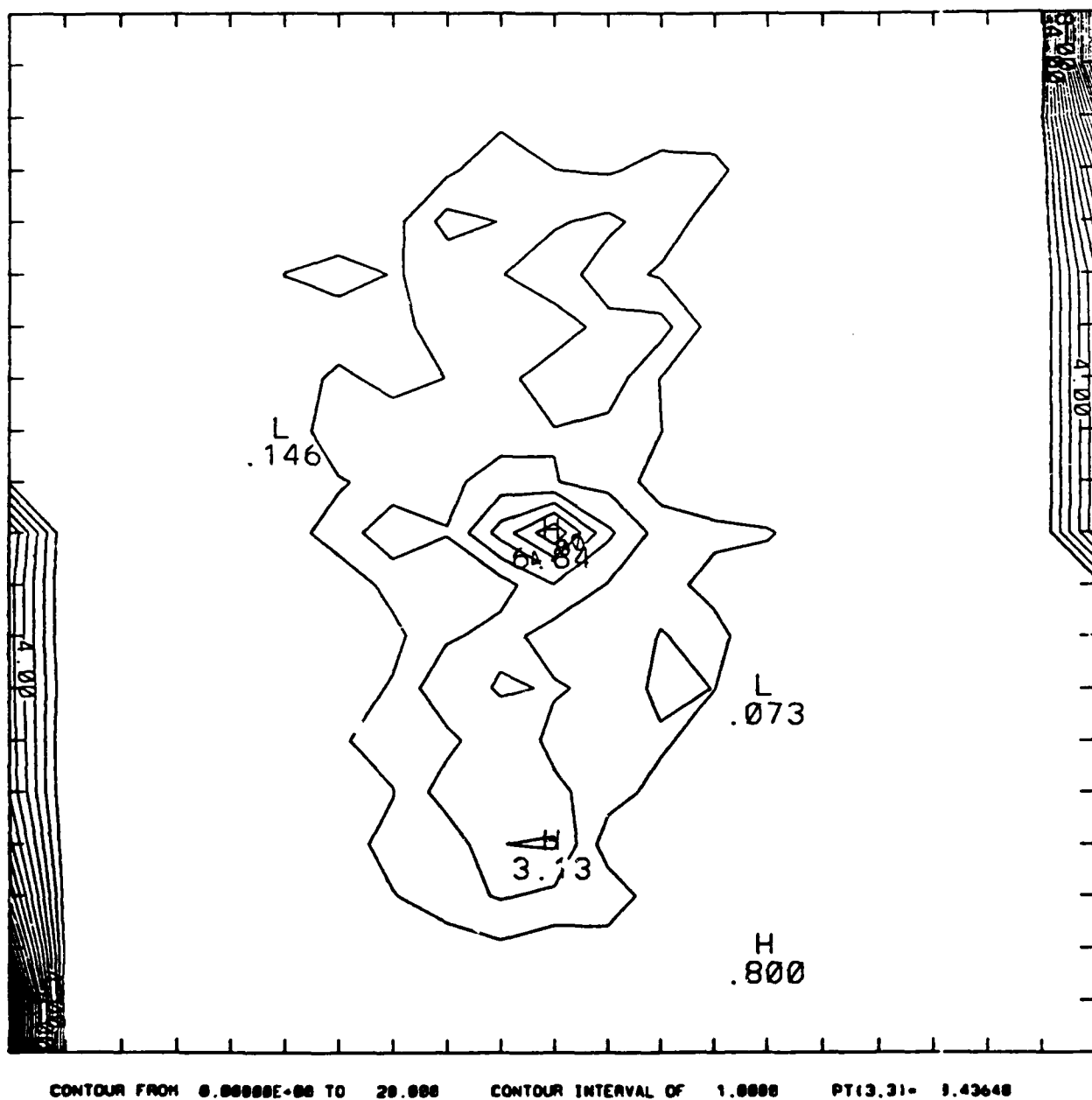
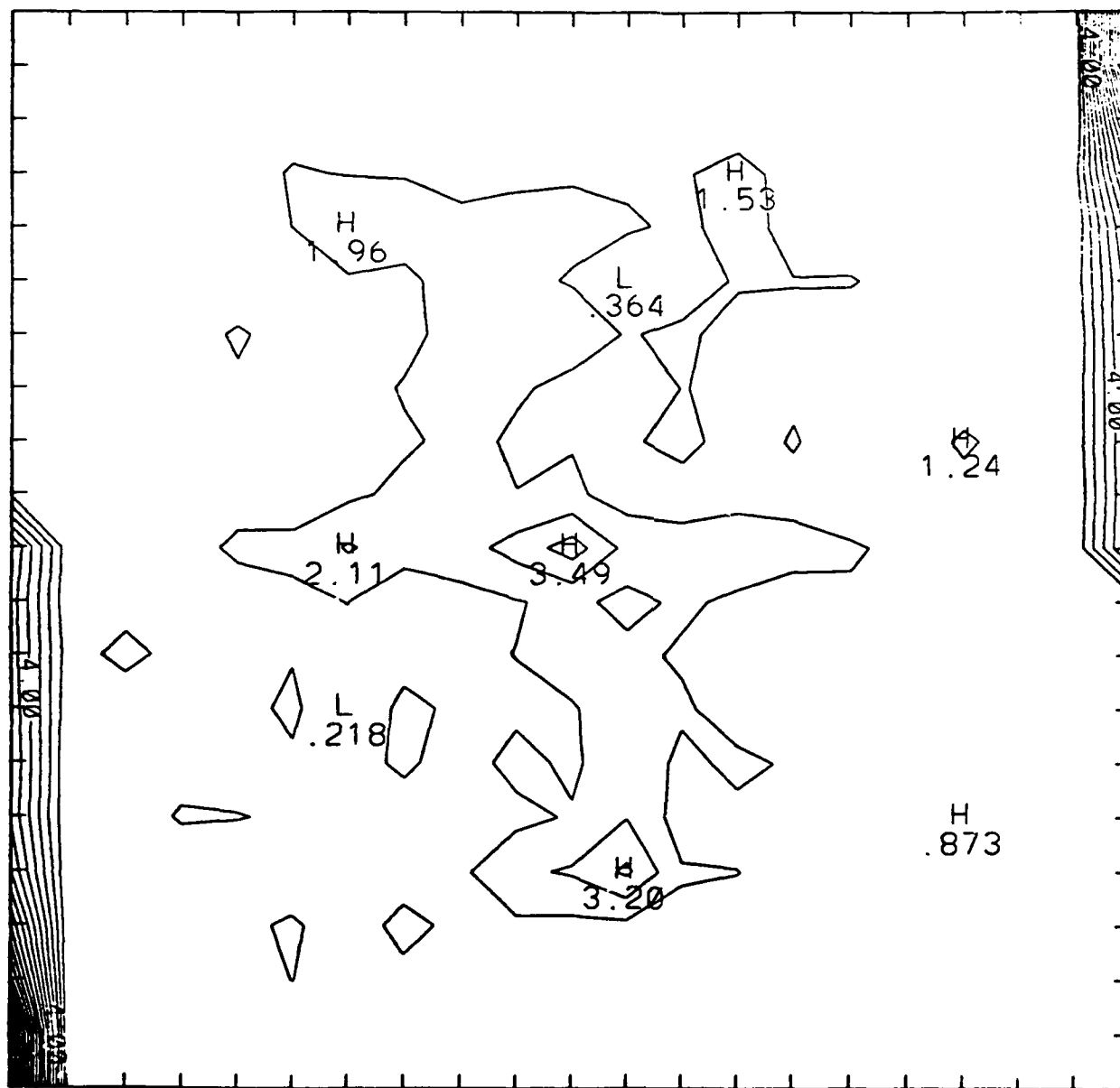


Figure C-7: PDF for $Re = 50$ and $Sc = 100$.



CONTOUR FROM 0.00000E+00 TO 20.000 CONTOUR INTERVAL OF 1.0000 PT(3,31)= 0.72730E-01

Figure C-8: PDF for $Re = 50$ and $Sc = 1000$.

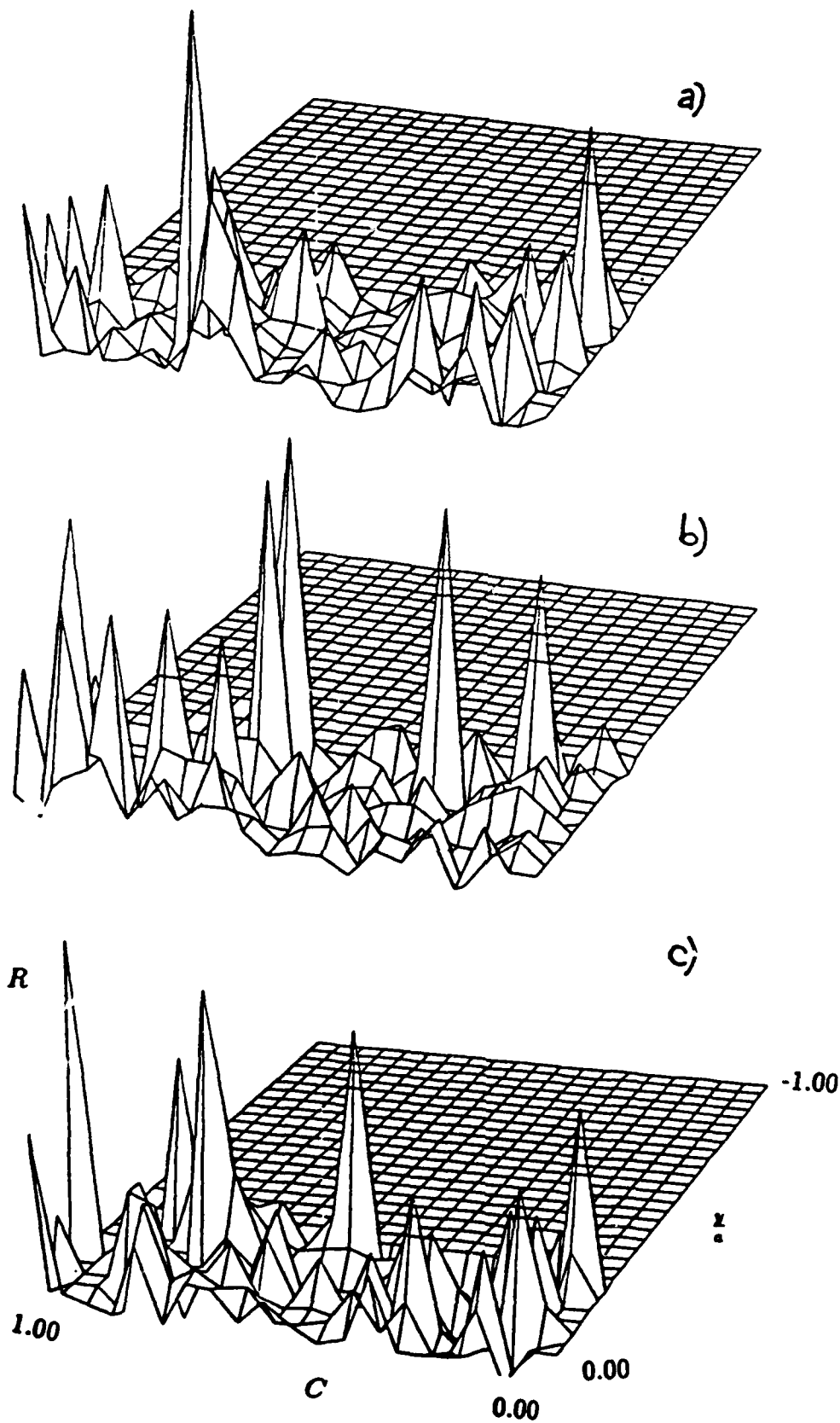


Figure C-9: Plot of the relative difference R between the PDF on the low-speed and high-speed streams, a) $Re = 50, Sc = 1000$ b) $Re = 10, Sc = 10$ c) $Re = 100, Sc = 1$

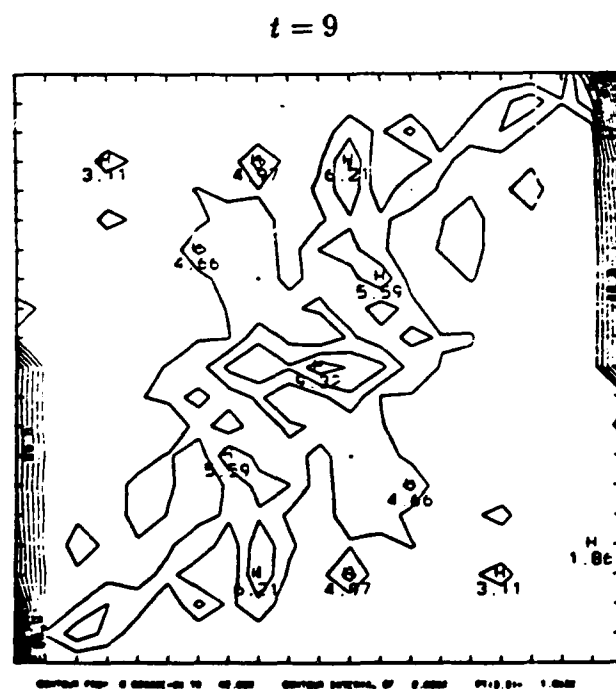
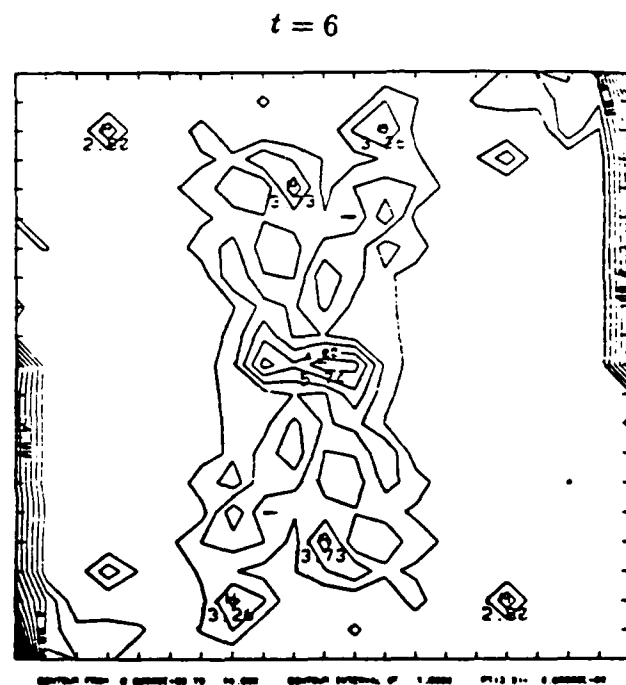
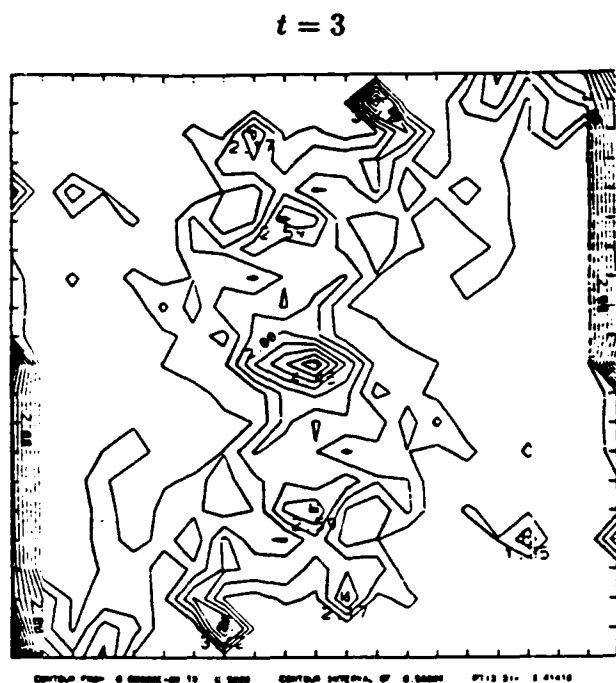
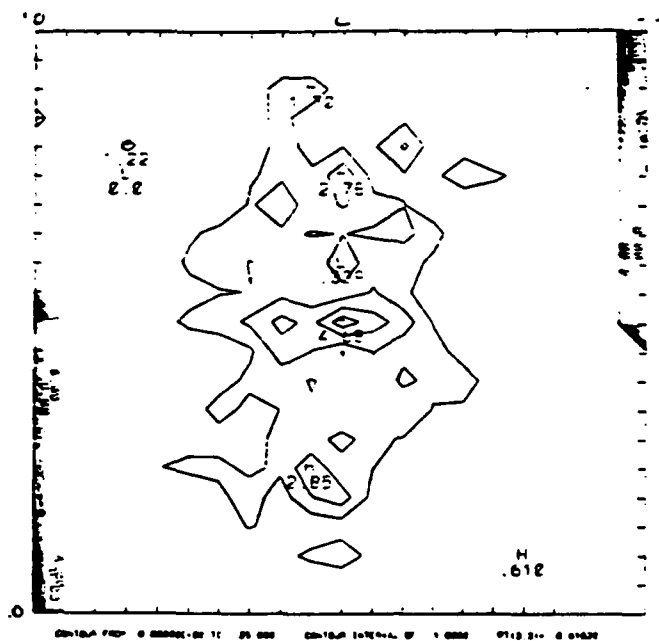
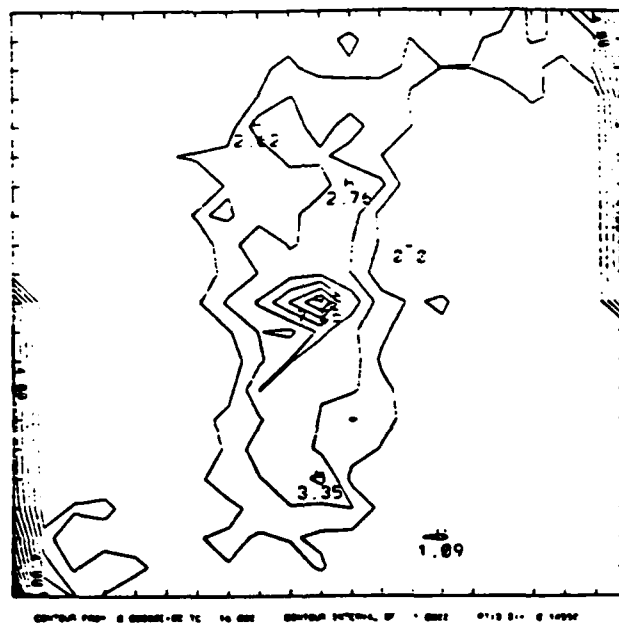


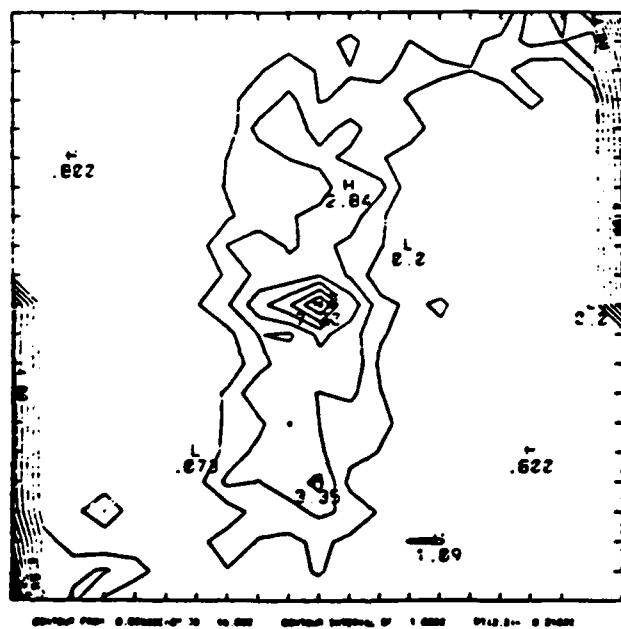
Figure C-10: PDF evolution in time for $Re = 50$ and $Sc = 1$.



probe located at $x = 3a$



probe located at $x = 6a$



probe located at $x = 9a$

Figure C-11: Numerical results for the spatially developing PDF.

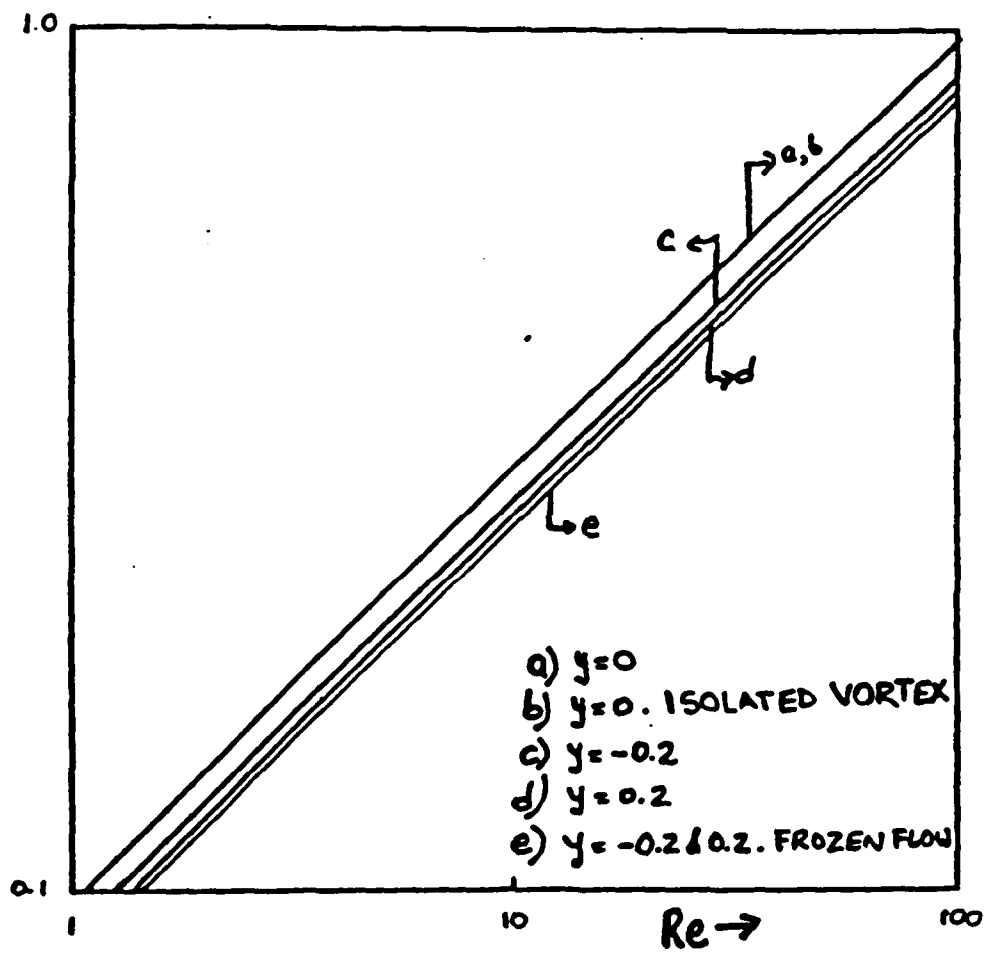


Figure C-12: Mixedness parameter as a function of Re for different heights above the mixing plane.

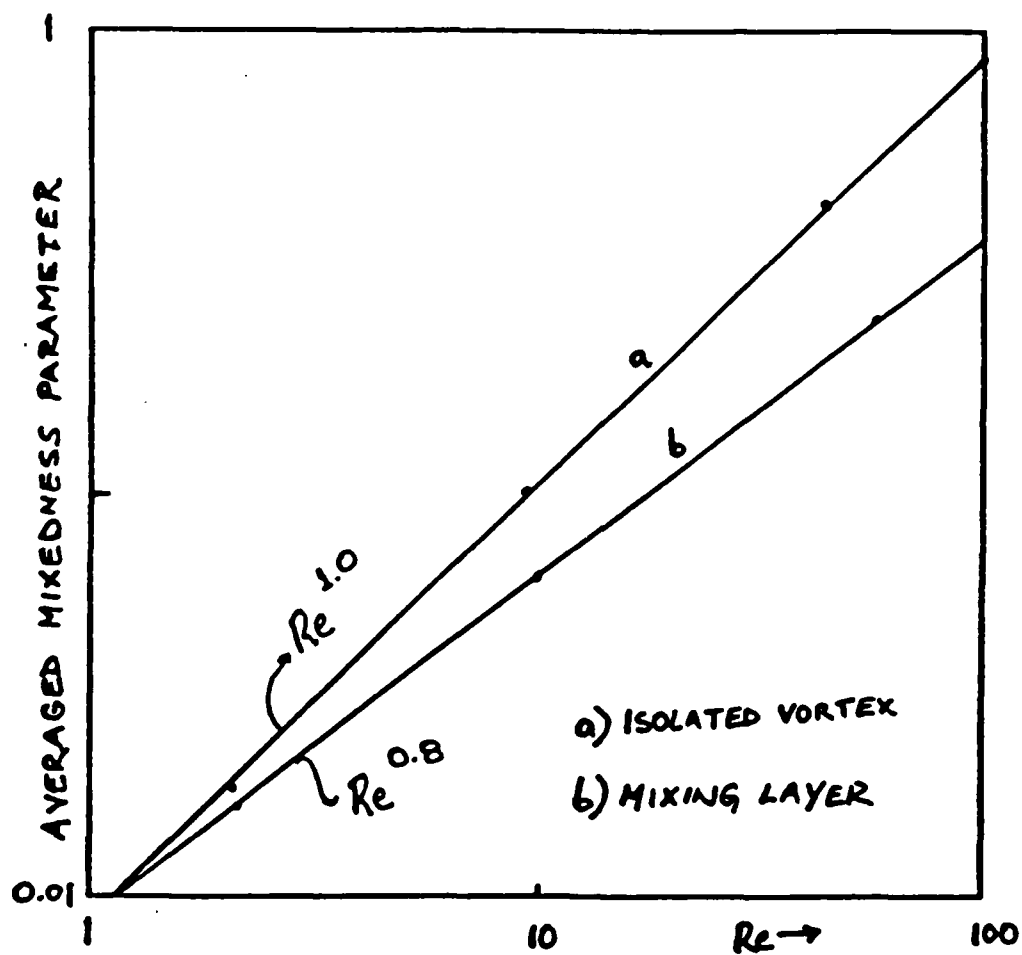
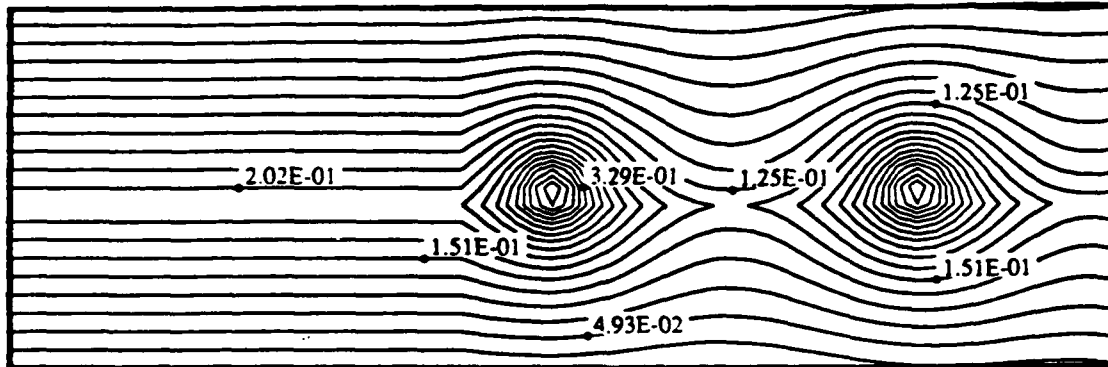
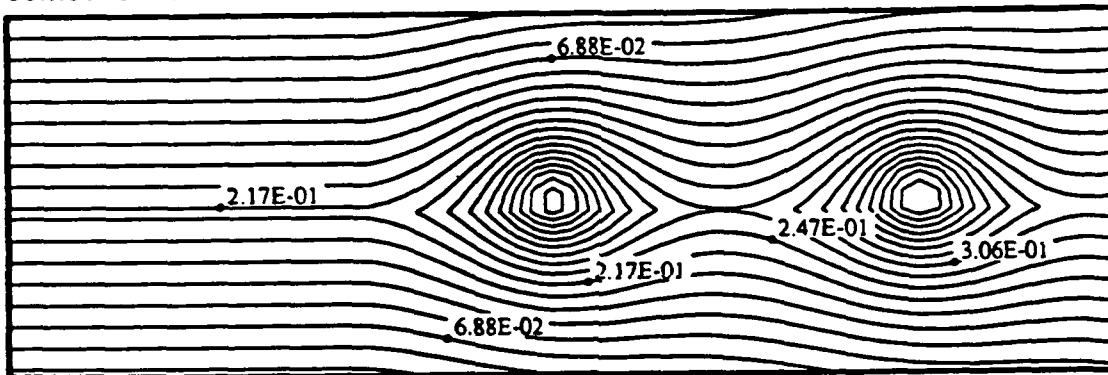


Figure C-13: Comparison of the overall mixedness parameter between a mixing layer and an isolated vortex.

contour interval: $2.54\text{E-}02$ from: $-5.23\text{E-}02$ to: $4.56\text{E-}01$ $t = 1.25$



contour interval: $2.97\text{E-}02$ from: $-5.00\text{E-}02$ to: $5.44\text{E-}01$ $t = 1.50$



contour interval: $3.24\text{E-}02$ from: $-5.00\text{E-}02$ to: $5.97\text{E-}01$ $t = 1.75$

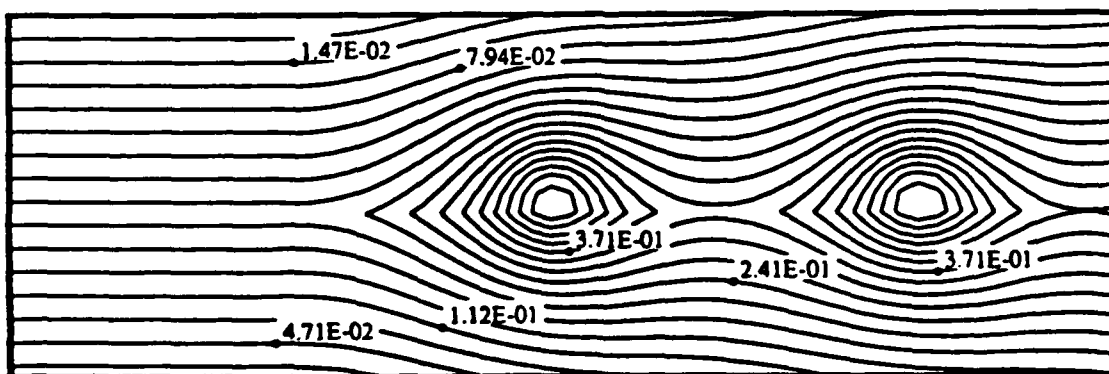
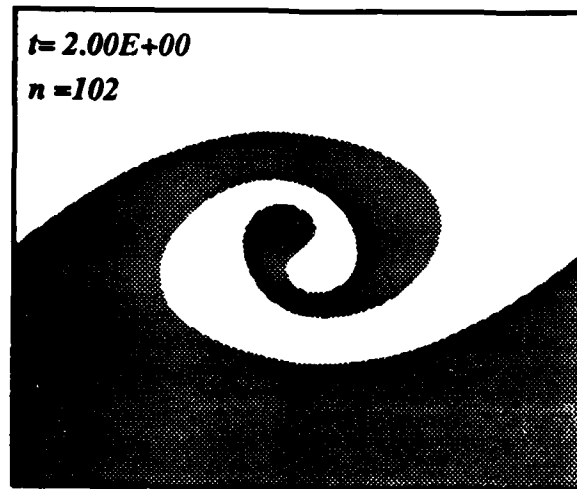
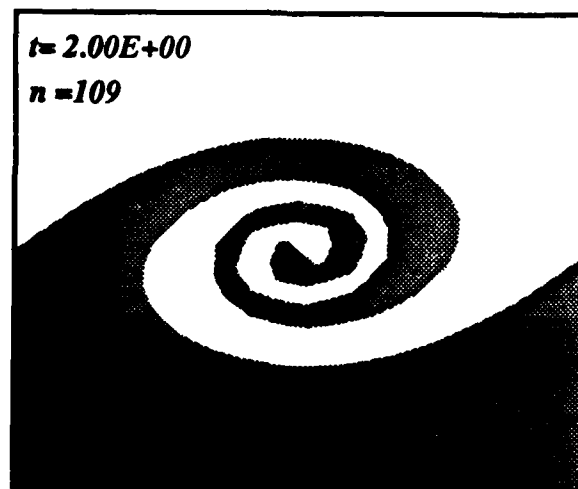


Figure C-14: Streamfunction contours for the simulated Mixing Layer.



(a)



(b)

Figure C-15: Rollup of an initially sinusoidal disturbance. (a) Rediscretization and addition of vortices. (b) Combination and addition of Vortices.

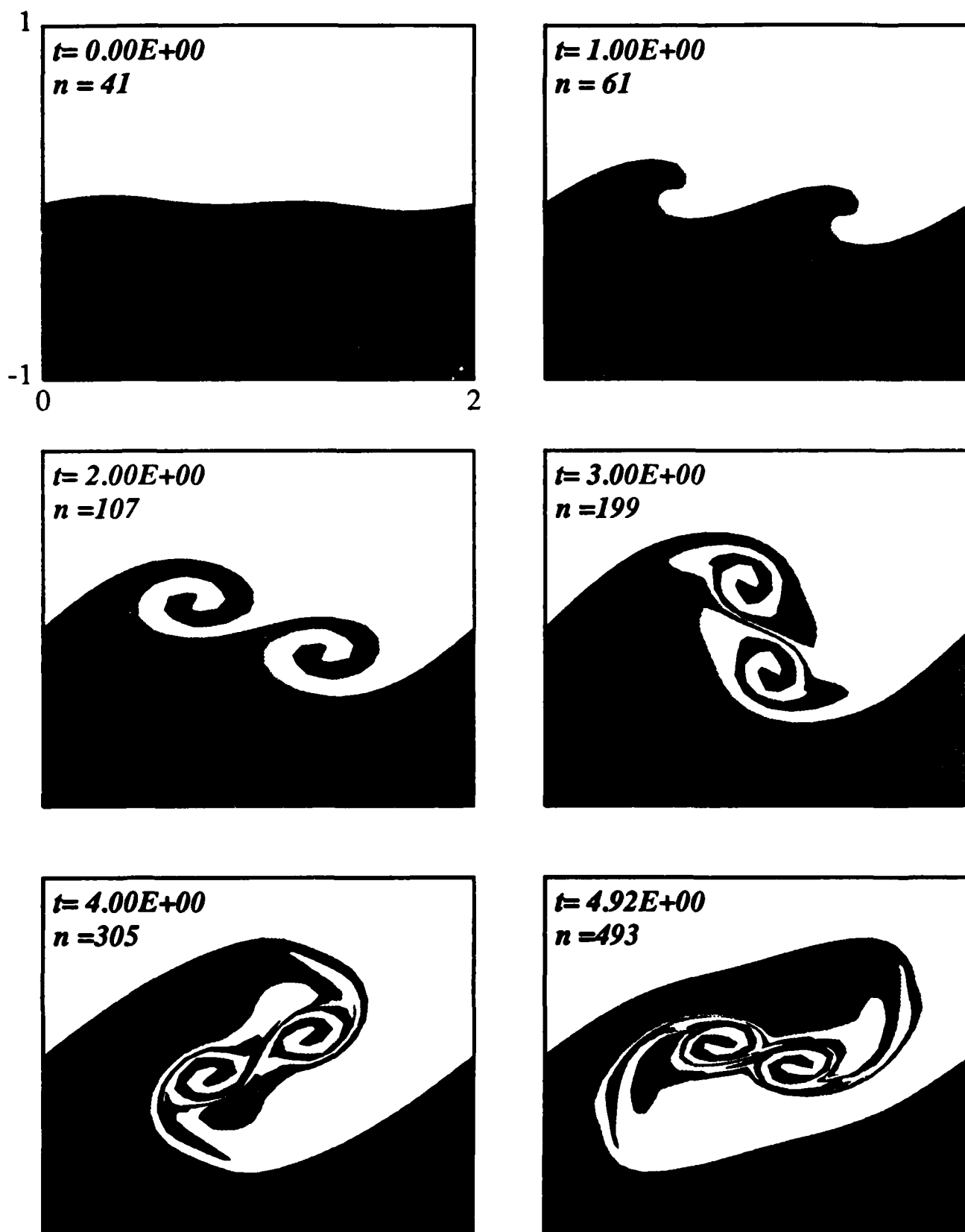


Figure C-16: Rollup of pairing of two vortical structures induced by the presence of the first subharmonic.

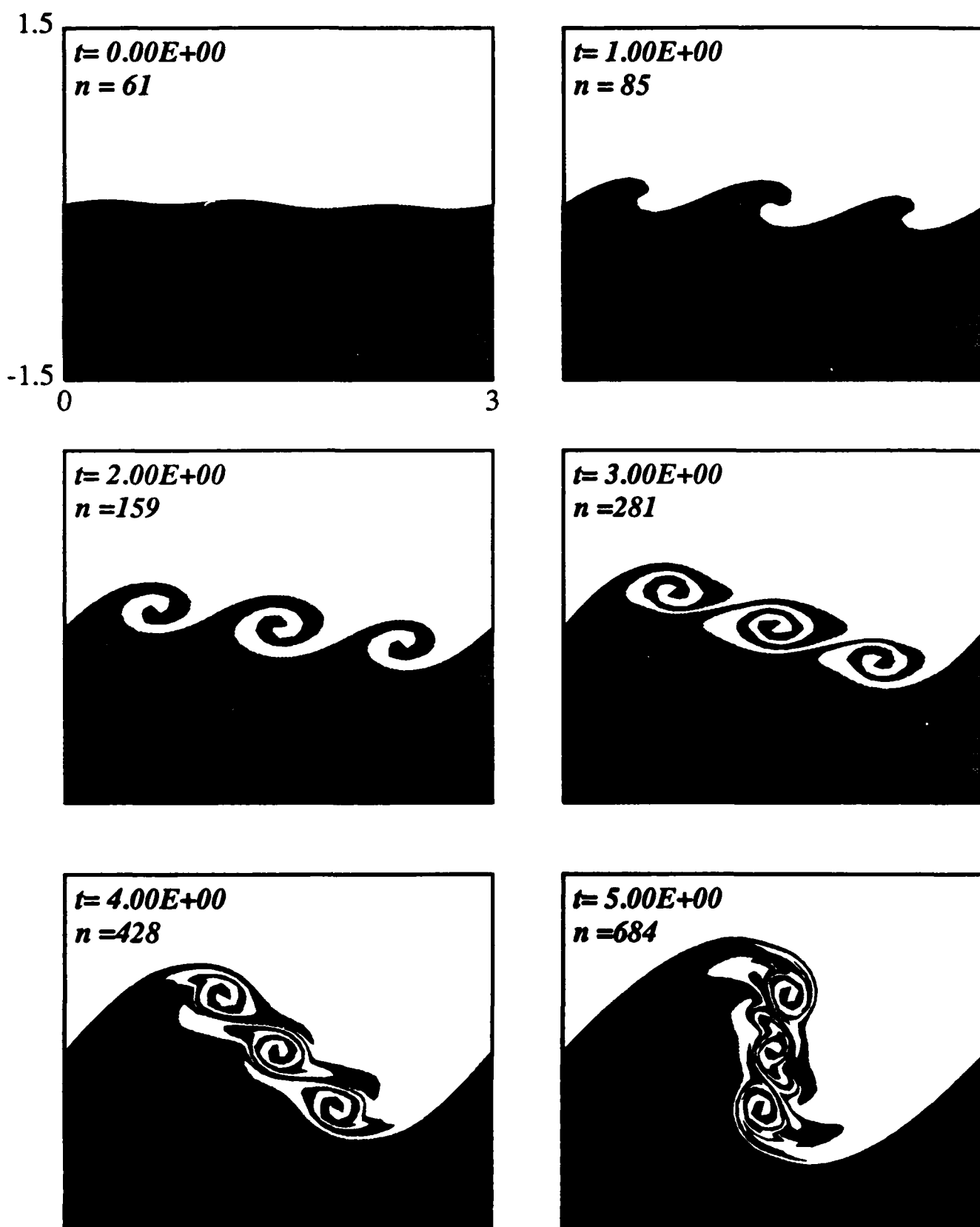


Figure C-17: Rollup and grouping of three vortical structures induced by the presence of the second subharmonic.

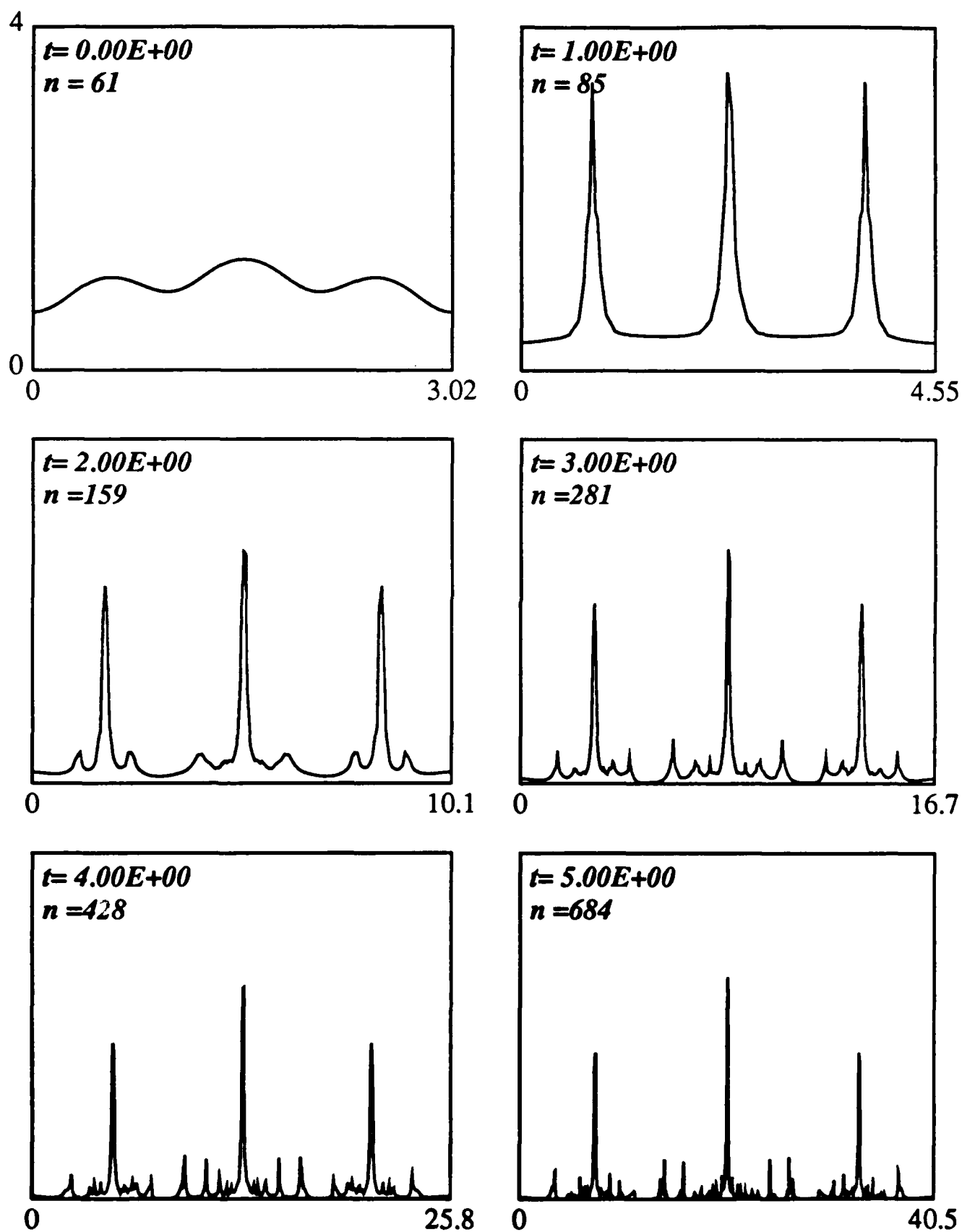


Figure C-18: Evolution of the vorticity distribution along the interface during the grouping of the three vortical structures.

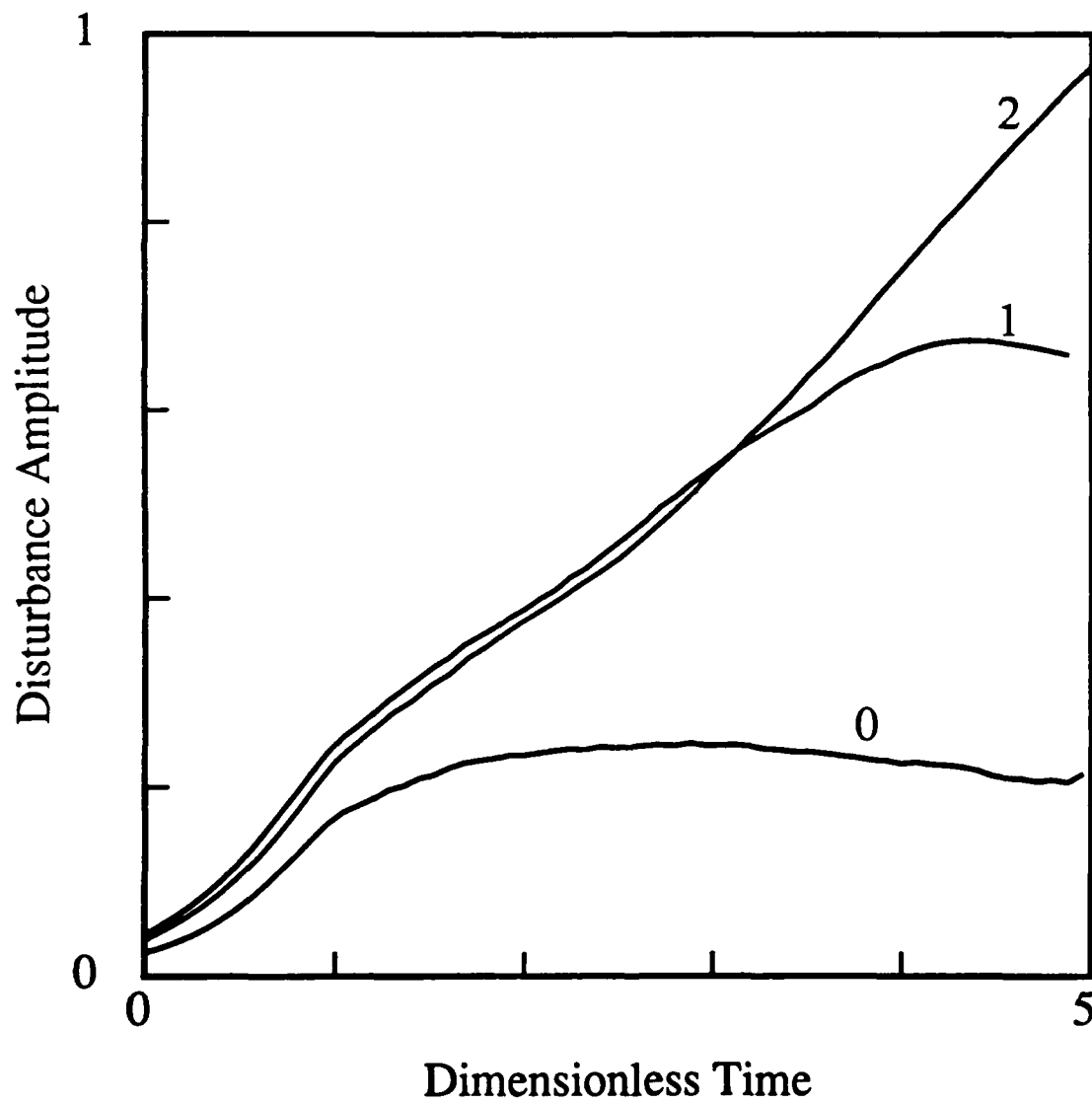


Figure C-19: Amplitude of the disturbance as a function of time for the fundamental disturbance alone (0), the fundamental plus the first subharmonic (1), and the fundamental plus the second subharmonic (2).

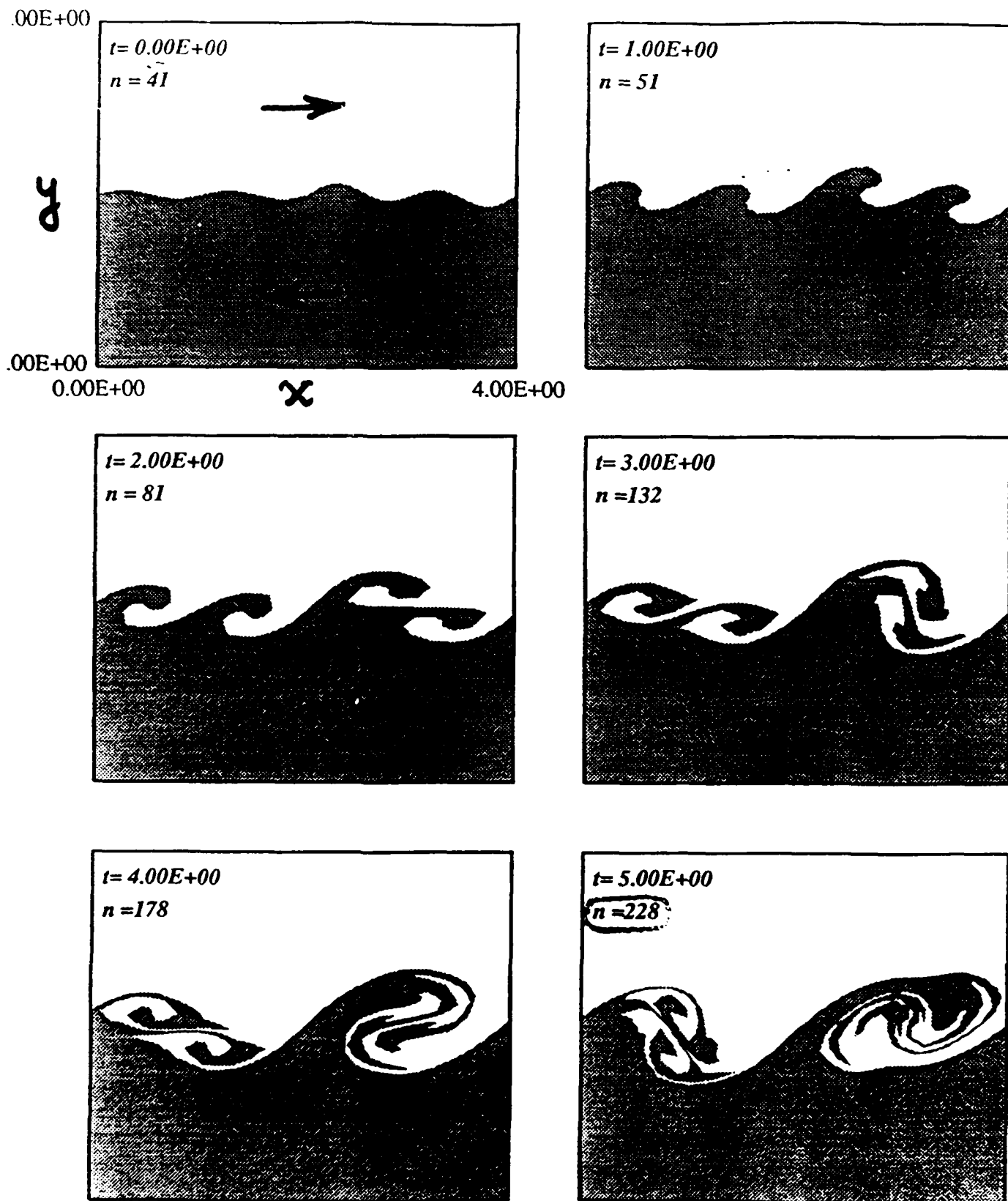


Figure C-20: Interface evolution with four vortical structures.

$$Pe = 2500$$

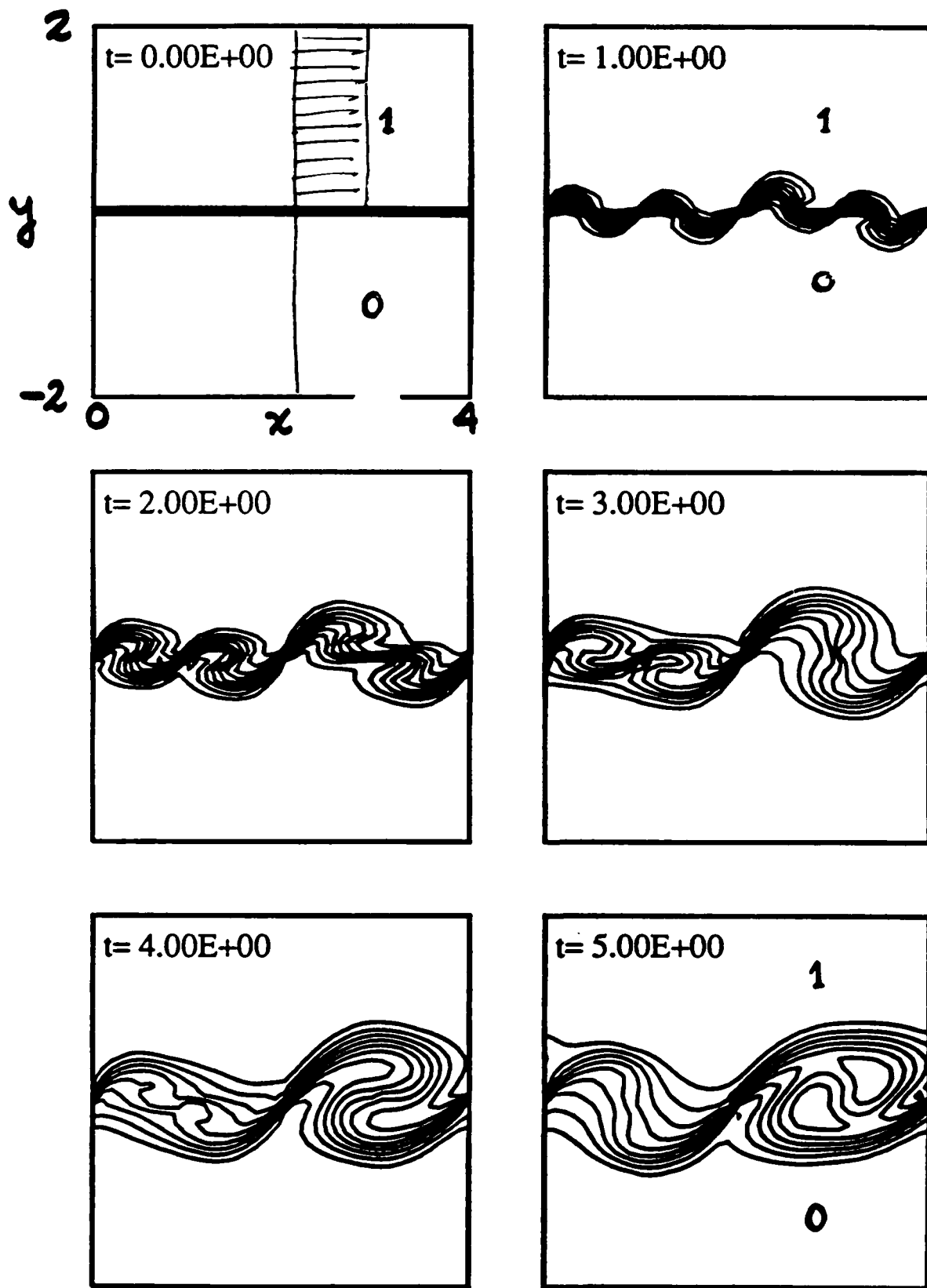


Figure C-21: Evolution of Mass Fraction Contours with four structures.

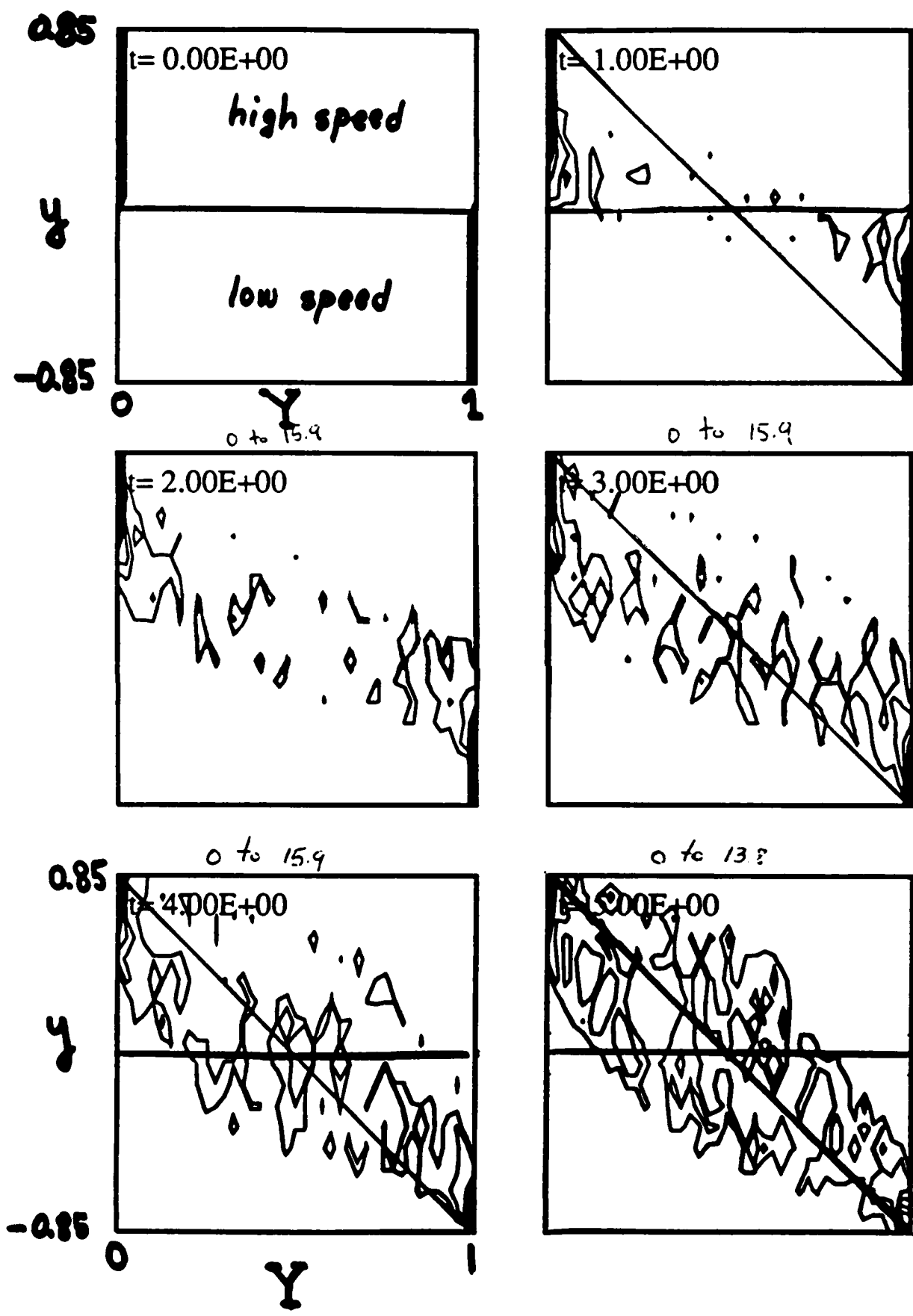


Figure C-22: Evolution of Instantaneous pdf with four vortex structures.

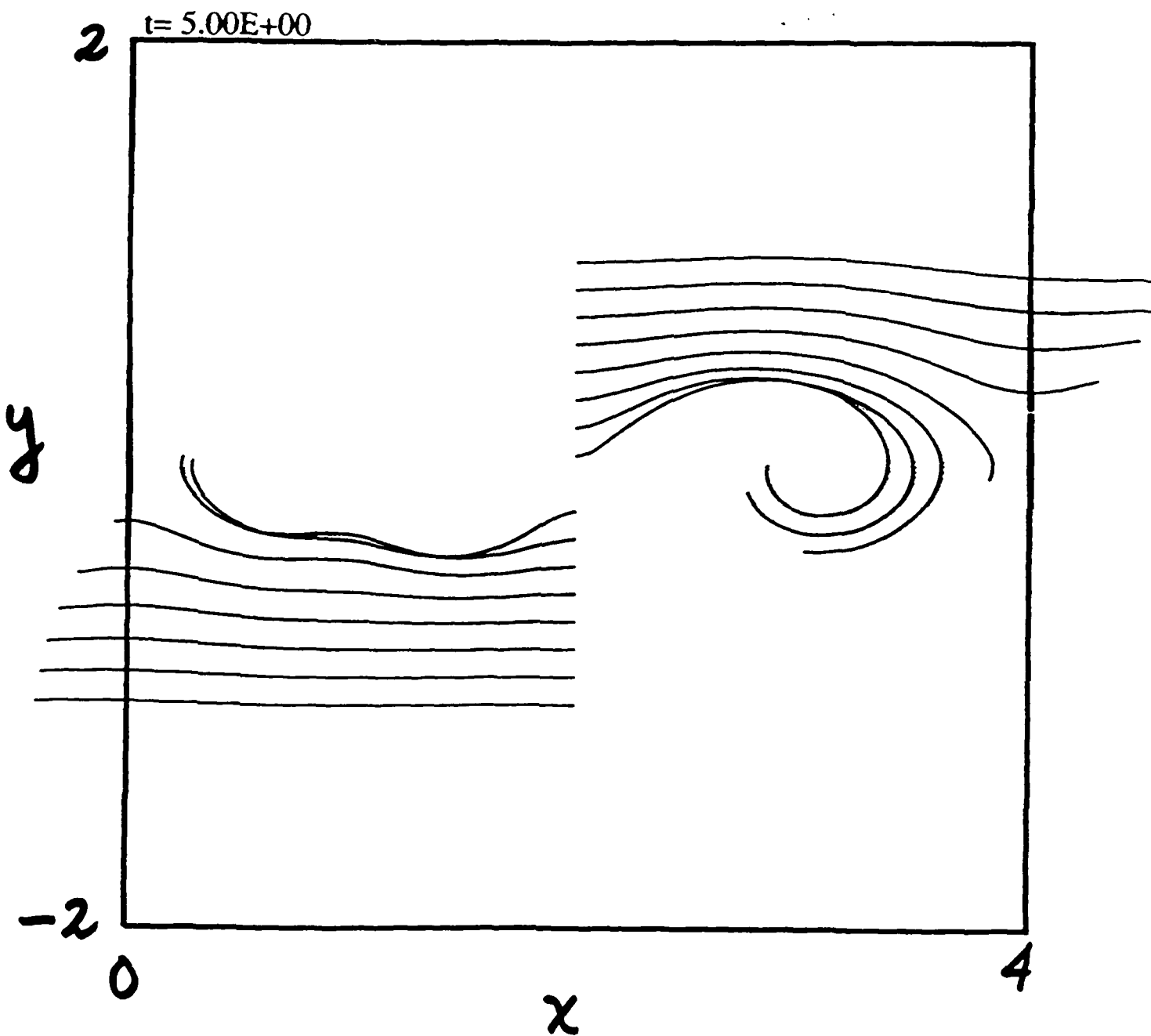


Figure C-23: Selected pathlines during the evolution of four vortex structures.

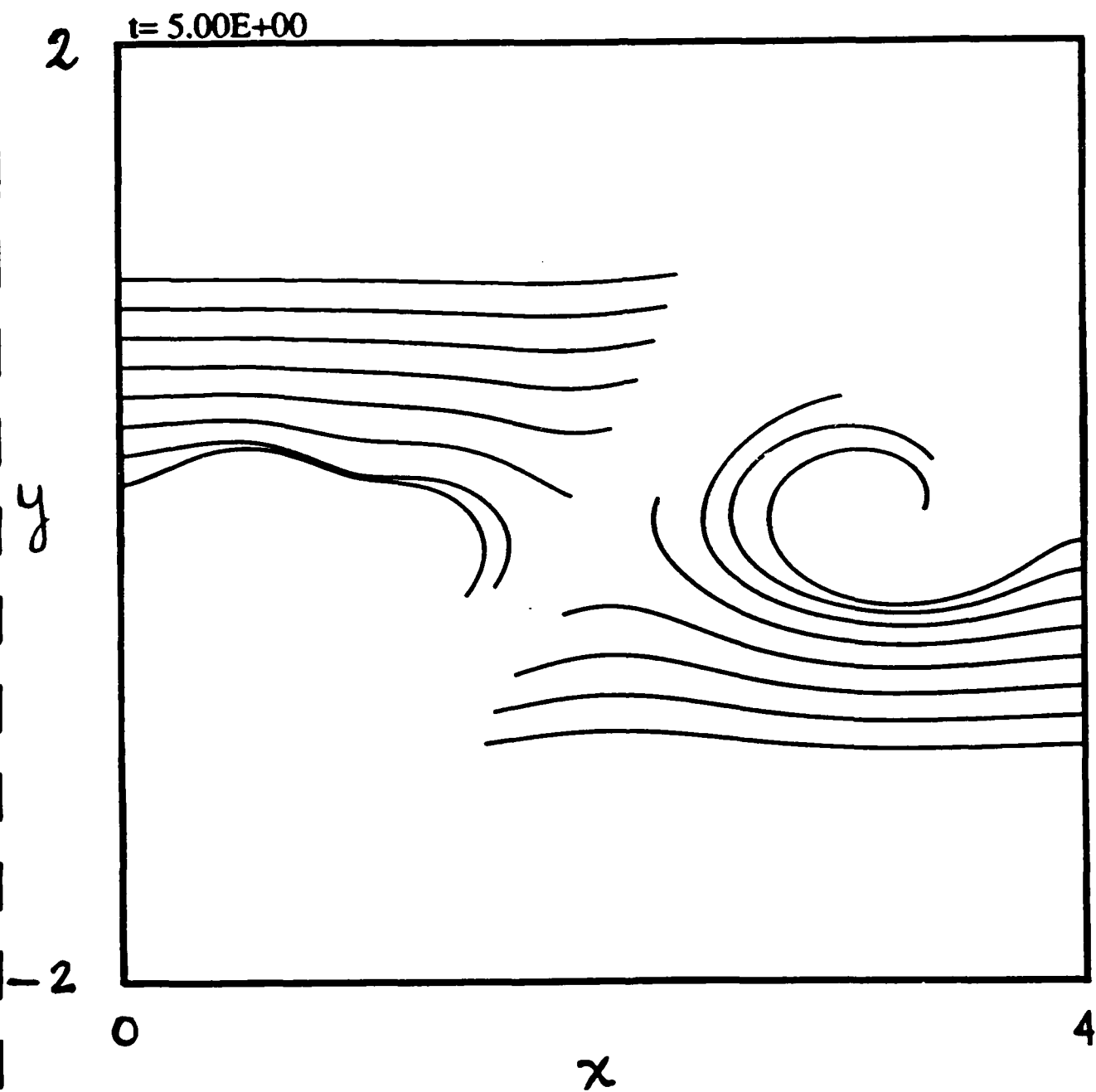
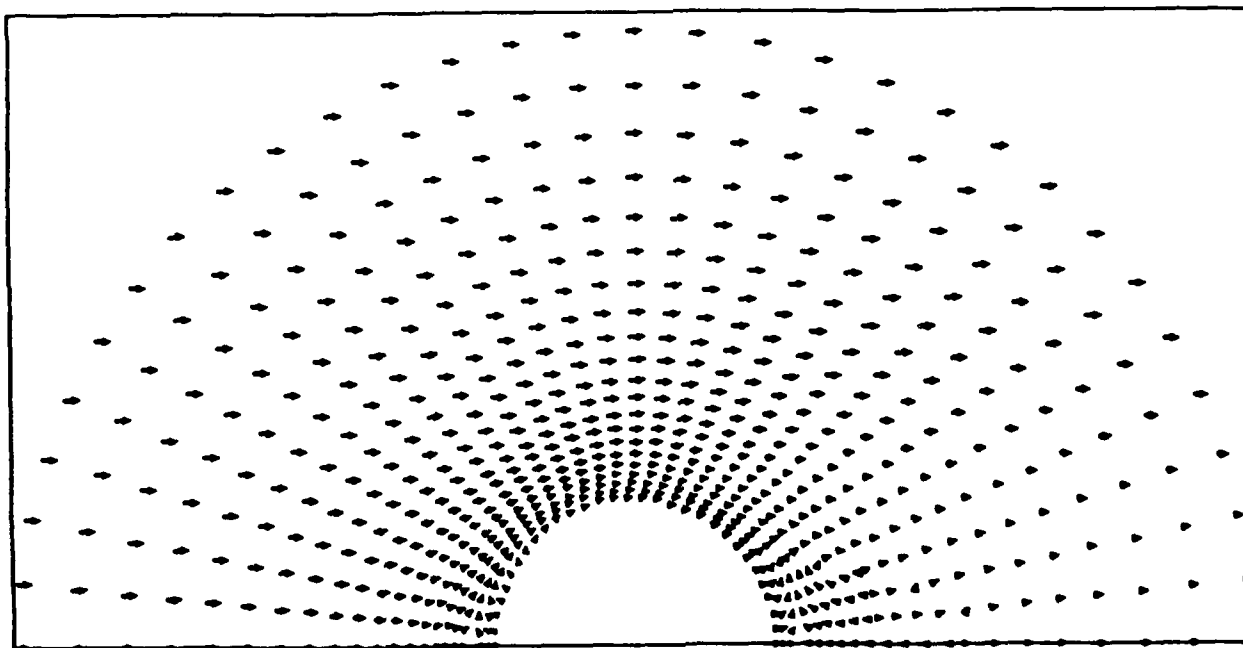


Figure C-24: Selected pathlines during the evolution of four vortex structures.

GAS PHASE VELOCITY VECTORS



Time = 25.00

Reynolds Number = 24.09

Fuel : n-octane

Ambient Temperature= 1250 K

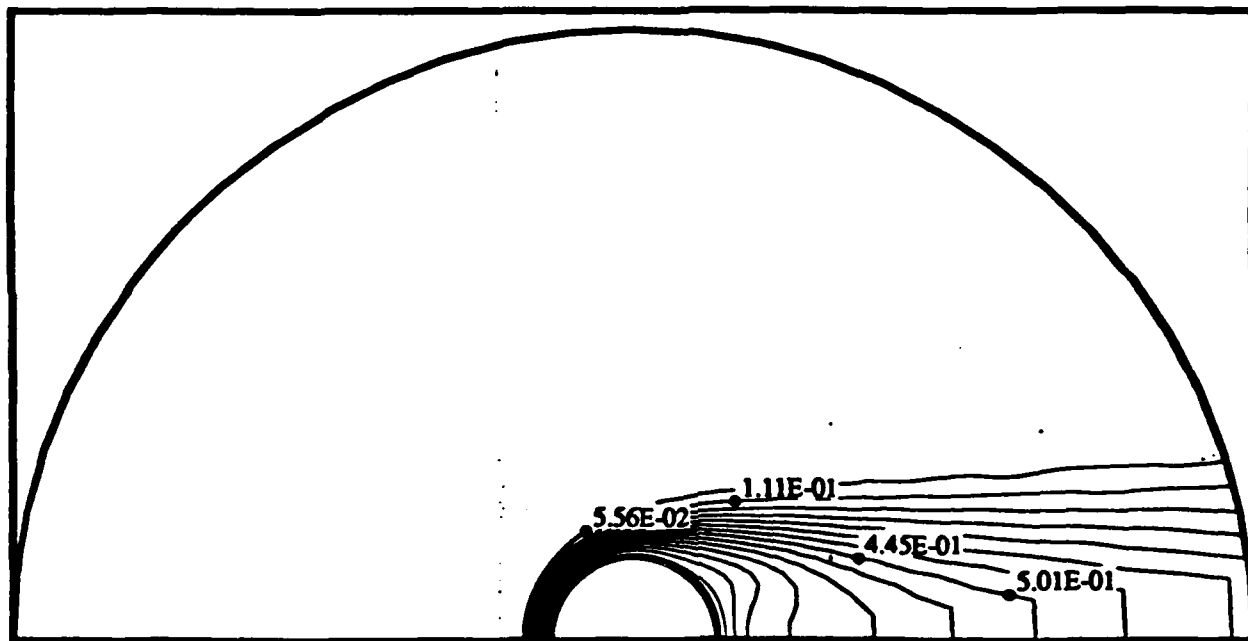
Initial Droplet Temperature= 300 K

Initial Reynolds Number = 100

Figure D-1(a) Instantaneous gas phase velocity at time = 25.

MASS FRACTION

Contour Interval: 5.56E-02 Min: 0.00E+00 Max: 8.35E-01



Time = 25.00

Reynolds Number = 24.09

Ambient Temperature= 1250 K

Initial Droplet Temperature= 300 K

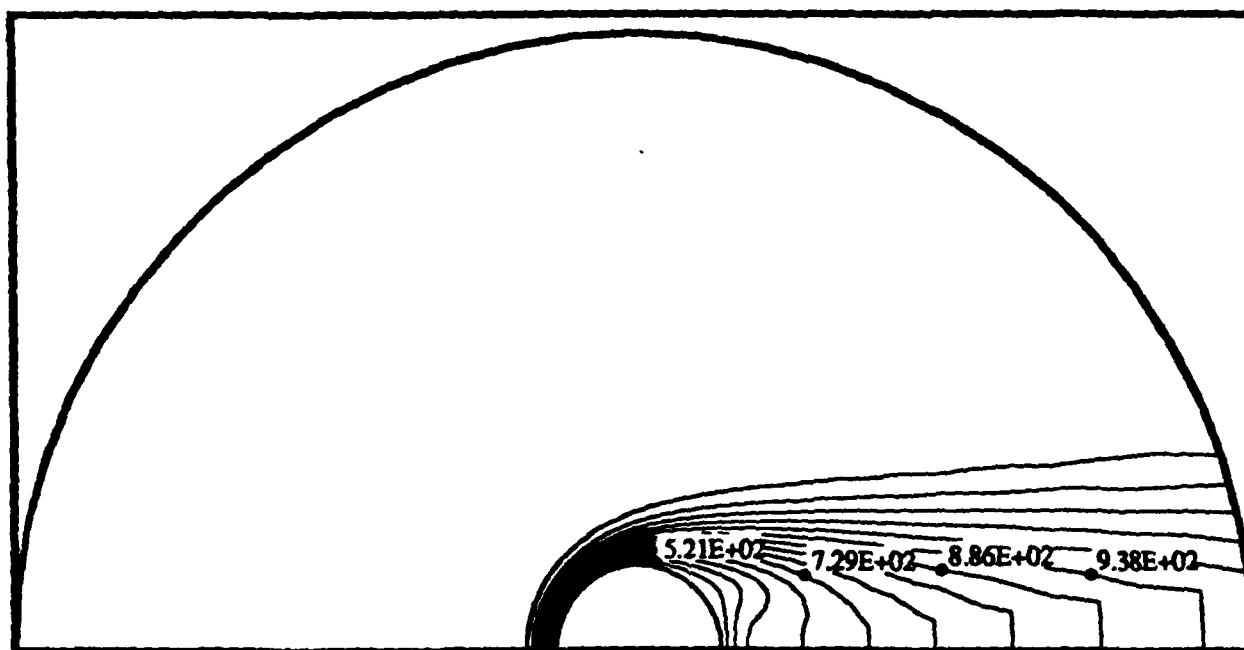
Initial Reynolds Number = 100

Fuel : n-octane

Figure D-1(b) Mass fraction contour plot at time = 25.

GAS AND LIQUID PHASE ISOTHERMS

Contour Interval: $5.21\text{E}+01$ Min: $4.69\text{E}+02$ Max: $1.25\text{E}+03$



Time = 25.00

Reynolds Number = 24.09

Ambient Temperature = 1250 K

Initial Droplet Temperature = 300 K

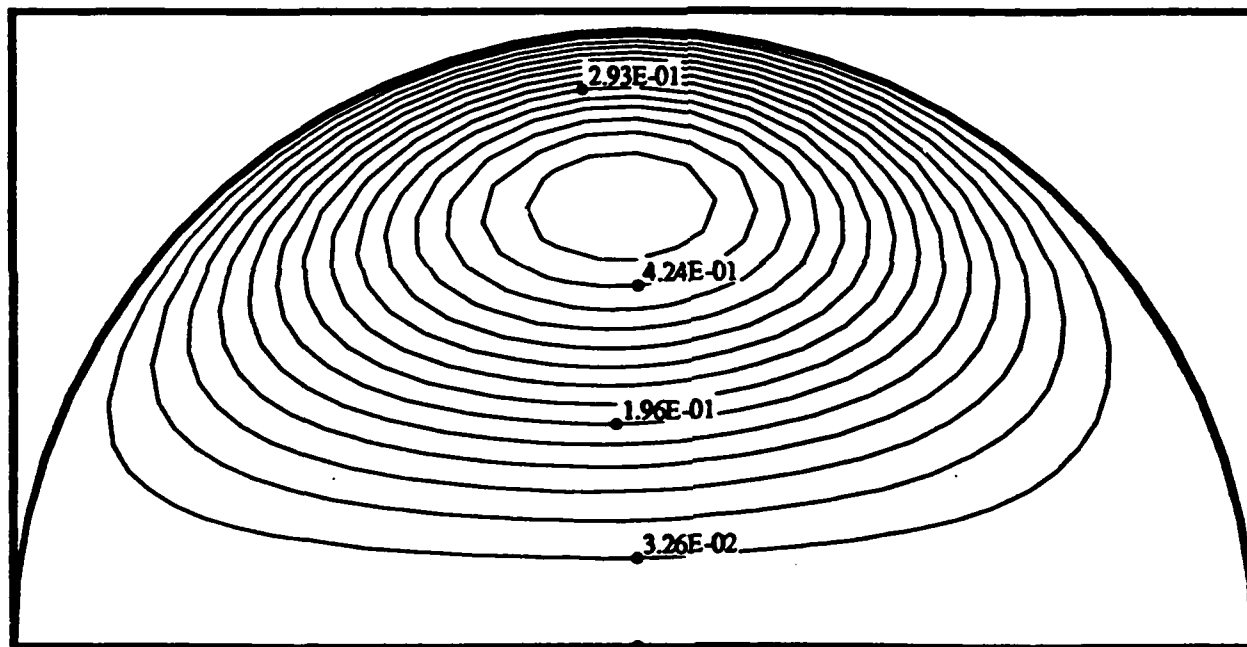
Initial Reynolds Number = 100

Fuel : n-octane

Figure D-1(c) Temperature contour plot at time = 25.

LIQUID PHASE STREAM FUNCTION

Contour Interval: $3.26\text{E-}02$ Min: $0.00\text{E+}00$ Max: $4.89\text{E-}01$



Time = 25.00

Reynolds Number = 24.09

Ambient Temperature= 1250 K

Initial Droplet Temperature= 300 K

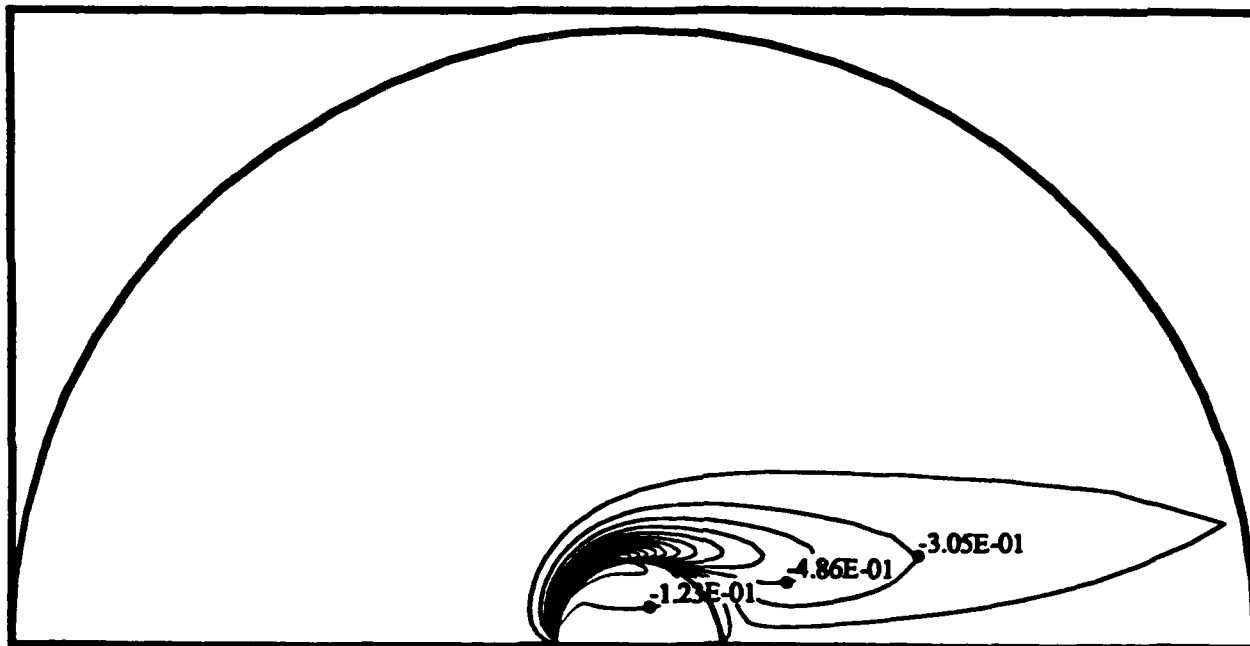
Initial Reynolds Number = 100

Fuel : n-octane

Figure D-1(d) Stream function of liquid phase at time = 25.

GAS AND LIQUID PHASE VORTICITY

Contour Interval: 1.81E-01 Min: -2.66E+00 Max: 2.40E-01



Time = 25.00

Reynolds Number = 24.09

Ambient Temperature = 1250 K

Initial Droplet Temperature = 300 K

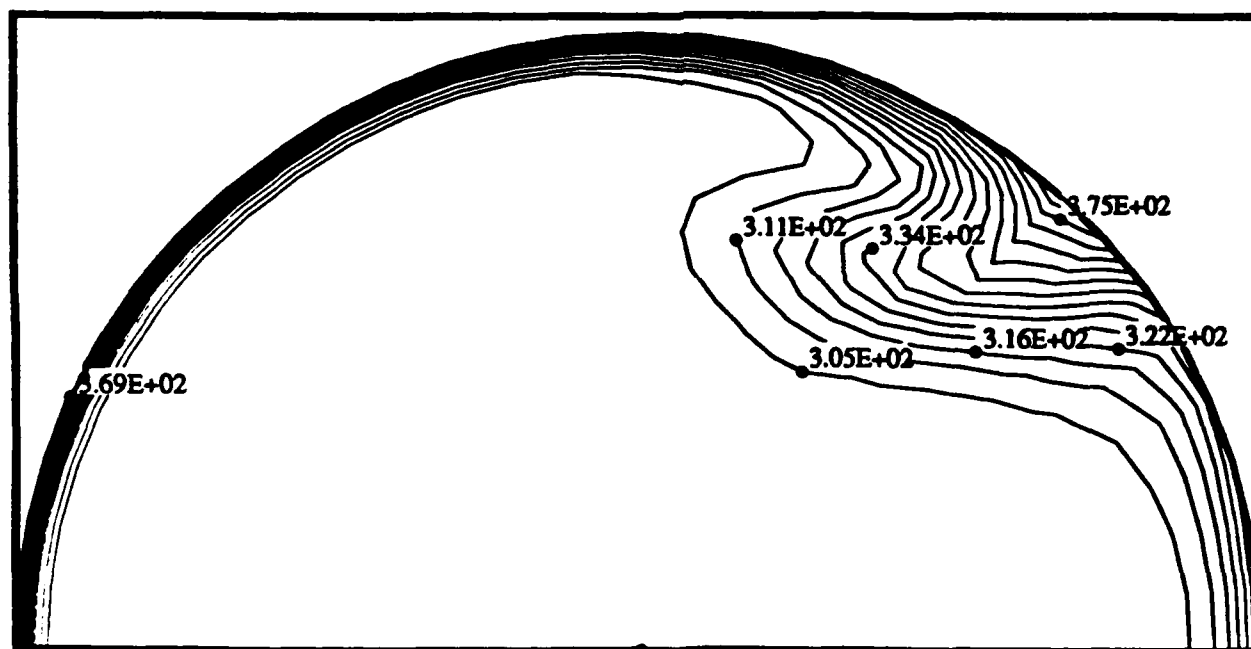
Initial Reynolds Number = 100

Fuel : n-octane

Figure D-1(e) Vorticity contour plot at time = 25.

LIQUID PHASE ISOTHERMS

Contour Interval: $5.84\text{E}+00$ Min: $2.99\text{E}+02$ Max: $3.86\text{E}+02$



Time = 0.50

Reynolds Number = 96.46

Ambient Temperature= 1250 K

Initial Droplet Temperature= 300 K

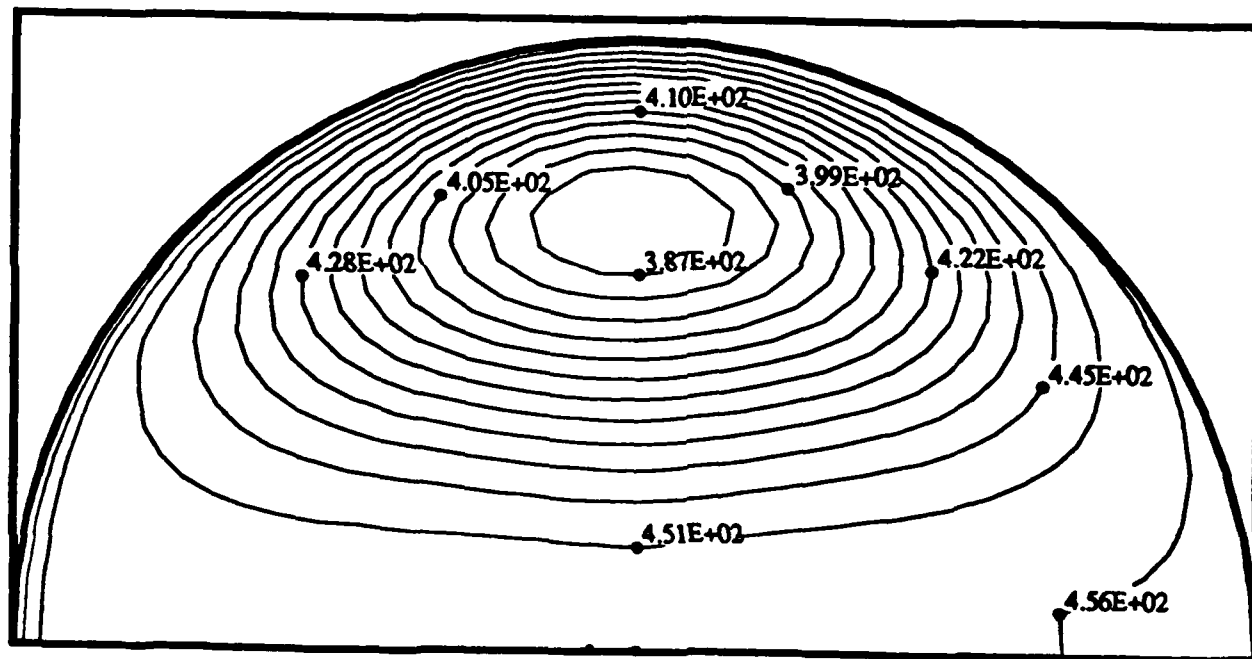
Initial Reynolds Number = 100

Fuel : n-octane

Figure D-2(a) Transient history of droplet heating. Time = 0.5

LIQUID PHASE ISOTHERMS

Contour Interval: $5.76\text{E}+00$ Min: $3.82\text{E}+02$ Max: $4.68\text{E}+02$



Time = 10.00

Reynolds Number = 59.90

Ambient Temperature = 1250 K

Initial Droplet Temperature = 300 K

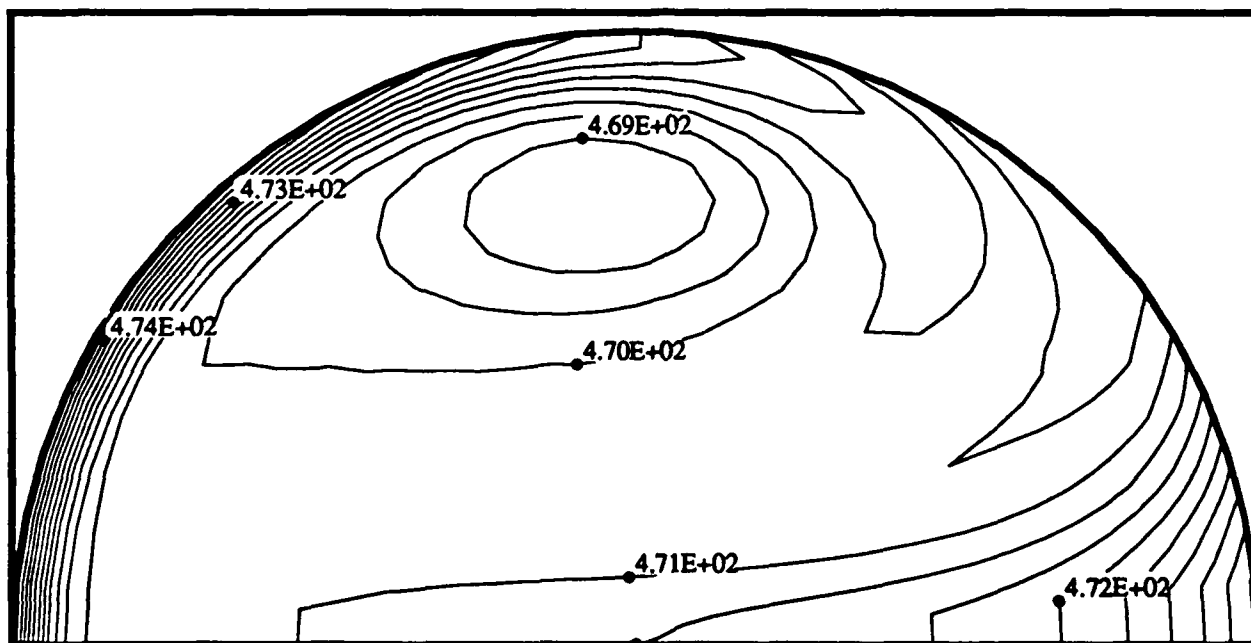
Initial Reynolds Number = 100

Fuel : n-octane

Figure D-2(b) Transient history of droplet heating. Time = 10.0

LIQUID PHASE ISOTHERMS

Contour Interval: $4.24\text{E-}01$ Min: $4.69\text{E+}02$ Max: $4.75\text{E+}02$



Time = 25.00

Reynolds Number = 24.09

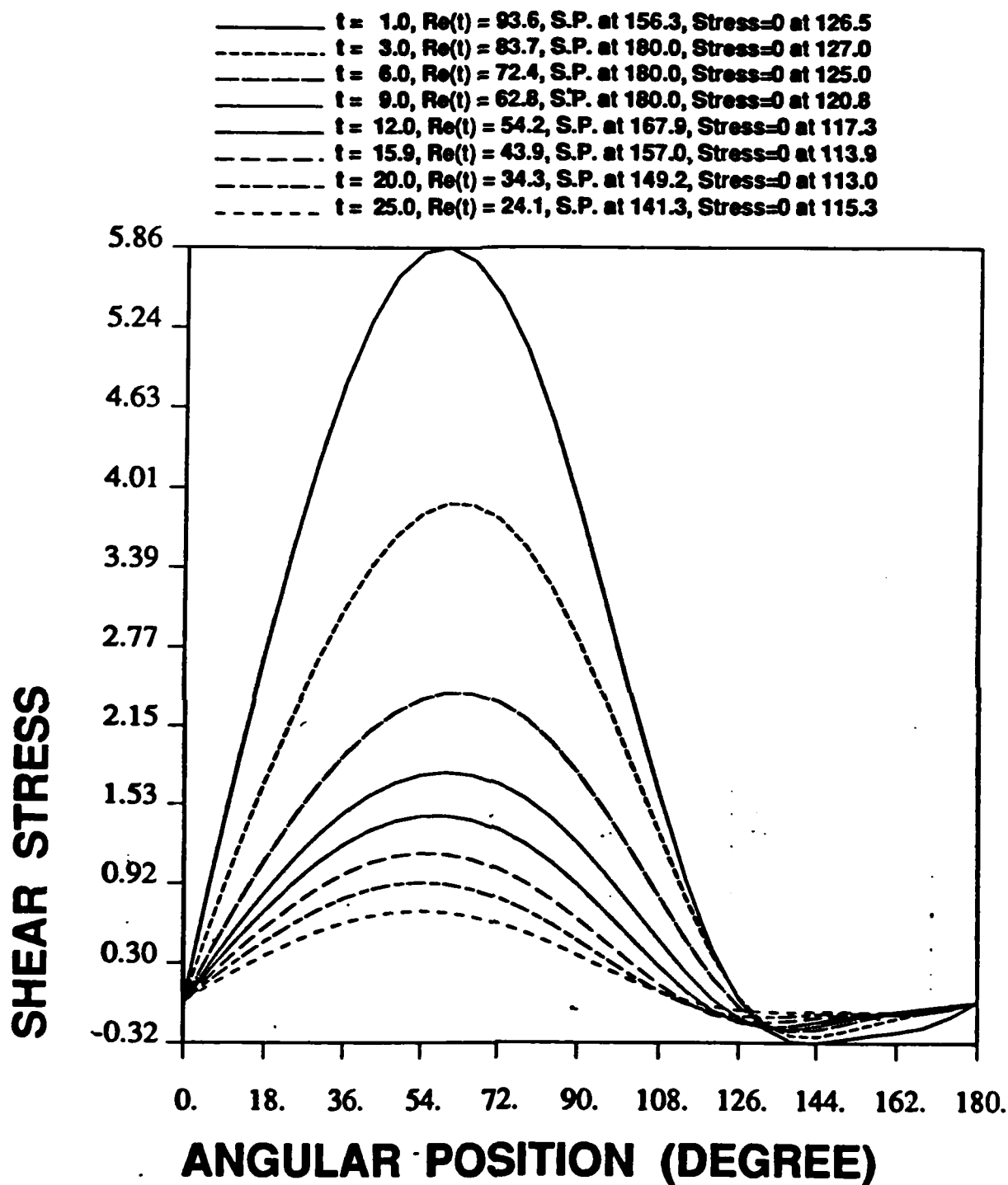
Ambient Temperature= 1250 K

Initial Droplet Temperature= 300 K

Initial Reynolds Number = 100

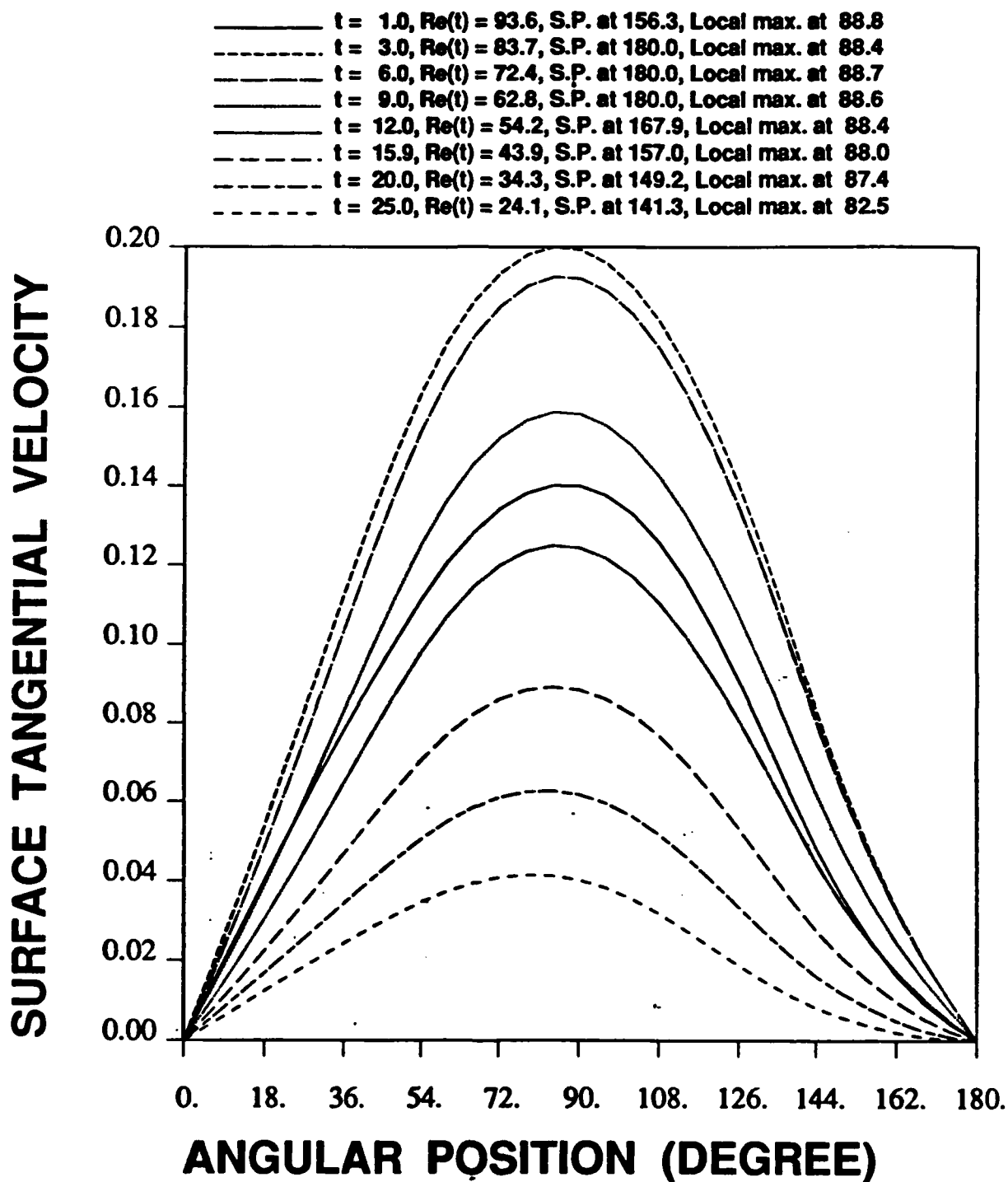
Fuel : n-octane

Figure D-2(c) Transient history of droplet heating. Time = 25.0



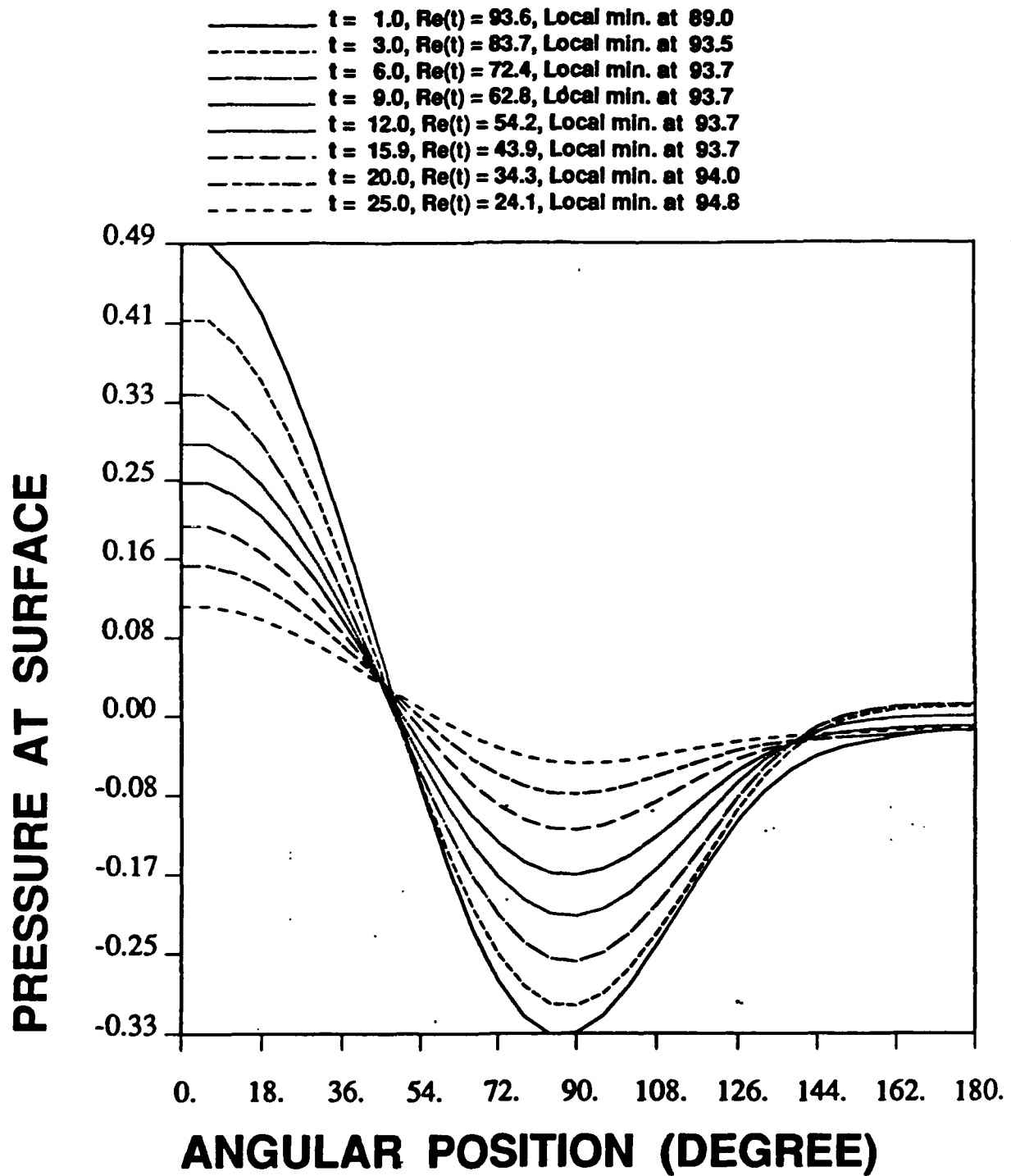
Fuel : n-octane
 Ambient Temperature = 1250. K
 Initial Droplet Temperature = 300. K
 Initial Reynolds Number = 100.

Figure D-3(a) Surface shear stress distribution at different times.



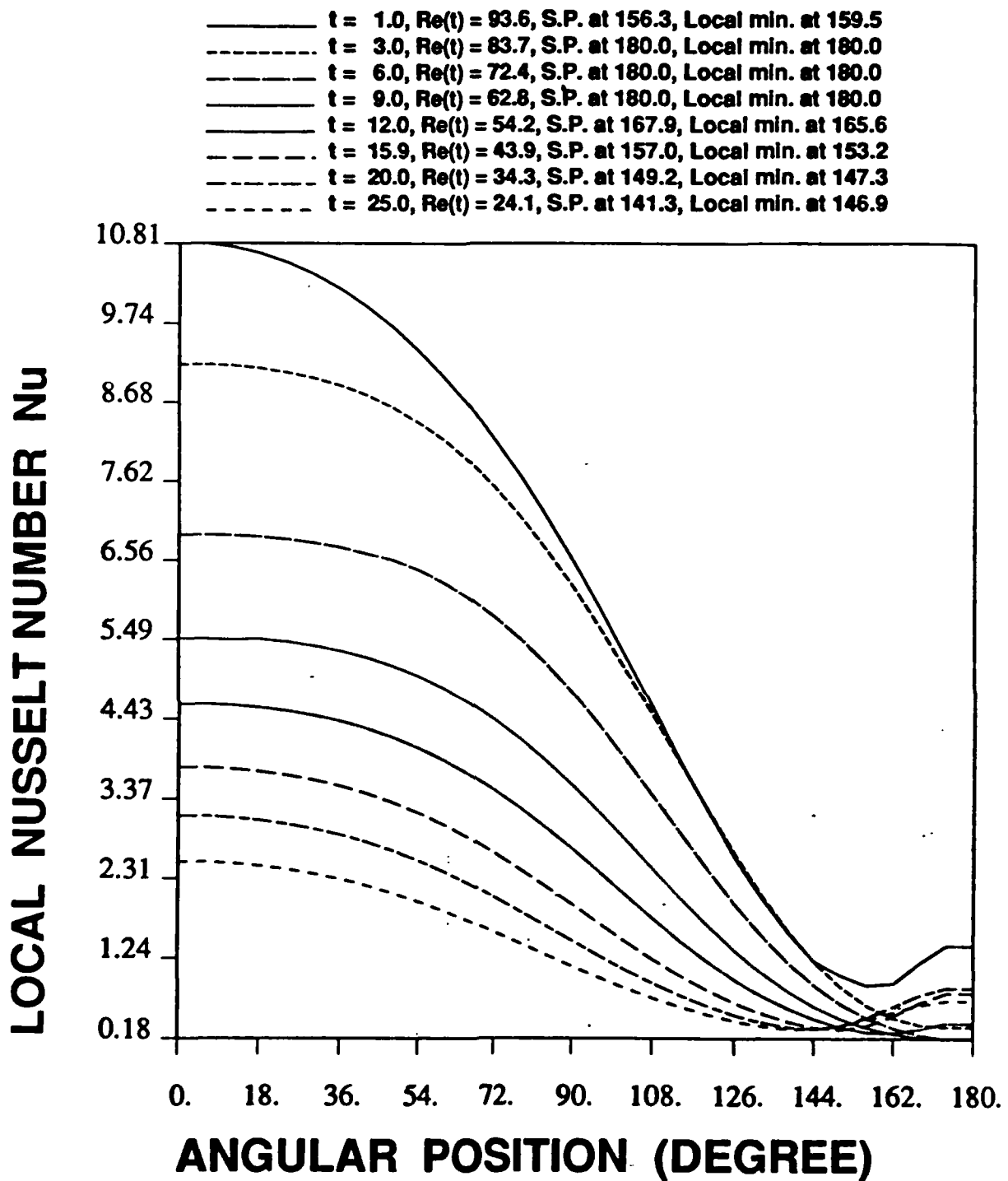
Fuel : n-octane
 Ambient Temperature = 1250. K
 Initial Droplet Temperature = 300. K
 Initial Reynolds Number = 100.

Figure D-3(b) Surface tangential velocity distribution at different times.



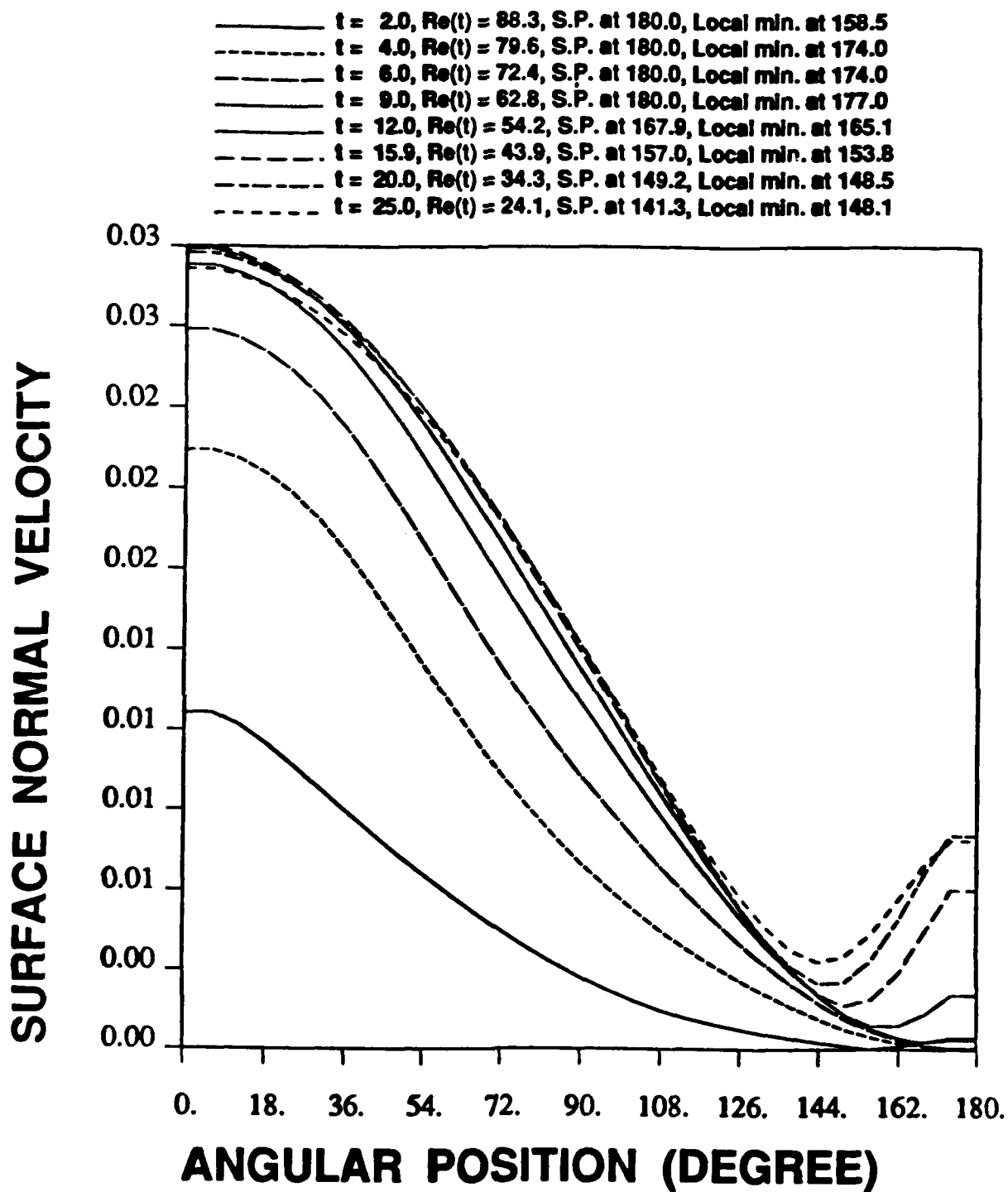
Fuel : n-octane
 Ambient Temperature = 1250. K
 Initial Droplet Temperature = 300. K
 Initial Reynolds Number = 100.

Figure D-3(c) Surface nondimensional pressure distribution at different times.



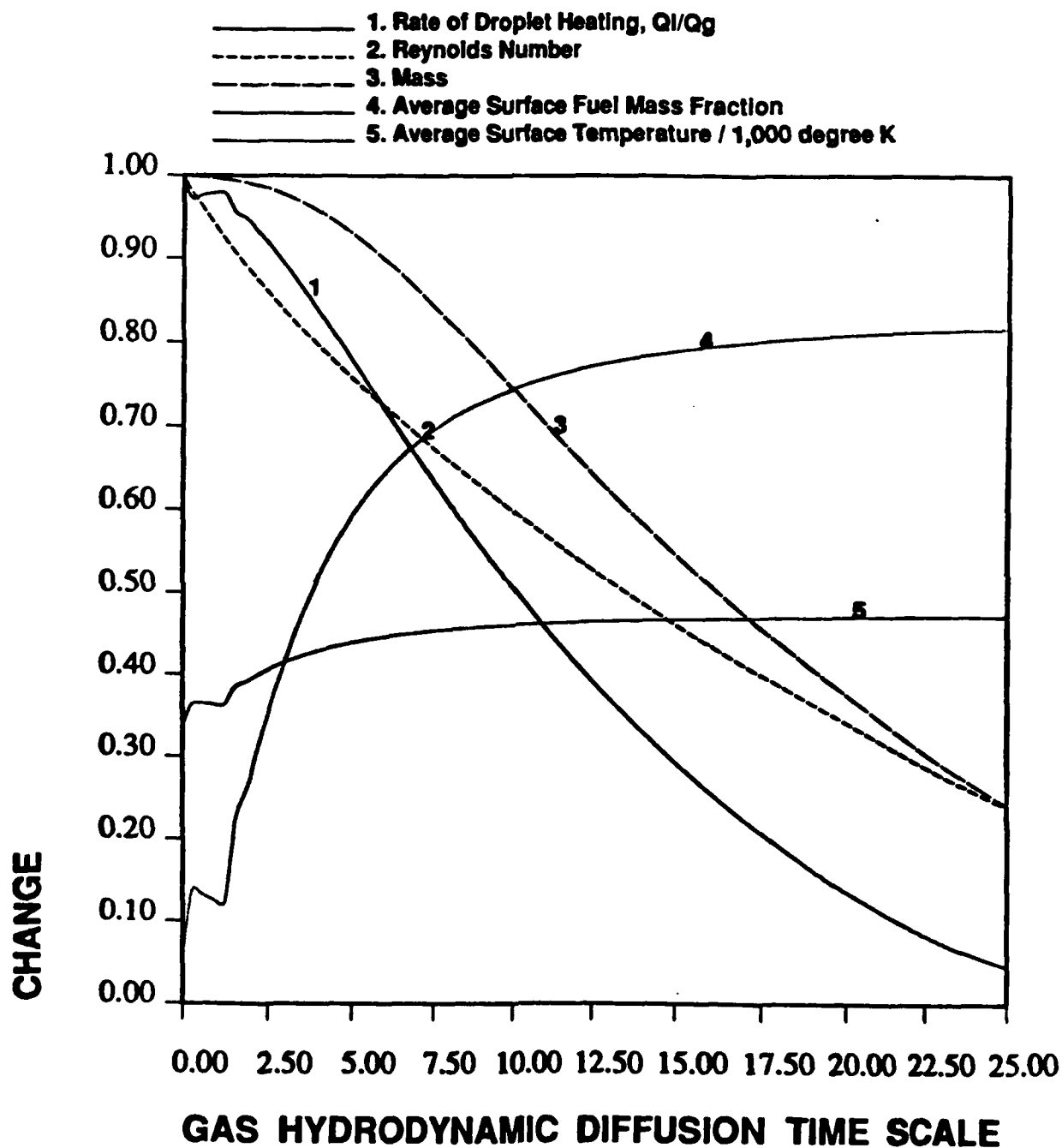
Fuel : n-octane
 Ambient Temperature = 1250. K
 Initial Droplet Temperature = 300. K
 Initial Reynolds Number = 100.

Figure D-3(d) Local Nusselt number distribution at different times.



Fuel : n-octane
 Ambient Temperature = 1250. K
 Initial Droplet Temperature = 300. K
 Initial Reynolds Number = 100.

Figure D-3(f) Surface normal velocity distribution at different times.



$T_g = 1250$ K, $T_i = 300$ K, Fuel = n-octane, $P = 10$ atm, $Re_i = 100$

Figure D-4 The transient evolution of the rate of droplet heating, Reynolds number, mass, average surface fuel mass fraction and temperature.

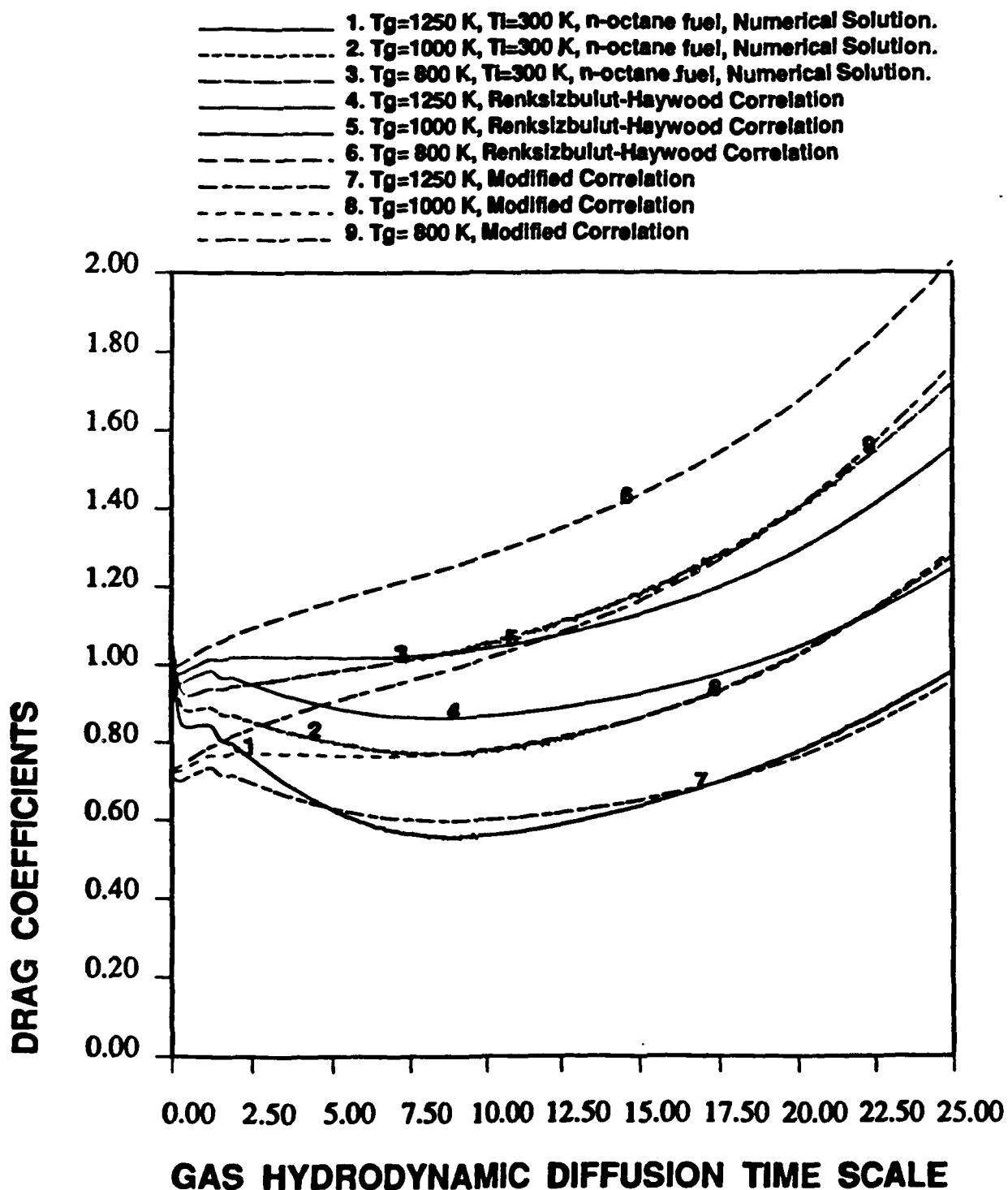


Figure D-5 Time variation of drag coefficients for different ambient temperatures as well as comparison with H-N-R correlation and modified correlation.

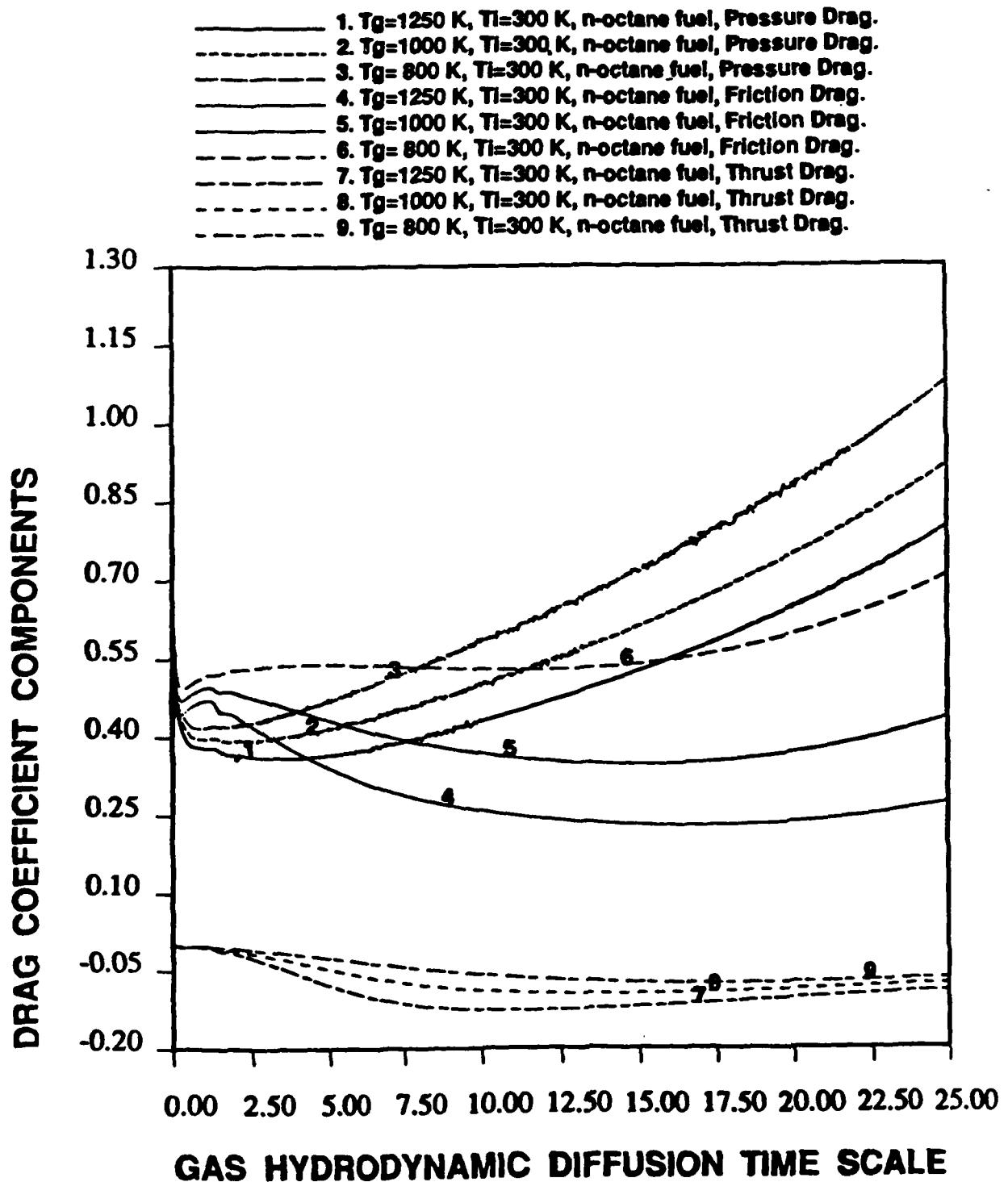


Figure D-6 Time variation of three drag components for different ambient temperatures.

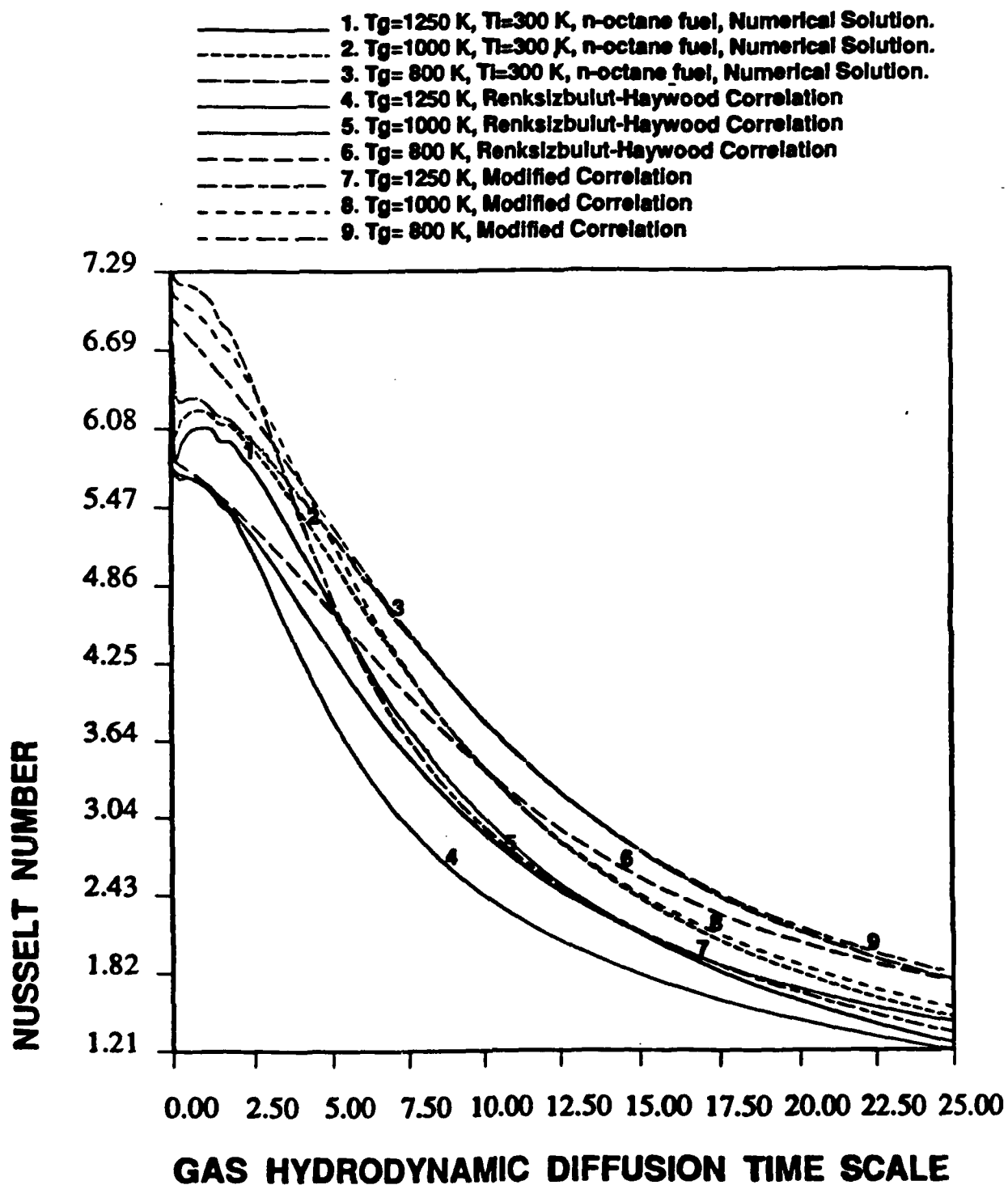


Figure D-7 Time variation of average Nusselt numbers for different ambient temperatures as well as comparison with H-N-R correlation and modified correlation.

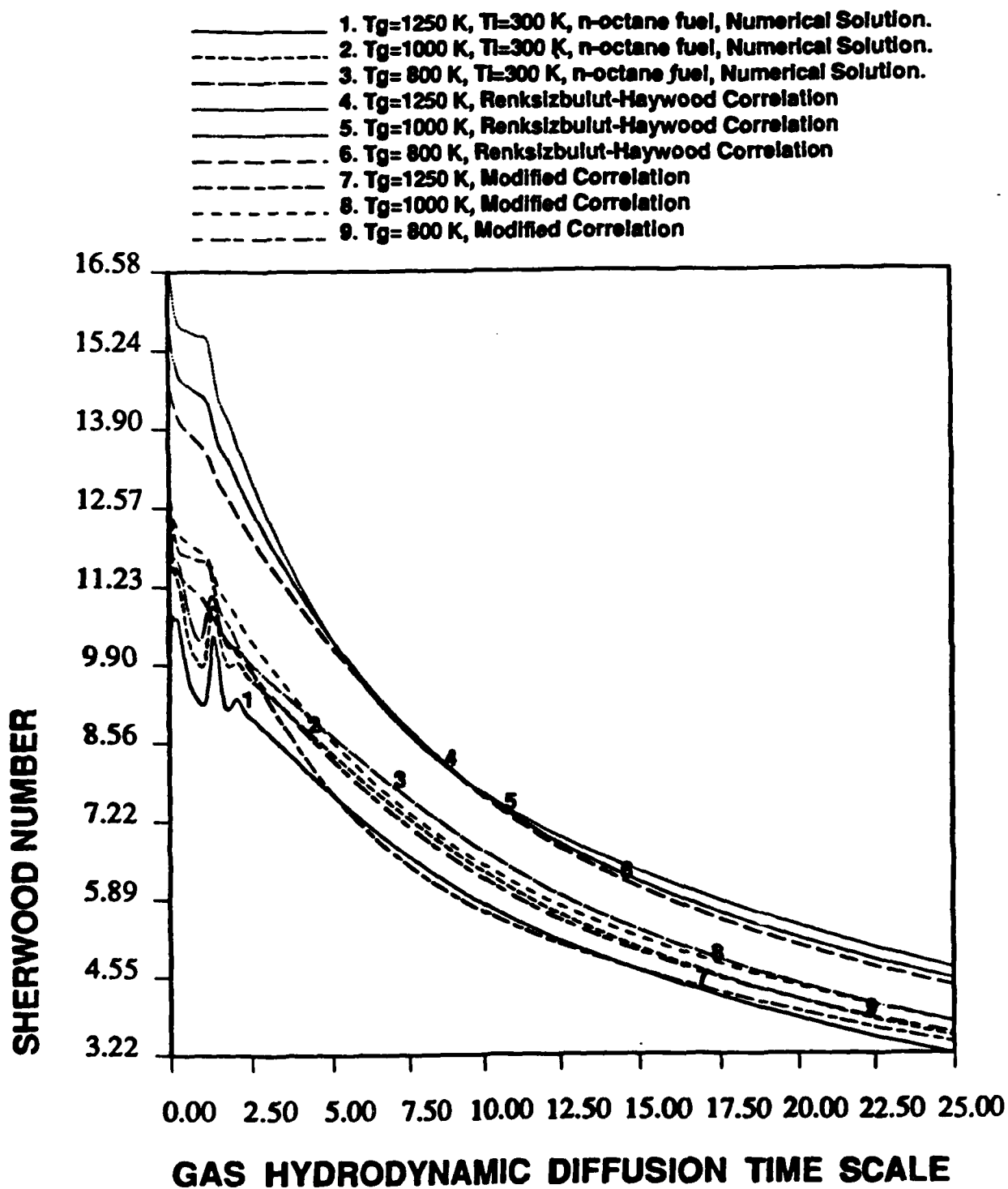


Figure D-8 Time variation of average Sherwood numbers for different ambient temperatures as well as comparison with H-N-R correlation and modified correlation.

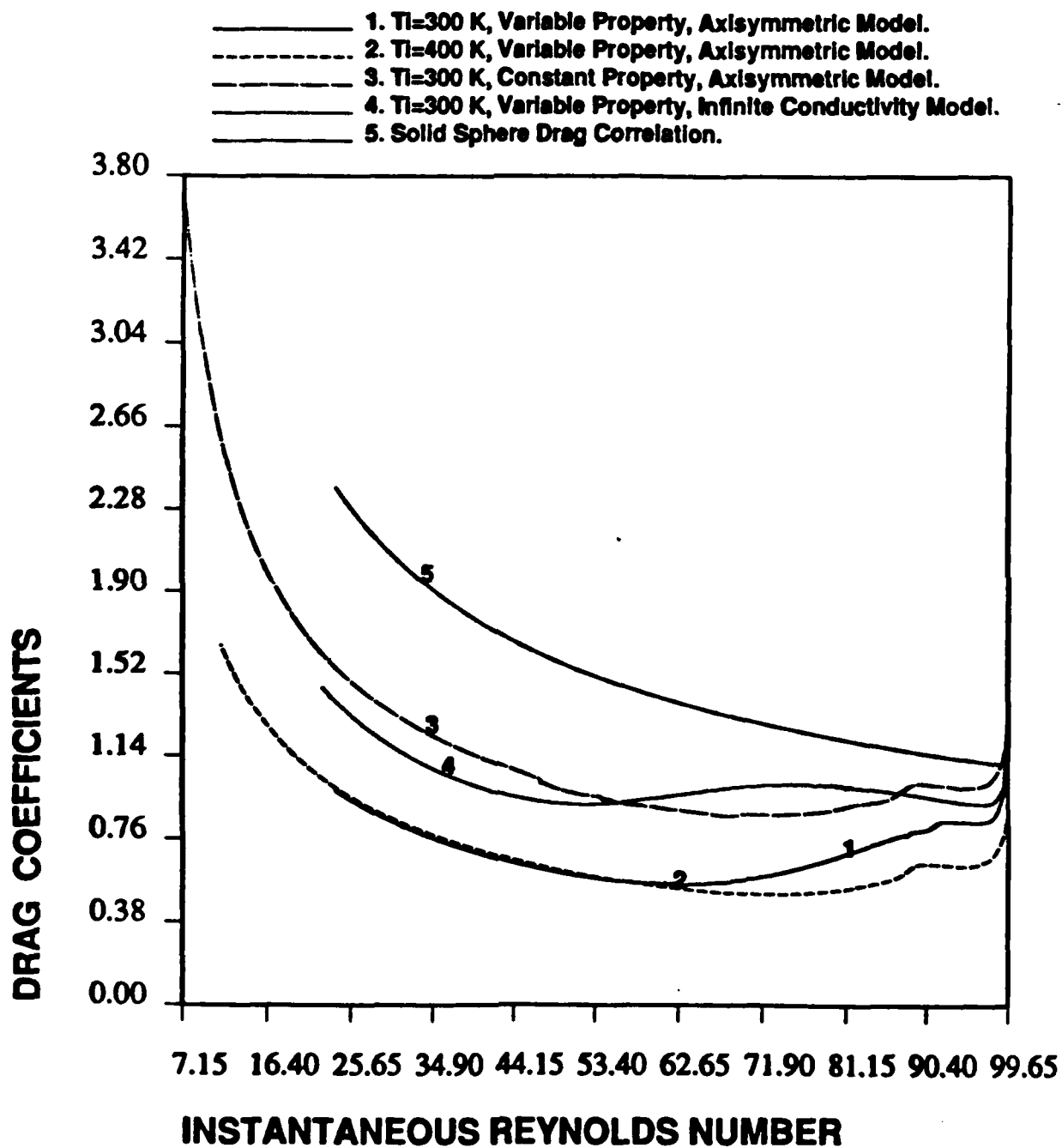


Figure D-9 Time variation of drag coefficients for the cases of different initial droplet temperatures, different droplet heating model and constant property assumption.

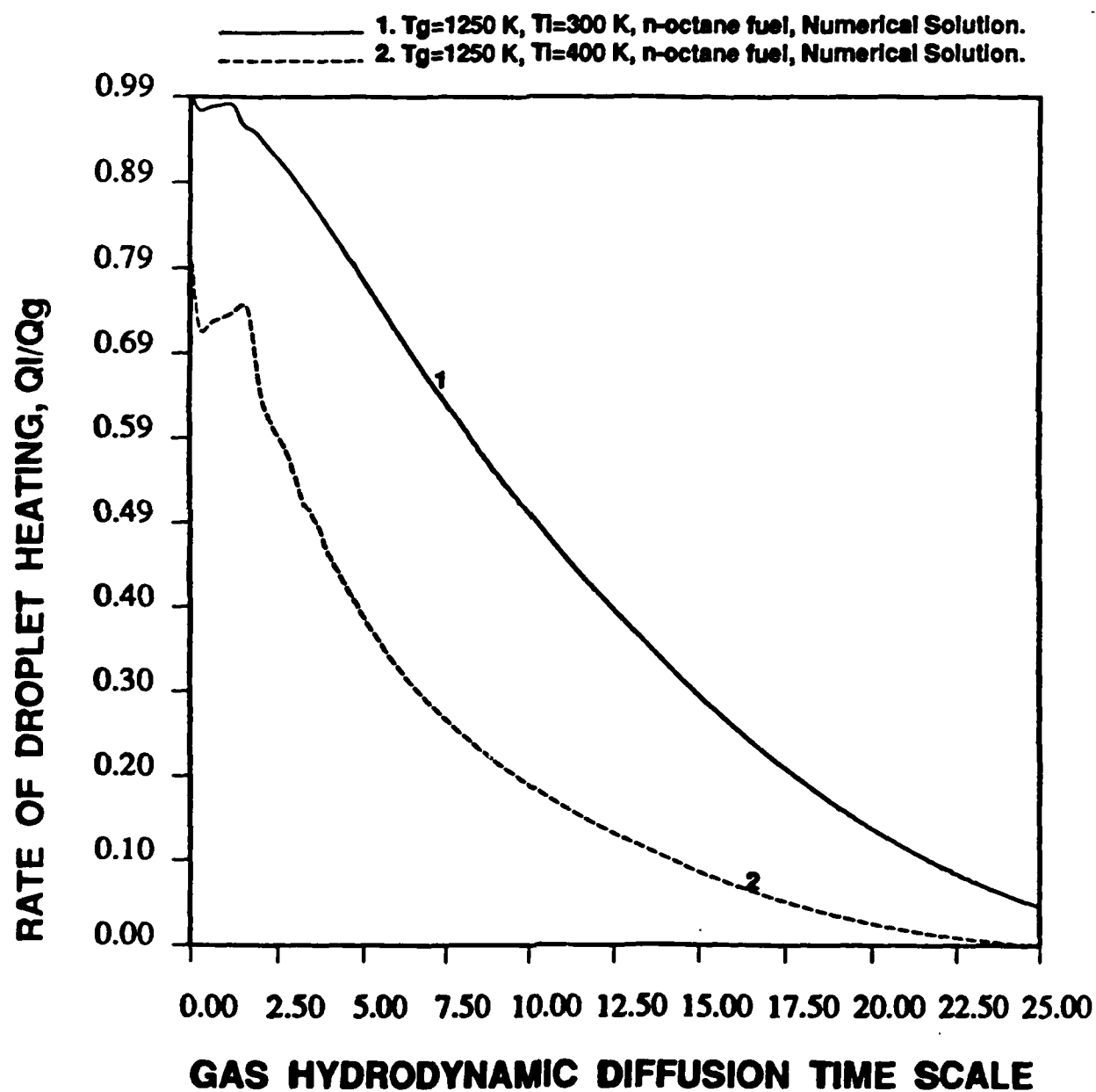


Figure D-10 Time variation of the rate of droplet heating for different initial droplet temperatures.

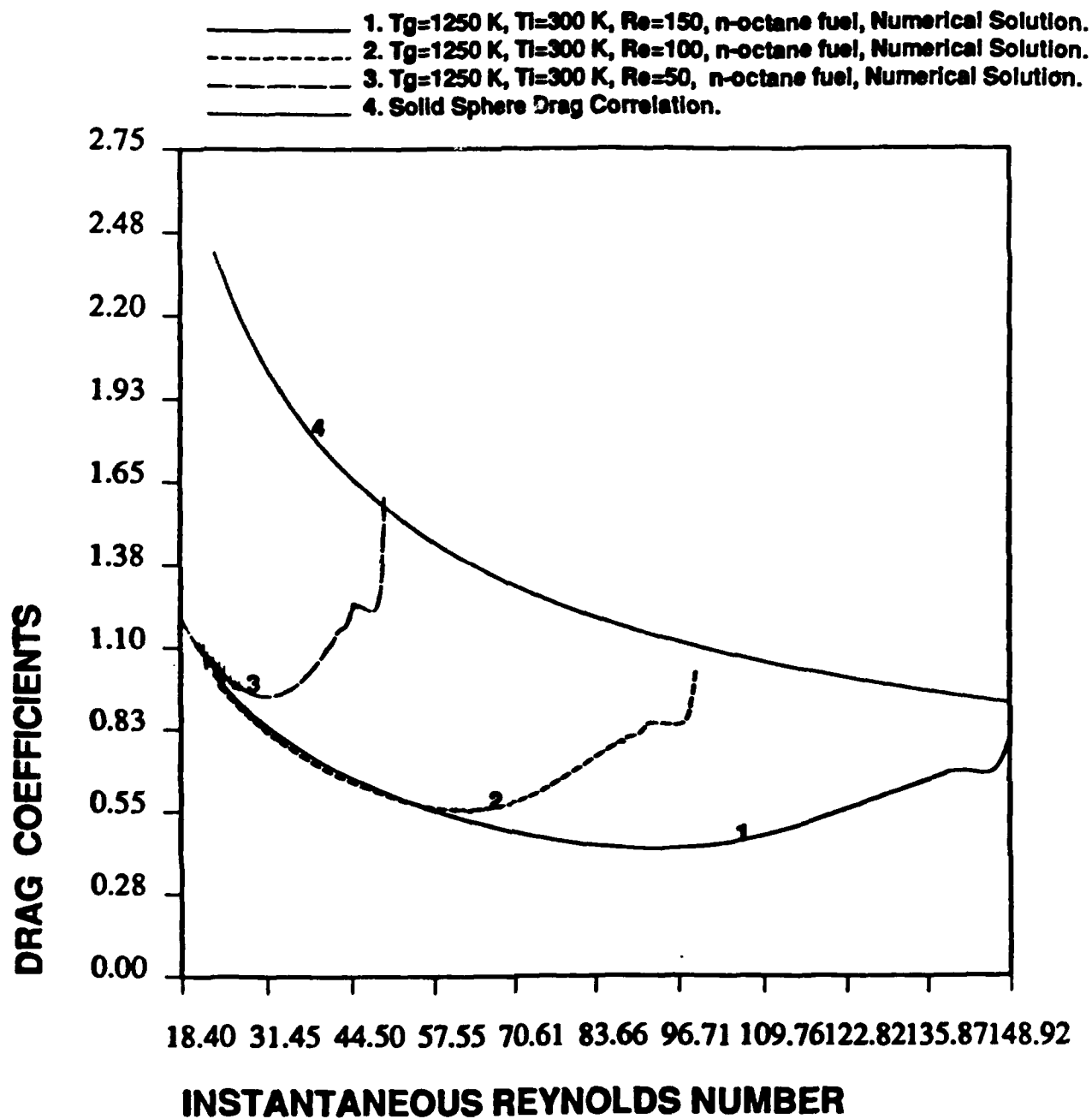


Figure D-11 Time variation of drag coefficients for different initial Reynolds numbers.

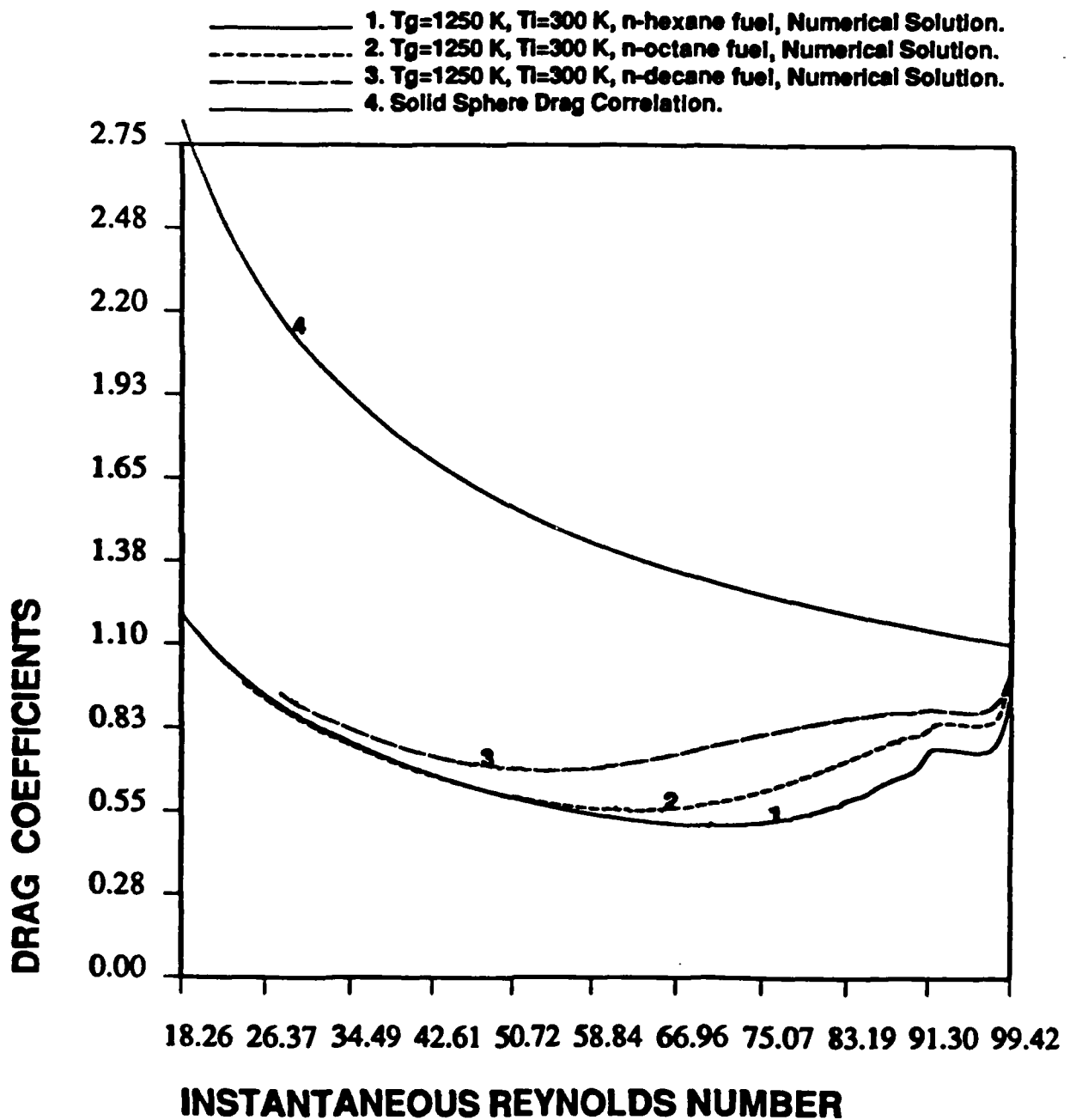
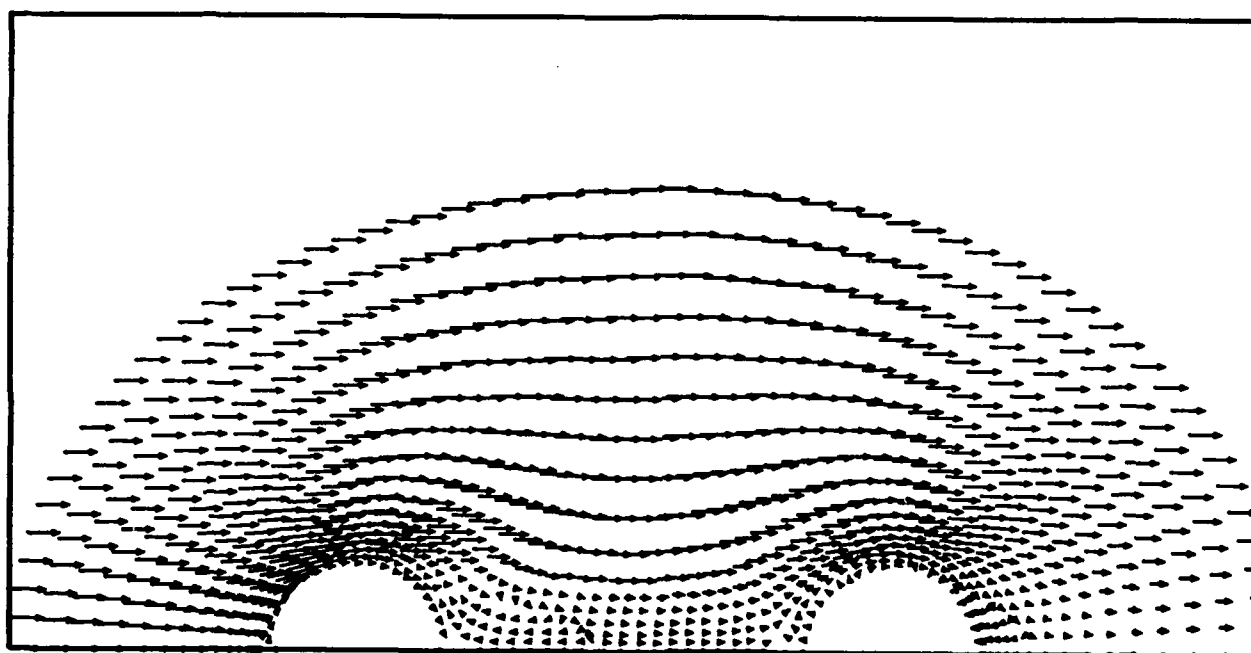


Figure D-12 Time variation of drag coefficients for different fuels.

GAS PHASE VELOCITY VECTORS

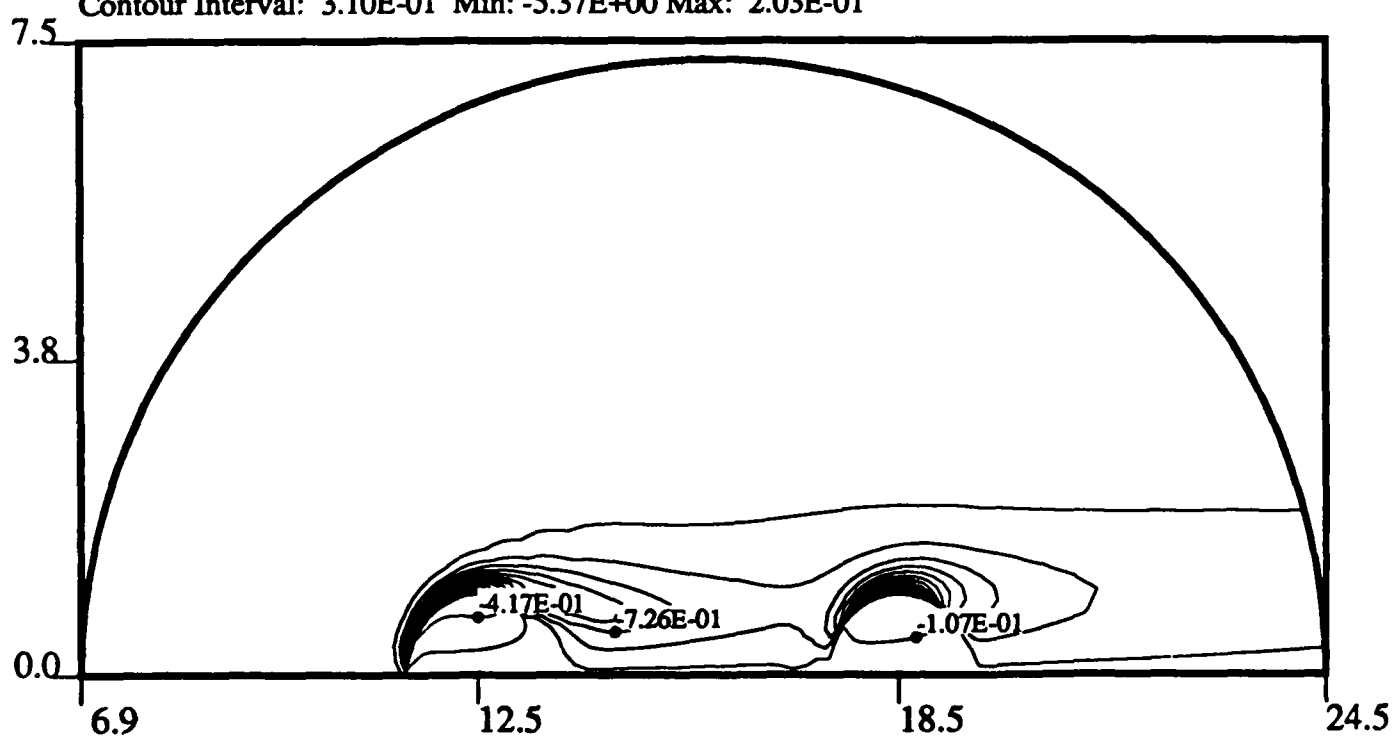


At time = 2.00
Re #(1) = 85.95 , Re #(2) = 90.35
R1 = 1.00 , R2 = 1.00 , Spacing = 6.00
Ambient Temperature= 1000 K
Initial Droplet Temperature= 300 K
Initial Reynolds Number = 100
Fuel : n-decane
Initial R1=1, R2=1, Spacing=8

Figure D-13(a) Instantaneous gas phase velocity at time = 2.

GAS AND LIQUID PHASE VORTICITY

Contour Interval: $3.10\text{E-}01$ Min: $-5.37\text{E+}00$ Max: $2.03\text{E-}01$



Time = 2.00

Re #(1) = 85.95 , Re #(2) = 90.35

R1 = 1.00 , R2 = 1.00 , Spacing = 6.00

Ambient Temperature = 1000 K

Initial Droplet Temperature = 300 K

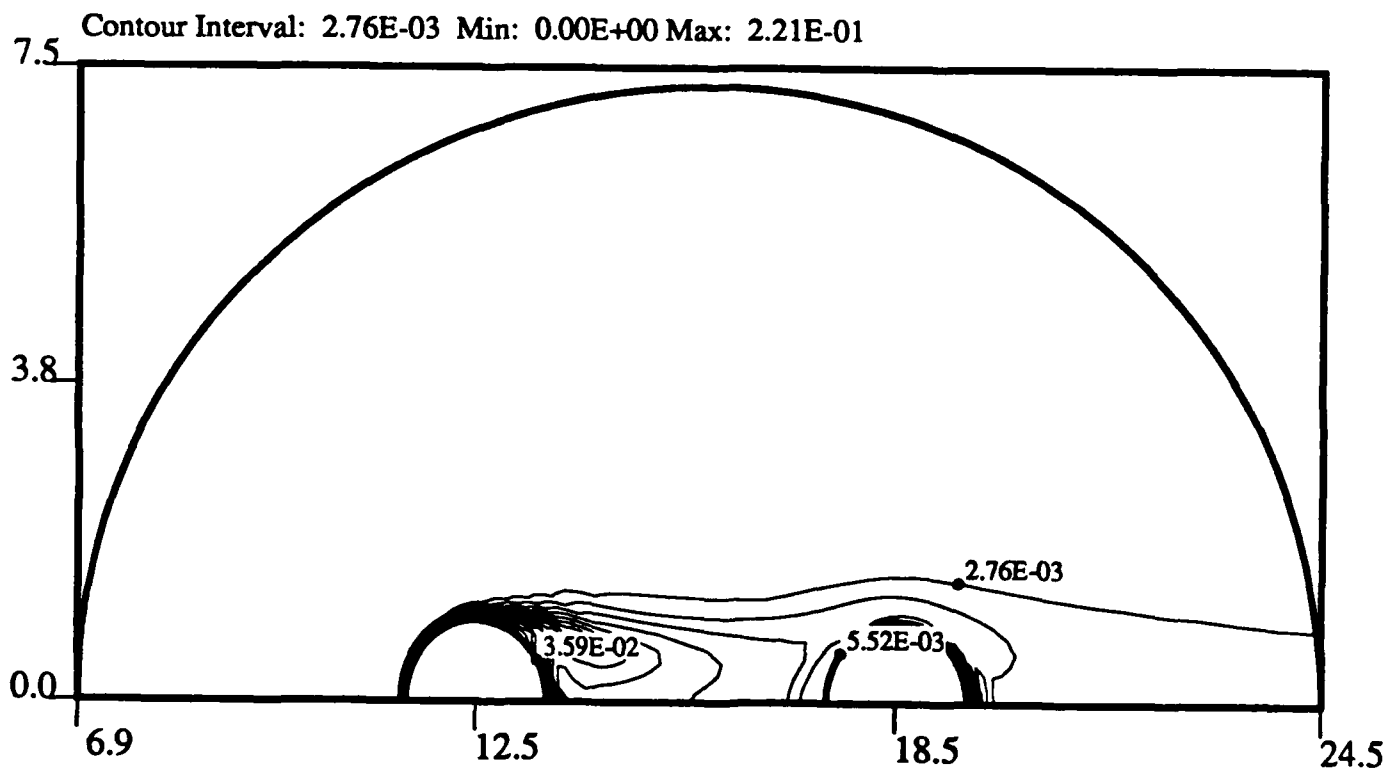
Initial Reynolds Number = 100

Fuel : n-decane

Initial R1=1, R2=1, Spacing=8

Figure D-13(b) Vorticity contour plot at time = 2.

MASS FRACTION



Time = 2.00

Re #(1) = 85.95 , Re #(2) = 90.35

R1 = 1.00 , R2 = 1.00 , Spacing = 6.00

Ambient Temperature = 1000 K

Initial Droplet Temperature = 300 K

Initial Reynolds Number = 100

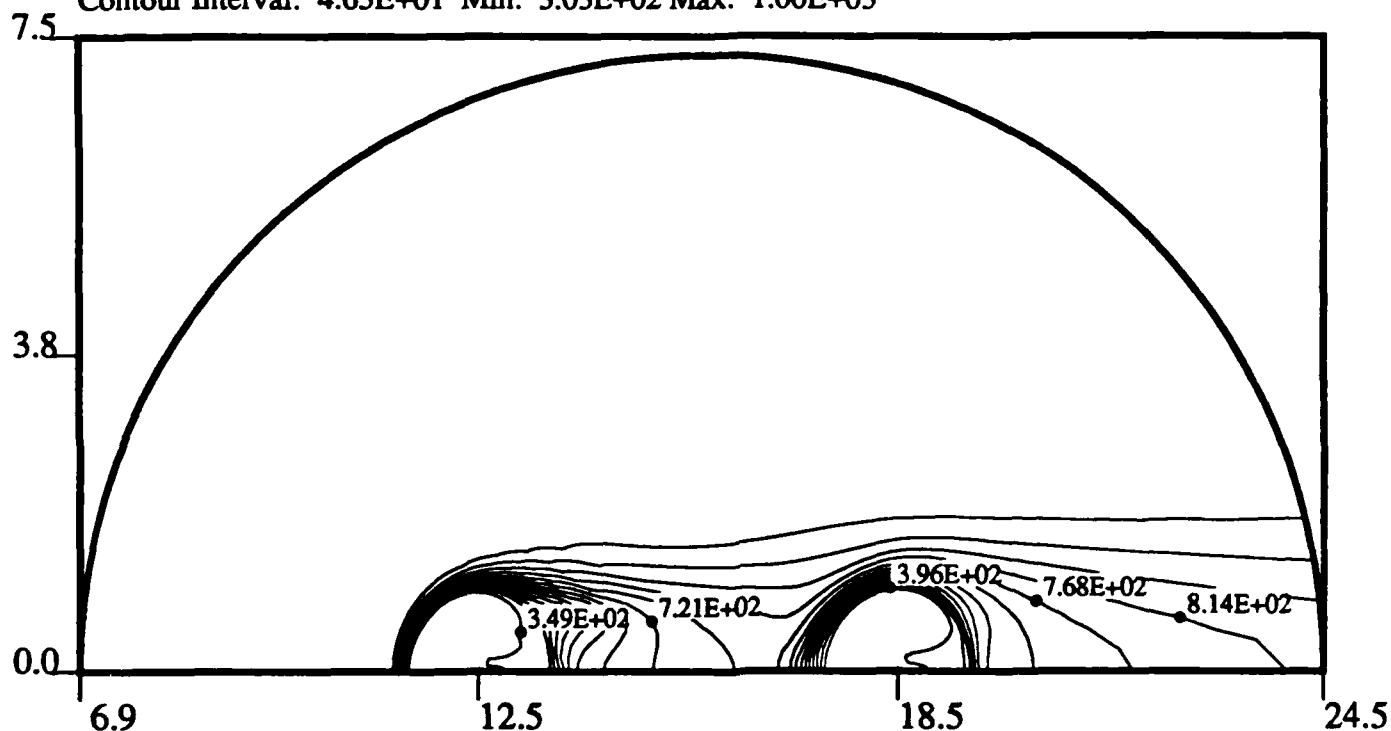
Fuel : n-decane

Initial R1=1, R2=1, Spacing=8

Figure D-13(c) Mass fraction contour plot at time = 2.

GAS AND LIQUID PHASE ISOTHERMS

Contour Interval: $4.65\text{E}+01$ Min: $3.03\text{E}+02$ Max: $1.00\text{E}+03$



Time = 2.00

Re #(1) = 85.95 , Re #(2) = 90.35

R1 = 1.00 , R2 = 1.00 , Spacing = 6.00

Ambient Temperature = 1000 K

Initial Droplet Temperature = 300 K

Initial Reynolds Number = 100

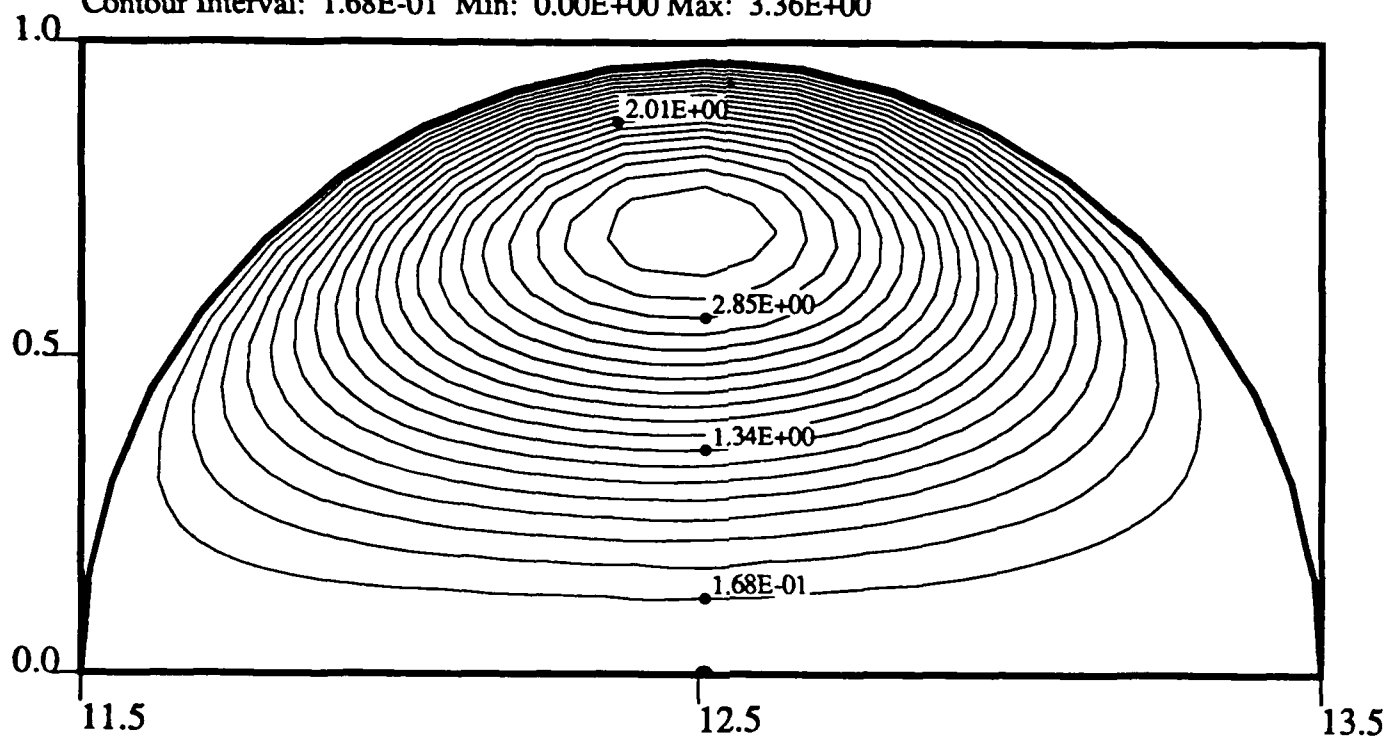
Fuel : n-decane

Initial R1=1, R2=1, Spacing=8

Figure D-13(d) Temperature contour plot at time = 2.

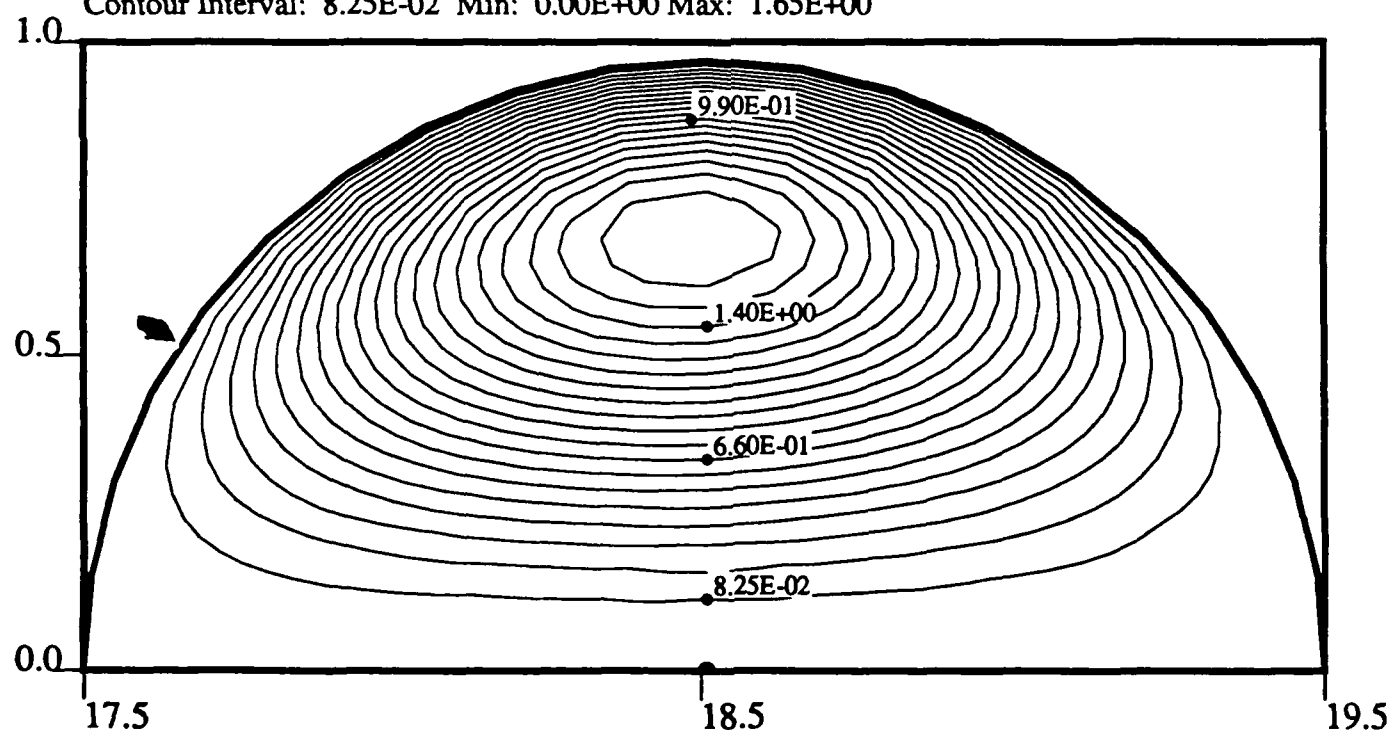
FIRST DROPLET LIQUID PHASE STREAM FUNCTION

Contour Interval: 1.68E-01 Min: 0.00E+00 Max: 3.36E+00



SECOND DROPLET LIQUID PHASE STREAM FUNCTION

Contour Interval: 8.25E-02 Min: 0.00E+00 Max: 1.65E+00



Time = 2.00

Re #(1) = 85.95 , Re #(2) = 90.35

R1 = 1.00 , R2 = 1.00 , Spacing = 6.00

Ambient Temperature= 1000 K

Initial Droplet Temperature= 300 K

Initial Reynolds Number = 100

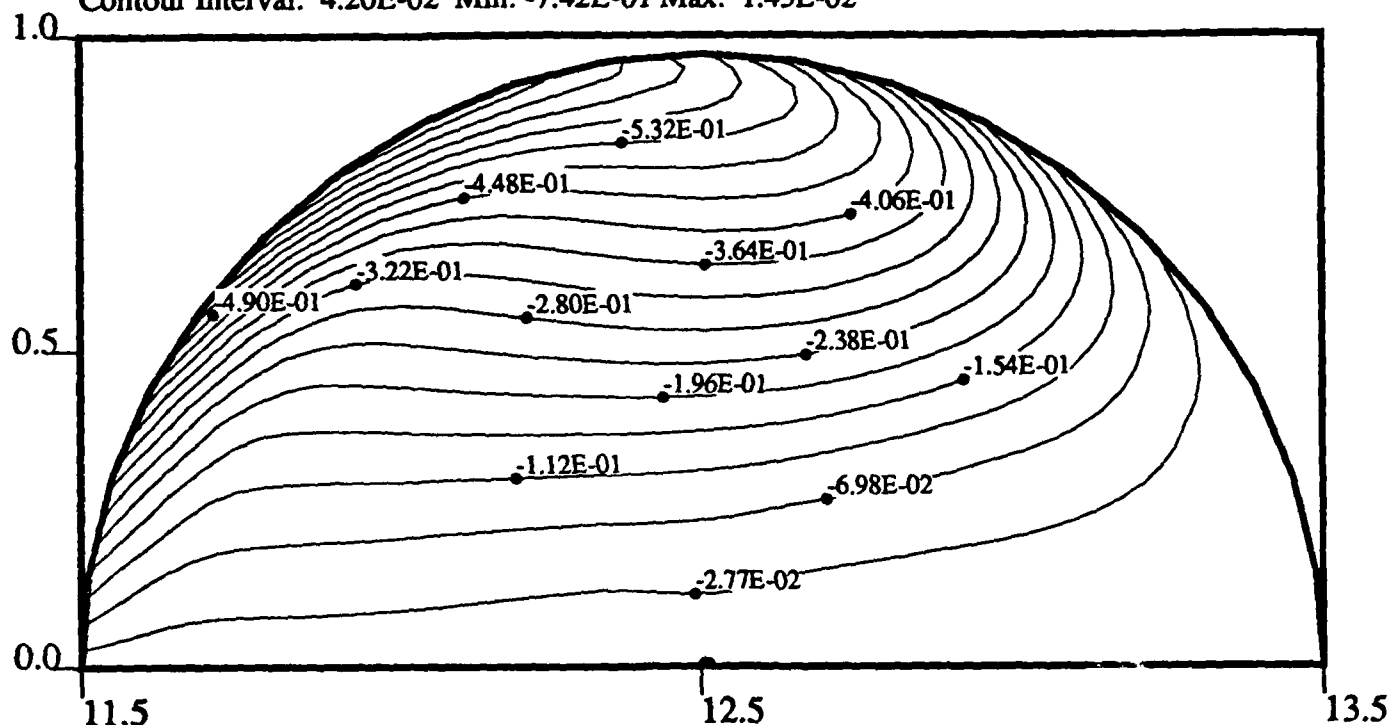
Fuel : n-decane

Initial R1=1, R2=1, Spacing=8

Figure D-13(e) Stream function of liquid phase at time = 2.

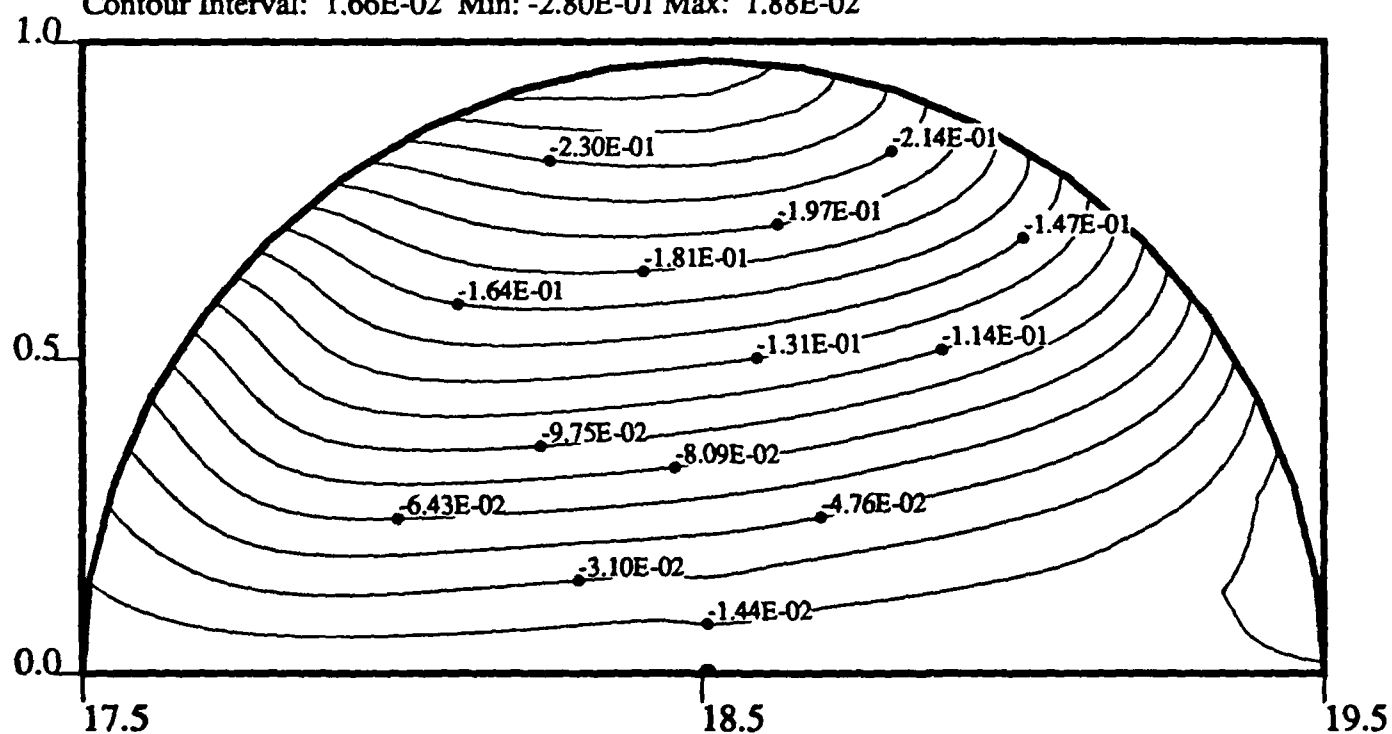
FIRST DROPLET LIQUID PHASE VORTICITY

Contour Interval: 4.20E-02 Min: -7.42E-01 Max: 1.43E-02



SECOND DROPLET LIQUID PHASE VORTICITY

Contour Interval: 1.66E-02 Min: -2.80E-01 Max: 1.88E-02



Time = 2.00

Re #(1) = 85.95 , Re #(2) = 90.35

R1 = 1.00 , R2 = 1.00 , Spacing = 6.00

Ambient Temperature= 1000 K

Initial Droplet Temperature= 300 K

Initial Reynolds Number = 100

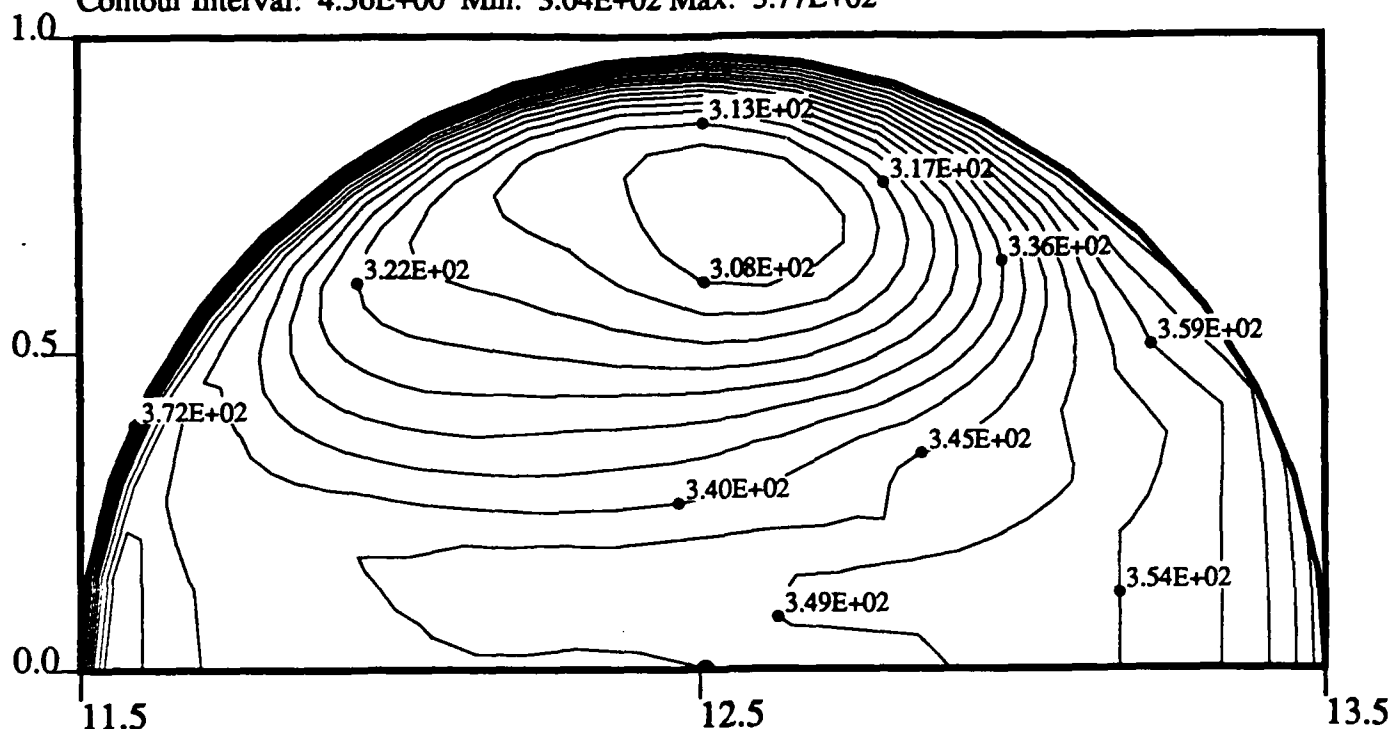
Fuel : n-decane

Initial R1=1, R2=1, Spacing=8

Figure D-13(f) Detailed vorticity contour of liquid phase at time = 2.

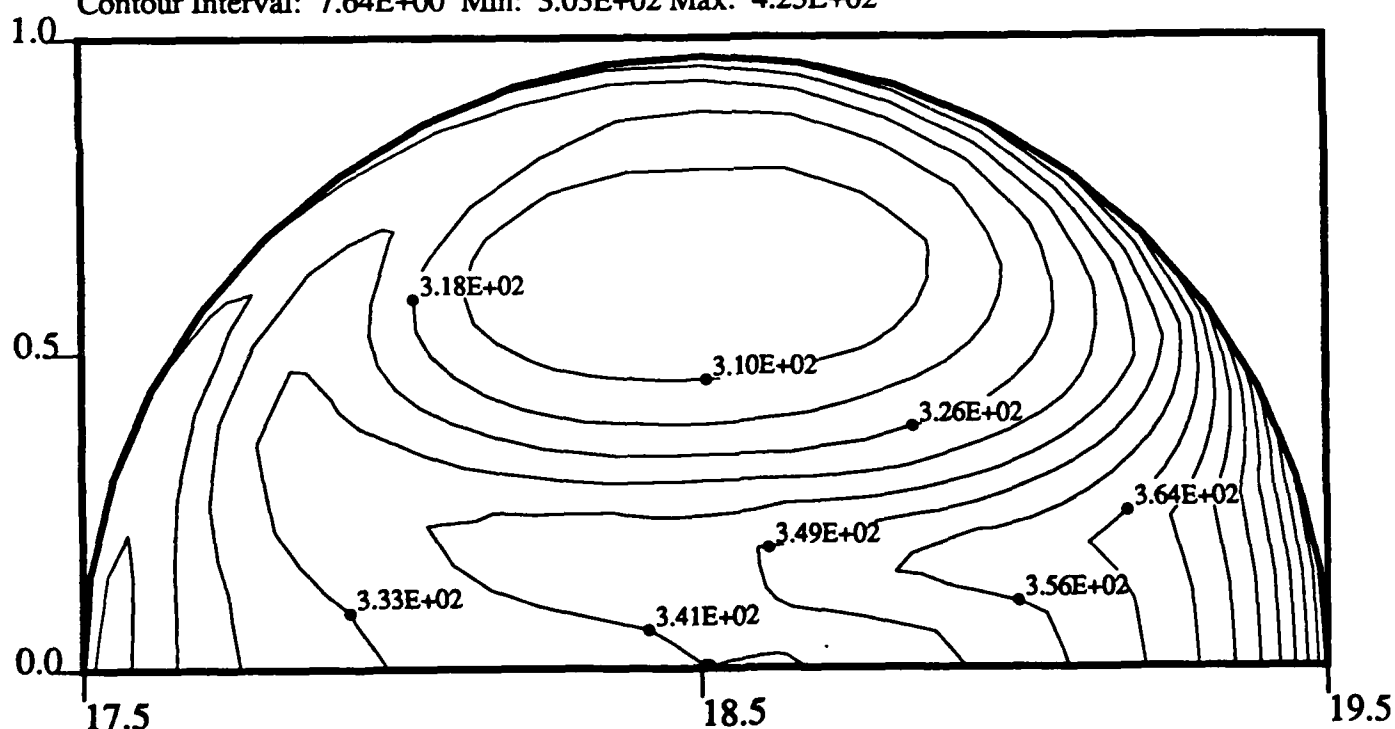
FIRST DROPLET LIQUID PHASE ISOTHERMS

Contour Interval: $4.56\text{E}+00$ Min: $3.04\text{E}+02$ Max: $3.77\text{E}+02$



SECOND DROPLET LIQUID PHASE ISOTHERMS

Contour Interval: $7.64\text{E}+00$ Min: $3.03\text{E}+02$ Max: $4.25\text{E}+02$



Time = 2.00

Re #(1) = 85.95 , Re #(2) = 90.35

R1 = 1.00 , R2 = 1.00 , Spacing = 6.00

Ambient Temperature = 1000 K

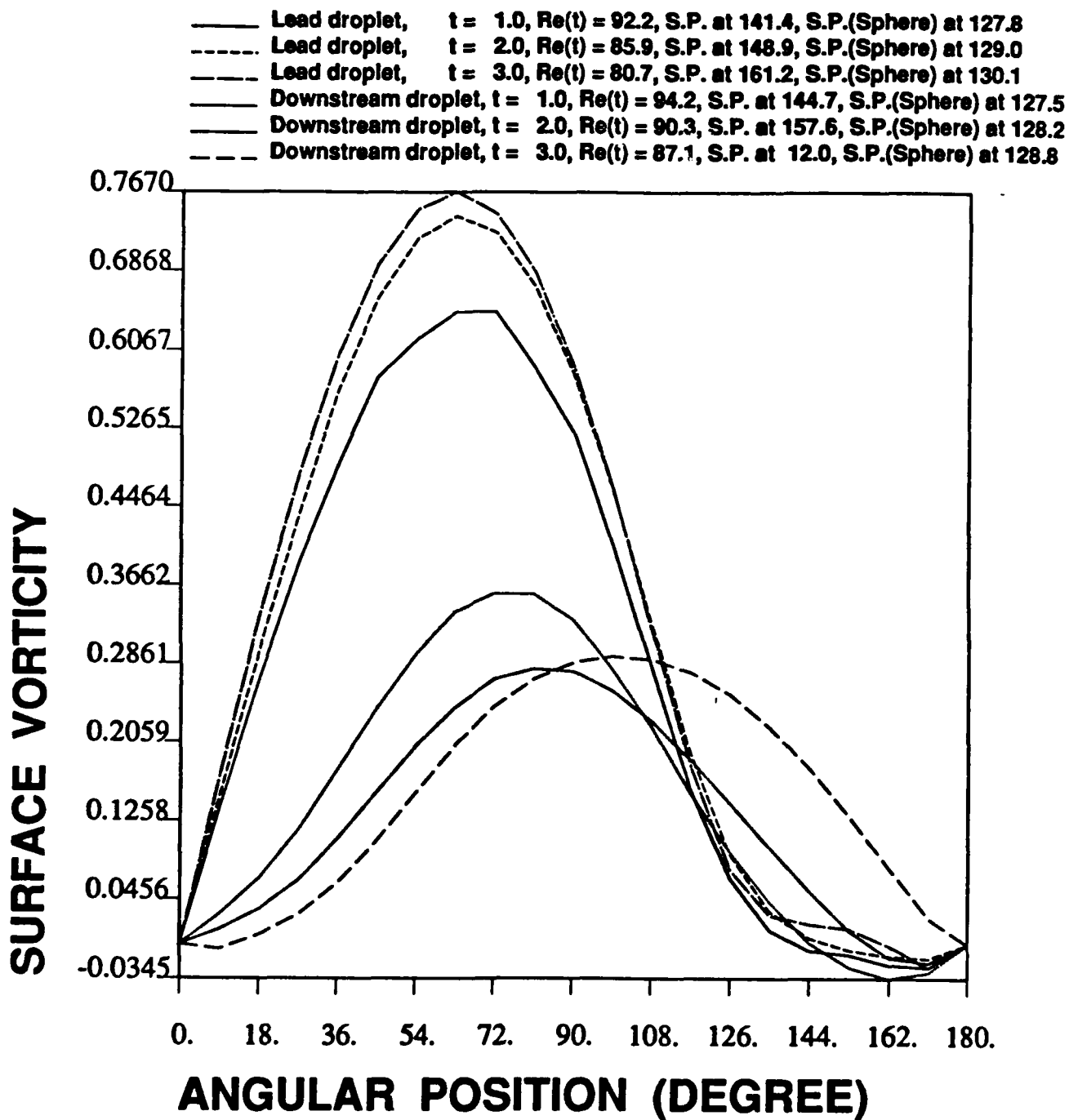
Initial Droplet Temperature = 300 K

Initial Reynolds Number = 100

Fuel : n-decane

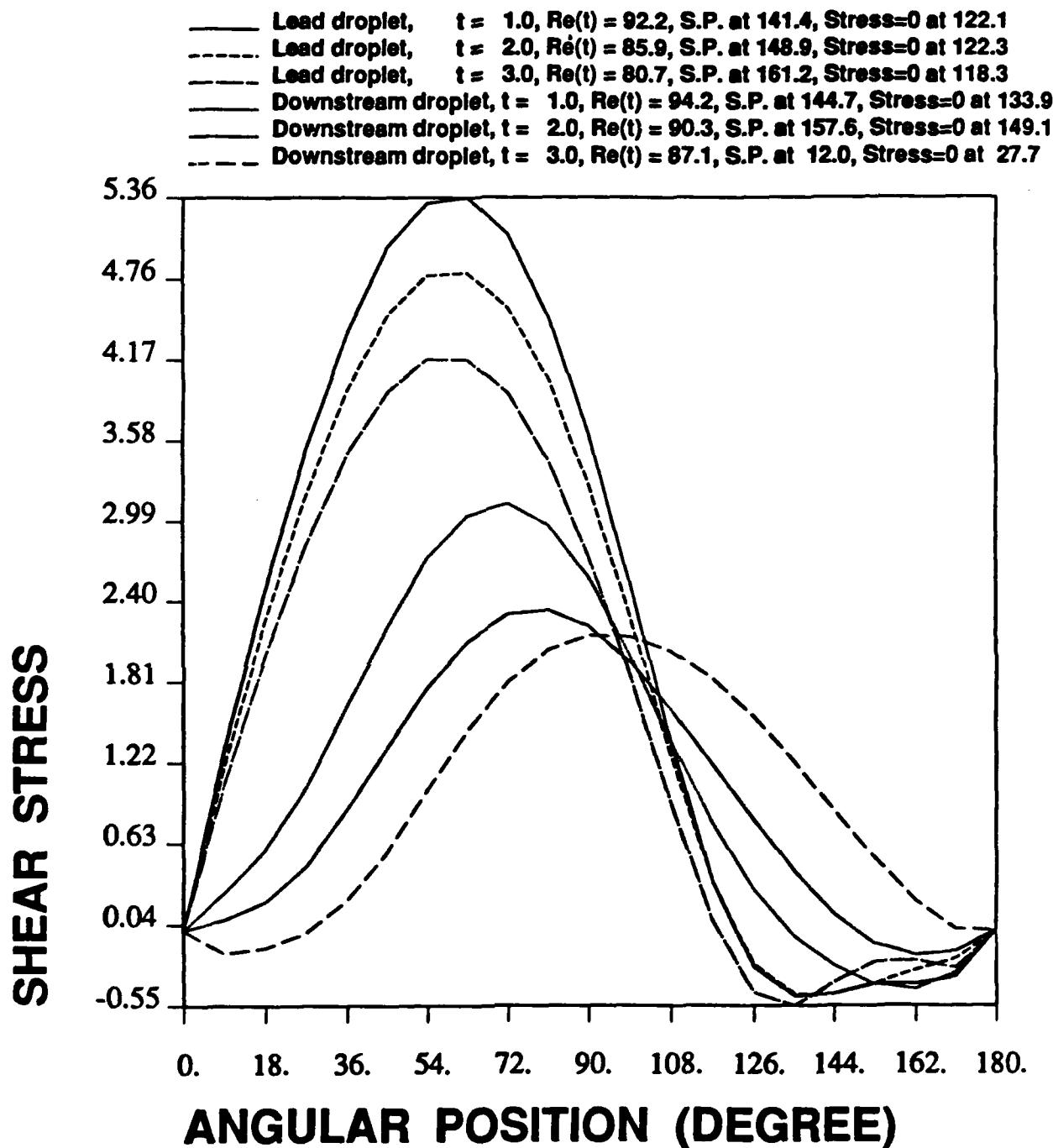
Initial R1=1, R2=1, Spacing=8

Figure D-13(g) Detailed temperature contour of liquid phase at time = 2.



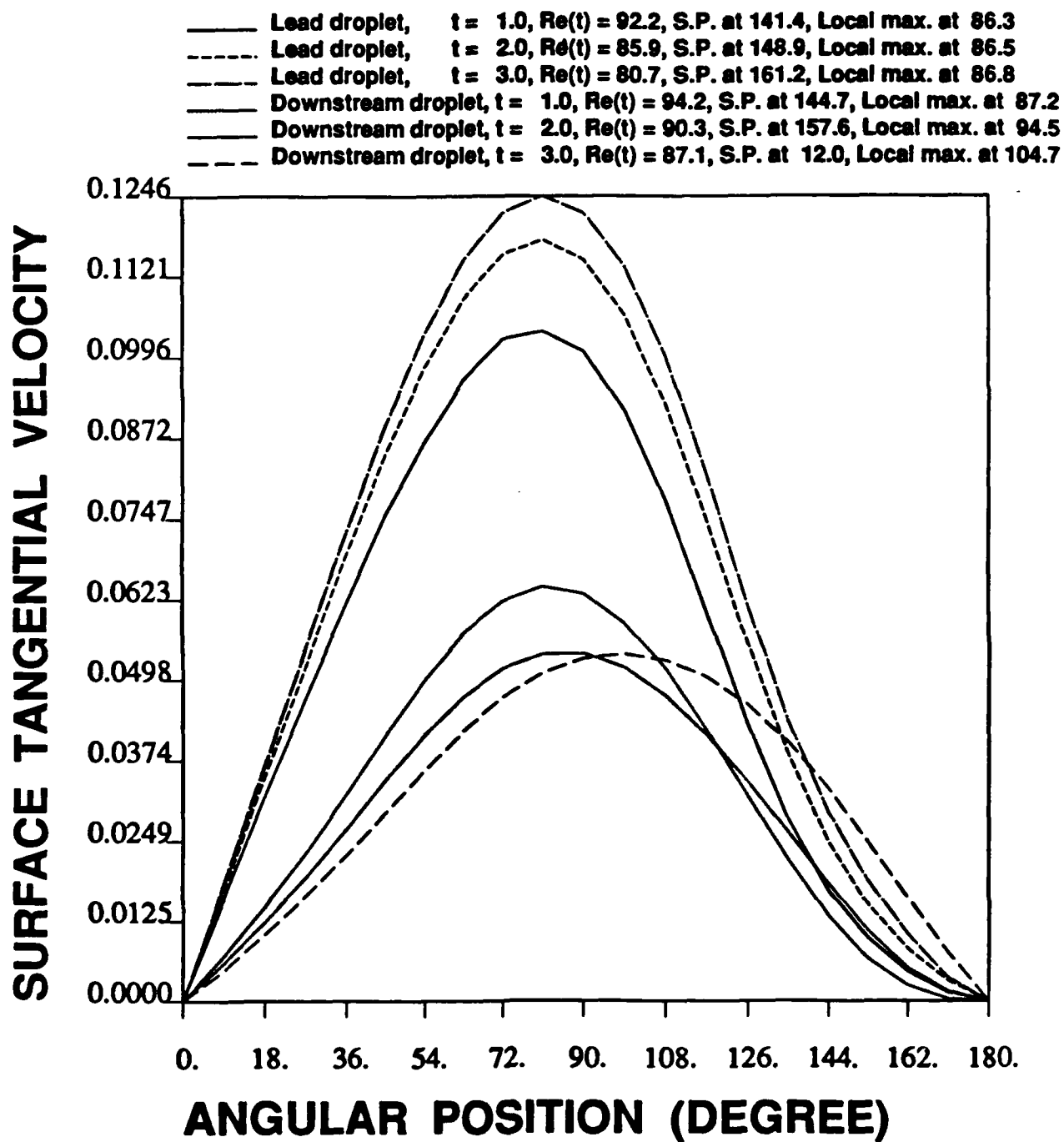
Fuel : N-DECANE
 Ambient Temperature = 1000. K
 Initial Droplet Temperature = 300. K
 Initial Reynolds Number = 100.
 Initial $R1 = 1.00$, $R2 = 1.00$, $D = 8.0$

Figure D-14(a) Surface vorticity distribution at different times for the lead droplet and the downstream droplet.



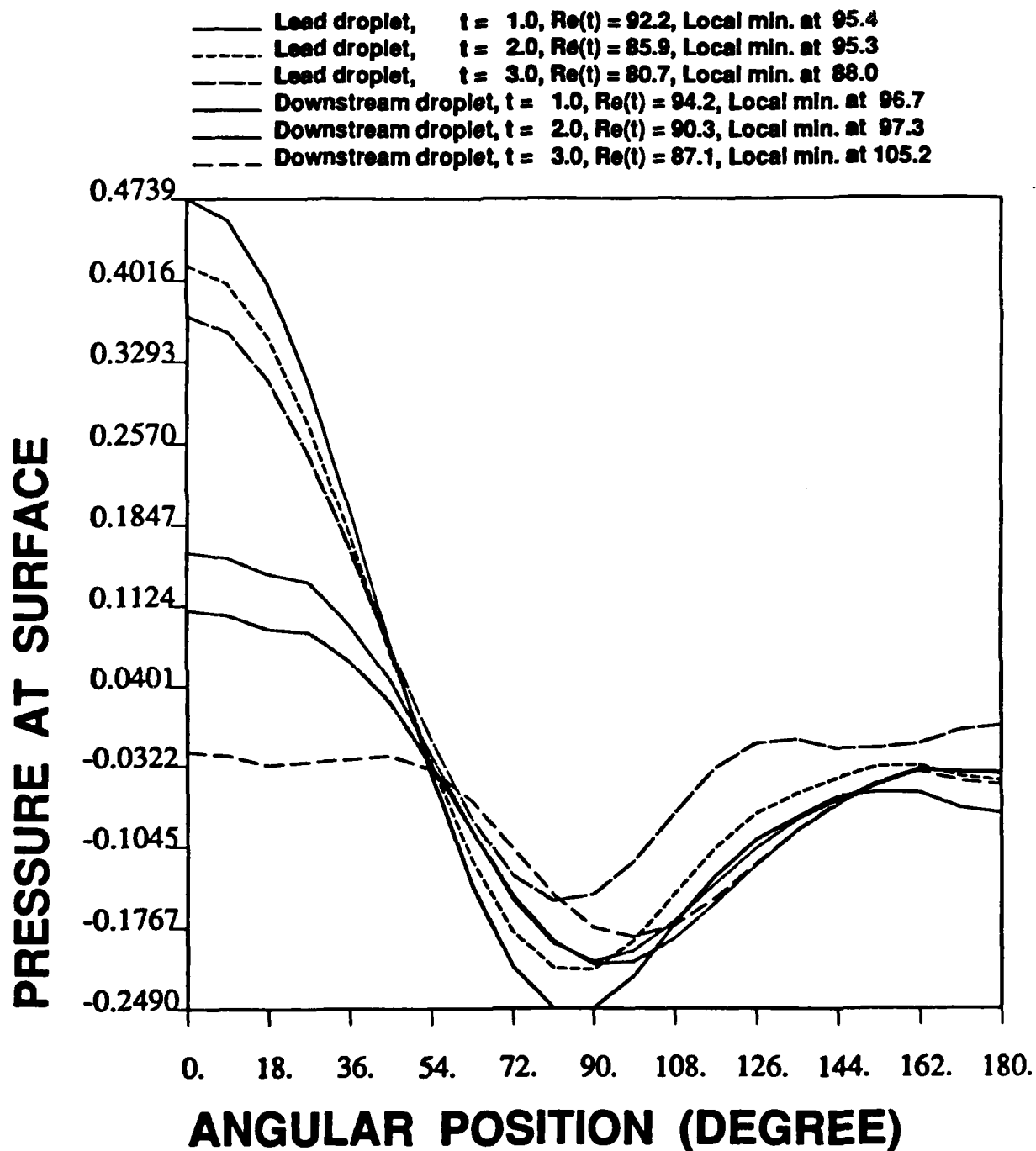
Fuel : N-DECANE
 Ambient Temperature = 1000. K
 Initial Droplet Temperature = 300. K
 Initial Reynolds Number = 100.
 Initial $R1 = 1.00$, $R2 = 1.00$, $D = 8.0$

Figure D-14(b) Surface shear stress distribution at different times for the lead droplet and the downstream droplet.



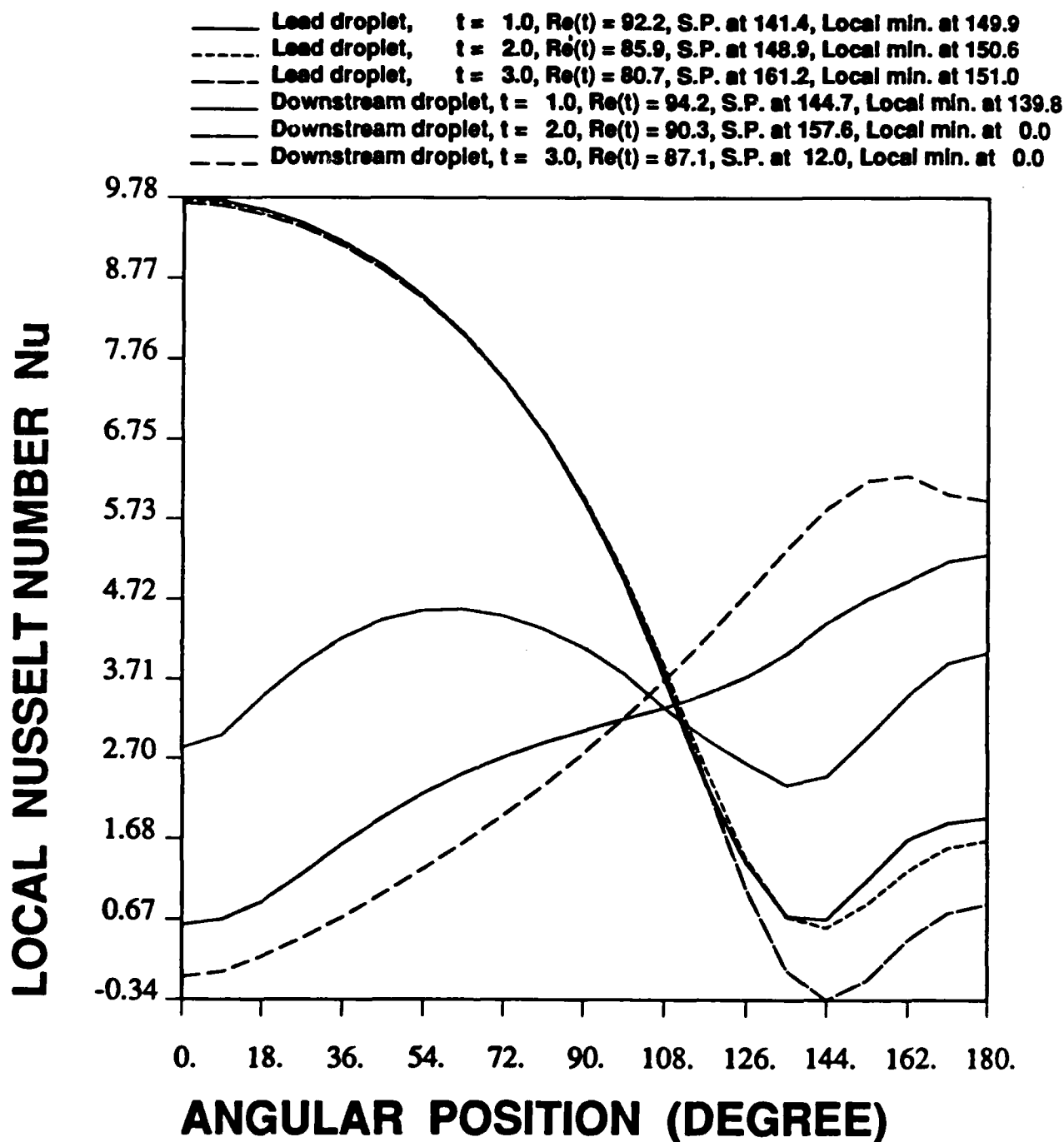
Fuel : N-DECANE
 Ambient Temperature = 1000. K
 Initial Droplet Temperature = 300. K
 Initial Reynolds Number = 100.
 Initial $R1 = 1.00$, $R2 = 1.00$, $D = 8.0$

Figure D-14(c) Surface tangential velocity distribution at different times for the lead droplet and the downstream droplet.



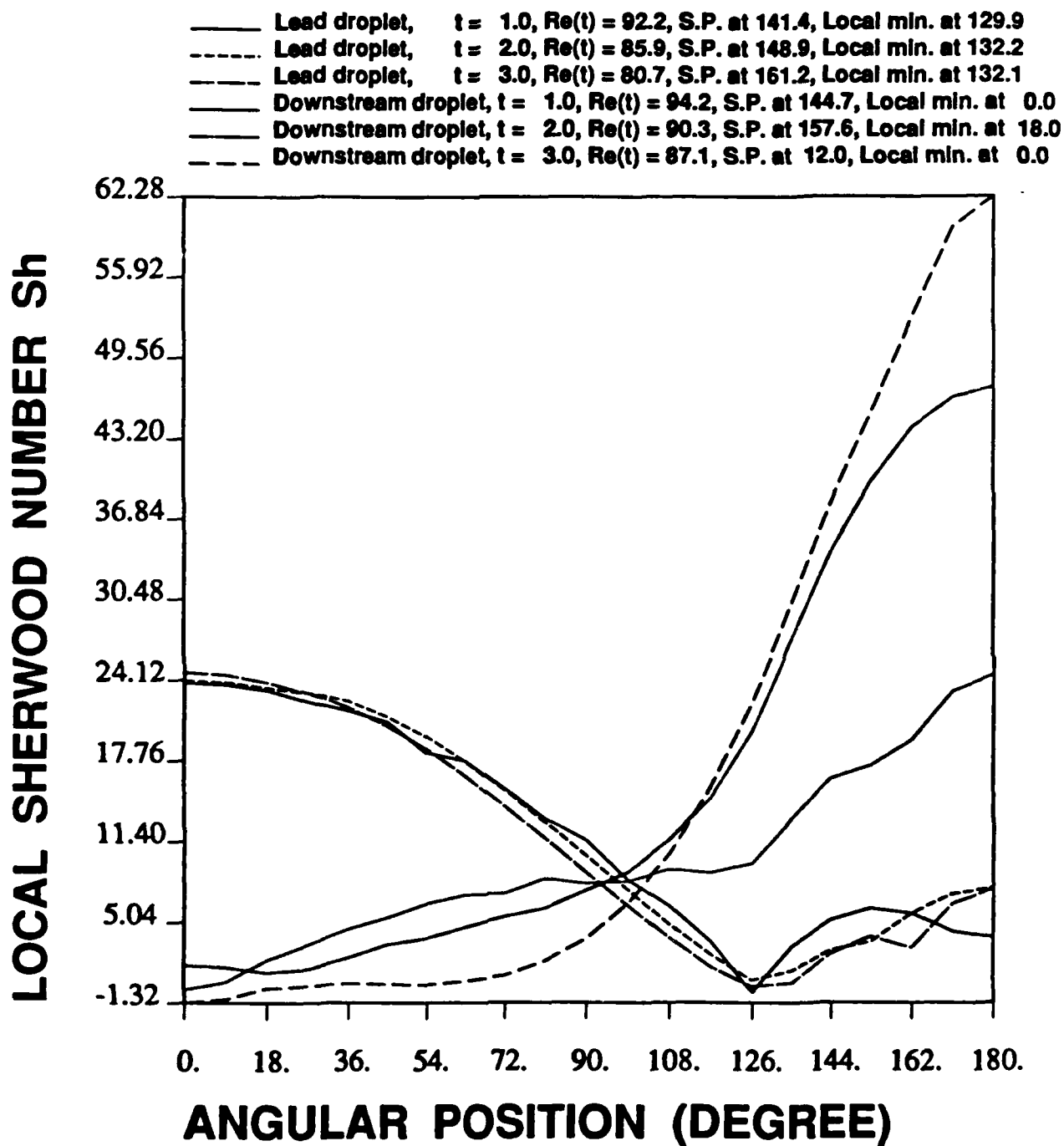
Fuel : N-DECANE
 Ambient Temperature = 1000. K
 Initial Droplet Temperature = 300. K
 Initial Reynolds Number = 100.
 Initial $R1 = 1.00$, $R2 = 1.00$, $D = 8.0$

Figure D-14(d) Surface nondimensional pressure distribution at different times for the lead droplet and the downstream droplet.



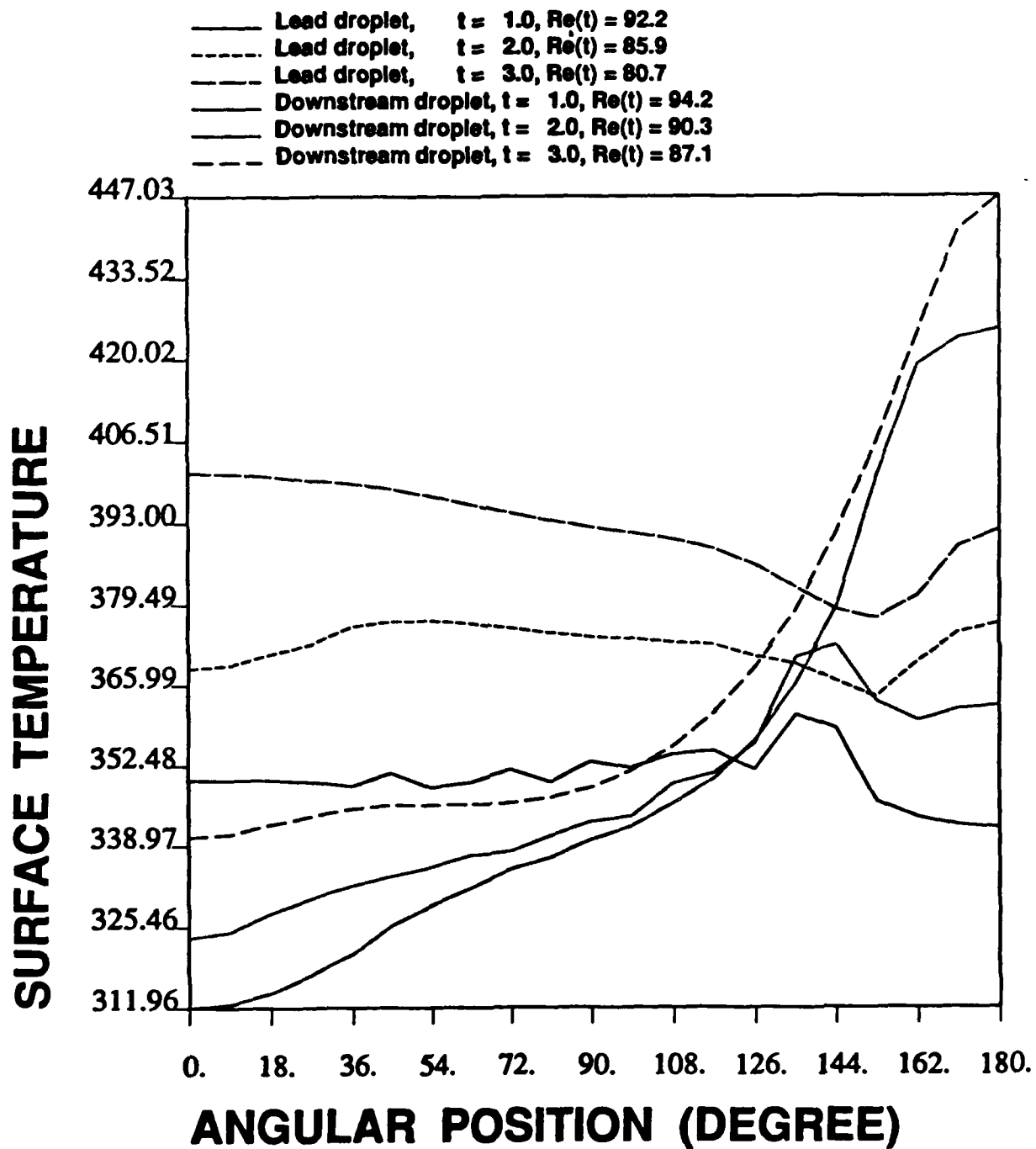
Fuel : N-DECANE
 Ambient Temperature = 1000. K
 Initial Droplet Temperature = 300. K
 Initial Reynolds Number = 100.
 Initial $R1 = 1.00$, $R2 = 1.00$, $D = 8.0$

Figure D-14(e) Local Nusselt number distribution at different times for the lead droplet and the downstream droplet.



Fuel : N-DECANE
 Ambient Temperature = 1000. K
 Initial Droplet Temperature = 300. K
 Initial Reynolds Number = 100.
 Initial $R1 = 1.00$, $R2 = 1.00$, $D = 8.0$

Figure D-14(f) Local Sherwood number distribution at different times for the lead droplet and the downstream droplet.



Fuel : N-DECANE
 Ambient Temperature = 1000. K
 Initial Droplet Temperature = 300. K
 Initial Reynolds Number = 100.
 Initial $R1 = 1.00$, $R2 = 1.00$, $D = 8.0$

Figure D-14(g) Surface temperature distribution at different times.

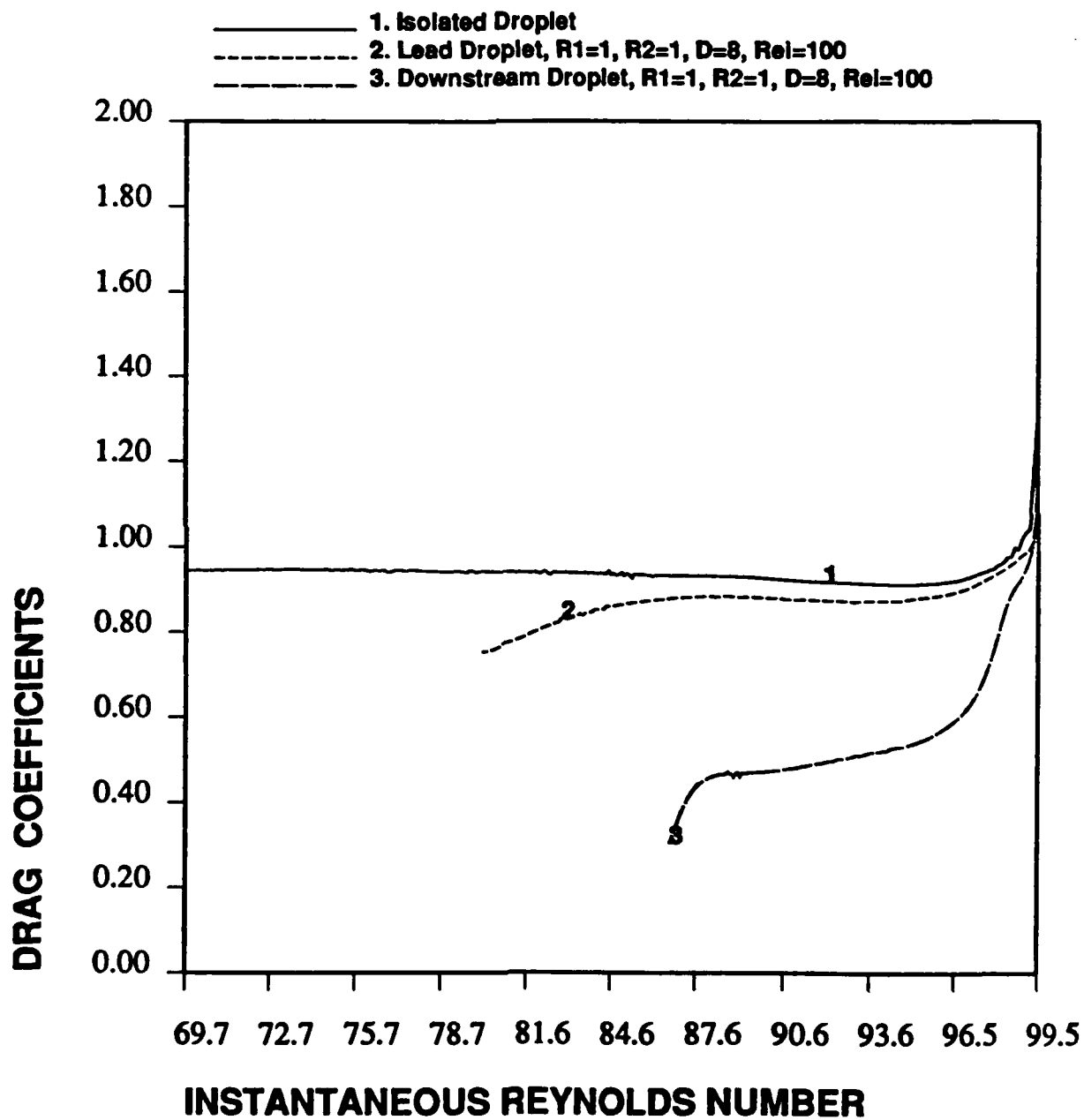


Figure D-15 Time variation of drag coefficients for the lead droplet and the downstream droplet.

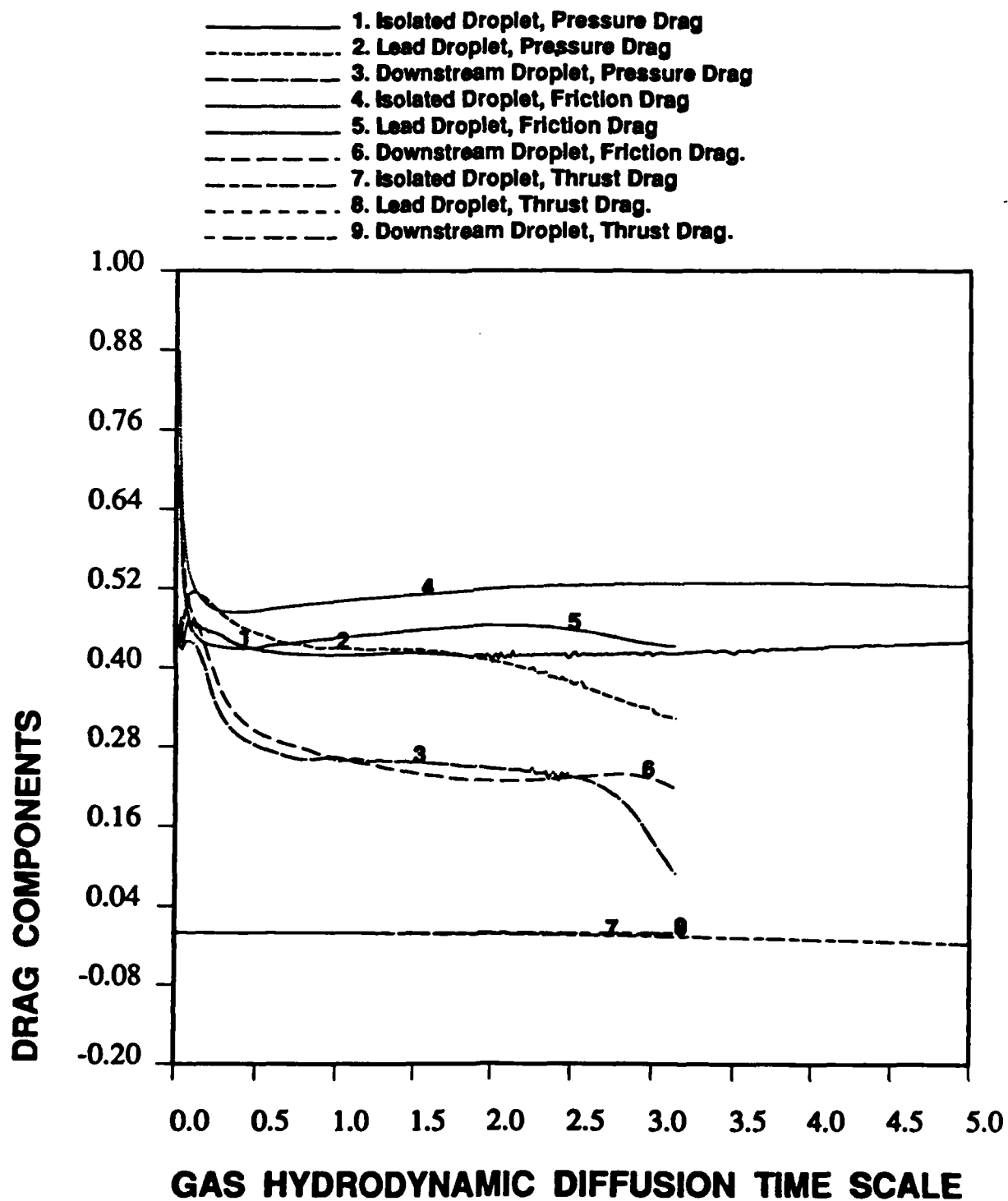


Figure D-16 Time variation of three drag components for the lead droplet and the downstream droplet.

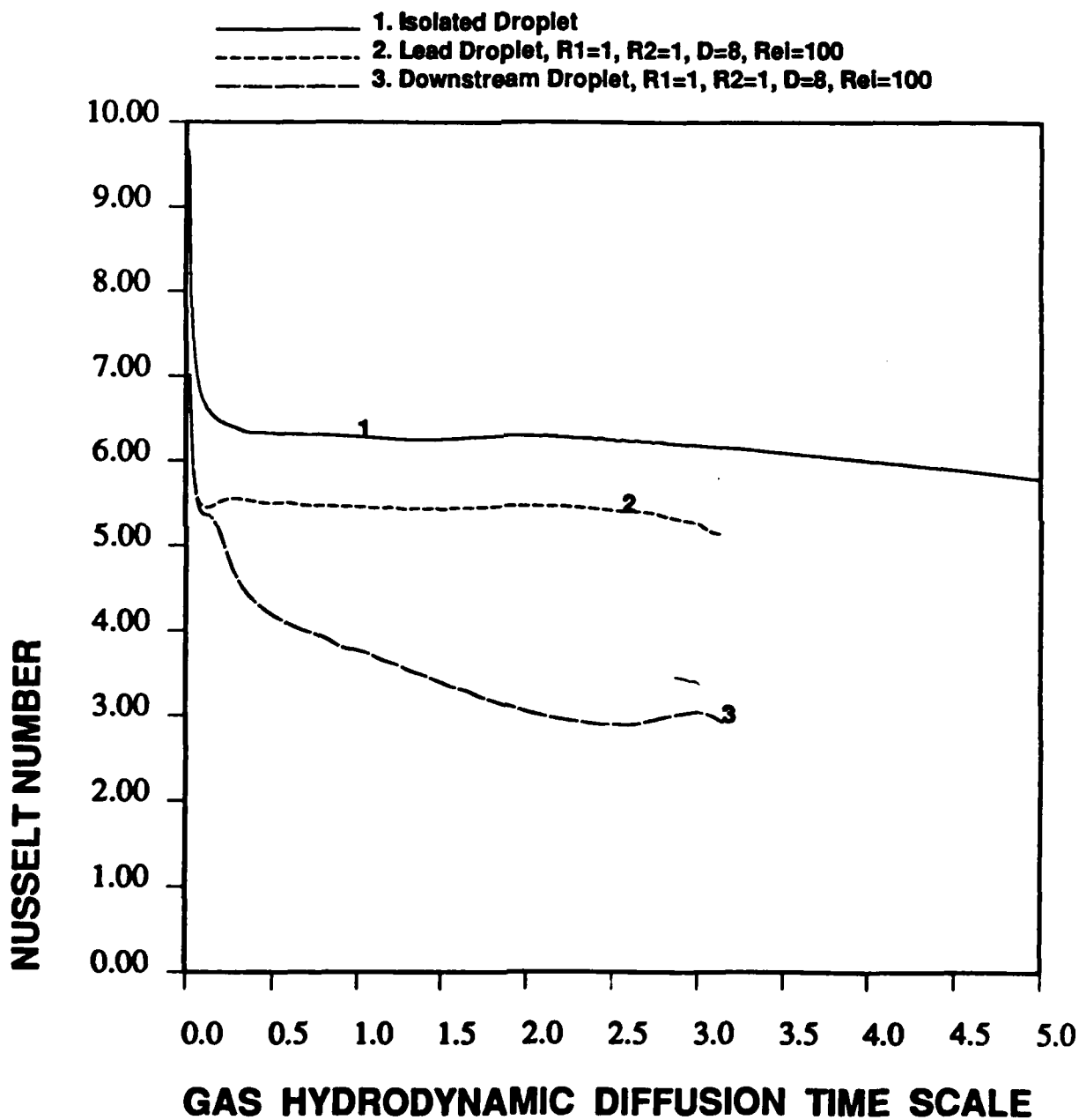


Figure D-17 Time variation of average Nusselt numbers for the lead droplet and the downstream droplet.

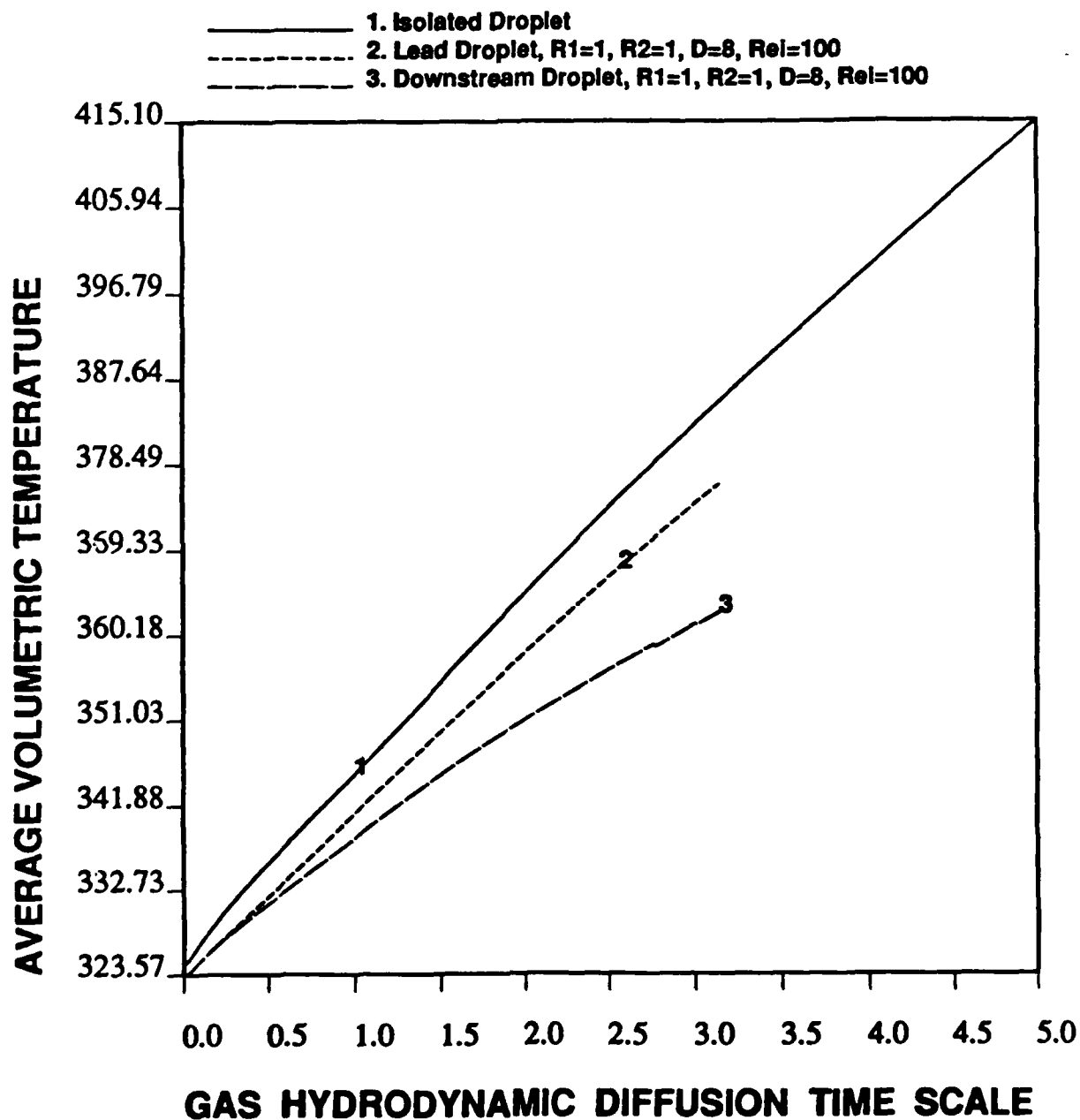


Figure D-18 Time variation of the average volumetric temperature for the lead droplet and the downstream droplet.

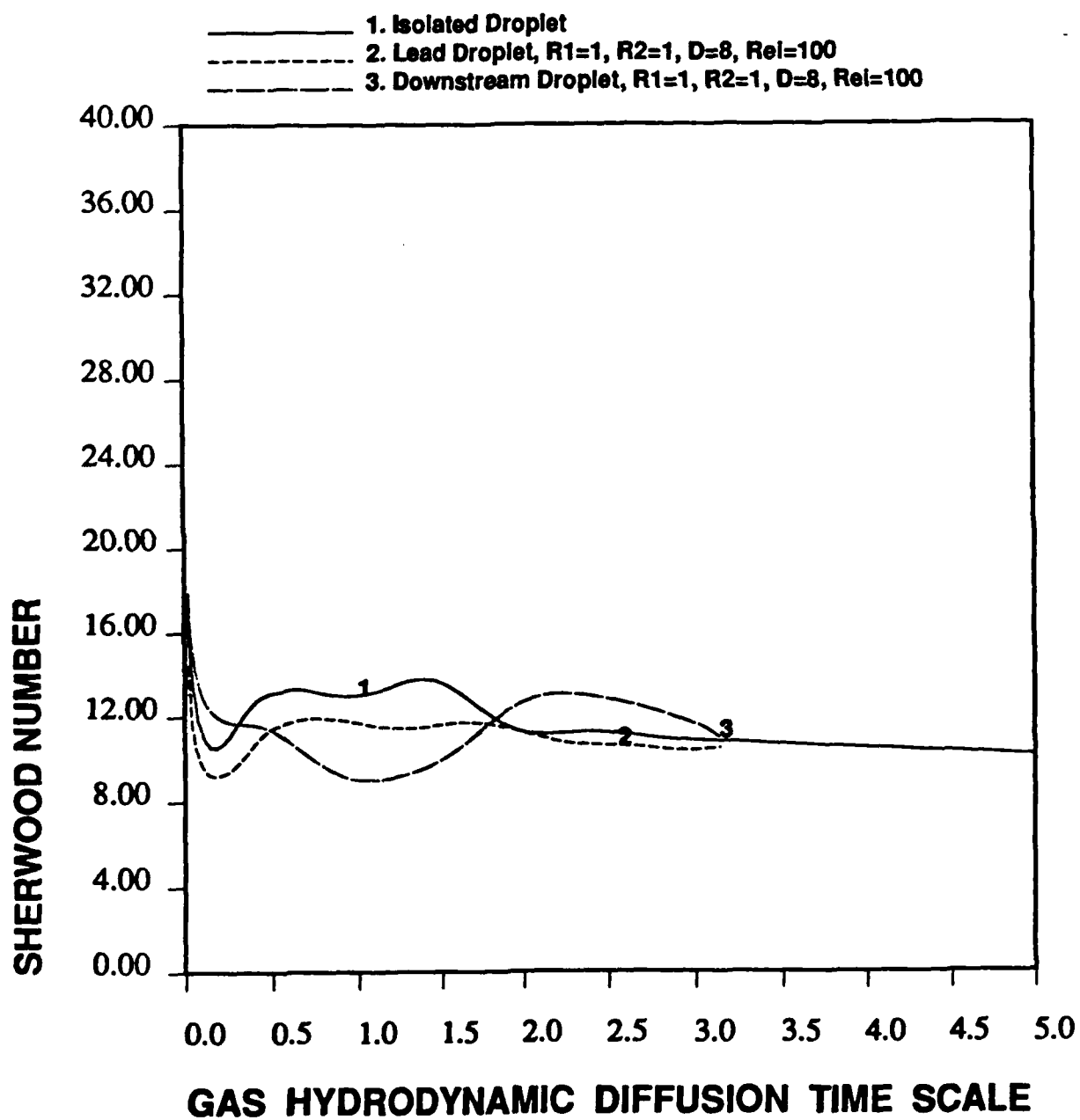


Figure D-19 Time variation of average Sherwood numbers for the lead droplet and the downstream droplet.

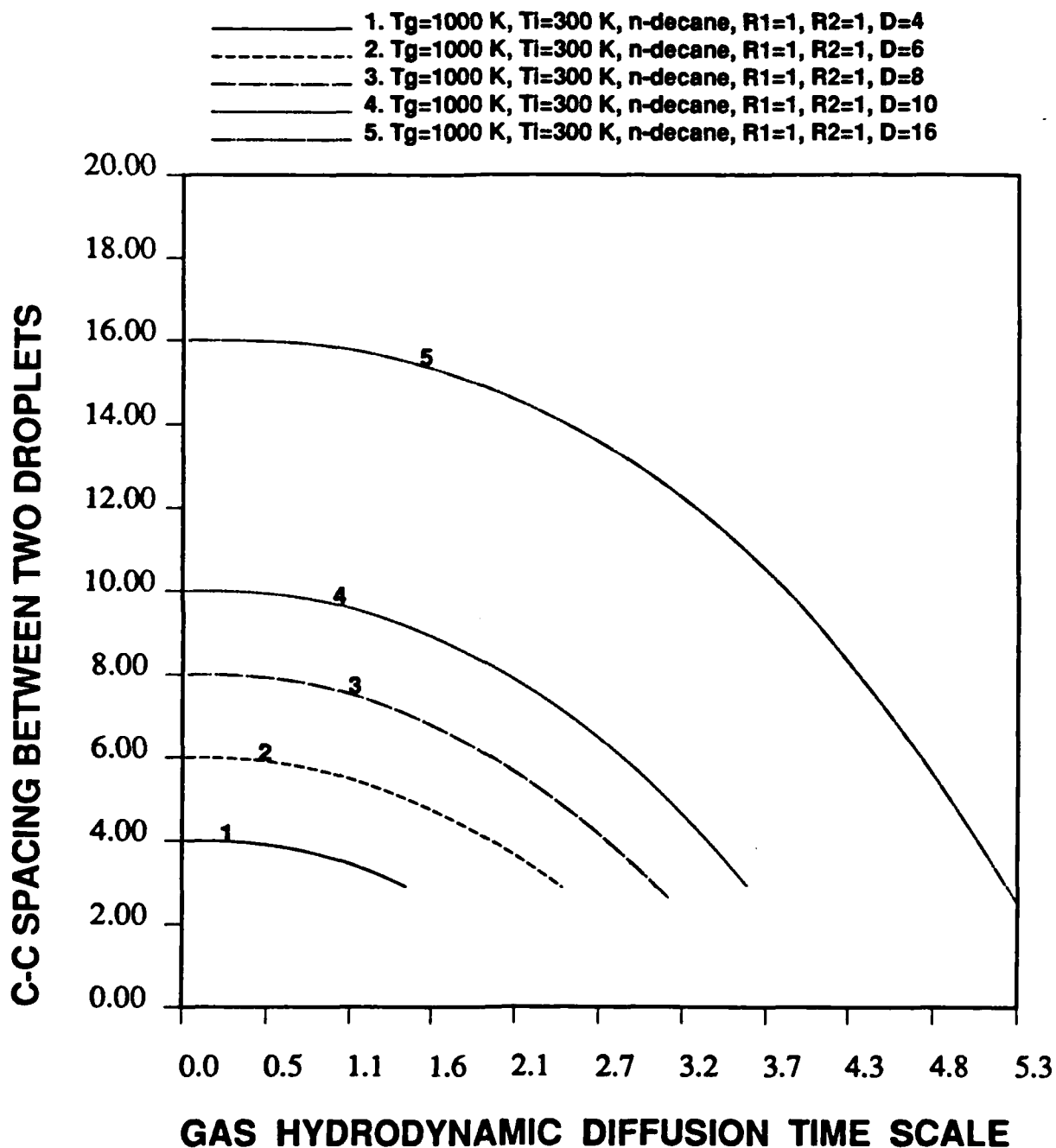


Figure D-20 Time variation of droplet spacing for different initial droplet spacing.

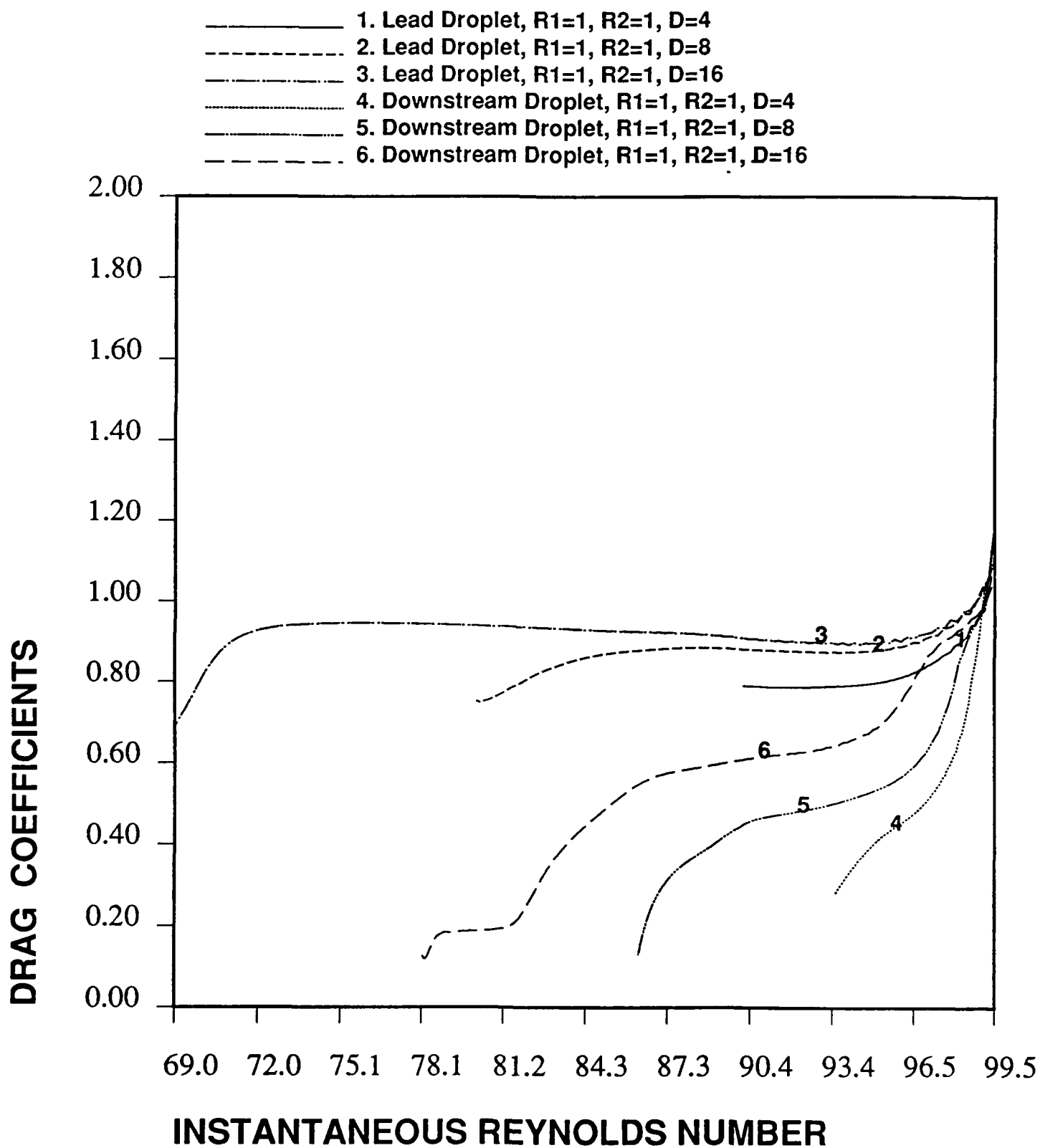


Figure D-21 Time variation of drag coefficients for different initial droplet spacing.

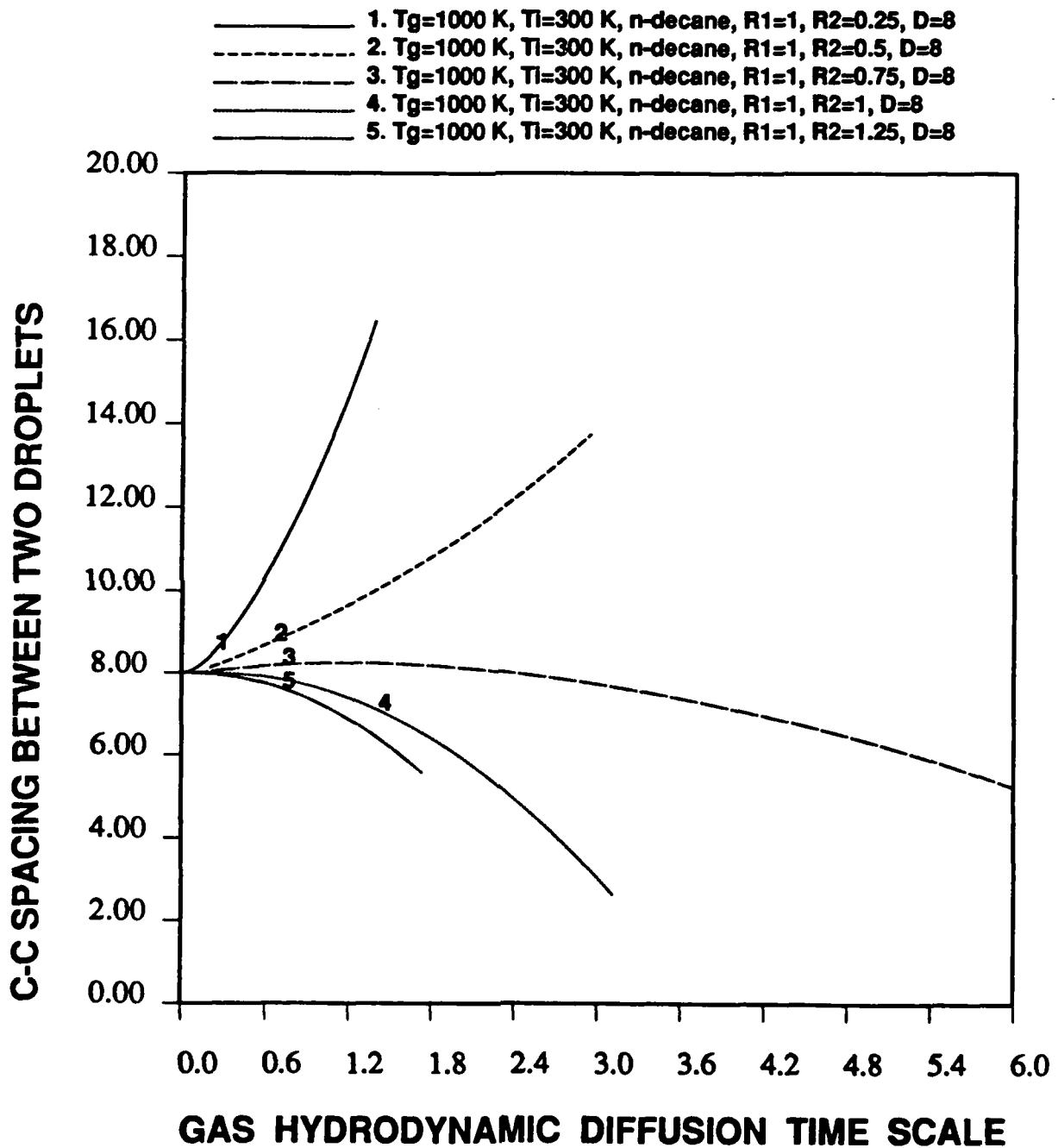


Figure D-22 Time variation of droplet spacings for different downstream droplet radius.

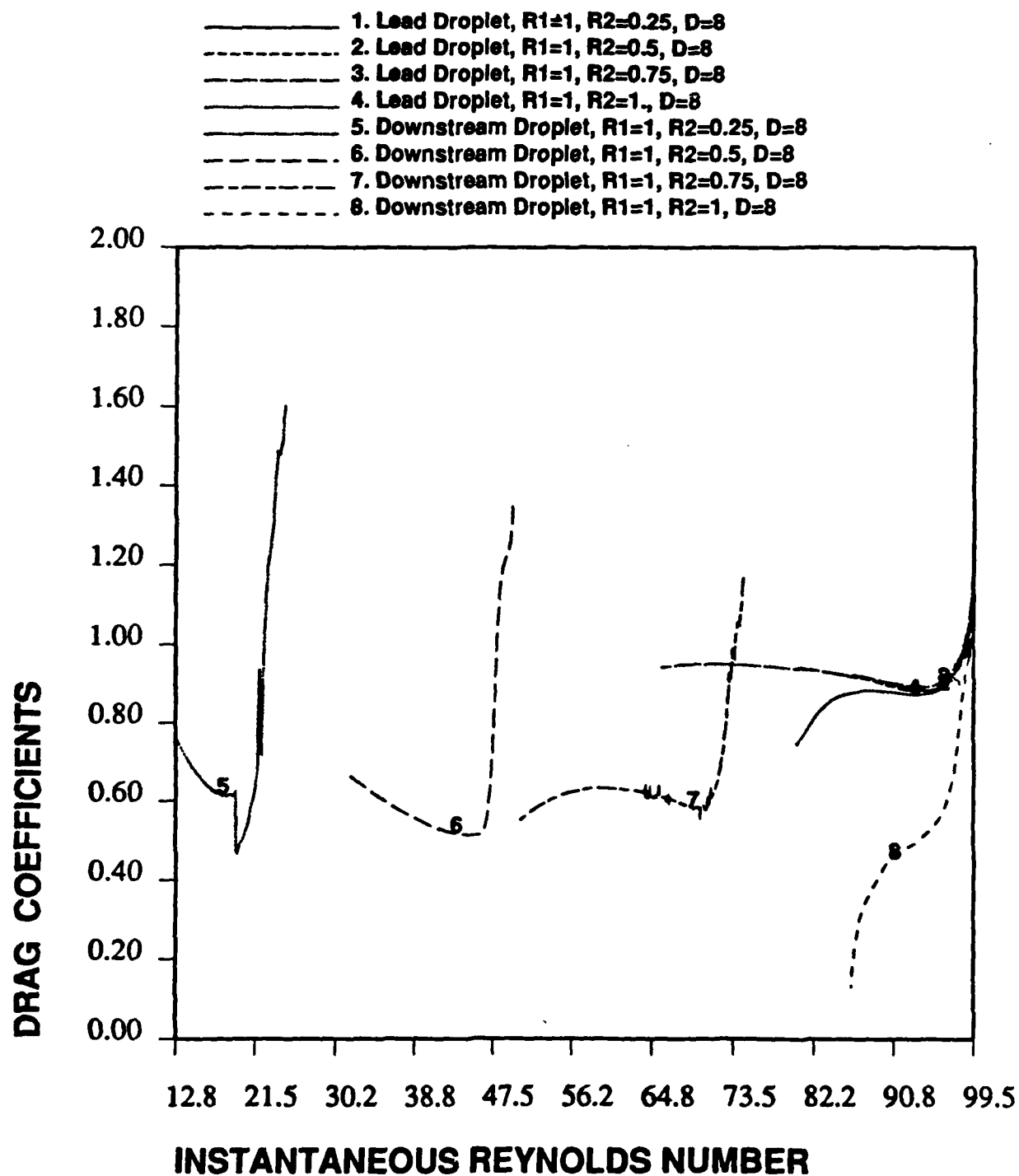


Figure D-23 Time variation of drag coefficients for different downstream droplet radius.

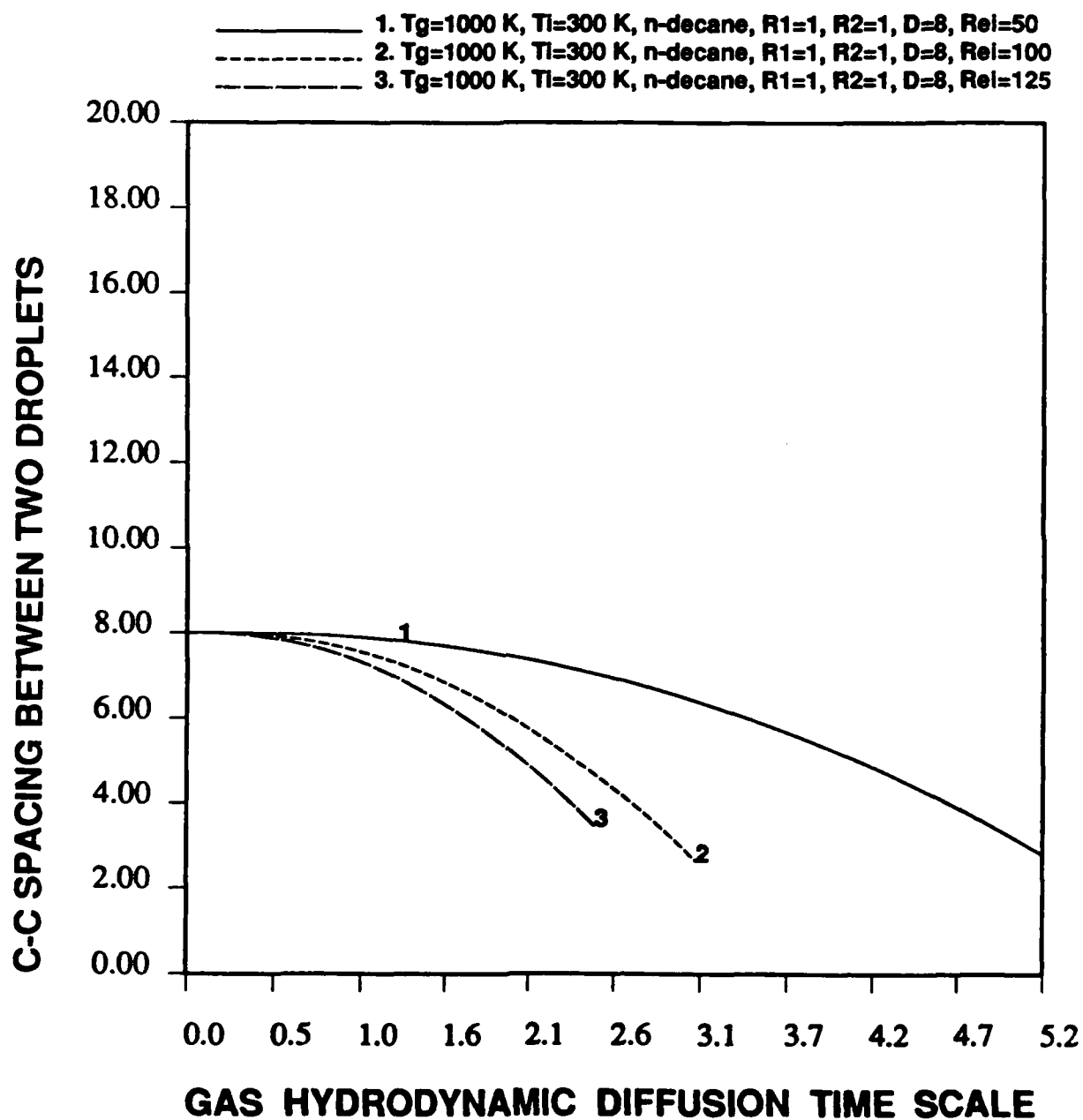


Figure D-24 Time variation of droplet spacings for different initial Reynolds numbers.

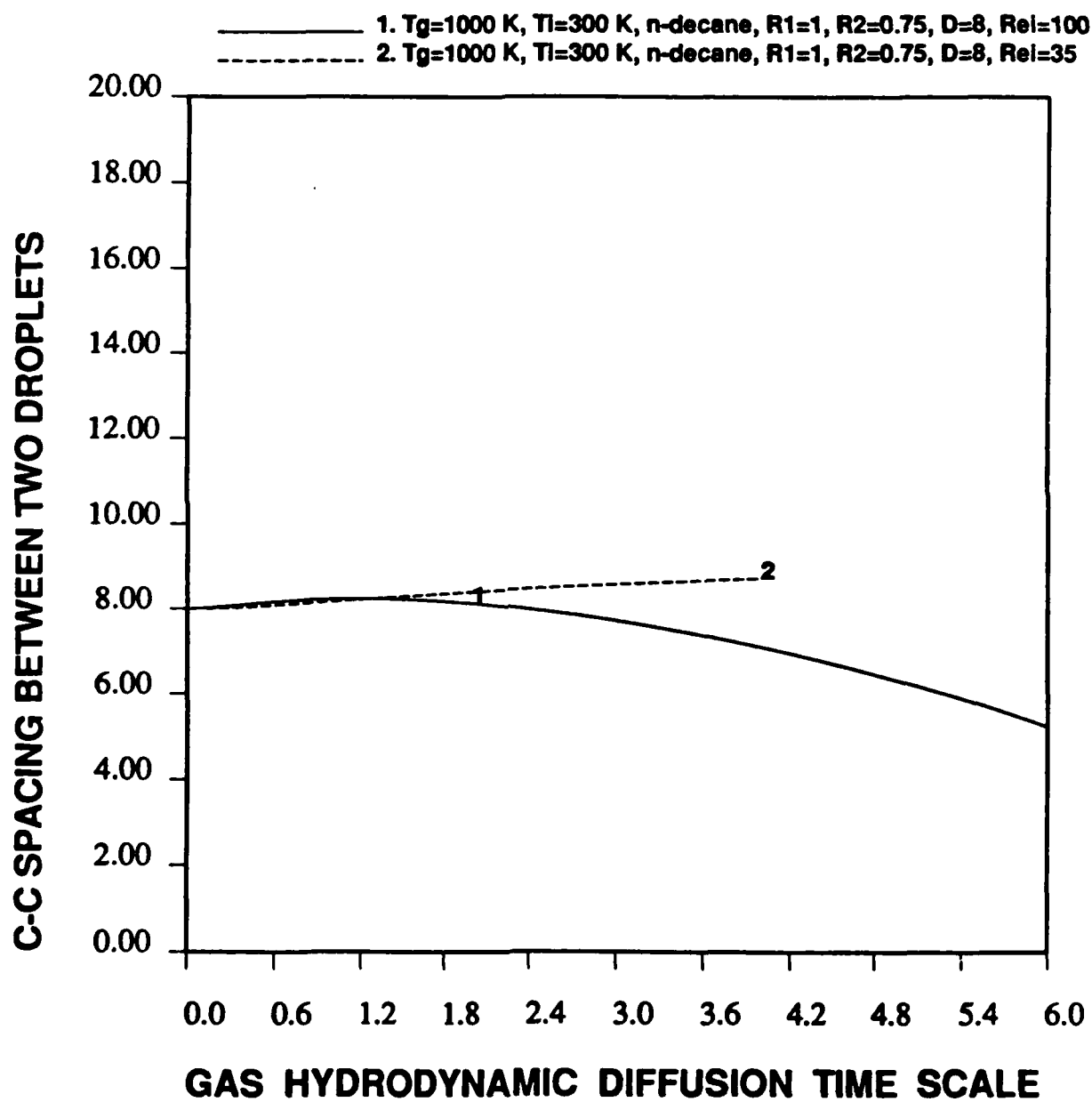


Figure D-25 Change of droplet-motion pattern from coalescence to separation by changing initial Reynolds numbers.

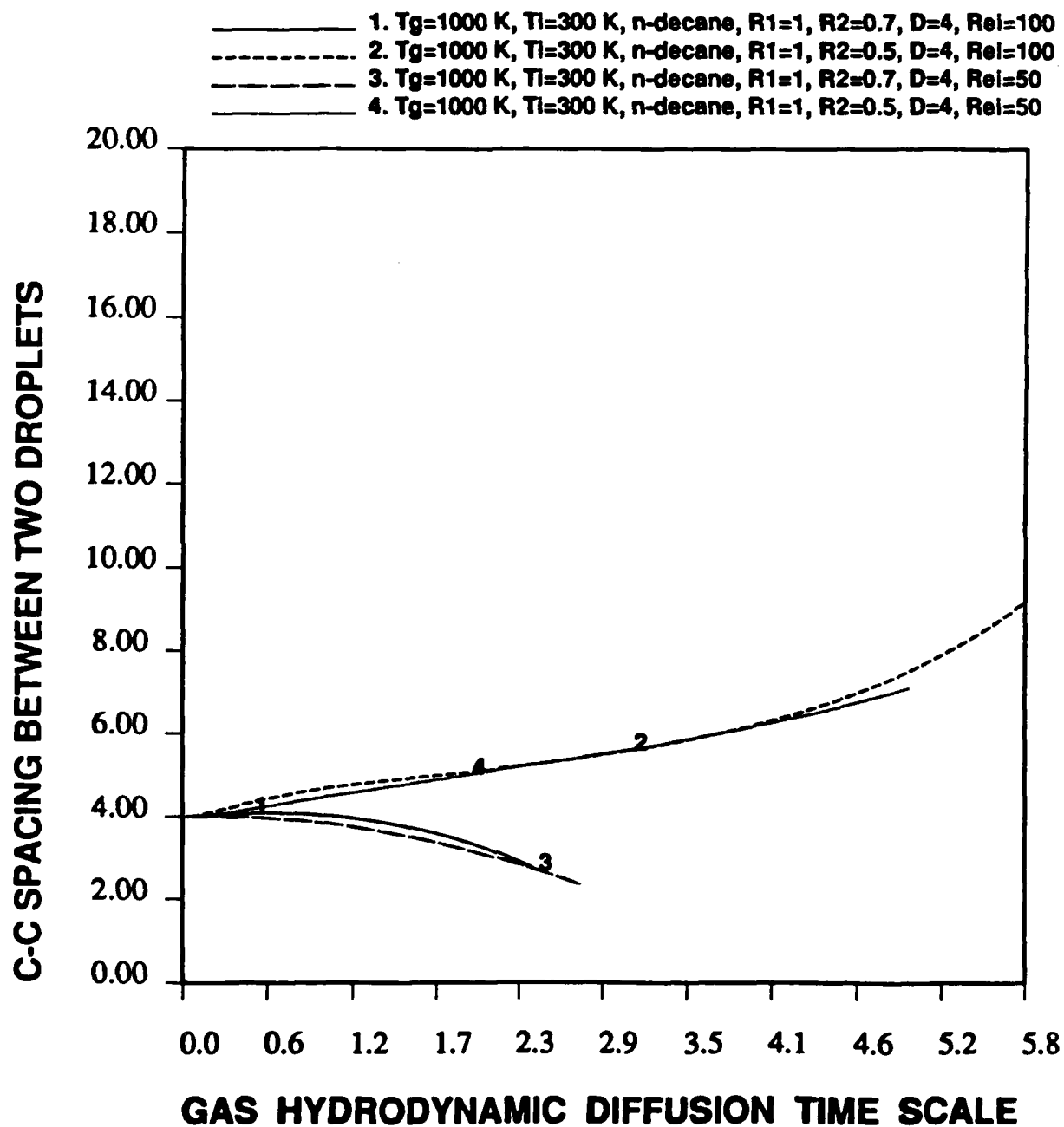


Figure D-26 Time variation of droplet spacings for different downstream droplet radius and different initial Reynolds numbers.